

File ID        uvapub:21073  
Filename      Thesis  
Version        unknown

---

SOURCE (OR PART OF THE FOLLOWING SOURCE):

Type            PhD thesis  
Title            Sea bottom parameter estimation by inversion of underwater acoustic  
                  sonar data  
Author(s)      M. Snellen  
Faculty         FNWI: Informatics Institute (II)  
Year            2002

FULL BIBLIOGRAPHIC DETAILS:

<http://hdl.handle.net/11245/1.203282>

---

*Copyright*

*It is not permitted to download or to forward/distribute the text or part of it without the consent of the author(s) and/or copyright holder(s), other than for strictly personal, individual use, unless the work is under an open content licence (like Creative Commons).*

---

Mirjam Snellen

**Sea bottom  
parameter  
estimation by  
inversion of  
underwater  
acoustic sonar  
data**



# Sea Bottom Parameter Estimation by Inversion of Underwater Acoustic Sonar Data

ACADEMISCH PROEFSCHRIFT

ter verkrijging van de graad van doctor aan de  
Universiteit van Amsterdam  
op gezag van de Rector Magnificus  
prof.mr. P.F. van der Heijden  
ten overstaan van een door het college voor  
promoties ingestelde commissie in het openbaar  
te verdedigen in de Aula der Universiteit  
op dinsdag 11 juni 2002, te 14:00 uur

door

MIRJAM SNELLEN

geboren te Amsterdam

PROMOTIECOMMISSIE:

Promotor: Prof.dr.ir.F.C.A. Groen

Co-promotor: Dr. D.G. Simons

Commissie: Prof.dr.ir. A. Gisolf  
Prof.dr.ir. G. Blacquièrè  
Prof. ir. C. van Schooneveld  
Prof.dr. P.M.A. Sloom  
Dr. W. Hoffmann

Faculteit der Natuurwetenschappen, Wiskunde en Informatica  
Universiteit van Amsterdam  
Plantage Muidergracht 24  
1018 TV Amsterdam

This work was carried out at the Underwater Acoustics Group of the TNO Physics and Electronics Laboratory and was sponsored by the Royal Netherlands Navy

# Contents

1	GENERAL INTRODUCTION .....	1
2	SEABED EFFECTS ON UNDERWATER ACOUSTIC PROPAGATION .....	5
2.1	Introduction	5
2.2	Propagation of sound through the water	5
2.3	The ocean-acoustic environment	6
2.3.1	The water column	6
2.3.2	The seafloor	7
2.4	Normal-mode solution of the wave equation	10
2.4.1	The normal-mode technique	10
2.4.2	Range-dependency through the adiabatic approximation	16
2.5	Examples	17
2.5.1	Interaction of sound with the seafloor	18
2.5.2	Influence of bottom type on transmission loss and received signal shape	23
2.5.3	An example from practice: a model validation exercise	27
3	SINGLE-FREQUENCY AND MULTI-FREQUENCY MATCHED FIELD INVERSION USING A GENETIC ALGORITHM.....	37
3.1	Introduction	37
3.2	The Genetic algorithm and simulated annealing	38
3.2.1	Genetic algorithms	38
3.2.2	Simulated annealing	40
3.3	Applying the GA for Matched Field Inversion	41
3.3.1	The acoustic problem	41
3.3.2	Setting of the GA parameters	43
3.4	Results	44
3.4.1	Single-frequency results	45
3.4.2	Multi-frequency results	53
3.5	Summary and conclusions	57
4	MULTI-FREQUENCY MATCHED FIELD INVERSION OF BENCHMARK DATA USING A GENETIC ALGORITHM.....	59
4.1	Introduction	59
4.2	The forward acoustic model	60
4.3	The test cases selected for inversion	62
4.4	The genetic algorithm	63
4.5	Results	66
4.6	Summary and conclusions	71
4.7	Acknowledgments	72

5	AN ENVIRONMENTAL ASSESSMENT IN THE STRAIT OF SICILY: MEASUREMENT AND ANALYSIS TECHNIQUES FOR DETERMINING BOTTOM AND OCEANOGRAPHIC PROPERTIES.....	75
5.1	Introduction	76
5.2	The EnVerse 97 experiments	77
5.2.1	Acoustic propagation measurements	77
5.2.2	Oceanographic measurements	78
5.2.3	Seismic analysis	85
5.3	Acoustic inversion method	88
5.3.1	The forward acoustic propagation	88
5.3.2	The geo-acoustic model for Adventure Bank	89
5.3.3	Matched field objective function	90
5.3.4	The Genetic Algorithm	90
5.3.5	Quality of the inversion results	91
5.4	Results and analysis	91
5.4.1	Assessment of the inversion results	93
5.4.2	Effect of sound speed variability on inversion	100
5.4.3	Layer speed and thickness sensitivity	102
5.5	Conclusions	102
5.6	Acknowledgments	103
6	AN EVALUATION OF THE ACCURACY OF SHALLOW WATER MATCHED FIELD INVERSION RESULTS.....	107
6.1	Introduction	108
6.2	The ADVENT99 experiment	109
6.2.1	Acoustic measurements	109
6.2.2	Ocean environmental measurements	111
6.3	Acoustic inversion method	117
6.3.1	The objective function	117
6.3.2	The genetic algorithm	118
6.3.3	The acoustic problem	119
6.4	Results and discussion	120
6.4.1	Assessment of the parameter estimates	122
6.4.2	Assessment of the parameter uncertainties	127
6.5	Summary and conclusions	133
6.6	Acknowledgements	133

7	APPLICATION OF THE DOWNHILL SIMPLEX ALGORITHM TO REDUCE THE UNCERTAINTY IN MATCHED FIELD INVERSION RESULTS .....	135
7.1	Introduction	135
7.2	The ADVENT99 experiment	137
7.3	Acoustic inversion method	137
7.3.1	The objective function	137
7.3.2	Global optimization: the genetic algorithm	138
7.3.3	Local optimization: The downhill simplex method	138
7.3.4	The acoustic problem	139
7.4	Inversion results	140
7.4.1	Applying DHS to SIM1 inversions	140
7.4.2	Applying DHS to the SIM2 inversion results	143
7.4.3	Applying DHS to the EXP results	144
7.4.4	Discussion	145
7.5	Cramer-Rao bounds	147
7.6	Conclusions	150
7.7	Acknowledgements	151
8	INVERSION FOR GEO-ACOUSTIC BOTTOM PARAMETERS AND THE WATER COLUMN SOUND SPEED PROFILE .....	153
8.1	Introduction	153
8.2	The ADVENT99 experiment	154
8.3	Empirical orthogonal functions	155
8.4	The inversion method	158
8.5	Results	159
8.6	Summary and conclusions	164
9	BOTTOM CLASSIFICATION CAPABILITIES OF MATCHED FIELD INVERSION .....	167
9.1	Introduction	167
9.2	The MAPEX experiments	167
9.3	Acoustic inversion method	169
9.4	Results	170
9.4.1	Malta Plateau	170
9.4.2	North of Elba	172
9.4.3	Southeast of Elba	176
9.5	Assessment of the inversion results	179
9.6	Applications	180
10	SUMMARY AND CONCLUSIONS .....	185
A	A NUMERICAL SOLUTION TO THE MODAL EQUATION .....	187
A.1	The finite-difference equations	189
A.2	Treatment of boundaries and interfaces	190
B	THE VERTICAL SONAR ARRAY AS RECEIVING SYSTEM .....	193

C	GLOBAL OPTIMIZATION OF A TEST FUNCTION.....	197
C.1	GA performance as a function of its setting	198
C.1.1	Influence of reproduction size	199
C.1.2	Influence of population size	201
C.1.3	Influence of the crossover rate and mutation rate	202
C.2	The optimal setting	203
D	APPLYING LEVENBERG-MARQUARDT AS A LOCAL OPTIMIZATION METHOD.....	207
D.1	Levenberg-Marquardt	207
D.2	Applying LM for local minimization of GA results	208
D.2.1	Influence of $\xi$	210
D.2.2	Influence of $\lambda_1$	211
D.2.3	Influence of the step size taken to calculate the derivatives	212
D.3	Applying DHS for local minimization of GA results	215
D.4	Which local optimization method to use?	217
E	EXISTING GEO-ACOUSTIC INFORMATION FOR THE MALTA PLATEAU AND THE ELBA AREA.....	219
E.1	The Malta Plateau	219
E.2	Area north of Elba	220
E.3	Area southeast of Elba	221
	SAMENVATTING.....	225
	DANKWOORD.....	229
	CURRICULUM VITAE.....	230

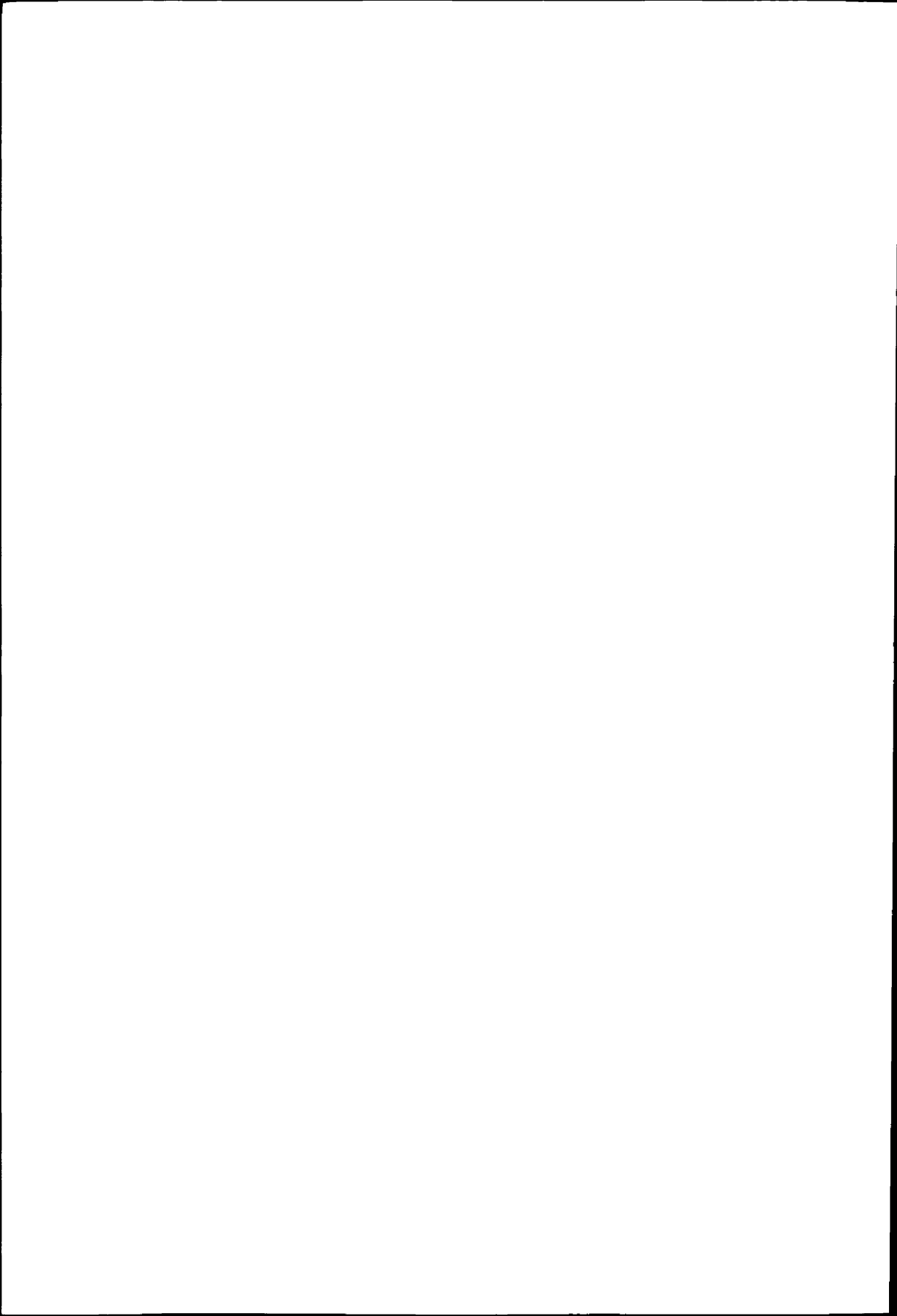
# List of publications

This thesis is based on a set of articles. Below an overview of these articles is presented and the chapters for which these articles have been used are specified.

Publication	Chapter
D.G. Simons, R. McHugh, M. Snellen, N.H. McCormick, and E.A. Lawson, "Analysis of shallow-water experimental acoustic data including a comparison with a broad-band normal-mode-propagation model," <i>IEEE Journal of Oceanic Engineering</i> , <b>26</b> (3), pp. 308-323 (2001).	*
D.G. Simons and M. Snellen, "Multi-frequency matched field inversion," <i>Journal of Computational Acoustics</i> , <b>6</b> (1&2), pp. 135-150 (1998).	4
M. Siderius, M. Snellen, D.G. Simons, and R. Onken, "An environmental assessment in the strait of Sicily: Measurement and analysis techniques for determining bottom and oceanographic properties," <i>IEEE Journal of Oceanic Engineering</i> , <b>25</b> (3), pp. 364-385 (2000).	5
M. Snellen, D.G. Simons, M. Siderius, J. Sellschopp, and P.L. Nielsen, "An evaluation of the accuracy of shallow water matched field inversion results," <i>Journal of the Acoustical Society of America</i> , <b>109</b> (2), pp. 514-527 (2001).	6
M. Siderius, P.L. Nielsen, J. Sellschopp, M. Snellen, D.G. Simons, "Experimental study of geo-acoustic inversion uncertainty due to ocean sound-speed fluctuations," <i>Journal of the Acoustical Society of America</i> , <b>110</b> (2), pp. 769-781 (2001).	**
M. Snellen, and D.G. Simons, "Application of the downhill simplex algorithm to reduce the uncertainty in matched field inversion results," submitted to the <i>Journal of the Acoustical Society of America</i> .	7
D.G. Simons, and M. Snellen, "Inversion for geo-acoustic bottom parameters and the water column sound speed profile using broadband shallow water data," <i>Proceedings of the Undersea Defence Technology Conference, Hamburg, 26-28 June, 2001</i> .	8

\* Section 2.5.3 of Chapter 2 presents a part of the contents of this article.

\*\* This article is not included in the thesis.





# Chapter 1

## General introduction

Knowledge about parameters of the sea bottom is of great interest in the field of underwater acoustics. These bottom parameters comprise, amongst others, the density, the attenuation, the porosity, the sound speeds, and the layering of the sea bottom. The applications requiring sea bottom information, or sea bottom classification, are manifold, and include for example the acoustic propagation models that are used on board of navy ships for sonar performance prediction, which need sea bottom parameters as input. Also in the area of mine hunting bottom information is essential, since for each type of bottom mines behave different. In a soft bottom mines get buried in the bottom, whereas they will stay on top of hard sea bottoms. Another application lies in the field of source localization. A promising method for source localization is a technique called 'matched field processing', which is capable of localizing sources in both range and depth. However, for a successful application of this technique accurate information on bottom type is essential. Also for dredging, investigating the sea bottom for off-shore activities, e.g. when considering an airport in sea, or tracing the sea bottom for certain types of material, bottom information is requisite.

Obtaining information about the sea bottom is not trivial. Often use is made of samples of the sea bottom. However, these samples are point measurements and therefore are not representative for large areas. For this, an extremely large number of samples are needed. Obtaining such a large amount of sea bottom samples is a very time consuming and costly operation, since a dedicated large ship is required for obtaining the samples, which then have to be analyzed either on board or in a laboratory. Seismic surveys can be carried out for determining the sea bottom layering. For bottoms with high sound speeds, roughly corresponding to rock type of bottoms, these seismic surveys can also provide information on the sea bottom sound speeds. It should be noted that, besides taking bottom samples, the only way to obtain sea bottom information is through acoustic means since all other kinds of radiation are attenuated too much.

In this thesis a bottom parameter estimation technique denoted by 'matched field inversion' is investigated. With this technique an acoustic field that is measured on a sonar array is compared with an acoustic field that is calculated by a propagation model. The model calculations are carried out for trial sets of the unknown parameters. The trial set that provides the maximum match between both acoustic fields should correspond to the true values of the unknown parameters. Clearly only those parameters that indeed influence the received signals can be estimated. Since the amount of possible combinations of the unknown parameters can be huge, and since the function that quantifies the match can contain a large number of local optima, global optimization methods are required for guiding the search for the set of unknown parameters that gives the maximum match.

The different chapters of this thesis and their cohesion are as follows. Since this thesis is made up mainly of articles that appeared in journals dedicated to the subject of (underwater) acoustics, in none of these articles basic knowledge on underwater acoustics is presented, as the readers of the before-mentioned journals are assumed to be familiar with the subject.

Chapter 2 provides this basic knowledge. The ocean environment and its essential parameters are discussed. The equations governing the propagation of sound are presented, and the influence of some of these parameters on the acoustic propagation is illustrated through the use of two bottoms with different properties. Note that if there is an effect of bottom type on the acoustic propagation, this implies that bottom parameters can be estimated through acoustic means. This is demonstrated by a model validation exercise at the end of Chapter 2, where a study is carried out for estimating the influence of the different model input parameters on the match between measured and modeled signals by considering a large amount of realistic input parameter sets. Since for some of the input parameters no information was available, the values corresponding to the maximum data/model match have been employed in the final data/model comparison. Only a limited amount of parameter values and parameter combinations were considered. Instead of this exhaustive search, more sophisticated global search, or optimization, methods can be applied.

In Chapter 3 these global optimization methods are applied with the goal to find the set of parameters that results in an optimal match between measured and modeled underwater acoustic data. These global optimization methods carry out a guided search through all possible combinations of the unknown parameters, and are especially applicable in problems with many unknowns and many local optima. Two global optimization methods are considered in Chapter 3, viz., simulated annealing and the genetic algorithm, and the performance of both methods is assessed.

In Chapter 4 the genetic algorithm is used for inversion of data that were supplied within a benchmark. The goal of this benchmarking exercise was to compare the various methods employed for matched field inversion during a dedicated workshop. The matched field inversion results presented in Chapter 4 indicate good performance in estimating the values for the unknown sea bottom parameters. When comparing the results of all workshop participants, 16 in total, the organizers of the workshop mention the following about the Chapter 4 results: "Their approach is exceptionally accurate and efficient for nearly all parameters."

Chapter 5 presents the results of inversions of experimental acoustic data obtained during an experiment conducted south of Sicily on the Adventure Bank in October 1997. The sound source was towed behind a ship and, therefore, this chapter can be seen as the first demonstration of the practical applicability of matched field inversion. The inversion results show good agreement with results from independent measurements.

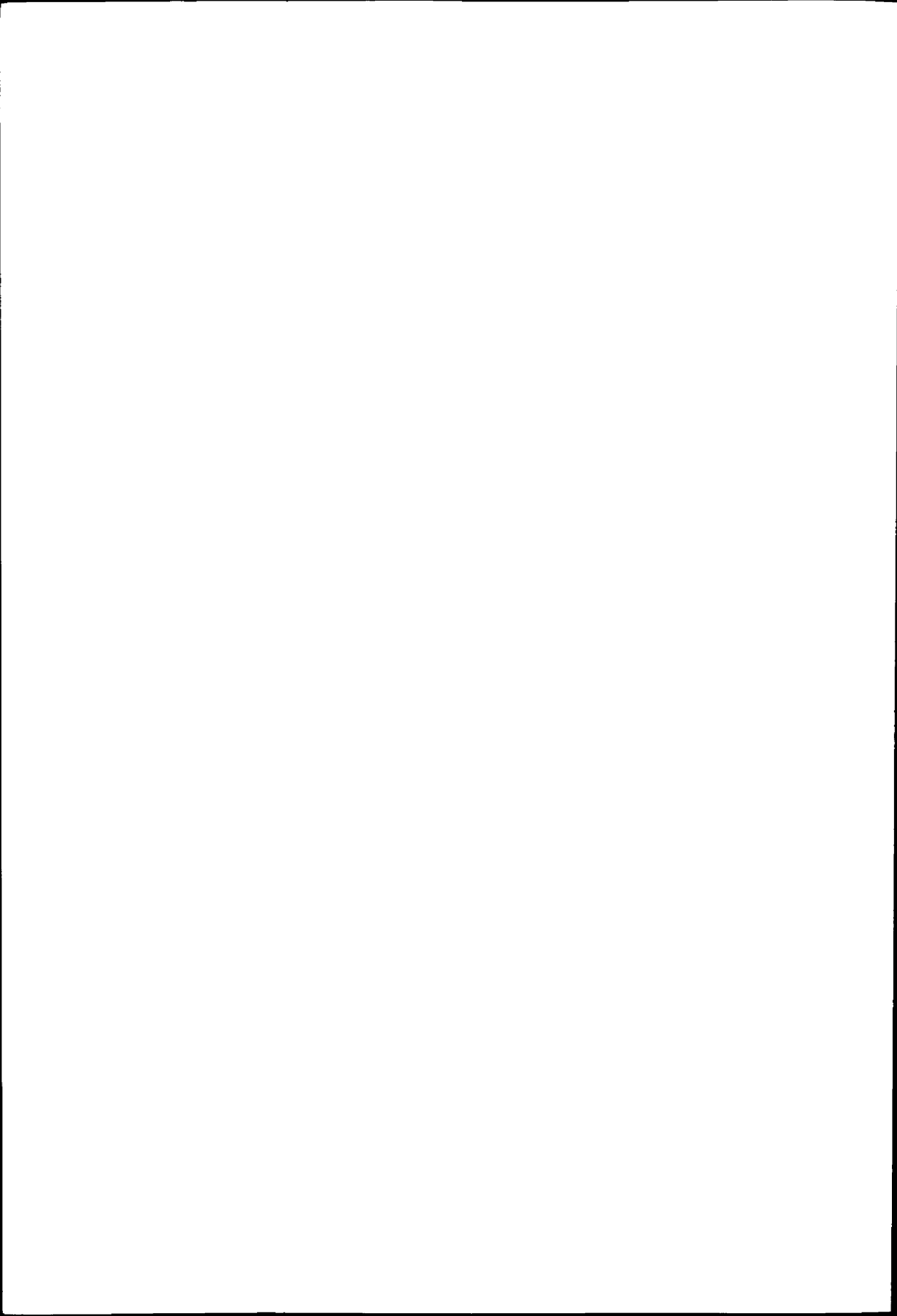
Chapter 6 presents results of inversions of experimental data obtained during an experiment carried out in April/May 1999 on the Adventure Bank as well. The sound source used during these experiments was mounted on a tower construction that was put at the sea bottom, to keep it at a fixed position. This configuration allows for assessing the effects of the varying ocean on the matched field inversion results. Use was made of data transmitted at a 2-km range from the receiver. Many snapshots of data, recorded over a period spanning 8 h, are used in the inversion in order to assess the variability in the inversion results. For this, it is assumed that all variation in the inversion results should be due to both the imperfect optimization method, and the temporal oceanographic variability. Inversions for synthetic data reveal the uncertainty that is due to the optimization method. It is found that the optimization method itself is a large contributor to parameter uncertainty. Inversions of synthetic data that also include oceanographic variability show uncertainties comparable to that of the inversions of experimental data. Consequently, it is concluded that the origins of uncertainty have been revealed.

In an effort to reduce the uncertainties due to the imperfect optimization method, a local optimization method is applied after the global optimization in Chapter 7, using the genetic algorithm results of Chapter 6. Inversions of synthetic data indicate that this approach almost completely eliminates the contribution of the optimization method to the parameter uncertainty.

In Chapter 8 the capability of the matched field inversion method to also estimate parameters of the water column is demonstrated. Use is made of the same data as in the previous two chapters.

Chapter 9 presents results of inversions of data obtained at several sites during an experiment carried out in November 2000. The goal of this experiment was to obtain data in environments that differ with respect to their bottom properties, in order to demonstrate the general applicability of matched field inversion for bottom classification purposes. The source was towed behind a ship, thereby providing acoustic data over a large area. When using such a set of acoustic data for the matched field inversion analysis, information on bottom parameters is obtained that is representative for the area in between source and receiver, thereby providing information on large regions (several km), contrary to bottom samples. At the end of Chapter 9, the importance of having a bottom classification technique is illustrated through the means of two applications, viz., source localization and a sonar performance model.

Finally, Chapter 10 presents the summary and conclusions.



## Chapter 2

# Seabed effects on underwater acoustic propagation

## 2.1 Introduction

In this chapter, the ocean environment is introduced from an acoustic point of view. In the scope of the thesis, devoted to estimating bottom properties through acoustic means, particular attention is paid to the interaction of the sound with the seabed. In addition, the model that is used for calculating the propagation of sound under water throughout this thesis is described.

In Section 2.2 the wave equation, governing the propagation of sound, is presented, and the parameters that influence the propagation of sound are identified. In Section 2.3 these parameters are considered in more detail and typical values for these parameters are given. In Section 2.4 the normal-mode technique for estimating solutions to the wave equation is described. The influence of bottom type on the acoustic propagation is illustrated in Section 2.5. To this end, two ocean environments are defined, which differ with respect to their bottom characteristics. The seabed reflection coefficient is introduced and calculated for the two environments. Further, the transmission loss, i.e., the difference between the transmitted and received signal level, is determined for these two environments. In addition, the effect of bottom type on the shape of the received signals is shown. As a last illustration, work carried out for model validation purposes is presented. This example from practice shows the impact of bottom type on the acoustic propagation using real acoustic data.

## 2.2 Propagation of sound through the water

The propagation of sound is governed by the wave equation<sup>1</sup>

$$\nabla \cdot \left( \frac{1}{\rho} \nabla P \right) - \frac{1}{\rho c^2} \frac{\partial^2 P}{\partial t^2} = 0 \quad (1)$$

with  $P$  the pressure,  $\rho$  the density, and  $c$  the sound speed.

From this equation it is seen that the propagation of sound is influenced by parameters of the medium, viz., the sound speed and the density. A parameter not yet introduced, but also influencing the propagation of sound, is the attenuation constant. When modeling the acoustic propagation, all these parameters need to be known both in the water column, and in the seabed underlying the water column. These parameters are considered in Section 2.3. In Section 2.4 a technique for determining solutions to Eq. (1) is described.

## 2.3 The ocean-acoustic environment

In this section the parameters, both in the water column and in the seafloor, influencing the propagation of sound are considered. In addition, this section presents guidelines for the typical values encountered for each of these parameters.

### 2.3.1 The water column

The ocean is an acoustic waveguide that is limited from above by the sea surface and from below by the ocean bottom. The sound speed in the waveguide plays the same role as the index of refraction in optics. It is a function of the temperature, the salinity, and the depth in the water column. A device that is often used for estimating the sound speed as a function of depth, the 'sound speed profile', is the Conductivity-temperature-Depth (CTD) sensor. Also expendable bathymetry temperature (XBT) measurements are sometimes carried out for measuring the sound speed profile (using independent measurements or a database for obtaining the salinity). Sound speed profiles show different behavior for different seasons and for different geographical positions. Figure 1 shows both a typical summer and a typical winter profile, respectively, both taken in the same shallow water area ( $\sim 100$  m water depth). The winter profile shows lower sound speeds due to the lower water temperature. The sound speed profile corresponding to the summer profile increases from the top to about 15 to 18 m water depth due to the increase of pressure with depth, with the water temperature remaining (almost) constant. The corresponding layer is denoted as the 'surface duct'. Below 18 m there is a strong decrease in sound speed due to a decrease in temperature. The layer corresponding to this strong decrease is called the 'thermocline'.

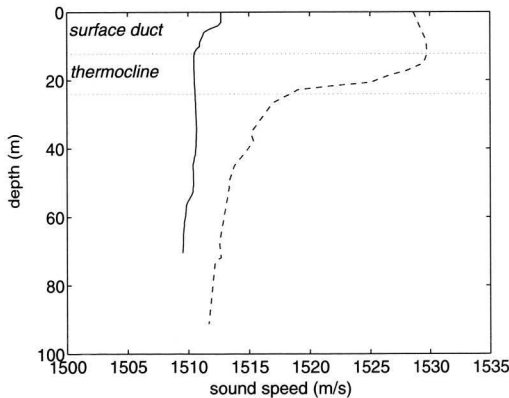


Fig. 1 Typical winter (solid) and summer (dashed) sound speed profile.

The sea surface is a rough surface due to the presence of sea surface waves. These waves result in scattering of sound, i.e., the sound is scattered away from the specular direction. The influence of the rough sea surface on the acoustic propagation is often modeled as a loss term. This loss term is dependent on the amount of roughness, i.e., the heights of the sea surface waves, and therefore on the speed of the wind above the water. Another effect of the rough sea surface is the presence of air bubbles in the upper part of the water column. These air bubbles result both in a scattering of the sound at the bubbles, and in a change of the sound speed in the bubble region. Typically, the entrainment depth of the bubbles equals 0.4 m for wind speeds less than 7 m/s, and increases, for example, to 0.8 m at 10 m/s wind speed.<sup>2</sup>

## 2.3.2 The seafloor

The other boundary of the waveguide is the sea floor. For shallow water environments (water depth of several 100 m), with sound propagating over distances that are many times larger than the water depth, the sound experiences a considerable interaction with the sea floor. Consequently, the sea floor has a large influence on the propagation of the sound. This influence is dependent on the sea bottom type, and therefore, information on the sea bottom parameters is essential when modeling the propagation of sound through shallow waters. At the same time, bottom parameter estimation through acoustic means becomes feasible. The bottom parameters comprise, for example, the density, the attenuation constant, and the sound speed in the sea bottom. In what follows we will consider some of these parameters and indicate the range of values encountered. The articles that are referred to have a widespread use in the underwater community, and form the standard literature on this topic.

Two sediment parameters not yet introduced are the porosity and the grain size. They are denoted as geo-technical parameters. It is relatively easy to determine these parameters with standard techniques, and they can be used, by employing empirical relations as shown below, for determining the density, the sound speed, and the attenuation. These latter three parameters directly influence the acoustic propagation and are called geo-acoustic parameters. When determining their values using bottom samples, they can either be measured directly from the sample, or be estimated indirectly from the geo-technical parameters.

Figure 2 shows the sediment grain size plotted versus the sediment porosity.

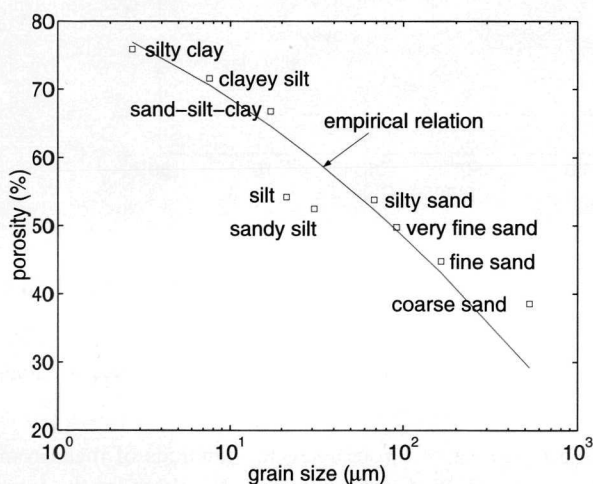


Fig. 2 Grain size versus porosity.

A term often used in relation to porosity is the 'void fraction', which is the volume of voids divided by the total volume. The porosity is known to depend on a number of factors, the most important of which is the grain size, which explains the strong correlation between these two parameters in Fig. 2.<sup>3</sup> In this figure also an empirical relation between these two parameters is presented, which is obtained as a fit through a large amount (> 500) of measurements.<sup>4</sup> The expression for this relation is

$$s = 20.8 + 9.43 \cdot \varphi - 0.334 \cdot \varphi^2 \quad (2)$$

with  $\varphi$  being the  $-2 \log$  of the grain size in mm, and  $s$  the porosity (%). No error on this regression equation is provided since this error could not be obtained from (Bachman<sup>4</sup>) unambiguously, but it roughly amounts to about 10 %. The regression equation is valid for porosities from 36.7 % to 85.8 %, and for grain sizes of  $\sim 1 \mu\text{m}$  to  $\sim 570 \mu\text{m}$ .

Figure 3 shows for a set of sediment types the density  $\rho$  ( $\text{g/cm}^3$ ) versus the porosity  $s$  (%). Also shown is the theoretical relation<sup>5</sup>

$$\rho = \rho_{\text{solid}}(1-n) + \rho_w n \quad (3)$$

In this expression  $n$  is the fractional porosity ( $n = s/100$ ), and the subscripts  $w$  and  $\text{solid}$  denote water and mineral solids. The value for  $\rho_{\text{solid}}$  amounts to about  $2.7 \text{ g/cm}^3$ .

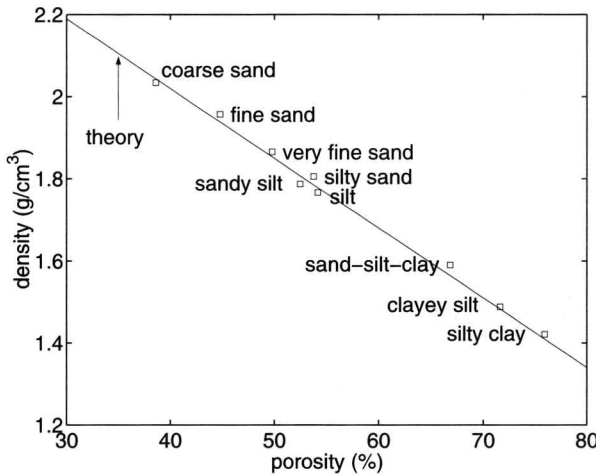


Fig. 3 Density versus porosity.

Figure 4 shows the compressional wave speed  $c_p$  versus the density. In addition, an empirical relation between these two is shown<sup>3</sup>

$$c_p = 2330.4 - 1257 \cdot \rho + 487.7 \cdot \rho^2 \pm 33 \text{ m/s} \quad (4)$$

This expression has been derived as a fit through several hundreds of measurements, and is valid for  $1520 < c_p < 1840 \text{ m/s}$  and  $1.25 < \rho < 2.10 \text{ g/cm}^3$ . Note that for the low densities ( $< 1.4 \text{ g/cm}^3$ ) the sound speed is relatively insensitive to density. In some sediments (see (Hamilton<sup>3</sup>) and (Orsi<sup>6</sup>)) velocity might decrease with increasing density in this range. This behavior appears only for high porosity sediments with no rigidity, i.e., without strength. It is well known that longitudinal sound speed depends on the two medium parameters compressibility ( $\beta$ ) and density according to

$$c_p = \sqrt{\frac{1}{\beta\rho}} \quad (5)$$

Regarding the sediment as a suspension of mineral particles in water, and thereby regarding  $\beta$  and  $\rho$  in Eq. (5) as the total compressibility and density,  $c_p$  becomes



$$c_p = \sqrt{\frac{1}{[n\beta_w + (1-n)\beta_{solid}][n\rho_w + (1-n)\rho_{solid}]}} \quad (6)$$

which is known as Wood's equation. The relation between compressional wave speed and density as predicted by the Wood's equation is shown in Fig. 4 as well, clearly exhibiting a minimum in sound speed as a function of density. The presence of gas bubbles in the sediment can further reduce  $c_p$ .

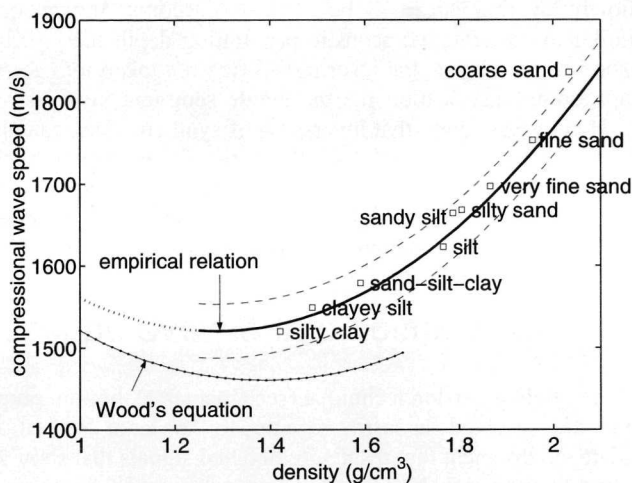


Fig. 4 Compressional wave speed versus density as obtained from measurements (squares). Also indicated is the empirical relation obtained as a fit through a large amount of measurements (solid line, and dotted below the densities for which the fit is valid). The dashed lines indicate the error. The (-.) line indicates the relation as predicted by Wood's equation.

From measurements it was found that the attenuation approximately increases linearly with frequency<sup>5</sup>, and can thus be expressed in  $\text{dB}/\lambda$ , with  $\lambda$  the acoustic wavelength. In (Hamilton<sup>7</sup>) the values of the attenuation constant  $\alpha$  are related to porosity. Roughly the attenuation constant amounts to about  $0.2 \text{ dB}/\lambda$  for high porosity sediments ( $s > 60\%$ ), whereas it has a value of about  $0.8 \text{ dB}/\lambda$  for sandy sediments ( $s < 40\%$ ).

All seabed parameters considered above can vary with depth, both as a result of the increase in pressure and temperature<sup>5</sup> when going deeper into the bottom, but also as a result of the fact that the sediment can consist of several layers on top of each other. The complete set of seabed parameters influencing the acoustic propagation is often denoted as the geo-acoustic model of the real seabed. The parameters for the geo-acoustic model need to be known up to the 'effective acoustic penetration depth'. At high frequencies (several kHz), bottom information is required only for the few upper meters, whereas at lower frequencies, information on bottom parameters is needed up to much deeper depths into the sediment (several tens of meters). A complete geo-acoustic model of the seabed requires information of all geo-acoustic parameters up to the effective acoustic penetration depth. Obtaining such a detailed description is not feasible under practical circumstances and approximations are necessary. Measurements roughly indicate that the attenuation increases with increasing depth for silt-clay sediments, whereas it decreases with depth for sand-silt sediments.<sup>5</sup> However, the effect is relatively small and is generally neglected. Also in (Hamilton<sup>5</sup>) measurements are presented that illustrate the effect of depth in the sediment on the density. The exact behavior depends on sediment type, but in general the density increases when going deeper into the

sediment. For example, the measurements indicate for a sediment with an upper sediment density of  $\sim 1.52 \text{ g/cm}^3$  an increase up to  $\sim 1.55 \text{ g/cm}^3$  over 20 m. The effect of this increase on the acoustic propagation can often be neglected. The effect of depth in the sediment on the sediment sound is dependent on sediment type. Velocity gradients in sediments are usually positive, with the velocity increasing linearly or parabolic. In the remainder of the thesis, the velocity is assumed to increase linearly. Typical values for the gradient are  $1 \text{ s}^{-1}$ . For sand type sediments the gradient is often somewhat higher ( $4 \text{ s}^{-1}$ ). Although a gradient of  $1 \text{ s}^{-1}$  results in an increase of sound speed of only 20 m/s over 20 m depth, this can have an impact on the sound propagation, and often is accounted for.

The effect of the sediment layering can easily be taken into account. However, for layers that have thicknesses similar to the effective acoustic penetration depth the layering can be neglected. Also for thinner sediment layers the layering is often not taken into account when modeling the sound propagation. Justification for the single sediment layer assumption is obtained from literature.<sup>8</sup> Here it was found that inversions of synthetic data, calculated for a multi-layer bottom, and using a two-layer model for the forward calculations with linearly varying sound speeds, resulted in properties of the two-layer bottom that fitted the properties of the actual multi-layer model reasonably well. The sediment is overlying a medium called the sub-bottom. This medium is modeled as a homogenous layer.

## 2.4 Normal-mode solution of the wave equation

When employing the matched field inversion technique (see Chapter 1), bottom properties are estimated by calculating the received acoustic signals for a large set of candidate environments. The candidate environment that results in modeled signals that show maximum similarity with the measured acoustic signals (as received on a dedicated receiving system) is taken to be the true environment. Since for each new unknown environment a large number of calculations are needed, a very strict requirement on the propagation model is that the calculations are fast. This prevents the use of models based on finite elements and finite differences. Also the model needs to be applicable to a wide range of frequencies, thereby excluding the use of ray based models which are only valid in the high frequency limit.<sup>1</sup> Another requirement is that the model should be suitable for environments that vary both in the depth- and the range-direction. These environments are called 'range-dependent', whereas environments that vary only with depth are called 'range-independent'. The requirement that the model should be applicable to range-dependent environments, is not easily met by the wavenumber integration approach.<sup>1</sup> The two remaining techniques are the parabolic equation method and the normal-mode method. Since for most situations the normal-mode technique is faster, the model applied in the succeeding chapters for calculating the propagation of the sound is based on the normal-mode technique. The current section presents the basics behind this normal-mode technique. For rigid sediments, part of the energy is transformed into a transversal or shear wave. Here, all layers are assumed to be fluids and, therefore, the seabed is not allowed to support shear waves.

### 2.4.1 The normal-mode technique

In this section the problem of determining the pressure field resulting from a point source in a horizontally stratified medium is considered. More detailed information can be found in (Jensen<sup>1</sup>).

For a single frequency  $\omega$  the wave equation has the following form

$$\nabla \cdot \left( \frac{1}{\rho} \nabla P \right) - \frac{1}{\rho c^2} \frac{\partial^2 P}{\partial t^2} = -S_\omega \delta(\mathbf{r} - \mathbf{r}_s) e^{-i\omega t} \quad (7)$$

with  $P$  the acoustic pressure at position  $\mathbf{r}$  and time  $t$ , due to a source at position  $\mathbf{r}_s$  and strength  $S_\omega$ .  $c$  and  $\rho$  are the sound speed, and the density, both as a function of depth.

Assuming that the ocean environment is cylindrically symmetric, with the source position at zero range, and accounting for the fact that the received signal must have the same time dependence as the source, the following relation is valid

$$P(x, y, z, t) = p(r, z) e^{-i\omega t} \quad (8)$$

with  $r$  the horizontal distance, or range, between source and receiver. By substituting this expression into Eq. (7), and using cylindrical symmetry, one obtains

$$\frac{\partial^2 p}{\partial r^2} + \frac{1}{r} \frac{\partial p}{\partial r} + \frac{\partial^2 p}{\partial z^2} - \frac{1}{\rho} \frac{d\rho}{dz} \frac{\partial p}{\partial z} + k^2 p = -\frac{S_\omega}{2\pi r} \delta(r) \delta(z - z_s) \quad (9)$$

with  $k$  the total wavenumber

$$k(z) = \frac{\omega}{c(z)} \quad (10)$$

Eq. (9) is the so-called Helmholtz equation for a cylindrically symmetric medium.

In the following the ocean environment is simplified and assumed to consist of three layers (see Fig. 5):

- A water column of depth  $H_w$  with density  $\rho_w (= 1 \text{ g/cm}^3)$ , sound speed profile  $c_w(z)$ , and attenuation constant  $\alpha_w$ ;
- A sediment layer of thickness  $H_s$ , and density  $\rho_s$ , sound speed profile  $c_s(z)$ , and attenuation constant  $\alpha_s$ ;
- A semi-infinite homogeneous sub-bottom with density  $\rho_b$ , sound speed  $c_b$  and, attenuation constant  $\alpha_b$ .

Thus the densities and attenuation constants are assumed to be constant in each of the layers, whereas the sound speed in the water column and the sediment layer is allowed to vary with depth  $z$ . The sub-bottom sound speed is however assumed to be constant. The total sound speed profile is

$$c(z) = \begin{cases} c_w(z) & \text{for } 0 \leq z \leq H_w \\ c_s(z) & \text{for } H_w \leq z \leq H_w + H_s \\ c_b & \text{for } z \geq H_w + H_s \end{cases} \quad (11)$$

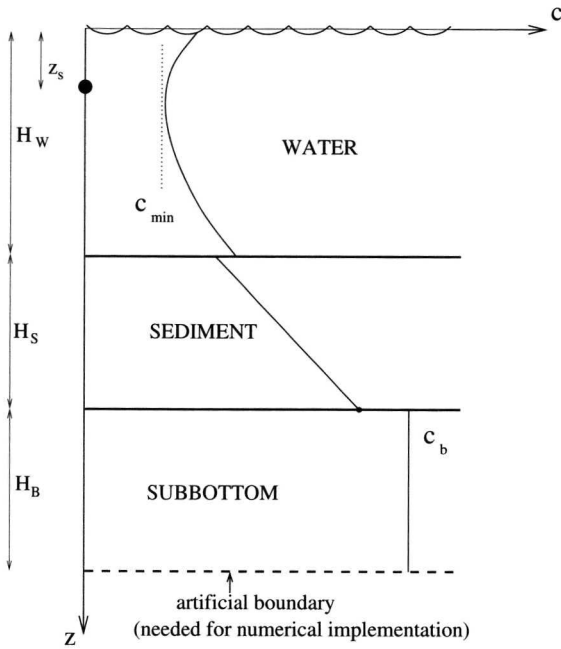


Fig. 5 Schematic of the simplified range-independent ocean environment.

It is assumed that the sea surface is a pressure release boundary, corresponding to a reflection coefficient of  $R = -1$  and a transmission coefficient  $T = 0$ , which means that there is no transmission of sound from the water to the air above the water, i.e.,

$$P(r, 0, t) = 0 \quad (12)$$

Further, it is assumed that at some sufficiently great depth  $H_t = H_w + H_s + H_B$  (see Fig. 5), a perfectly rigid boundary exists, i.e.,

$$\frac{\partial P}{\partial z}(r, H_t, t) = 0 \quad (13)$$

$H_B$  should be selected such that there is no contribution from below  $H_t$  to the total acoustic field. Experience has learned that taking  $H_B$  equal to 20 acoustic wavelengths is sufficient.

The Helmholtz equation can be solved by applying the technique of separation of variables, which implies substitution of

$$p(r, z) = R(r)\Psi(z) \quad (14)$$

in the homogeneous Helmholtz equation, i.e., Eq. (9) with the right-hand side equal to zero. One then obtains the following two differential equations

$$\frac{d^2 R}{dr^2} + \frac{1}{r} \frac{dR}{dr} + \mu R = 0 \quad (15)$$

$$\frac{d^2\Psi}{dz^2} - \frac{1}{\rho} \frac{d\rho}{dz} \frac{d\Psi}{dz} + (k^2 - \mu)\Psi = 0 \quad (16)$$

where  $\mu$  is the separation constant. The boundary conditions are

$$\begin{aligned} \Psi(0) &= 0 \\ \frac{d\Psi}{dz}(H_i) &= 0 \end{aligned} \quad (17)$$

Eq. (16), the depth-dependent Helmholtz equation or modal equation, together with the boundary conditions, is a standard Sturm-Liouville eigenvalue problem. It has an infinite number of solutions  $\Psi_n(z)$  (eigenfunctions or modes) for distinct real values  $\mu_n = k_n^2$  (the eigenvalues) of the separation constant. For an arbitrary sound speed profile  $c(z)$  this problem has to be solved numerically.

The eigenfunctions of a Sturm-Liouville problem are orthogonal and can be normalized, i.e.,

$$\int_0^{H_i} \frac{\Psi_n(z)\Psi_{n'}(z)}{\rho(z)} dz = \delta_{n,n'} \quad (18)$$

with  $\delta_{n,n'}$  Kronecker's delta. Since the eigenfunctions form a complete orthonormal set, the solution of Eq. (9) can be written as

$$p(r, z) = \sum_{n=1}^{\infty} R_n(r)\Psi_n(z) \quad (19)$$

The coefficients  $R_n(r)$  are determined as follows: Substituting Eq. (19) into Eq. (9), multiplying by  $\Psi_n(z)$ , integrating over  $z$ , and using the orthonormality of the eigenfunctions (Eq. (18)) one obtains

$$\frac{\partial^2 R_n}{\partial r^2} + \frac{1}{r} \frac{\partial R_n}{\partial r} + \mu_n R_n = \frac{-\delta(r)S_\omega \Psi_n(z_s)}{2\pi\rho(z_s)}, \quad (20)$$

This standard equation (Bessel's equation of order zero<sup>10</sup>) has the following solutions

$$R_n(r) = \frac{iS_\omega}{4\rho(z_s)} \Psi_n(z_s) H_0^{(1,2)}(k_n r) \quad (21)$$

with  $H_0^{(1)}$  and  $H_0^{(2)}$  the zeroth order Hankel functions of the first and second kind, respectively. The radiation condition (energy must radiate outward as  $r \rightarrow \infty$ ) and the choice of  $e^{-i\omega t}$  for the time dependence of  $P$  imply that the Hankel function of the first kind has to be taken.

Now the final solution becomes

$$p(r, z) = \frac{iS_\omega}{4\rho(z_s)} \sum_{n=1}^{\infty} \Psi_n(z_s)\Psi_n(z) H_0^{(1)}(k_n r) \quad (22)$$

being the normal-mode solution to the wave equation.

Using the asymptotic expression for the Hankel function (to a good approximation valid for  $k_n r > 2$ )

$$H_0^{(1)}(k_n r) = \sqrt{\frac{2}{\pi k_n r}} e^{i(k_n r - \pi/4)} \quad (23)$$

Eq. (22) can be written as

$$p(r, z) = \frac{e^{i\pi/4} S_\omega}{\rho(z_s) \sqrt{8\pi\omega}} \sum_{n=1}^{\infty} \Psi_n(z_s) \Psi_n(z) \frac{e^{ik_n r}}{\sqrt{k_n}} \quad (24)$$

According to Eq. (8) and (24) the pressure field  $P(r, z, t)$  can be regarded as a superposition of cylindrical waves

$$P_{c,n}(r, z, t) = \frac{A_n(z)}{\sqrt{r}} e^{i(k_n r - \omega t)} \quad (25)$$

with phase speeds  $c_n = \frac{\omega}{k_n}$ . The eigenvalues  $k_n$  can therefore be interpreted as horizontal wavenumbers, i.e., wavenumbers in the  $r$ -direction.

The modal equation, Eq. (16), has an infinite number of solutions  $\Psi_n(z)$  for distinct values  $k_n^2$  of the separation constant  $\mu$ . All eigenvalues  $k_n^2$  are real and are all less than  $\omega/c_{\min}$ , with  $c_{\min}$  being the lowest value in the total sound speed profile (Eq. (11)). Consequently, all corresponding phase velocities are greater than  $c_{\min}$ , i.e.,  $c_n > c_{\min}, \forall n$ . The  $n^{\text{th}}$  mode function  $\Psi_n$  has  $n$  zeros on the interval  $[0, H_1]$ . The phase speed spectrum can be divided in two different regions, comprising the discrete modes and the so-called leaky modes. The eigenvalues of the discrete modes satisfy

$$\frac{\omega}{c_b} < k_n < \frac{\omega}{c_{\min}} \quad (26)$$

assuming  $c_b$  to be the highest sound speed value in the total profile, Eq. (11). The corresponding phase velocities satisfy

$$c_{\min} < c_n < c_b \quad (27)$$

Hence, for discrete modes to exist  $c_b$  must be greater than  $c_{\min}$ . The number of discrete modes ( $L$ ) is finite. The eigenvalues of the leaky modes satisfy

$$0 < k_n < \frac{\omega}{c_b} \quad (28)$$

with corresponding phase velocities

$$c_b < c_n < \infty \quad (29)$$

Fig. 6 illustrates the two regions of phase speeds.

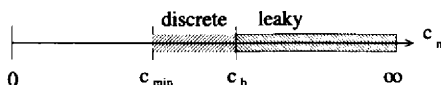


Fig. 6 The two phase speed regions.

These leaky modes correspond to sound rays traveling at grazing angles greater than the critical angle at the sediment/sub-bottom interface, and therefore part of the energy carried by these modes leaks into the sub-bottom. Hence, the contribution of these modes to the pressure field becomes negligible at a sufficient distance from the source. This is only legitimate for 'long-range' propagation in shallow water for ranges that are an order of magnitude larger than the depth. This is the case for the remainder of this thesis. The leaky modes are also denoted by 'continuous modes'. If the leaky modes contribution is not taken into account, the solution becomes

$$p(r, z) = \frac{e^{i\pi/4} S_\omega}{\rho(z_s) \sqrt{8\pi r}} \sum_{n=1}^L \Psi_n(z_s) \Psi_n(z) \frac{e^{ik_n r}}{\sqrt{k_n}} \quad (30)$$

In the above discussion no losses due to attenuation, both in the water column and in the seabed, and due to the scattering of sound at the rough sea surface are taken into account. Their contribution is implemented through perturbation theory<sup>1</sup>, where a small imaginary part is added to the total wavenumber. This leads to modal attenuation coefficients  $\alpha_n$  for each mode  $n$ , where

$$\alpha_n = \alpha_n^w + \alpha_n^s + \alpha_n^b + \alpha_n^{scat} \quad (31)$$

with the superscripts  $w$ ,  $s$ ,  $b$ , and  $scat$  denoting water, sediment, sub-bottom, and scattering, respectively. The expressions for the water, sediment, sub-bottom, and scattering modal attenuation constants can be found in (Ingenito<sup>11</sup>) and (Kuperman<sup>12</sup>). For illustrative purposes we present the expressions for the water, sediment and sub-bottom modal attenuation constants:

$$\alpha_n^{w,s,b} = \frac{\alpha^{w,s,b} f}{\bar{c}^{w,s,b} 20^{10} \log e} \frac{\omega}{\rho^{w,s,b} k_n} \int \frac{\bar{c}^{w,s,b} \Psi_n(z)^2}{c(z)} dz \quad (32)$$

with  $\alpha^{w,s,b}$ , denoting the attenuation constants in the water ( $w$ ), sediment ( $s$ ), and sub-bottom ( $b$ ), respectively.  $\bar{c}^{w,s,b}$  denotes the mean sound speed in the water column, the sediment, and the sub-bottom layer, respectively. The integral has to be taken over the corresponding layer, i.e., for determining  $\alpha_n^w$  the integral is taken from 0 to  $H_w$ , for determining  $\alpha_n^s$  the integral is taken from  $H_w$  to  $H_w + H_s$ , and for determining  $\alpha_n^b$  the integral is taken from  $H_w + H_s$  to  $H_w + H_s + H_b$ . The factor  $f / (\bar{c}^{w,s,b} 20^{10} \log e)$  converts the units from dB/ $\lambda$  to 1/m. Including the loss terms the expression for  $p(r, z)$ , Eq. (30), now becomes

$$p(r, z) = \frac{e^{i\pi/4} S_\omega}{\rho(z_s) \sqrt{8\pi r}} \sum_{n=1}^L \Psi_n(z_s) \Psi_n(z) \frac{e^{(ik_n - \alpha_n)r}}{\sqrt{k_n}} \quad (33)$$

For obtaining  $\Psi_n$  and  $k_n$ , the modal equation Eq. (16) has to be solved numerically. Finite-difference discretization is applied for transforming the modal equation, and the corresponding boundary conditions, Eq. (17), into an eigenvalue problem. This is considered in Appendix A. This resulting algebraic eigenvalue problem is solved by using EISPACK routines that determine the eigenvalues and eigenvectors (or eigenfunctions) for a real symmetric tridiagonal matrix in a specified interval.<sup>13</sup>

## 2.4.2 Range-dependency through the adiabatic approximation

In Section 2.4.1 the environment is allowed to vary with depth, but is assumed to be constant in the range direction. In situations where the range-dependence of the environment is such that it cannot be neglected, still use can be made of the normal-mode solution. As a result of its relatively (compared to other techniques for calculating the sound propagation in range-dependent environments) short calculation times, the approach most commonly used is to employ the 'adiabatic approximation'.

In the adiabatic approximation, the environment is divided in segments that all together span the entire source-receiver range. Figure 7 shows an example of such segmentation. Within each of these segments the environment is assumed range-independent.

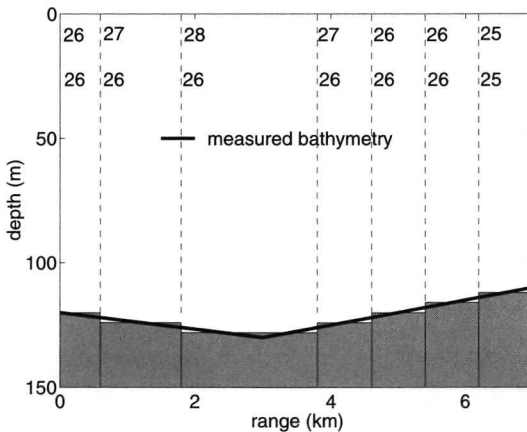


Fig. 7 Example of segmentation applied for the adiabatic normal-mode approach. In each range segment the upper number indicates the amount of modes calculated for that particular range segment. The lower number indicates the amount of modes accounted for as a function of range  $r$ .

For each of the segments the eigenvalues and eigenvectors are determined. The assumption made in the adiabatic approximation is that from one range segment to another, the modes couple without any transfer of energy to higher or lower order modes. This means that there is no energy transfer in between modes of different orders, i.e., mode  $n$  does not couple with modes  $n+1$ ,  $n+2$ , ...,  $L$ , and with modes  $n-1$ ,  $n-2$ , ...,  $1$ . Considering Fig. 7, a result of the approximation applied is observed: for the situation considered the amount of modes increases from 26 to 28 when going to larger water depths. This however is not accounted for in the adiabatic approximation, since the new modes (at larger water depth) have no



neighboring modes to couple with at the left side. Similarly, when going to smaller water depths, modes will disappear. For the example shown in Fig. 7 and for a receiver at range  $r = 7$  km, 25 modes will be accounted for in all range segments.

For the cases considered in this thesis, the adiabatic approximation can be applied when accounting for range-dependency, since the slopes are small. However, up to what slopes the adiabatic approximation is valid is still a topic of research.

The derivation of the expressions for the adiabatic approximation is given in (Jensen<sup>1</sup>) and here only the resulting expression is presented

$$p(r, z) = \frac{e^{i\pi/4} S_\omega}{\rho(z_s) \sqrt{8\pi r}} \sum_{n=1}^{L_{min}} \Psi_n(0, z_s) \Psi_n(r, z) e^{\frac{i \int_0^r k_n(r') dr' - \int_0^r \alpha_n(r') dr'}{\sqrt{\int_0^r k_n(r') dr'}}} \quad (34)$$

with  $L_{min}$  the minimum amount of modes encountered over all segments up to range  $r$ . Note that employing the adiabatic approximation requires solving for the eigenvalues of the modal equation in all segments. The eigenfunctions are needed only for the segments that contain the source and the receiver. For calculating the received complex pressure (Eq. (34)) use is made of the averaged (over range) horizontal wavenumber and the averaged modal attenuation coefficient.

## 2.5 Examples

In this section the effect of the sea bottom properties on the sound propagation is illustrated through the use of two bottoms with different properties. The first is a sand-silt-clay like bottom, with geo-acoustic bottom parameters as shown in Fig. 8. The second is a muddy bottom, i.e., a mixture of silt and clay with a sound speed lower than that in the water column. The corresponding geo-acoustic model is shown in Fig. 9. The sub-bottom is taken the same for the two environments. Note that this model for the seabed corresponds to the model discussed at the end of Section 2.3.

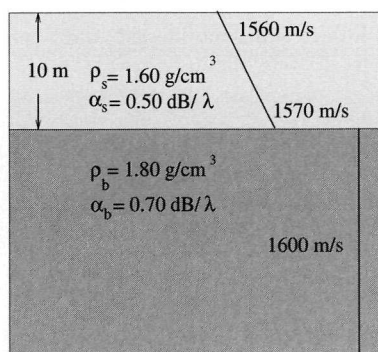


Fig. 8 Geo-acoustic model for the sand-silt-clay environment.

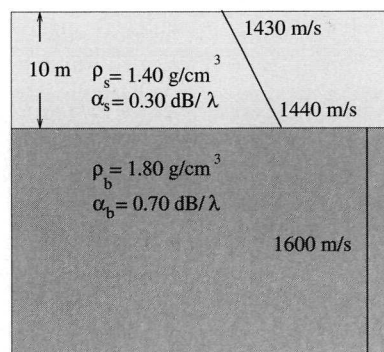


Fig. 9 Geo-acoustic model for the mud environment.

First, the influence of bottom type on the bottom reflection coefficient is considered. The bottom reflection coefficient is the ratio of the amplitudes of the reflected plane wave to the plane wave incident on the water/sediment interface, and provides a measure for the effect of the sound interacting with the sea bottom. The practical applications of the reflection

coefficient are limited and it is not used for the forward modeling, but the concept is a means for illustrating the energy transport in and out of the ocean waveguide. By showing the influence of bottom type on the reflection coefficient, it is demonstrated that it is indeed feasible to estimate bottom properties through acoustic means. As a next example for the influence of bottom type the transmission loss, i.e., the amount of energy lost in between source and receiver, is calculated for the two environments.

At the end of this section results of a model validation exercise are presented, demonstrating the influence of sea bottom type on the underwater acoustics in real life.

### 2.5.1 Interaction of sound with the seafloor

Figure 10 shows the reflection of sound at an interface that separates two homogeneous fluid media. The environment considered is 2D, i.e., there is no variation in the  $y$ -direction.

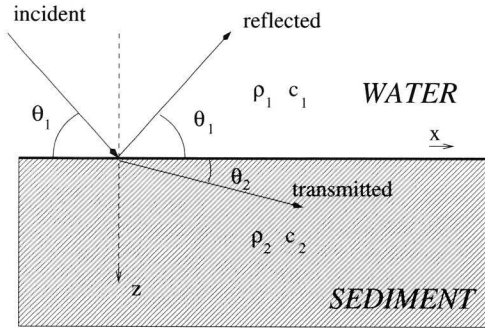


Fig. 10 Reflection and transmission.

For deriving expressions for the reflected and transmitted waves we consider a plane harmonic wave

$$p(x, z, t) = p(\mathbf{r}, t) = e^{i(\mathbf{k} \cdot \mathbf{r} - \omega t)} \quad \text{with } \mathbf{k} \cdot \mathbf{r} = k_x x + k_z z \quad (35)$$

The wavenumber  $k$  is the absolute value of  $\mathbf{k}$ , i.e.,  $\|\mathbf{k}\| = k$ .

Assuming the incident wave to have unit amplitude, and denoting the amplitudes of the transmitted and reflected waves by  $T$  and  $R$ , respectively, one obtains

$$p_r = R e^{ik_1(x \cos \theta_1 - z \sin \theta_1)} \quad k_1 = \frac{\omega}{c_1} = \|\mathbf{k}_1\| \quad (36)$$

$$p_t = T e^{ik_2(x \cos \theta_2 + z \sin \theta_2)} \quad k_2 = \frac{\omega}{c_2} = \|\mathbf{k}_2\|$$

In these expressions,  $\theta_1$  is the grazing angle of incidence (which equals the grazing angle of reflection) and  $\theta_2$  is the grazing angle of transmission. The time factor  $e^{-i\omega t}$  is omitted, since it is common for  $p_i$ ,  $p_r$ , and  $p_t$ . ( $R$  and  $T$  are the amplitude reflection-coefficient and the amplitude transmission-coefficient, respectively).  $p_i$ ,  $p_r$ , and  $p_t$  are the incident, reflected, and transmitted waves. In the above expressions,  $R$ ,  $T$  and  $\theta_2$  are unknowns that have to be determined from the boundary conditions. The following two boundary conditions are valid<sup>1</sup> for  $z = 0$

1) Continuity of pressure:

$$p_i + p_r = p_t \quad (37)$$

2) Continuity of particle velocity in the  $z$ -direction:

$$\frac{1}{i\omega\rho_1} \frac{\partial(p_i + p_r)}{\partial z} = \frac{1}{i\omega\rho_2} \frac{\partial p_t}{\partial z} \quad (38)$$

Employing the first boundary condition results in the following expression

$$(1 + R) = T e^{i(k_2 \cos\theta_2 - k_1 \cos\theta_1)x} \quad (39)$$

Eq. (39) is only valid if the right side of the expression is independent of  $x$

$$k_2 \cos\theta_2 - k_1 \cos\theta_1 = 0 \quad (40)$$

This expression is known as Snell's law of refraction, and is often written as (using Eq. (36))

$$\frac{\cos\theta_2}{c_2} = \frac{\cos\theta_1}{c_1} \quad (41)$$

According to Eq. (39) also the following expression is valid, where both  $R$  and  $T$  can become complex,

$$(1 + R) = T \quad (42)$$

which together with the second boundary condition, gives

$$1 - R = T \frac{\rho_1 c_1 \sin\theta_2}{\rho_2 c_2 \sin\theta_1} \quad (43)$$

Finally, this leads to the following expressions for  $R$  and  $T$

$$R = \frac{Z_2 - Z_1}{Z_2 + Z_1} \quad \text{and} \quad T = \frac{2Z_2}{Z_2 + Z_1}$$

with (44)

$$Z_1 = \frac{\rho_1 c_1}{\sin\theta_1} \quad \text{and} \quad Z_2 = \frac{\rho_2 c_2}{\sin\theta_2}$$

$R$  in these above expressions is often referred to as the Rayleigh reflection coefficient;  $Z_1$  and  $Z_2$  are called the generalized acoustic impedances of the two media.

For illustrating the effect of bottom type on the reflection coefficient,  $R$  is determined for the bottoms of Figs. 8 and 9. In the underwater acoustics community, often, instead of  $R$  a quantity called bottom loss ( $BL$ ) is employed, which is defined as  $-20^{10} \log R$ . In the following we will make use of both  $R$  and  $BL$ . First, however, the critical angle, and the angle of intromission are considered.

### 2.5.1.1 The critical angle

If  $c_2 > c_1$ , then a critical angle  $\theta_c$  for which perfect reflection occurs, exists. For  $0 < \theta < \theta_c$ ,  $|R|=1$ , and  $R < 1$  for  $\theta > \theta_c$ .  $\theta_c$  can be determined from Snell's law

$$\theta_c = \arccos\left(\frac{c_1}{c_2}\right) \quad (45)$$

For  $0 < \theta < \theta_c$ ,  $\cos \theta_2 > 1$ , i.e.,  $\theta_2$  is purely imaginary. For these angles  $|R|=1$ , i.e., perfect reflection, but with an angle dependent phase shift, i.e.,  $R$  is complex. For  $\theta > \theta_c$ ,  $R < 1$  and real.

### 2.5.1.2 Angle of intromission

The angle of intromission,  $\theta_0$ , is the angle at which all energy is transmitted into the bottom, i.e.,  $R = 0$ . This requires that  $\frac{\rho_2 c_2}{\sin \theta_2} = \frac{\rho_1 c_1}{\sin \theta_1}$  (see Eq. (44)). Applying Snell's law, this results in

$$\theta_0 = \arctan \sqrt{\frac{1 - \left(\frac{c_2}{c_1}\right)^2}{\left(\frac{\rho_2 c_2}{\rho_1 c_1}\right)^2 - 1}} \quad (46)$$

This expression has a solution only if

- 1)  $\rho_2 c_2 > \rho_1 c_1$  and  $c_2 < c_1$ ;
- 2)  $\rho_2 c_2 < \rho_1 c_1$  and  $c_2 > c_1$ .

Condition 1 occurs in muddy media. Condition 2, however, does not occur for real ocean sediments.

### 2.5.1.3 The influence of attenuation

Plane wave attenuation  $\alpha'$  is defined through the following expression

$$\frac{dA}{dx} = -\alpha' A \Rightarrow A = A_0 e^{-\alpha' x} \quad (47)$$

with  $A_0$  the *rms* amplitude at  $x = 0$ . The unit of  $\alpha'$  is in  $\text{m}^{-1}$  if  $x$  is in m. A plane wave in free space with sound speed  $c$ , and angular frequency  $\omega$ , will be of the following form

$$e^{(ikx - \alpha x)} \quad (48)$$

with  $k$  the wavenumber, i.e.,  $k = \omega/c$ .

Attenuation is accounted for by including an imaginary part to the sound speed, i.e.,  $c(z) = c_r(z) - ic_i(z)$ . Now the plane wave takes the form

$$e^{\frac{i\omega x}{c}} = e^{i\omega x \frac{c_r + ic_i}{c_r^2 + c_i^2}} \quad (49)$$

Comparing Eq. (49) with Eq. (48), and assuming that  $c_i^2 \ll c_r^2$  leads to the following relation

$$c_i = \frac{\alpha'}{\omega} c_r^2 \quad (50)$$

In Figs. 8 and 9 the attenuation  $\alpha$  is given in  $\text{dB}/\lambda$ . The relation between  $\alpha$  and  $\alpha'$  is obtained by considering the ration of the amplitudes in dB between points that are a wavelength apart

$$\alpha = -20^{10} \log \frac{e^{-\alpha'(x+\lambda)}}{e^{-\alpha'x}} = \alpha' \lambda 20^{10} \log e \approx 8.686 \alpha' \lambda \quad (51)$$

Figure 11 shows the effect of the attenuation on  $BL$ , for the two bottoms, with the upper plot corresponding to the sand-silt-clay bottom and the lower plot corresponding to the mud bottom, respectively. All sediment properties are taken constant and equal throughout both the sediment and the sub-bottom, with the values equal to those at the top of the sediments of Figs. 8 and 9.  $c_p$ ,  $\rho$ , and  $\alpha$  are the seabed compressional wave speed, the density, and the attenuation constant, respectively.

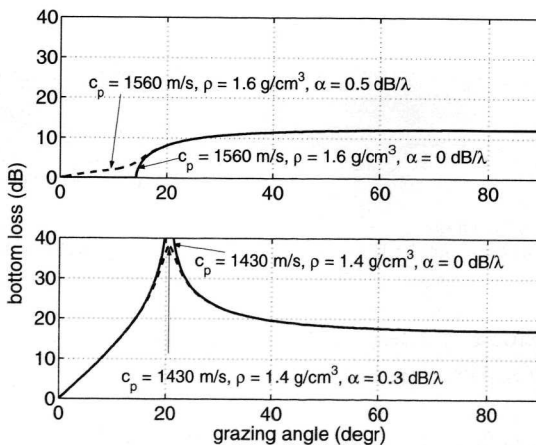


Fig. 11  $BL$  for a high speed (upper subplot) and a low speed (lower subplot) bottom, both with and without the effect of attenuation.

In the upper plot of Fig. 11, for the situation with an attenuation constant of zero, clearly the critical angle is seen at an angle of 15 degrees. The effect of the non-zero attenuation is especially noticeable at angles below the critical angle, where  $|R|$  no longer equals one. For the mud sediment, with a sound speed in the seabed that is lower than the water sound speed, the intromission angle is observed at 20 degrees, which is in accordance with Eq. (46).

### 2.5.1.4 Theory for layered structures

Theory of the reflection and transmission coefficients for layered media can be found in e.g. (Jensen<sup>1</sup>). For example, expressions for  $R$  and  $T$ , for a seabed consisting of a homogeneous top layer on a homogeneous half-space are

$$R = \frac{R_{12} + R_{23} e^{2i\varphi_2}}{1 + R_{12} R_{23} e^{2i\varphi_2}} \quad (52)$$

$$T = \frac{T_{12} + T_{23} e^{i\varphi_2}}{1 + R_{12} R_{23} e^{i\varphi_2}}$$

with the subscript  $ij$  indicating that the propagation direction is from medium  $i$  to medium  $j$ .  $\varphi_2$  is the vertical phase delay for sound crossing the layer of thickness  $h_2$ , i.e.,  $\varphi_2 = k_2 h_2 \sin \theta_2$ . Note that for this layered situation both  $R$  and  $T$  now depend on the frequency.

Figures 12 and 13 illustrate the effect of the increasing sediment sound speed on the reflection coefficient.

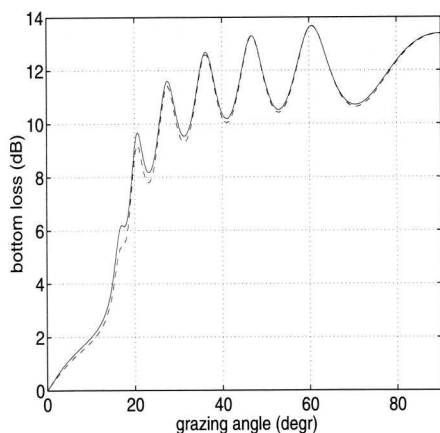


Fig. 12.  $BL$  for the sand-silt-clay sediment, and a frequency of 500 Hz. The solid line corresponds to a varying sediment sound speed (see Fig. 8). The dashed line corresponds to a homogeneous sediment, with a sound speed of 1565 m/s.

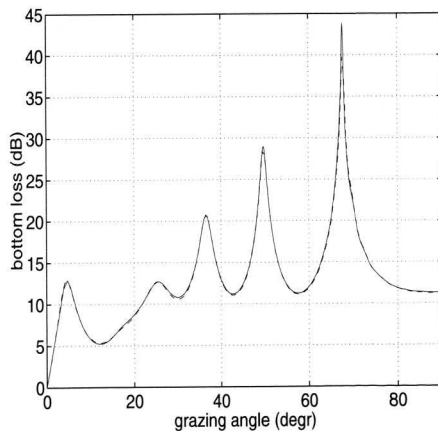


Fig. 13.  $BL$  for the mud sediment, and a frequency of 500 Hz. The solid line corresponds to a varying sediment sound speed (see Fig. 9). The dashed line corresponds to a homogeneous sediment, with a sound speed of 1435 m/s.

The figures show  $BL$  as a function of grazing angle (but for a fixed frequency of 500 Hz) for the two environments with an increasing (see Figs. 8 and 9), and a constant sediment sound speed. The constant sediment sound speed was taken as the average of the corresponding varying sound speeds, i.e., 1435 m/s and 1565 m/s, respectively. The theory for estimating the

bottom reflection coefficient for sediments with varying sound speeds goes beyond the scope of this chapter. We limit ourselves to showing that for the bottoms of Figs. 8 and 9, with a thin sediment and a small sound speed variation, there is no need to account for the sound speed variation, since the two curves, both in Fig. 12 and Fig. 13, almost coincide. In the remainder of this Section 2.5.1 we will therefore use the expressions for a constant sediment sound speed, Eq. (52). It should be mentioned here, that the normal-mode solution, which is used for calculating the acoustic propagation in the remainder of the thesis, does account for the variation of the sound speed in the sediment. In Fig. 12 clearly the critical angle belonging to the water/sediment interface at an angle of 15 degrees is seen. Although the mud sediment has values for the density and sound speed such that an intromission angle is expected (at 20 degrees, see Fig. 11), this feature is not seen in Fig. 13 due to the influence of the sub-bottom. Note in both figures the interference patterns due to the layered structure.

Figures. 14 and 15 show  $BL$  for the two bottoms as a function of grazing angle and frequency. Clearly  $BL$  is higher for the mud sediment than for the sand-silt-clay sediment.

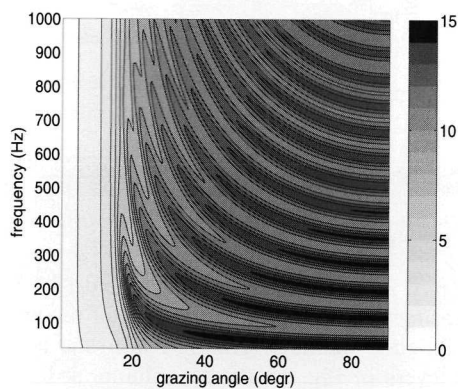


Fig. 14  $BL$  in dB for the sand-silt-clay sediment as a function of frequency and grazing angle.

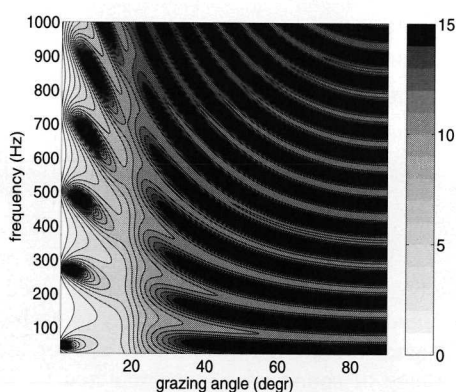


Fig. 15  $BL$  in dB for the mud sediment as a function of frequency and grazing angle.

## 2.5.2 Influence of bottom type on transmission loss and received signal shape

Transmission loss  $TL$  is defined as

$$TL(r, z) = -20^{10} \log \left| \frac{p(r, z)}{p_0(r = 1 \text{ m})} \right| \quad (53)$$

with  $p(r, z)$  given by Eq. (33) and  $p_0$  the solution to the Helmholtz equation for a homogeneous medium without boundaries

$$p_0(r) = \frac{1}{4\pi r} e^{ikr} \quad (54)$$

i.e., a spherical wave with wavenumber  $k = \omega / c$ , with  $c$  being the sound speed of the homogeneous medium. For further illustrating the effect of bottom type on the acoustic

propagation,  $TL$  is calculated for the two bottoms of Figs. 8 and 9. To this end, Eq. (33) is used for determining the received pressures for the two bottoms, for a large set of receiver depths (ranging from 0–190 m) and for a large set of distances from the source (ranging from 0–5 km). The sound source is positioned at 70 m of water depth. These pressures have been used to determine  $TL$ . Figs. 16 and 17 show again the two environments, but now the complete sound speed profile (in water column, sediment layer and sub-bottom) is indicated as well.

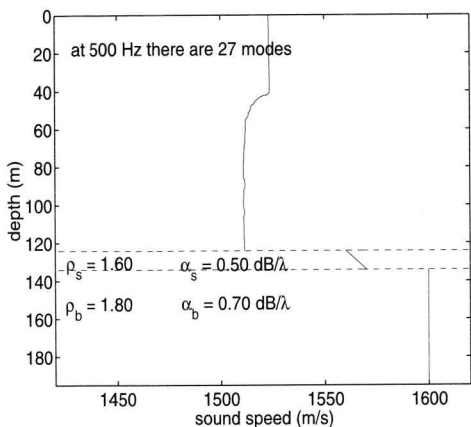


Fig. 16 The sand-silt-clay sediment.

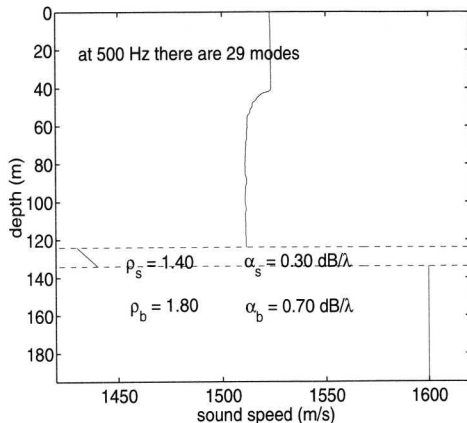


Fig. 17 The mud sediment.

The sea is perfectly flat, i.e., a wind speed of zero m/s. Also indicated in Figs. 16 and 17 is the amount of modes corresponding to each of the sediments. Note that the amount of modes is higher for the mud sediment than for the sand-silt-clay sediment. This is due to the larger range of sound speeds encountered in the three layers of Fig. 16 (water column, sediment layer, and sub-bottom).

Figure 18 shows  $TL$  for the sand-silt-clay sediment, whereas  $TL$  for the mud sediment is shown in Fig. 19.

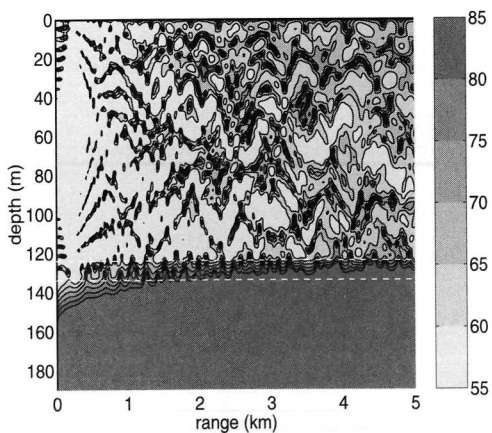


Fig. 18  $TL$  (dB) as a function of depth and range for the sand-silt-clay environment. The sediment layer is indicated by white dashed lines. The sound source is at 70 m depth.

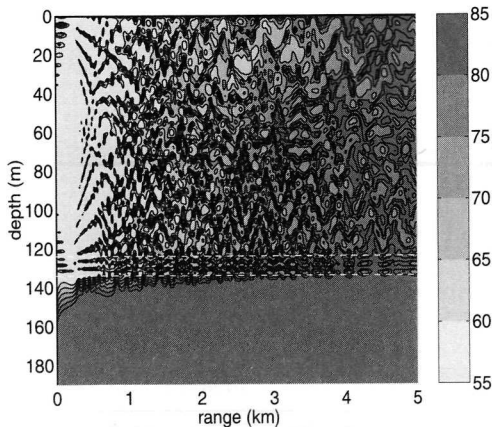


Fig. 19  $TL$  (dB) as a function of depth and range for the mud environment. The sediment layer is indicated by white dashed lines. The sound source is at 70 m depth.



Clearly  $TL$  is much higher for the mud sediment than for the sand-silt-clay sediment. This can be understood by looking at Figs. 20 and 21, showing all modes for the two sediments, respectively. For the mud sediment all modes are oscillatory in the sediment, thereby experiencing high losses due to the sediment attenuation, see Eq. (32). On the contrary, for the sand-silt-clay sediment there are modes, viz., modes 1-19, that are only oscillating in the water column and exponentially decaying in the sediment, and thus experience hardly any losses due to the sediment attenuation.

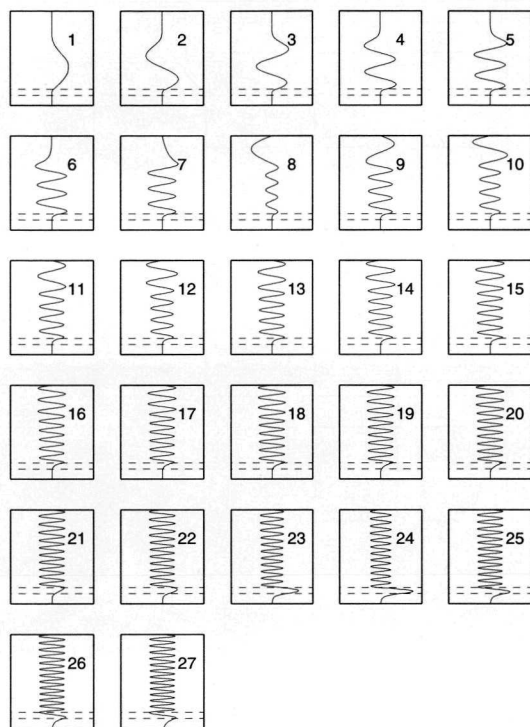


Fig. 20 All modes corresponding to the sand-silt-clay sediment. Depth is along the y-axis, mode amplitude is plotted along the x-axis. The horizontal dashed lines indicate the sediment layer.

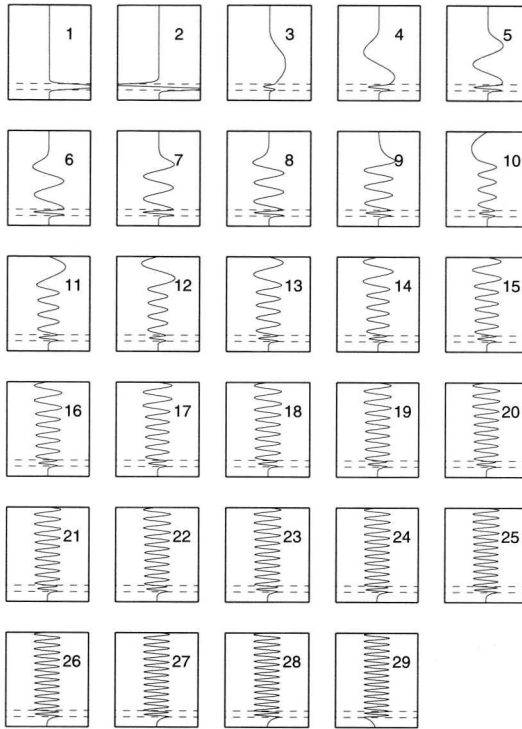


Fig. 21 All modes corresponding to the mud sediment. Depth is along the y-axis, mode amplitude is plotted along the x-axis. The horizontal dashed lines indicate the sediment layer.

In the majority of the chapters to follow, the signal that is used in the analysis consists of the received complex pressures as a function of hydrophone position and frequency. For all experiments described in this thesis use is made of a vertical array of hydrophones as the receiving system. (In none of the succeeding chapters information on the receiving system equipment used during the experiments is provided. Therefore, Appendix B briefly describes this receiving equipment). The resulting complex pressures as a function of depth are referred to as 'pressure fields'. Figure 22 shows, for the two sediments, the absolute values of the pressure fields as a function of depth for two frequency values and three range values. For the mud sediment, the pressure field becomes less oscillatory due to the sediment attenuation. Sediment attenuation has less influence for the sand-silt-clay sediment, see the discussion above.

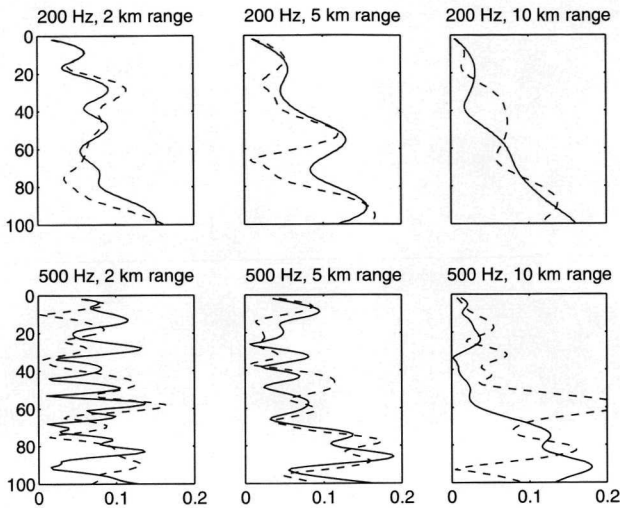


Fig. 22 Absolute values of complex pressure fields as obtained for both the sand-silt-clay (dashed lines) and the mud sediment (solid lines) for frequencies of 200 and 500 Hz, and for distances of 2, 5, and 10 km.

### 2.5.3 An example from practice: a model validation exercise

In (Simons<sup>14</sup>) results of an acoustic model validation exercise are presented. The acoustic data used for the validation were collected from shallow waters in the Firth of Clyde off the West Coast of Scotland in the summer of 1997. The received signals were compared with simulations using a normal-mode propagation model. Here part of the results of (Simons<sup>14</sup>) are presented with the purpose of illustrating both the importance of knowing the geo-acoustic parameters with sufficient accuracy, and the effect of temporal oceanographic variability on the received signals.

Figure 23 shows the track along which the acoustic propagation experiments were performed. The water depth along the track amounts to about 70 m. The receiving system consisted of a vertical receiving array containing three hydrophones, located under water at approximately 10, 35, and 55 meters. The source depth amounted to ~30-40 m.

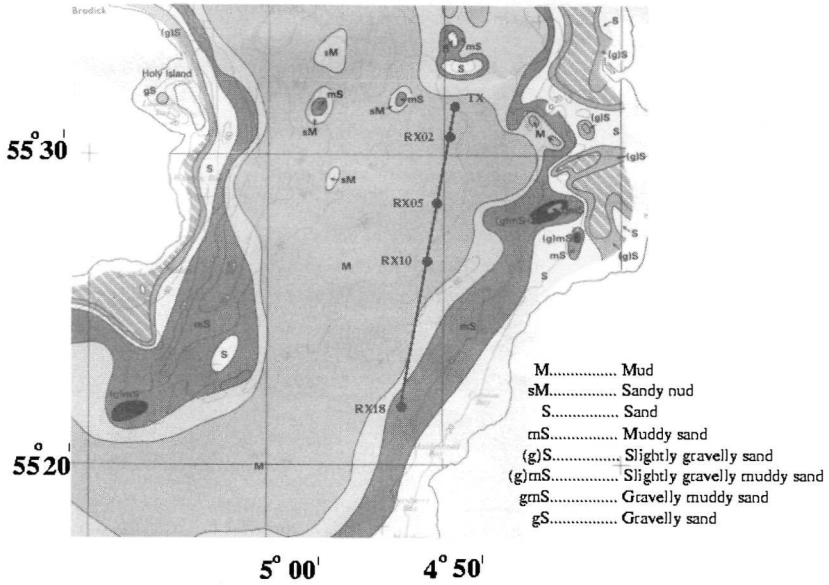


Fig. 23 Acoustic track in the Clyde area. TX denotes the position of the transmitting station, whereas RX02, RX05, RX10, and RX18 denote the positions of the receiving station. "02", "05", "10", and "18" indicate the source/receiver distances (2, 5, 10, and 18 km).

A frequency modulated (FM) signal (chirp) of bandwidth 1-8 kHz with a pulse duration of 1 s was transmitted. The source pulse was transmitted every 35 s over a period of 70 min, giving a total of 120 pulses for each configuration. The received signals were correlated with the transmitted signal. This technique is called 'matched filtering' and reveals the multipath arrivals as a function of time. This is illustrated in Fig. 24, showing the result of applying the matched filter technique to a signal that contains two FM's, starting at 1 and 1.5 s, respectively.

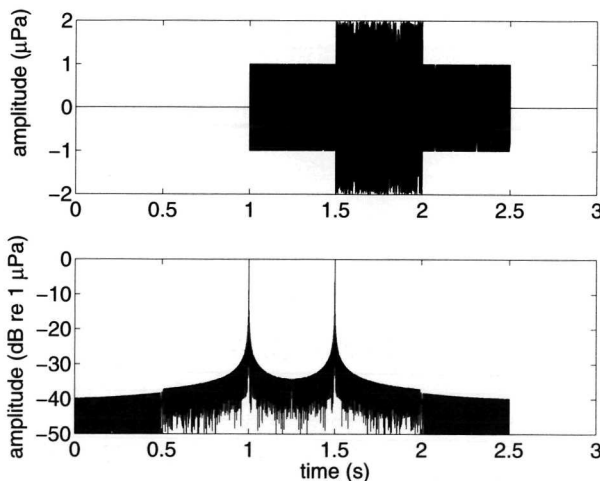


Fig. 24 Illustration of the matched filter technique: the upper subplot line indicates the original signal, the lower subplot indicates the result after matched filtering (in dB).

In the following we will compare the measured multipath structure with modeled multipath structures, i.e., the model/data comparison is carried out using signals in the time domain, in contrast to the remainder of the thesis, where the model/data comparison is carried out in the frequency domain.

### 2.5.3.1 Input data for the normal-mode model

Certain inputs to the model are explicitly known. These include the geometrical configuration, viz., the ranges between the ships (as calculated from the GPS ship positions) and the source and receiver depths (as obtained from the depth sensors mounted on the source and receiving hydrophone string).

The water column sound speed profiles that were used for the model input were obtained from CTD casts carried out from the receive ship close to the times of transmission. A single profile was selected for each configuration, and therefore range-dependence of the sound speed in the water column was not accounted for.

The bathymetry of the track was measured by an echosounder and appeared to be fairly range-dependent. To run a normal-mode model employing the adiabatic approximation, the track has to be divided into a number of segments, each with a constant water depth (see Section 2.4.2). The division in segments is based on bathymetry changes along the track and is such that the jump in water depth between adjacent segments is a constant. The water-depth jump should be sufficiently small such that decreasing this jump, and thereby adding more segments, has no further influence on the received signal. From the received signals calculated as a function of depth jump (ranging from 0.5 to 10 m), it was concluded that a 4-m jump is sufficiently small.

For a range of 10 km the 4-m depth jump resulted in six range segments. Figure 25 shows the measured bathymetry and the applied segmentation. The echosounder track does not exactly coincide with the acoustic track, and therefore, the actual bathymetry along the acoustic track can deviate from the bathymetry shown in Fig. 25. This allows the bathymetry to be varied within a few meters when improving the match between modeled and measured signals.

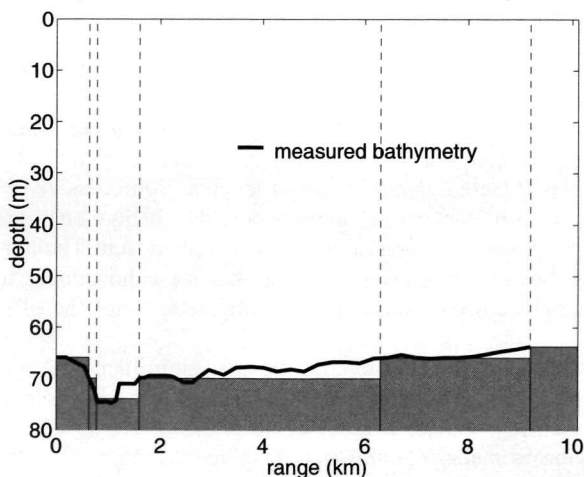


Fig. 25 Measured bathymetry along the acoustic track and the corresponding constant water-depth segments (indicated by the vertical dashed lines).

The normal-mode model used assumes the bottom to consist of a single sediment layer overlying a homogeneous sub-bottom. The sound speed in the sediment is allowed to vary

with depth. The densities and attenuation constants in sediment and sub-bottom are assumed constant.

For obtaining information on the geo-acoustic bottom parameters, use has been made of a geological map of the British Geological Survey (BGS) as a guide.<sup>15</sup> Figure 23 shows this geological map of the Clyde area, according to which the sediment type along the acoustic track is classified as type mud (i.e., silt and clay). According to (McCann<sup>16</sup>) the majority of the sound speeds that were measured for mud sediments have values ranging from 1450 up to 1575 m/s. The average density of mud sediments<sup>5</sup> amounts to  $1.5 (\pm 0.2) \text{ g/cm}^3$ . Measured attenuation constants in marine sediments are known to exhibit a large spread. A realistic start value for the attenuation constant in mud is taken to be  $0.15 \text{ dB}/\lambda$ .<sup>5</sup> We assumed a linearly increasing sound speed in the sediment. The typical sound speed gradient found in mud sediments<sup>16</sup> is about  $1 \text{ s}^{-1}$ . According to the BGS map the sediment thickness along the acoustic track varies between 20 and 40 m.<sup>15</sup> At the given frequency band of interest (centered around 4.5 kHz) and for the given sediment attenuation, the penetration of sound in the sediment is less than about 10 m. For sediment thickness we therefore adopted a value larger than 10 m, viz. 20 m, being the minimum value according to the map. For this set of sediment parameters, all sub-bottom parameters were found to have no influence on the model output. In order to limit the number of normal modes and hence the computation time, the sub-bottom sound speed was set to 1600 m/s. Further, the sub-bottom density and the attenuation constant were set arbitrarily at  $1.75 \text{ g/cm}^3$  and  $0.7 \text{ dB}/\lambda$ , respectively. In contrast, sediment sound speed, sediment attenuation, and geometrical parameters such as the water depth can have a pronounced effect on the received signals.

### 2.5.3.2 Comparison of measured and modeled signals

In an attempt to model this complicated environment at the relatively high frequencies of interest, the following approach was taken. As a first step the 2-km range data were considered. From a preliminary set of model runs it was found that the sediment density and the sediment sound speed gradient have only a very small influence on the received signals. The sub-bottom parameters and sediment thickness ( $> 10 \text{ m}$ ) have no influence at all.

From all geo-acoustic parameters, the upper sediment sound speed has by far the most significant influence on the propagation: increasing or decreasing the upper sediment sound speed results in an increase or decrease, respectively, of the amount of multipaths, but not in a time shift of the individual multipath arrivals. From varying the upper sediment sound speed, using the nominal values for the geometrical parameters, a value of about 1525 m/s was found to result in modeled signals with a time dispersion comparable to that of the measured signals.

As a next step, to further improve the precise match of the multipath arrival structure the geometrical input parameters (source depth, receiver depths, source/receiver range, and bathymetry) were varied within acceptable limits. For the bathymetry the measured bathymetry as shown in Fig. 25 was used and an offset was applied to it. The justification for applying an offset to the echosounder measurements is that the echosounder track did not exactly coincide with the acoustic track. According to bathymetry maps the offset can be as large as 6 m.

As expected, water-depth offset turned out to have the greatest influence. Applying a water depth offset of  $-5 \text{ m}$  resulted in the best model/data match for all three hydrophones simultaneously. This offset corresponds to a water depth at the source of 61 m, which is in accordance with the bathymetry maps. For this new bathymetry again the influence of the source depth, source/receiver range and receiver depth was considered. Adjusting the receiver depths from their baseline values resulted in a further improved model/data match.

For the obtained 'optimized' geometrical parameter set, a new search for upper sediment speed was carried out in the range 1505 m/s - 1565 m/s (in 10 m/s steps). A value of 1545 m/s resulted in the best model/data match.

Finally the sediment attenuation constant was 'optimized'. From all values considered (0.15 dB/ $\lambda$  to 0.85 dB/ $\lambda$  in steps of 0.1 dB/ $\lambda$ ) 0.55 dB/ $\lambda$  resulted in an improved match, compared to the start value of 0.15 dB/ $\lambda$ .

It is emphasized that although a large amount of model runs (several hundreds) were carried out, only a small subset of all possible parameter combinations was considered. Performing an exhaustive full inversion for all parameters of the geo-acoustic profile would require a huge amount of model runs, which at these high frequencies of interest is not practical. (A single normal-mode model run for the band 1-8 kHz requires about 30 min on a state-of-the-art workstation).

For the 2-km range (deep source), Figs. 26-28 show the 120 individual measured signals for the three hydrophones, respectively. Also plotted in each figure are the medians of the experimental data, and the modeled received signals employing the optimized parameter set derived above. The measured and modeled signals are time aligned to allow a direct comparison.

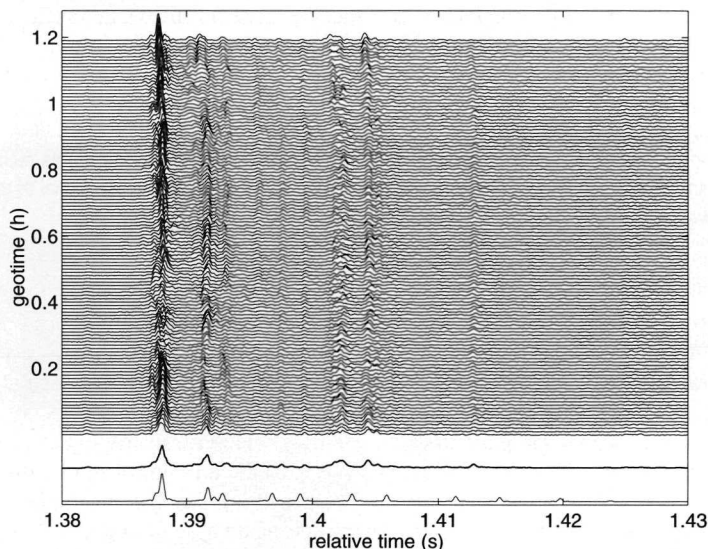


Fig. 26 The 120 individual received signals (showing the amount of time variability) as received during the 2-km experiment on the upper hydrophone. Also shown are the median signal of the experimental data (thick curve) and the modeled signal (lowest curve).



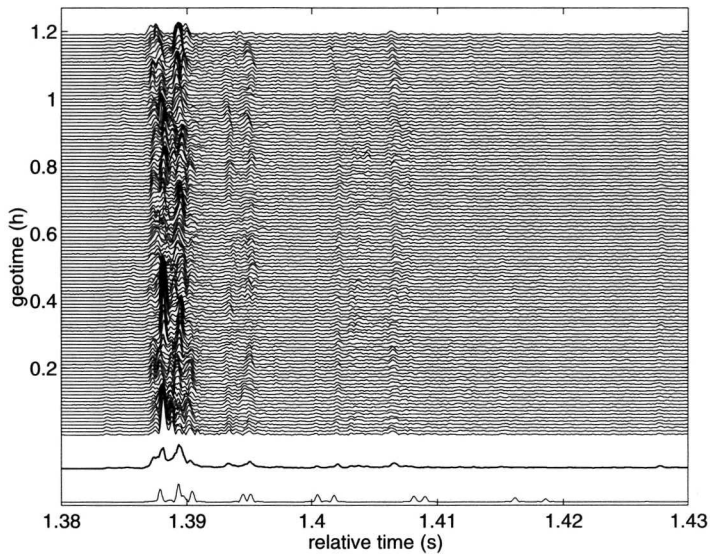


Fig. 27 The 120 individual received signals (showing the amount of time variability) as received during the 2-km experiment on the middle hydrophone. Also shown are the median signal of the experimental data (thick curve) and the modeled signal (lowest curve).

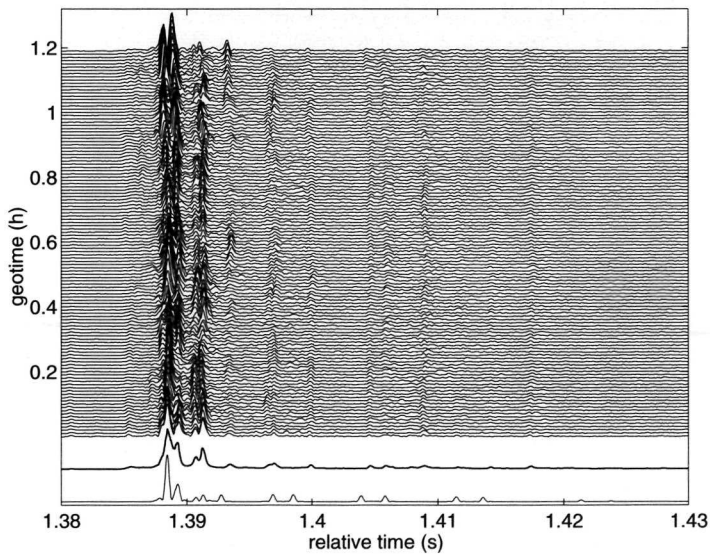


Fig. 28 The 120 individual received signals (showing the amount of time variability) as received during the 2-km experiment on the deepest hydrophone. Also shown are the median signal of the experimental data (thick curve) and the modeled signal (lowest curve).

It can be concluded that a set of parameters, comprising both geometrical and geo-acoustic parameters, is derived that, for the 2-km range, results in an acceptable match between data



and model. Especially the first two groups of multipaths (within the first 10 ms) are modeled quite well for all three hydrophones simultaneously. The locations of the later arrivals are less well modeled.

Figure 29 shows the received signals for the 5-km range (deep source, middle hydrophone). Although an extensive search was carried out for a set of both geometrical and geo-acoustic parameters in an attempt to model these signals, none of the tested input parameter sets has resulted in an acceptable match. Obviously, the strong time variability at this range precludes a deterministic modeling of the precise multipath arrival structure. However, the decreased time dispersion for the 5-km range, compared to that at 2 km, can only be explained with a lower sediment sound speed, i.e., sediment sound speed has to decrease with range. This is also in accordance with the expected transition from sandy mud to mud with increasing range (see Fig. 23). Ignoring range-dependence in the surficial sediment speed would have resulted in an increase in time dispersion with increasing range. On the contrary, measured time dispersion decreases with increasing range. A sediment speed of 1510 m/s at 5-km range from the source can explain the observed time dispersion.

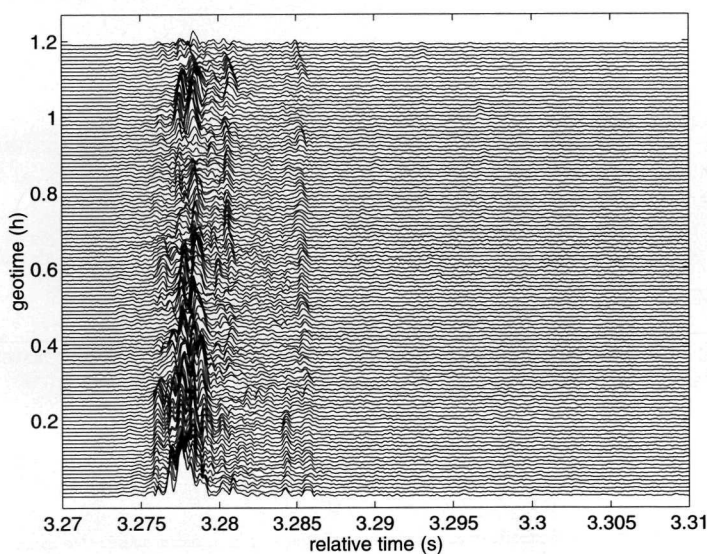


Fig. 29 The 120 individual received signals for the 5-km, middle hydrophone, experiment.

Due to the very high time variability of the 10-km range signals, an acceptable model/data agreement could not be obtained. Further, it should be emphasized that we are considering propagation of relatively high frequency sound in only 70 meters of water over a range of 10 km (which is over 140 times the water depth). It is therefore postulated that at 10 km the applied modeling is too simple.

### 2.5.3.3 Relation with matched field inversion

The approach taken is actually the 'matched field inversion' approach described in the introduction, where the set of unknown parameters that results in modeled data that have a maximum match with the measured data is assumed to comprise the 'true' unknown parameter values. However, no use is made of an optimization method, and the optimization, in this case the maximization of the match, can be considered to be a search 'by hand' and using physical intuition. Only a limited amount of parameter values and parameter

combinations are considered. It can easily be understood that this procedure for obtaining estimates for the unknown parameters is not very practical. This is especially true for problems with a large number of unknowns, and a large number of parameter combinations containing parameter values that are significantly different from the 'true' parameters, but that nevertheless look like a good optimization result. These parameter combinations that correspond to an optimum within a part of the entire search domain containing all possible parameter combinations, are denoted by local optima. More sophisticated global search methods exist, and will be considered in the next chapters.

From the previous it can be concluded that the influence of the oceanographic time variability on the received signals increases with increasing range. At 5-km range the variability in received signals is such that for obtaining an acceptable match the temporal (and spatial) variation of the sound speed profile should be accounted for. Not only increasing the range, but also increasing the frequency is expected to hamper the matched field inversion performance. This is the result of the smaller wavelengths at higher frequencies. When modeling the propagation of sound, features as small as the wavelength have to be accounted for.

The applicability of matched field inversion as a function of range and frequency is schematically illustrated in Fig. 30.

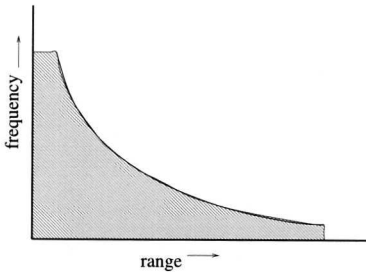
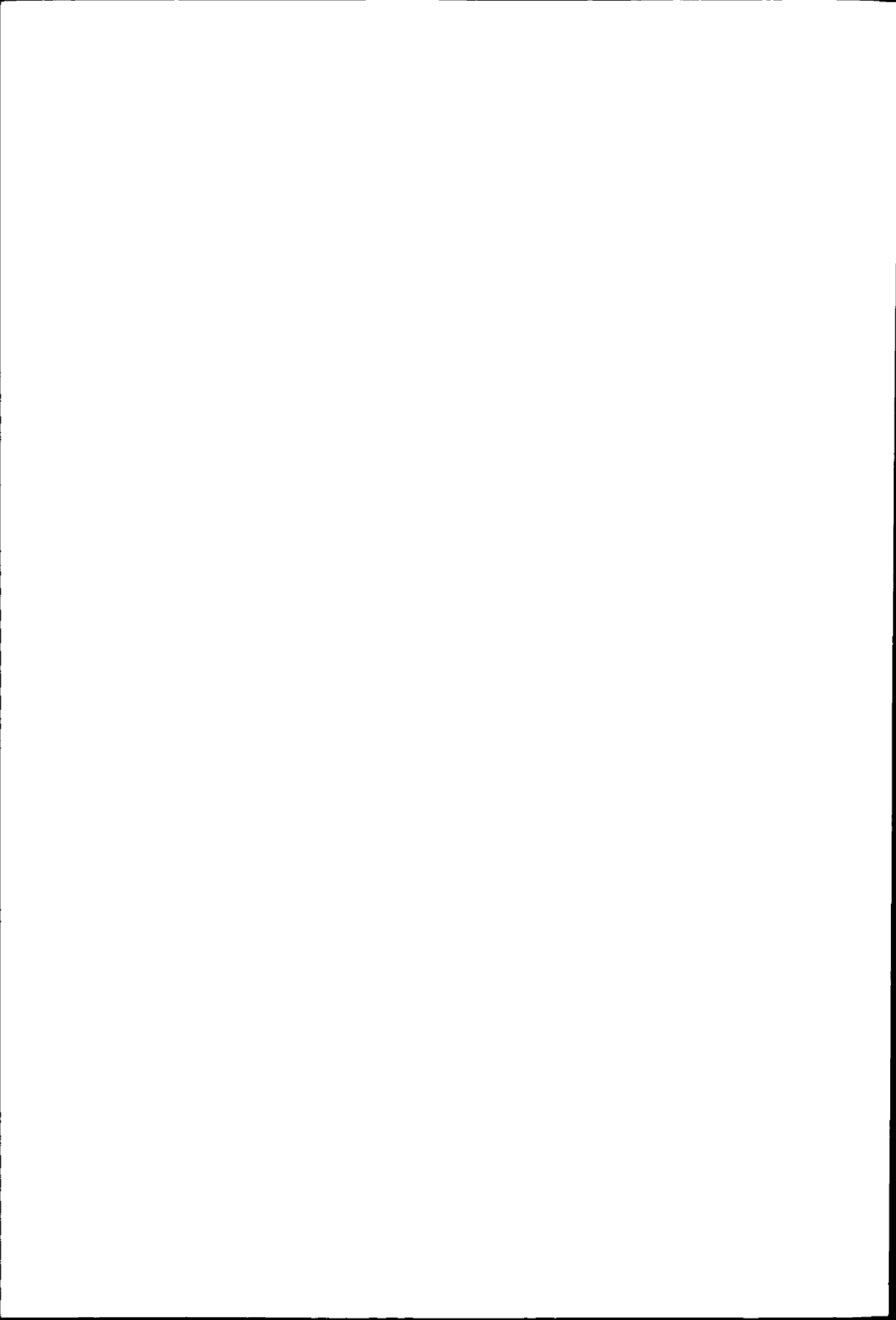


Fig. 30 Schematic of range/frequency combinations allowing for matched inversion, indicated by shaded areas.

## References

- 1 F. B. Jensen, W. A. Kuperman, M. B. Porter, and H. Schmidt, *Computational ocean acoustics*, American Institute of Physics, Inc., New York, 1994.
- 2 J. Wu, "Bubbles in the near-surface ocean: a general description," *Journal of Geophysical Research* **93**, 587-590 (1988).
- 3 E. L. Hamilton, and R. T. Bachman, "Sound velocity and related properties of marine sediments," *J. Acoust. Soc. Am.* **72** (6), 1891-1904 (1982).
- 4 R. T. Bachman, "Acoustic and physical property relationships in marine sediments," *J. Acoust. Soc. Am.* **78** (2), 616-621 (1985).
- 5 E. L. Hamilton, "Geoacoustic modeling of the sea floor," *J. Acoust. Soc. Am.* **68** (5), 1313-1331 (1980).
- 6 T. H. Orsi, and D. A. Dunn, "Sound velocity and related physical properties of fine-grained abyssal sediments from the Brazil Basin (South Atlantic Ocean)," *J. Acoust. Soc. Am.* **88** (3), 1536-1542 (1990).
- 7 E. L. Hamilton, "Compressional-wave attenuation in marine sediments," *Geophysics* **37** (4), 620-645 (1972).
- 8 M. Siderius, P. Gerstoft, and P. Nielsen, "Broadband geoacoustic inversion from sparse data using genetic algorithms," *J. Comp. Acoust.* **6** (1&2), 117-134 (1998).
- 9 E. L. Hamilton, "Sound velocity gradients in marine sediments," *J. Acoust. Soc. Am.* **65** (4), 909-922 (1978).
- 10 C. A. Boyles, *Acoustic waveguides, Applications to ocean science*, John Wiley & Sons, Wiley-Interscience, USA, 1984.
- 11 F. Ingenito, "Measurement of mode attenuation coefficients in shallow water," *J. Acoust. Soc. Am.* **53**, 858-863 (1973).
- 12 W. A. Kuperman, and F. Ingenito, "Attenuation of the coherent component of sound propagation in shallow water with rough boundaries," *J. Acoust. Soc. Am.* **61**, 1178-1187 (1977).
- 13 Lectures Notes in Computer Science 6: Matrix Eigensystems Routines-EISPACK Guide, Section 2.1.17, Springer-Verlag, 1976.
- 14 D. G. Simons, R. McHugh, M. Snellen, N. H. McCormick, and E. A. Lawson, "Analysis of shallow water experimental acoustic data including a comparison with a broadband normal-mode propagation model," *IEEE J. Oceanic Eng.* **26** (3), 308-323 (2001).
- 15 Seabed sediments & quaternary, Clyde, Sheet 55N, 06W, Scale 1:25000, British Geological Survey.
- 16 C. McCann, S. G. Marks, L. M. Grimbely, D. M. McCann, and I. R. Dermot, *Seismic properties of sea floor sediments and rocks*, British Geological Survey, Technical report WN/94/7/C, 1994.



## Chapter 3

# Single-frequency and multi-frequency matched field inversion using a genetic algorithm

### 3.1 Introduction

During the last years, matched field processing (MFP) has become an important research topic in underwater acoustics since it is a promising method for both source localization and for determining parameters of the ocean environment.

When applying MFP for source localization, a pressure field, measured using an array of hydrophones, is correlated with pressure fields that are calculated for different ranges and depths of the source using an appropriate propagation model. The source range and depth combination that results in the highest correlation should correspond to the true range and depth of the source.

Often many of the environmental, and also geometrical input parameters, are not known very accurately or are not known at all, prohibiting a successful source location estimation. This problem is referred to as mismatch. (Collins<sup>1</sup>) describes the so-called focalization-approach. In this approach not only the source position, but also the environmental and geometrical parameters are the unknowns that have to be determined. In this way the problem has become an optimization problem where the function that has to be optimized, i.e., the correlation between measured and modeled pressure field, depends on many variables. In addition, this function can have local minima. Finding the global optimum of a function of many variables requires the use of global optimization methods, such as simulated annealing (SA) and genetic algorithms (GA). This process of finding values for that set of unknown parameters that provides the maximum correlation is denoted by matched field inversion (MFI).

In (Simons<sup>2</sup>) MFI results obtained using SA are presented for real experimental data (shallow water). (Gerstoft<sup>3</sup>) presents the use of genetic algorithms for MFI. When comparing these results with results obtained with SA, GA showed better performance. For other comparisons the author refers to (Davis<sup>4</sup>)-(Stoffa<sup>7</sup>), where the use of GA and SA for geophysical applications is described, generally favoring the GA. It is mentioned in (Gerstoft<sup>3</sup>) that one reason for this better performance of the genetic algorithm is the fact that when using SA all parameters are altered separately. However, in inversion problems there often is a parameter hierarchy, i.e., some parameters are more important than others and hence the least important parameters cannot be determined until the most important parameters are close to their correct values. Consequently there will be a lot of ineffective alternations to the parameter value combinations at the start of the optimization process, and therefore a lot of ineffective calculations. This drawback can be overcome by using adaptive simulated

annealing, where the importance of each parameter during the course of the run is determined and used for directing the search for new parameter value combinations.<sup>8</sup>

Genetic algorithms, however, automatically show adaptive behavior. When using genetic algorithms all parameters are changed simultaneously. By favoring the most promising parameter value combinations at all stages of the optimization process, first the most important parameters will converge to their correct values, followed by a search for the values of the less important parameters.

Another drawback of changing the parameters separately is that it might be difficult to find the optimum for problems in which the parameters are very dependent on each other. In (Collins<sup>9</sup>) an efficient SA algorithm that can overcome this problem is described.

In this chapter the SA and GA performance in finding the global optimum are compared. Also, the use of multiple frequencies is assessed.

Section 3.2 provides a description of the basic principles behind genetic algorithms. Also the simulated annealing algorithm is described shortly. In Section 3.3 the application of genetic algorithms for matched field inversion is described. An unambiguous *a posteriori* analysis method is presented (Gerstoft<sup>3</sup>), and both single- and multi-frequency (Section 3.4) results are presented. Section 3.5 presents the summary and conclusions

## 3.2 The Genetic algorithm and simulated annealing

### 3.2.1 Genetic algorithms

Genetic algorithms can be used for the optimization of a function that is dependent on many variables and with many local optima.<sup>10-12</sup> They were first used by Holland<sup>13</sup> in the early 1970's, and are based on a direct analogy with those processes in natural populations that are essential to the evolution process. The basic principle of a genetic algorithm is explained in what follows.

For the problem considered, we want to minimize a function that is a measure for the difference between a pressure field obtained from a measurement, and a pressure field that is computed for a certain set of the unknown parameters. This function is called the energy function. The energy function  $E$  is normalized such that the fitness  $\phi$  is given by,  $\phi = 1 - E$ , i.e., a low value for the energy function  $E$  means a high value for the fitness  $\phi$ .

A genetic algorithm starts with creating an initial population. Each member of this population represents a certain parameter value combination, i.e., a possible solution to the optimization problem. This initial population, consisting of  $q$  members, is created randomly. The population size  $q$  should be large enough to ensure that the problem space is searched thoroughly. On the other hand, the population size should be small enough to allow for the evaluation of a large number of generations with a limited amount of energy function evaluations. At this stage the members of the population are in their binary encoded form, i.e., the parameter value combinations are represented by a string of zeros and ones. In the following these strings will be denoted as chromosomes.

Each parameter is represented by a certain part of the chromosome. These parts are called genes. This encoded form of the parameter value combinations is needed when applying certain operators, as will be explained later. The encoding applied here is such that the least significant bit is located at the end of the gene. In the literature also applications of genetic algorithms can be found in which operators are used that can be applied to real numbers, and no use needs to be made of the parameter value combinations in encoded form.<sup>11</sup>

The next step is to decode the members of the population and to calculate for all members of the population the value of the energy function. Based on these energy function values, a parental distribution is selected from the initial population in such a way that a higher fitness

implies a larger probability of being selected, thus resulting in a parental distribution with a higher proportion of fit members. However, at the beginning the selection criterion should not be chosen too strict, as that would force the algorithm to converge to a local minimum. On the other hand, a criterion that allows nearly all members to reproduce will result in a slow convergence.

From the members of the parental population a new population, denoted by the children population, is established by applying two operators, viz., crossover and mutation. In order to apply crossover the members of the parental distribution are paired randomly. Crossover results in the exchange of corresponding chromosome parts between the two chromosomes of each set of parents. Applying crossover at more than one chromosome location is called multiple-point crossover. Other ways of applying crossover include single-point crossover, where there is only one cut-point at the entire chromosome, and uniform crossover, where use is made of a randomly generated string containing zeros and ones, that in some way defines where exchange of chromosome bits should occur. It is clear that adding additional crossover points results in a more thorough search of the problem space. On the other hand, an enlarged amount of crossover points also implies a larger probability that good parameter values and parameter value combinations are disrupted.

Finding a global optimum using single-point crossover might be difficult in cases where there is a lot of interaction between the different parameters. As this is the case in our problem the use of multiple-point crossover has been selected for our application. Following (Gerstoft<sup>3</sup>) a crossover point is selected at each gene, i.e., the number of crossover points is equal to the number of parameters for which the optimization is performed.

Consider for example the following two genes, representing different values for the same parameter:

$$(a_0, a_1, \dots, a_{N-1}) \quad \text{and} \quad (b_0, b_1, \dots, b_{N-1})$$

with  $a_i$  and  $b_j = 0, 1$ . The parameter has been encoded using  $N$  bits.

Applying crossover at location  $i$  will result in the creation of two different genes:

$$(a_0, \dots, a_{i-1}, b_i, \dots, b_{N-1}) \quad \text{and} \quad (b_0, \dots, b_{i-1}, a_i, \dots, a_{N-1})$$

Crossover is applied with a crossover probability  $p_c$ . Using a value of  $p_c$  less than one will allow genes to be passed onto the next generation without the disruption of crossover (usually  $0.6 < p_c < 1.0$ , see (Beasley<sup>10</sup>)). The crossover point, i.e., the location on the gene at which it is cut, resulting in a gene 'head' segment and a gene 'tail' segment, is selected at random.

After crossover another operator called mutation is applied to the chromosomes. Mutation randomly changes each element (bit) of the chromosomes with a mutation probability  $p_m$ . The value of  $p_m$  is very dependent on the values of other genetic algorithm parameters, such as the amount of bits used for encoding the different parameters (in general  $p_m < 0.1$ ).

Crossover is considered to be a mechanism for rapid exploration of the search space. More crossover points or a higher crossover probability imply a more thorough search, but also more disruption. Mutation is a process that provides a small amount of random search, thus ensuring that no point in the search space has zero possibility of being explored. However, the mutation rate should not be chosen too high, as then the search becomes effectively random. Generally it is thought that at the start crossover is the more productive operator, but that as the population converges mutation becomes more and more important. Different researchers have tried to obtain better performance by using crossover and mutation rates that change as the process continues, but the effects of using these kind of operators are not clear yet.<sup>10,11</sup>

A new population is now established by taking at random  $f_c q$  members of the children population, and the  $(1-f_c)q$  most fit members of the previous population.

How to choose a value for  $f_r$  is an important item. Until recently, generational replacement, i.e., the entire population is replaced ( $f_r = 1$ ) has been the standard. The elitist strategy is generational replacement, but now the best member of a population is copied directly into the succeeding generation<sup>12</sup>, i.e., the next generation will consist of  $(q-1)$  members of the children population and of the best member of the previous generation. It is clear that even with the elitist strategy many of the best population members might not get the opportunity to reproduce. Also good genes can get lost due to crossover or mutation. A solution to these problems is applying steady state: only a part of the population is replaced. Often this part consists of a few members only.<sup>12</sup> In this way the GA is given the opportunity to immediately exploit a promising individual. However, using a small value for  $f_r$  might promote convergence to a local minimum. In our work two different values for  $f_r$  have been employed.

The new population is used as the next generation on which the same procedure is applied as described in the previous paragraphs. It is thought that by continuing this process over many generations, good characteristics will spread throughout the population, while being mixed with other good characteristics, thus exploring the most promising areas of the search space. The amount of generations should be chosen large enough to allow convergence of the optimization process.

Tuning of the genetic algorithm is needed in order to ensure that there is a large probability that the parameter value combination that is close to the global optimum is present in the final population. Each application requires its own tuning.

### 3.2.2 Simulated annealing

Since the results obtained with the GA are compared with the results obtained by simulated annealing (SA), the SA algorithm is described briefly here. SA is based on an analogy between mathematical optimization problems and the thermodynamic process of slowly cooling a pure liquid substance to form a perfect crystal (annealing), i.e., the lowest energy state of the system.

For explaining how the SA works we will consider the minimization of an energy function  $E$ . First,  $E$  is evaluated for the initial parameter combination. Then the individual parameters are randomly perturbed one at a time, according to

$$m_i' = m_i + \xi \Delta_i \quad (1)$$

with  $\xi$  a random number drawn from a uniform distribution on  $[-1, 1]$ .  $\Delta_i$  is the maximum perturbation allowed for each parameter  $m_i$  (here taken as half of the corresponding search interval). Whenever the new parameter falls outside the search interval, a new value is drawn.

After each perturbation the energy function is evaluated. A decrease in  $E$  is accepted unconditionally, whereas an increase in  $E$  is accepted with a probability that is given by the Boltzmann distribution

$$e^{-\Delta E/T_j} \quad (2)$$

with  $T_j$  a control parameter analogous to the temperature. When all parameters have been perturbed a certain number of times (twice in this work), the temperature is slightly reduced according to a cooling schedule. A logarithmic cooling has been employed, i.e.,

$$T_{j+1} = c_f T_j \quad (3)$$

The cooling factor  $c_f$  is a constant  $< 1$ , but close to 1. From Eqs. (2) and (3) it is seen that the probability of accepting an increase in  $E$  decreases as the temperature decreases. The concept



of accepting perturbations that increase  $E$  allows the algorithm to escape from local minima. More details can be found in (Simons<sup>2</sup>).

### 3.3 Applying the GA for Matched Field Inversion

#### 3.3.1 The acoustic problem

The data used in the inversions were obtained during a SACLANT Centre MFP experiment in a virtually range-independent shallow water area, north of the island of Elba (October 1993).<sup>15</sup> The water depth amounts to approximately 127 m. The receiving system is a vertical array consisting of 48 hydrophones with 2-m spacing. Due to array tilt and/or imprecise measurement of the water depth, the actual array depth  $h_I$  is not known exactly and therefore  $h_I$  has to be determined in the optimization (in accordance with (Gingras<sup>15</sup>) and (Gerstoft<sup>3</sup>),  $d_R$  is defined as the depth of the deepest hydrophone, being nominally 112.7 m).

The source is deployed at a range of 5.5 km from the receiving array at a depth of 75 m. Two broadband signals were transmitted by the source (not simultaneously). The signal used in our analysis has a frequency band of 160-180 Hz. From the spectrum that is obtained after Fourier transformation of 8.192 seconds of the data, six frequencies around the center of the 160-180 Hz band are selected for the analysis, i.e., the Fourier coefficients at:

- 164.43 Hz
- 166.87 Hz
- 168.95 Hz
- 171.14 Hz
- 172.85 Hz
- 174.44 Hz

These frequencies are such that the differences in the pressure fields at the six frequencies in the 160-180 Hz band are maximal.<sup>15</sup>

The sound speed profile used for calculating the replica fields is the sound speed profile as measured at the array site. The profile exhibits a 60-m deep surface duct.

It has already been mentioned that for mismatch conditions the focalization approach has to be applied. In this approach, not only the source range and depth, but also other environmental and geometrical model input parameters are determined in the optimization process. The vector containing the parameters for which the inversion is performed is:

$$\mathbf{m} = \begin{pmatrix} \alpha_b \\ \rho_b \\ c_b \\ r_s \\ z_s \\ H_w \\ d_R \end{pmatrix}$$

with  $\alpha_b$  the attenuation in the bottom,  $\rho_b$  the density of the bottom,  $c_b$  the compressional velocity in the bottom,  $r_s$  and  $z_s$  the range and depth of the source,  $H_w$  the water depth and  $d_R$  the array depth.

Figure 1 shows the assumed ocean environment. In contrast with (Gingras<sup>15</sup>) the ocean bottom is assumed to consist of a single semi-infinite homogeneous medium only. In fact the sediment is omitted in this study, since propagation will not be sensitive to sediment parameters when sediment thickness ( $\sim 5$  m) is small compared to the acoustic wavelength ( $\sim 9$  m).<sup>2</sup>

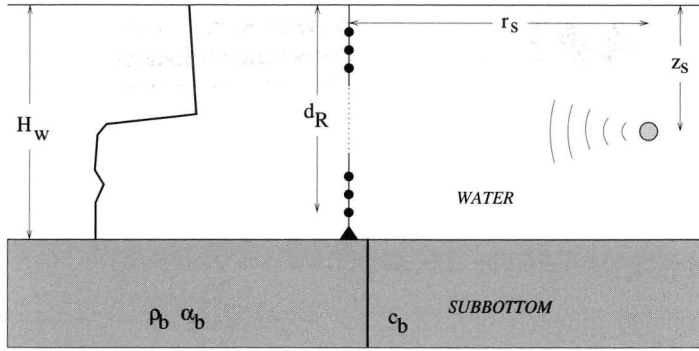


Fig. 1 The ocean environment discussed in this chapter.

The function that is optimized is a function that provides a measure for the difference between a measured and a calculated pressure field, i.e., a measure for the difference between  $\mathbf{p}_{obs}$  and  $\mathbf{p}_{calc}(\mathbf{m})$ .

The following expression for the (complex) pressure on the  $k^{\text{th}}$  hydrophone in the frequency domain is used<sup>2</sup>

$$p_{obs,k}(\omega_{m'}) = \sum_{n=1}^M f_k(t_m) e^{2\pi i(m'-1)(m-1)/M} \quad (4)$$

with and  $M$  the FFT length (8192). This is the complex conjugate of the discrete Fourier transform of  $f_k(t_m)$  at the selected frequency  $\omega_{m'}$ . Here  $f_k(t_m)$  is the received signal time sequence ( $k^{\text{th}}$  hydrophone). The reason for using the complex conjugate is the assumption of time dependence  $e^{-i\alpha t}$  in the calculation of the normal-mode solution.<sup>16</sup>

The time samples are

$$t_m = \frac{(m-1)}{f_s} \quad \text{for } m = 1, 2, \dots, M \quad (5)$$

where  $f_s$  is the sample frequency (1 kHz).

The discrete frequencies are

$$\omega_{m'} = 2\pi \frac{(m'-1)f_s}{M} \quad \text{for } m' = 1, 2, \dots, M \quad (6)$$

The (complex) pressure calculated for the parameter combination  $\mathbf{m}_j$  at the  $k^{\text{th}}$  hydrophone (at a depth  $z_k$ ) and a source at a range  $r_s$  and depth  $z_s$  is given by the normal-mode solution<sup>16</sup>

$$p_{calc,k}(\mathbf{m}_j) = \frac{e^{\frac{i\pi}{4}}}{\rho(z_s)\sqrt{8\pi r_s}} \sum_{n=1}^L \psi_n(z_s)\psi_n(z_k) \frac{e^{ik_n r_s - \alpha_n r_s}}{\sqrt{k_n}} \quad (7)$$

with  $\psi_n$ ,  $k_n$  and  $\alpha_n$  the mode functions, the eigenvalues, and the modal loss coefficients, respectively.  $L$  is the number of normal modes.

### 3.3.2 Setting of the GA parameters

Two different scenarios have been considered. One in which the optimization was performed using data at a single frequency (168.95 Hz), and one in which the inversion was performed using data at all six frequencies mentioned in Section 3.3.1. A well-known measure for the difference between calculated pressure field  $\mathbf{p}_{calc}$ , and measured pressure field  $\mathbf{p}_{obs}$  is the linear, or Bartlett, processor. We have applied an energy function based on this Bartlett processor, viz.,

$$E(\mathbf{m}_j) = 1 - P_{lin}(\mathbf{m}_j) \quad (8)$$

with  $P_{lin}$  the Bartlett processor, or

$$E(\mathbf{m}_j) = 1 - \frac{\left| \mathbf{p}_{obs} \cdot \mathbf{p}_{calc}^*(\mathbf{m}_j) \right|^2}{\left\| \mathbf{p}_{obs} \right\|^2 \left\| \mathbf{p}_{calc}(\mathbf{m}_j) \right\|^2} \quad (9)$$

The  $*$  means that use is made of the complex conjugate transposed. The calculated pressure field is obtained for the parameter vector  $\mathbf{m}_j$ .

In (Gerstoff<sup>3</sup>) using another form for the energy function is recommended, as this function is less peaked

$$E(\mathbf{m}_j) = \sqrt{1 - \frac{\left| \mathbf{p}_{obs} \cdot \mathbf{p}_{calc}^*(\mathbf{m}_j) \right|^2}{\left\| \mathbf{p}_{obs} \right\|^2 \left\| \mathbf{p}_{calc}(\mathbf{m}_j) \right\|^2}} \quad (10)$$

In the single-frequency scenario we have performed the optimization with the GA using these two different energy functions, viz., the expressions of Eqs. (9) and (10). For the cases where use was made of all six frequencies we have selected the following energy function

$$E(\mathbf{m}_j) = 1 - \frac{1}{K} \sum_{k=1}^K \left( \frac{\left| \mathbf{p}_{obs,k} \cdot \mathbf{p}_{calc,k}^*(\mathbf{m}_j) \right|^2}{\left\| \mathbf{p}_{obs,k} \right\|^2 \left\| \mathbf{p}_{calc,k}(\mathbf{m}_j) \right\|^2} \right) \quad (11)$$

This is the incoherent multi-frequency Bartlett processor ( $K$  is the number of frequencies, 6 in our case).

As explained in Section 3.2.1 members for the parental distribution are selected according to their fitness ( $1-E$ ). The probability  $p_j$  for the member  $\mathbf{m}_j$  to be selected is taken as in (Gerstoff<sup>3</sup>)

$$p_j = \frac{\exp\left(\frac{-E(\mathbf{m}_j)}{T}\right)}{\sum_{i=1}^q \exp\left(\frac{-E(\mathbf{m}_i)}{T}\right)} \quad (12)$$

with  $T$  a factor called the temperature. Following (Gerstoff<sup>3</sup>) the temperature is chosen equal to the lowest value of the energy function found in the entire current population. This choice results in a flat distribution at the beginning, but as the optimization process continues the temperature will decrease, resulting in a more peaked probability distribution and therefore more emphasis will be put on the most fit members at a later stage.

For the remaining genetic algorithm parameters the following values have been used. Most values have been taken equal to those used in (Gerstoff<sup>3</sup>) (here denoted by \*)

- The population size  $q$ : 64\*
- The number of generations: 400
- The crossover rate  $p_c$ : 0.8\*
- The mutation rate  $p_m$ : 0.05\*
- The fraction of the population of children that is put in the next generation,  $f_r$ : 0.5\*, 0.8
- Number of bits used for encoding the parameter values: [8 8 8 8 8 8]\*, [7 7 8 11 10 7 7]

### 3.4 Results

Table I gives the search bounds for all parameters for which the optimization is performed (see Chapter 2 for the typical range of values encountered).

Table I Boundaries for the parameters that are optimized.

$m_i$	Lower bound	Upper bound
$\rho_b$ (g/cm <sup>3</sup> )	1.2	3.2
$\alpha_b$ (dB/ $\lambda$ )	0.0	1.0
$c_b$ (m/s)	1550	1750
$r_s$ (m)	100	11000
$z_s$ (m)	1	120
$H_w$ (m)	125	135
$d_R$ (m)	110	114

The optimization has been performed for the genetic algorithm parameter settings given in Table II. For each setting the GA has been run 50 times.

Table II The different GA settings.

	$q$	$p_c$	$p_m$	$f_r$	Bits	Number of frequencies ( $K$ )	$E$
Setting1	64	0.8	0.05	0.5	[8 8 8 8 8 8]	1	$\sqrt{1 - P_{lin}}$
Setting2	64	0.8	0.05	0.5	[7 7 8 11 10 7 7]	1	$\sqrt{1 - P_{lin}}$
Setting3	64	0.8	0.05	0.8	[7 7 8 11 10 7 7]	1	$\sqrt{1 - P_{lin}}$
Setting4	64	0.8	0.05	0.5	[7 7 8 11 10 7 7]	1	$1 - P_{lin}$
Setting5	64	0.8	0.05	0.5	[7 7 8 11 10 7 7]	6	$1 - \frac{1}{K} \sum_{k=1}^K P_{lin,k}$

Figures 2 and 3 show the results for a typical run. In Fig. 2 the value for the energy function,  $(1 - P_{lin})$ , of the most fit member of a population, i.e., the lowest  $(1 - P_{lin})$  value found for a

generation, is displayed as a function of generation. Figure 3 shows the corresponding parameter values.

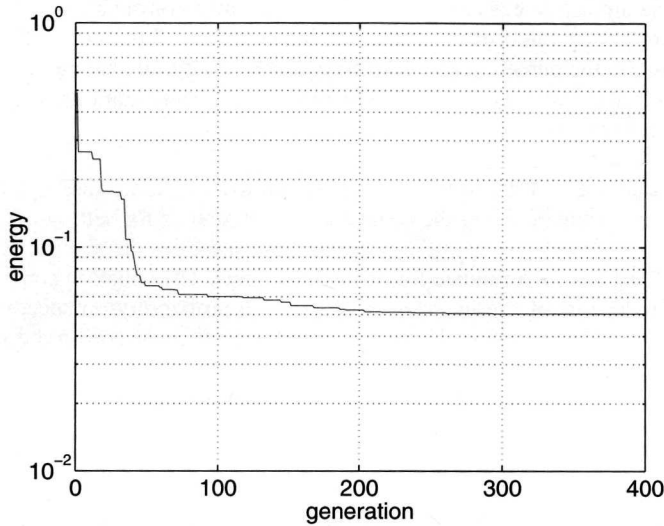


Fig. 2 Convergence of energy ( $1 - P_{tin}$ ) of most fit chromosome as a function of generation.

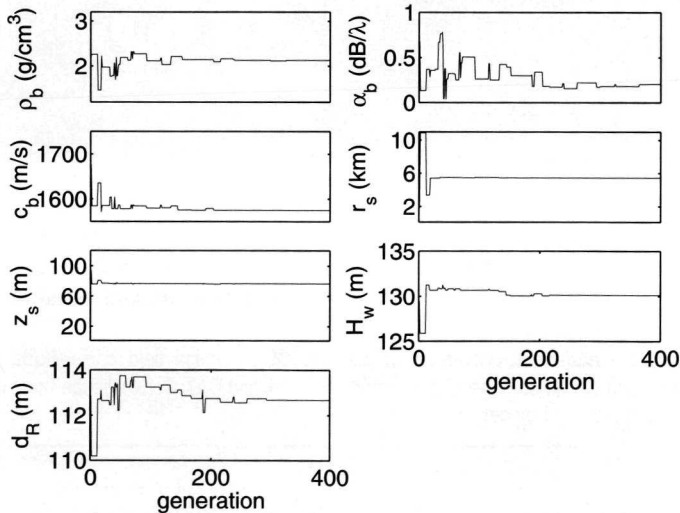


Fig. 3 Convergence of the different parameters, belonging to the most fit chromosome.

### 3.4.1 Single-frequency results

#### 3.4.1.1 Performance of the Genetic Algorithm

First, results obtained using a single frequency (168.95 Hz, setting1-setting4, see Table II) are considered. In order to get an indication for how good the genetic algorithm performs for the

different settings, and to be able to compare the results to those obtained using simulated annealing the following questions are posed:

- How often has the algorithm converged to a parameter value combination with a value of  $r_s$  around 5.4 km, and a value of  $z_s$  around 75 m within say 7000 calls of the forward model? This provides the percentage of converged runs, i.e., the success rate.
- What is the speed of convergence to these parameter value combinations, i.e., how many replica field calculations are needed?

The results can be found in Table III. Results obtained using SA, are displayed in the last row. These results were obtained using the same energy function as for setting4. Since only a finite amount of runs is considered, also the uncertainties on the results should be taken into account when comparing the performance for different settings. The situation considered here, comprising a set of independent events, each with a certain probability on success, typically corresponds to a binomial distribution. Then, denoting the amount of converged runs by  $N_c$ , the fraction of the total amount of runs ( $N_r$ ) that has converged by  $f_c$ , and assuming this fraction to be the probability on convergence, the standard deviation of the amount of converged runs,  $\sigma_{N_c}$ , is

$$\sigma_{N_c} = \sqrt{f_c(1-f_c)N_r} \quad (13)$$

Assuming statistically independent observations, the uncertainty (or error) on the mean and the uncertainty (or error) on the standard deviation can be determined by

$$\sigma_M = \frac{\sigma}{\sqrt{N_c}} \quad (14)$$

$$\sigma_\sigma = \frac{\sigma}{\sqrt{2N_c}}$$

with  $\bar{M}$  and  $\sigma$  the mean and standard deviation, respectively, of the amount of replica field calculations needed for convergence, and  $\sigma_M$  and  $\sigma_\sigma$  the corresponding uncertainties.

Table III Means  $\bar{M}$  and standard deviations  $\sigma$  of the amount of replica field calculations needed for convergence, and the percentage of converged runs (GA and SA). Convergence must occur within 7000 calls for the forward model.

	$\bar{M}$	$\sigma_M$	$\sigma$	$\sigma_\sigma$	Percentage converged (%)
Setting1	868	117	732	83	78±6
Setting2	767	124	843	88	92±4
Setting3	1054	150	992	106	88±5
Setting4	747	165	951	117	66±7
SA	953	124	849	88	52±5

It follows that about 70/90% of all GA runs converge to the correct source range and source depth. The percentage of converged runs is significantly less, viz., about 50 %, when use is made of SA. Use can be made of a slower cooling law for increasing the percentage of converged SA runs. However, this will also result in an increased  $\bar{M}$ .

Figure 4 shows the histograms of the number of calls for the forward model needed for convergence for the situation of setting2 and for the situation where simulated annealing was used for the optimization, respectively. It is seen that in most cases convergence occurs somewhere between 0 and ~1500 calls for the forward model.

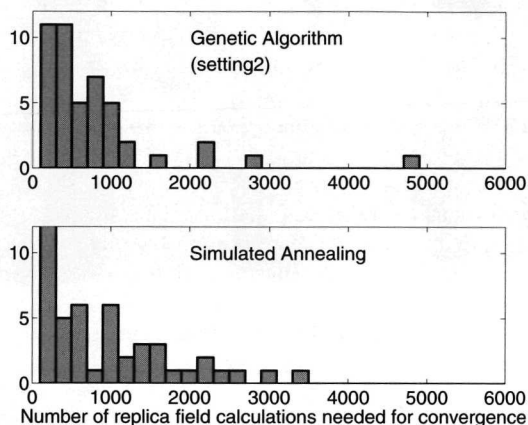


Fig. 4 Histograms of the number of calls for the forward model needed for convergence, both for the GA with setting2, and for SA.

Using 8 bits for the discretization in range results in range increments of 43 meters. This is of the same order of magnitude as the standard deviation in range obtained in (Gerstoff<sup>3</sup>). Using 11 bits for the discretization in range results in range increments of 5 meters, which is a sufficient sampling of the expected range probability distribution. Similarly 8 bits for the discretization in source depth is insufficient. Therefore, we will not further consider the results obtained for setting1.

It follows that changing the value of  $f_r$  from 0.5 to 0.8 results in an increase of  $\bar{M}$  (setting2 and setting3). In the situation with  $f_r = 0.5$ , 50% of a current population is directly passed onto the next generation. In the situation with  $f_r = 0.8$ , only 20% of a current population is passed directly onto the next generation (so 80% of this next generation consists of new parameter value combinations). Consequently, there is a lot more disruption in the situation with  $f_r = 0.8$ , resulting in a higher probability on good parameter values and good parameter value combinations being disrupted. This explains the higher value for  $\bar{M}$ . Trying to enlarge the success rate often is the reason for using a high value for  $f_r$ . However, the differences we observed in the success rates for the GA with setting2 and for the GA with setting3, respectively, are not statistically significant. Comparing the results for setting2 and setting4 shows a lower percentage of converged runs for setting4. This is due to the use of a more peaked energy function. The amount of forward calculations needed for convergence is not statistically significant smaller.

### 3.4.1.2 A posteriori analysis

In Section 3.4.1.1 results of a single run have been shown and the different success rates and rates of convergence have been determined. In the following we will take a closer look at the parameter estimates.

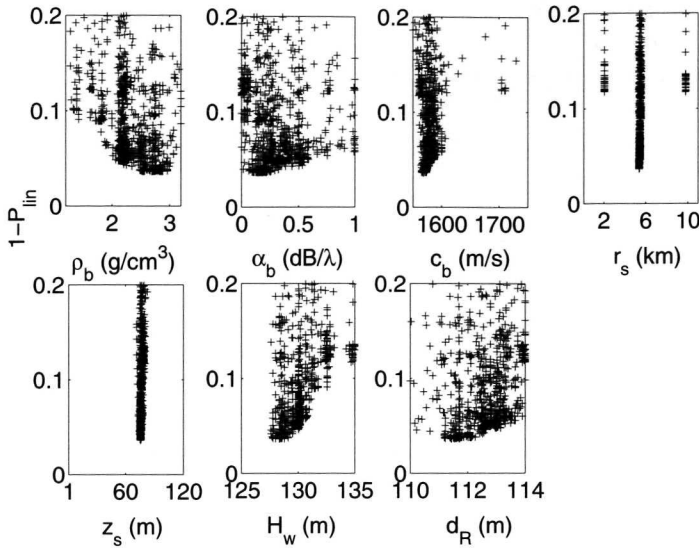


Fig. 5 Values for  $(1-P_{lim})$  plotted against the different parameters, GA, single-frequency results.

Figure 5 shows the values for  $1-P_{lim}$  plotted against the different parameter values. The local minima in the range-depth ambiguity surface<sup>3</sup> can easily be identified in the plot of  $1-P_{lim}$  against the range  $r_s$ . Figure 6 zooms in onto the lowest  $1-P_{lim}$  values. The parameter value combinations with a sub-bottom density greater than 2.6 are indicated by circles. In fact, densities greater than  $\sim 2.6$  are not physically realistic for the type of bottom considered ( $c_b < 1750$  m/s).

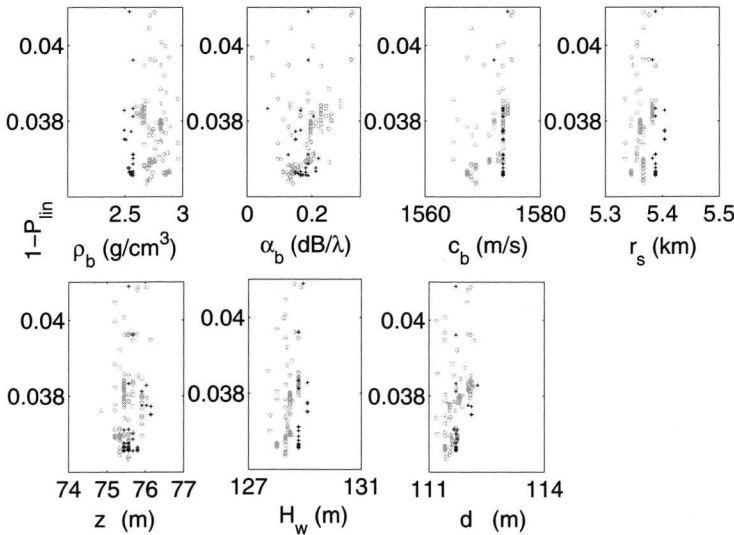


Fig. 6  $(1-P_{lim})$  plotted against the different parameters, obtained using the GA (single-frequency results). The parameter value combinations with a  $\rho_b > 2.6$  are marked by circles.

From the set of parameter value combinations consisting of all members of all final populations (of the runs with GA setting2) estimates for the unknown parameters can be derived, i.e., an estimation for the solution of the inverse problem. As the goal is to examine



the area around the global optimum, only parameter value combinations with values for the range in between 4.0 and 6.0 km are accounted for. According to (Gerstoft<sup>3</sup>) for each particular parameter  $m_i$  ( $i = 1, \dots, 7$ ) the probability distribution for obtaining the particular value  $\kappa$  is determined

$$\sigma_{\kappa} = \frac{\sum_{j=1}^{N_T} \exp[-(1 - P_{lin}(\mathbf{m}_j))/T'] \delta((\mathbf{m}_j)_i = \kappa)}{\sum_{j=1}^{N_T} \exp[-(1 - P_{lin}(\mathbf{m}_j))/T']} \quad (15)$$

Here  $N_T$  is the total number of parameter value combinations found in all final populations ( $N_T = 64 \cdot 50 = 3200$ ),  $\mathbf{m}_j$  is the  $j^{\text{th}}$  parameter combination, and  $T'$  is a temperature parameter. All samples are weighted according to a Boltzmann distribution, similarly to the weighting performed during the optimization. Choosing the temperature equal to the lowest energy will favor the fittest part of the population. Choosing the temperature equal to the energy of the least fit corresponds to a more even weighting of the population. In (Gerstoft<sup>3</sup>) this temperature is taken equal to the average energy function value of the 50 best members. Since there is only a limited amount of SA runs (the non-converged SA runs do not meet the restriction that the range should be in between 4.0 and 6.0 km), we used a temperature equal to the lowest of all values found for  $(1 - P_{lin})$  in all final populations. However, using for the GA results the average energy of the 50 best members did not result in a significant change, since a large part of the population has converged to the same result. Following the method described in (Gerstoft<sup>3</sup>) we determined the following *a posteriori* mean and covariance of the model parameters,  $A(\mathbf{m})$  and  $C(\mathbf{m})$ , respectively.

$$A(\mathbf{m}) = \sum_{j=1}^{N_T} \mathbf{m}_j \sigma(\mathbf{m}_j) \quad (16)$$

with  $\sigma(\mathbf{m}_j)$  the probability for the  $j^{\text{th}}$  parameter combination

$$\sigma(\mathbf{m}_j) = \frac{\exp[-(1 - P_{lin}(\mathbf{m}_j))/T']}{\sum_{j=1}^{N_T} \exp[-(1 - P_{lin}(\mathbf{m}_j))/T']} \quad (17)$$

$$C(\mathbf{m}) = E \left\{ [\mathbf{m} - A(\mathbf{m})][\mathbf{m} - A(\mathbf{m})]^T \right\} = \sum_{j=1}^{N_T} \mathbf{m}_j (\mathbf{m}_j)^T \sigma(\mathbf{m}_j) - A(\mathbf{m})A(\mathbf{m})^T \quad (18)$$

with superscript  $T$  the transpose operator.

In Table IV the means and standard deviations found for of the parameter estimates obtained by the GA with setting2 are presented (the means and standard deviations found for the situations of setting3 and setting4 are almost equal to those of setting2). Also the means and standard deviations obtained by the SA runs can be found.

Table IV Means (second column) and standard deviations (third column) of the different parameter values obtained in the final populations (GA setting2). For comparison the means (fourth column) and standard deviations (fifth column) of the final parameter values obtained with SA are also given.

	GA, setting2		SA	
$T$	0.037		0.038	
$\rho_b$	2.46±0.006	0.30±0.004	2.56±0.055	0.38±0.039
$\alpha_b$	0.30±0.003	0.17±0.002	0.29±0.031	0.22±0.022
$c_b$	1578±0.18	9.5±0.13	1579±2.50	17.1±1.77
$r_s$	5414±0.96	50.7±0.68	5402±10.1	69.2±7.13
$z_s$	75.7±0.010	0.52±0.007	75.7±0.121	0.83±0.086
$H_w$	129.4±0.018	0.97±0.013	129.2±0.188	1.29±0.133
$d_R$	112.3±0.012	0.65±0.009	112.2±0.11	0.76±0.079

It is clear that the mean parameter values obtained with GA are in good agreement with the mean parameter values obtained with SA. However, using the SA algorithm results in somewhat higher standard deviations than those obtained when using a genetic algorithm. Note also that the errors on the means and standard deviations are much smaller for the GA results than for the SA results. The reason for this is that there are much more GA results, since each GA run provides 64 parameter sets.

Figures 7 and 8 show the probability distributions obtained for the runs with setting2 and the SA runs, respectively, calculated according to Eq. (15).

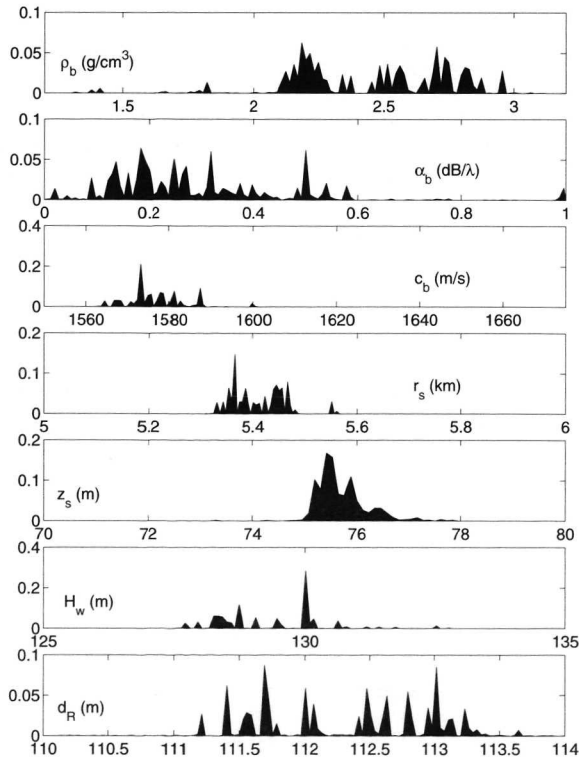


Fig. 7 Probability distributions for the GA results with setting2.

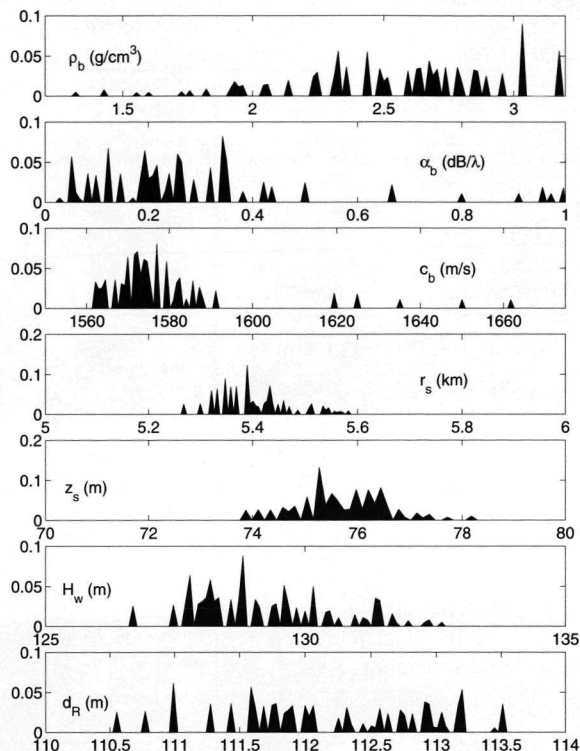


Fig. 8 Probability distributions for the SA results.

In Figs. 9 and 10 all parameters are displayed as a function of one of the other parameters. The parameter value combinations displayed in these figures are the parameter value combinations as they were obtained in the simulated annealing optimization runs (converged runs). Therefore, all parameter combinations have low, but not equal, energy function values. The figures clearly show that some parameters are strongly coupled, e.g.  $r_s$  to  $H_w$ , and  $c_b$  to  $\alpha_b$ . This latter relation states the adverse effects on the bottom loss resulting from an increase in  $c_b$  and in  $\alpha_b$ , respectively.

As already mentioned, strong parameter coupling can cause difficulties when looking for the global optimum. In our application of the genetic algorithm this problem has been avoided by using multiple crossover points, i.e., a crossover point at each gene. Probably this feature is a reason for the better performance of the genetic algorithm compared to the performance of the simulated annealing algorithm.

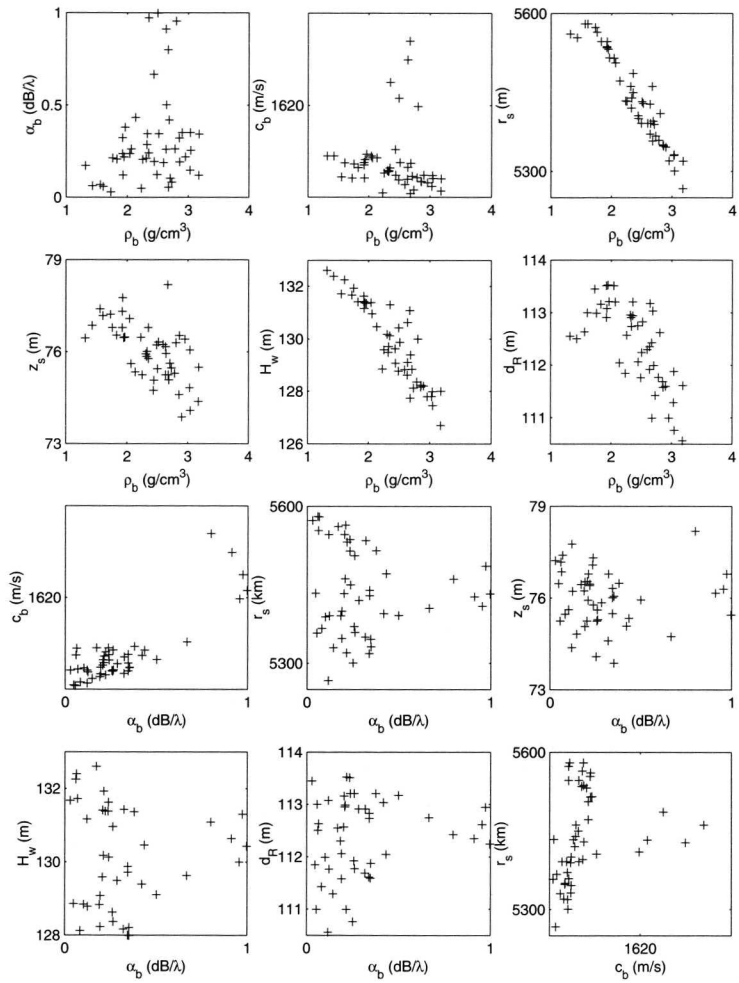


Fig. 9 Parameters displayed versus the other parameters.

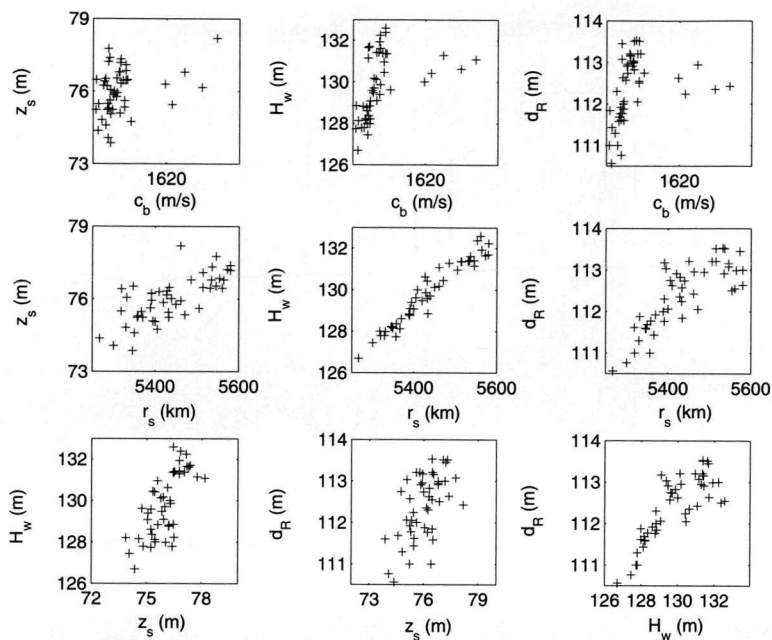


Fig. 10 Parameters displayed versus other parameters.

## 3.4.2 Multi-frequency results

### 3.4.2.1 Multi-frequency optimization

Inversions have also been performed using six frequencies, all in the 160-180 Hz band (see Section 3.3.1). Setting5 in Table II specifies the values for the different genetic algorithm parameters. The expression for the energy function is given by Eq. (11).

The percentage of converged runs for this setting is  $(90 \pm 5)\%$ . The mean amount of replica field calculations needed for convergence,  $\bar{M}$ , is 627, with a standard deviation of 845.  $\sigma_{\bar{M}}$  is 127, and  $\sigma_{\sigma}$  amounts to 90. Compared to the single-frequency results (Tables III and IV), using the genetic algorithm with setting5 (6 frequencies) seems to result in a better performance, i.e., a larger percentage of converged runs and less replica field calculations needed for convergence. Using multiple frequencies instead of a single frequency results in a different energy surface, i.e., a different function for which the optimization is performed. The better performance is probably because the minimum of the energy function corresponding to the multiple-frequency case is easier to locate.

Figure 11 shows for the different frequencies the measured pressure fields and the calculated pressure fields. The calculated pressure fields belong to a solution of the optimization problem that gave a low value for the energy function.

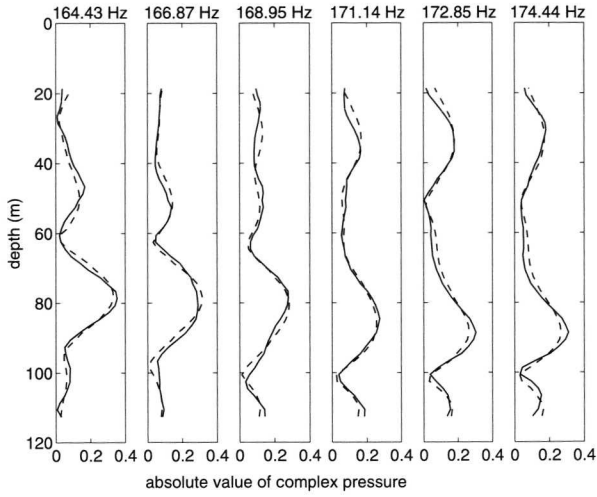


Fig. 11 Measured pressure fields (solid) and calculated pressure fields (dashed) for the different frequencies.

Figure 12 shows the plots in which the values for the energy function are plotted against the different parameter values. Figure 13 zooms in on the lowest  $(1 - \frac{1}{K} \sum_{k=1}^K P_{ln,k})$  values.

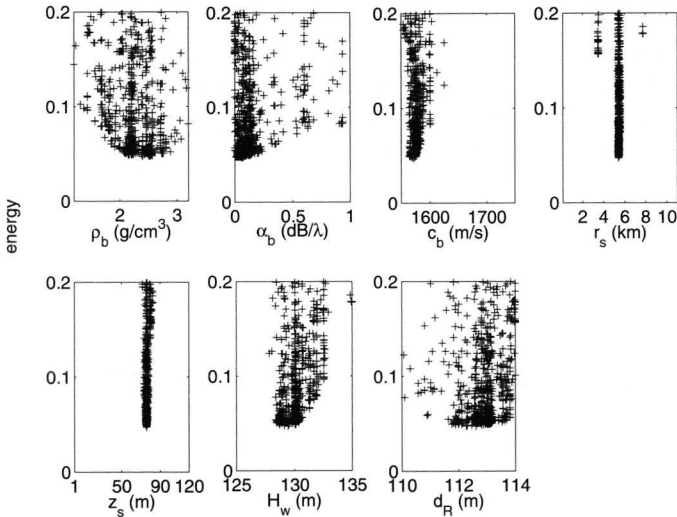


Fig. 12 The values for the energy  $(1 - \frac{1}{K} \sum_{k=1}^K P_{ln,k})$  plotted versus the different parameters, GA, multi-frequency results.

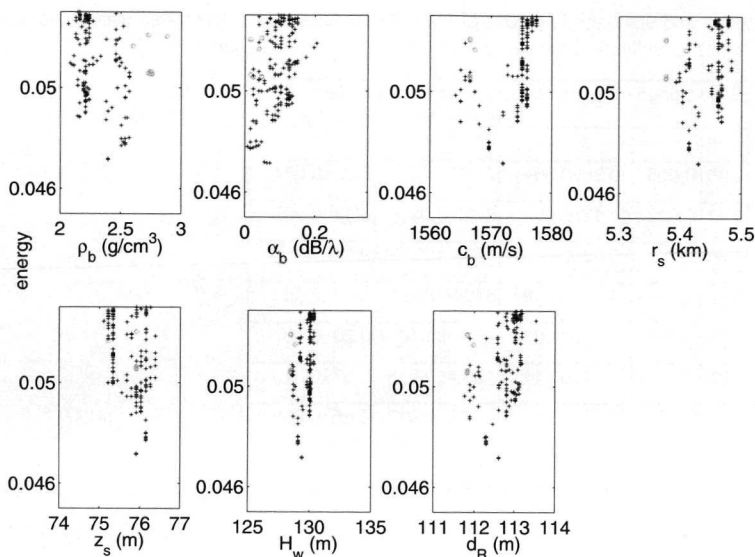


Fig. 13 Energy  $(1 - \frac{1}{K} \sum_{k=1}^K P_{lin,k})$  versus the different parameters; GA, multi-frequency results. The parameter value combinations with a  $\rho_b > 2.6$  are marked indicated by circles.

Comparing Figs. 12 and 5 clearly shows that using multiple frequencies results in a somewhat higher value for the lowest energy function value found. This is due to the fact that in the multi-frequency case the parameter value combination found to give the lowest energy function value is some kind of compromise between different parameter value combinations that belong to the optimum for a single frequency. From the figures it can also be seen that the use of multiple frequencies considerably increases the energy in the local minima of the range/depth ambiguity surface. In addition, the local minimum around the unrealistic high compressional wave speeds with values around 1650 m/s disappears.

Comparing Figs. 13 and 6 reveals an important difference in the energy surfaces at one and at six frequencies, respectively: Parameter combinations with non-realistic high values for the density ( $> 2.6$ ) disappear from the global minimum when use is made of six frequencies.

### 3.4.2.2 A posteriori analysis

Again expressions (15) to (18) are used to determine the mean and covariance of the different parameters. Instead of  $(1 - P_{lin})$  now use is made of  $(1 - \frac{1}{K} \sum_{k=1}^K P_{lin,k})$ . The results are listed in Table V.

Comparing the single-frequency GA results to the multi-frequency GA results (Table V) shows a shift of  $\alpha_b$  and  $\rho_b$  towards (more realistic) lower values for these parameters. Also the standard deviation in the compressional wave speed is much smaller in the multi-frequency case. This is a result of the (already mentioned) disappearance of a local minimum. The decrease in standard deviation when using multiple frequencies instead of a single frequency is seen for all parameters, except for the source/receiver range  $z_s$ .

Table V Means and standard deviations of the different parameters, calculated using a genetic algorithm. Results for setting2 (6 frequencies) and setting2 (single frequency).

	GA, setting5 (6 frequencies)		GA, setting2 (single frequency)	
$T$	0.047		0.037	
$\rho_b$	2.25±0.005	0.26±0.004	2.46±0.006	0.30±0.004
$\alpha_b$	0.11±0.002	0.12±0.002	0.30±0.003	0.17±0.002
$c_b$	1575±0.11	5.52±0.076	1578±0.18	9.5±0.13
$r_s$	5457±0.84	43.15±0.59	5414±0.96	50.7±0.68
$z_s$	75.9±0.010	0.52±0.007	75.7±0.010	0.52±0.007
$H_w$	130.0±0.016	0.81±0.011	129.4±0.018	0.97±0.013
$d_R$	112.8±0.009	0.48±0.007	112.3±0.012	0.65±0.009

Figure 14 shows the probability distributions obtained for the genetic algorithm with setting5.

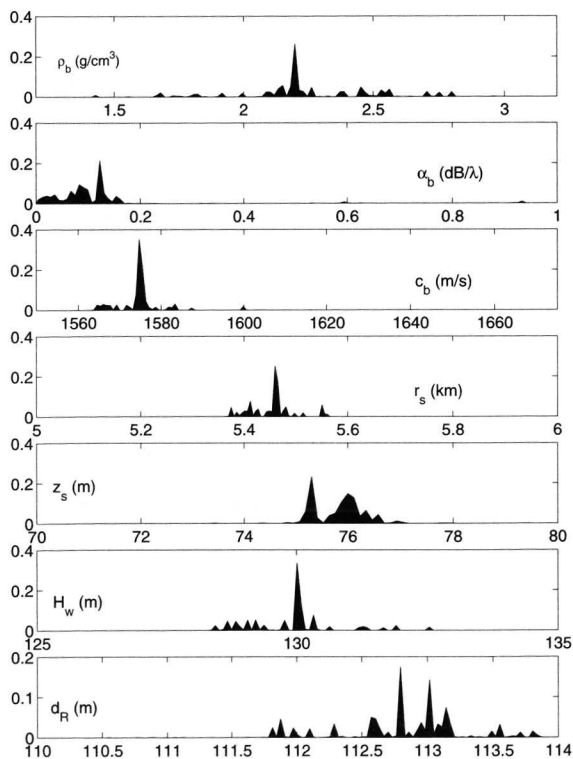


Fig. 14 Probability distributions for the results of GA setting5 (multi-frequency results).



## 3.5 Summary and conclusions

A genetic algorithm (GA) is applied to the matched field inversion (MFI) problem of geo-acoustic and geometric parameter estimation using real acoustic data. The GA is capable of finding solutions close to the global optimum, i.e., one obtains parameter values for which the modeled pressure field optimally matches the measured field. The performances for different settings of the GA are compared, resulting in a more or less optimal setting of the algorithm. (A further assessment of the effect of the GA setting on the GA performance is presented in Appendix C, where use is made of a computationally inexpensive function, which allows for performing a large amount of runs for an extensive number of GA settings). The solutions obtained when using the GA are in excellent agreement with those obtained when using simulated annealing (SA) being another global optimization method applied in MFI.

A comparison of the performances of the two global optimization methods indicates a better performance of the GA: The performance of the GA (in its optimal setting) with respect to success rate and speed of convergence is significantly better than that of SA.

Another advantage is that GAs do not return a single solution, but a set of possible solutions (close to the global optimum). Therefore, only one GA run is needed in order to get an indication on the acoustical importances of the different unknown parameters (and hence the accuracy with which these parameters can be determined). When using SA this essential information can only be obtained after a large number of independent runs (requiring more computation time).

A second MFI research item described in this chapter is the performance of multi-frequency inversion. Compared to inversion at a single frequency, employing multiple frequencies in the inversion results in more accurate and (for some parameters) more physically realistic estimates. This is due to the additional constraints imposed when matching modeled and measured pressure fields at several frequencies.

## References

- 1 M. D. Collins, and W. A. Kuperman, "Focalization: Environmental focusing and source localization," *J. Acoust. Soc. Am.* **90** (3), 1410-1422 (1991).
- 2 D.G. Simons, "Source localization and Estimation of Geoacoustic Bottom Parameters by Matched Field Inversion of Real Acoustic Data," TNO report FEL-95-A260, 1995.
- 3 P. Gerstoft, "Inversion of seismoacoustic data using genetic algorithms and a *posteriori* probability distributions," *J. Acoust. Soc. Am.* **95** (2), 770-782 (1994).
- 4 L. Davis, ed., *Genetic Algorithms and Simulated Annealing*, Pithman, London, 1990.
- 5 J. A. Scales, M.L. Smith and T.L. Fisher, "Global optimization methods for highly nonlinear inverse problems," *J. Comput. Phys.* **103**, 258-268 (1992).
- 6 M. Sambridge and G. Drijkoningen, "Genetic algorithms in seismic waveform inversion," *Geophys. J. Int.* **109**, 323-343 (1992).
- 7 P.L. Stoffa and M.K. Sen, "Multiparameter optimization using genetic algorithms: Inversion of plane wave seismograms," *Geophysics* **56**, 1794-1810 (1991).
- 8 C.E. Lindsay and N.R. Chapman, "Matched Field Inversion for Geoacoustic Model Parameters Using Adaptive Simulated Annealing," *IEEE J. Oceanic Eng.* **18**, 224-231 (1993).
- 9 M.D. Collins and L. Fishman, "Efficient navigation of parameter landscapes," *J. Acoust. Soc. Am.* **98** (3), 1637-1644 (1995).
- 10 D. Beasley, D.R. Bull and R.R. Martin, *An Overview of Genetic Algorithms: Part 1, Fundamentals*, University Computing, **15** (2) 568-69 (1993).
- 11 D. Beasley, D.R. Bull and R.R. Martin, *An Overview of Genetic Algorithms: Part 2, Research Topics*, University Computing, **15** (4) 170-181 (1993).
- 12 D. Lawrence, *Handbook of genetic algorithms*, Van Nostrand Reinhold, New York, 1991.
- 13 J.H. Holland, *Adaptation in Natural and Artificial Systems*, MIT Press, 1975.
- 14 D.E. Goldberg and K. Deb, *A comparative analysis of selection schemes used in genetic algorithms*. In G.J.E. Rawlins, editor, *Foundations of Genetic Algorithms*, 69-93, Morgan Kaufmann, 1991.
- 15 D.F. Gingras, and P. Gerstoft, "Inversion for geometric and geoacoustic parameters in shallow water: Experimental results," *J. Acoust. Soc. Am.* **97**, 3589-3598 (1995).
- 16 D.G. Simons, Normal-mode Propagation Modeling for Matched Field Processing, TNO report FEL-95-A084, Mei 1995.

## Chapter 4

Multi-frequency matched field inversion of  
benchmark data using a genetic algorithm<sup>A</sup>

## Abstract

For a selected number of shallow water test cases of the 1997 Geo-acoustic Inversion Workshop we have applied matched field inversion to determine the geo-acoustic and geometric (source location, water depth) parameters. A genetic algorithm has been applied for performing the optimization, whereas the replica fields have been calculated using a standard normal-mode model. The energy function to be optimized is based on the incoherent multi-frequency Bartlett processor. We have used the data sets provided at a few frequencies in the band 25-500 Hz for a vertical line array positioned at 5 km from the source. A comparison between the inverted and true parameter values is made.

## 4.1 Introduction

For the Geo-acoustic Inversion Workshop (Vancouver, 24-26 June, 1997) broadband acoustic field data were generated for a series of range-independent shallow water environments. The SAFARI model was used to calculate the acoustic fields for all these test cases. Participants of the workshop were instructed to invert the simulated data to estimate the geo-acoustic model parameters. These parameters were unknown to the participants, except for a calibration test case. For some cases the source location and water depth were unknown as well. The sound speed profile in the water column is downward refracting for all cases and known to the users. The data were generated for a total of seven test cases.

For the first five of the test cases (including the calibration test case), the geo-acoustic model consists of a single fluid sediment on top of a fluid homogeneous half-space. The unknown parameters for the sediment are layer thickness, sound speed at the top and bottom of the sediment, density and attenuation. It is hereby assumed that the sound speed profile in

---

<sup>A</sup> Published in the Journal of Computational Acoustics, Volume 6 (1&2), pp. 135-150 (1998).

the sediment is linear. For the half-space the unknown geo-acoustic parameters are sound speed, density and attenuation.

For the sixth test case the geo-acoustic model is a multiple fluid layer sediment. Each layer is homogeneous and the number of layers is unknown. The geo-acoustic model of the seventh test case again consists of a single sediment and half-space, but now the layers are supposed to be elastic.

For each test case there are three realizations (denoted by a, b, and c), i.e., field data were generated for three sets of parameter values.

The bounds from which the values for each parameter were selected, i.e., the search ranges, were known to the participants, whereas the specific values were unknown (except for the calibration test case).

The acoustic field data were provided as the complex pressure at specific vertical and horizontal slices in the water column, so that participants could design their own 'experiments' to invert the data (e.g. using either vertical or horizontal line arrays). At the ranges 1, 2, 3, 4, and 5 km the data were provided at 1 m depth intervals from 1-m to 100 m throughout the water column. At depths of 75 m and 100 m the data were provided at 50-m range intervals from 50 m to 5000 m. Further, at each grid point the complex pressure was provided from 25 to 199 Hz in 1-Hz intervals, and from 200 to 500 Hz in 5-Hz intervals.

For a selected number of test cases, we have applied matched field inversion (MFI) to determine the unknown parameters. In MFI the unknown parameters are determined by minimizing an energy function  $E$ . In this study  $E$  should provide a measure for the difference between the pressure field calculated by SAFARI and the pressure field calculated by a model (the replica field) for a set of values for the unknown parameters. As such, the unknown parameters are determined through an optimization procedure, which involves finding a set of parameter values that minimizes the discrepancy between the two pressure fields. The number of possible parameter value combinations is extremely large, as the number of unknown parameters is in the order of ten. In addition, the parameter search space can have a large number of local minima. Finding the global minimum of the energy function requires modern global optimization methods, such as simulated annealing<sup>1</sup> or genetic algorithms.<sup>2</sup>

The replica pressure fields in the inversion were calculated using a standard normal-mode model. A brief description of this model is given in Section 4.2. For the calibration test case a direct comparison of the pressure fields generated by SAFARI and those generated by our normal-mode code has been performed, the results of which are also presented in Section 4.2.

The test cases for which inversion was performed are described in Section 4.3. The choice for the test cases taken in consideration is partly based on the specific capabilities of the normal-mode model that has been used.

We have used a genetic algorithm as the global search method. Section 4.4 provides a description of the basic principles of a genetic algorithm. It also provides the specific setting of the algorithm for the current inversion, including the type of energy function used.

Results are presented and discussed in Section 4.5.

## 4.2 The forward acoustic model

The model used for the forward replica calculations is a standard normal-mode model, which has been developed in our group in MATLAB.<sup>3</sup> For this model the ocean environment is assumed to consist of three layers: water column, sediment layer and homogenous half-space. Densities and attenuation constants in all layers are assumed to be independent of depth. The density in the water column is  $1 \text{ g/cm}^3$ . Of course, the attenuation can be dependent on frequency. The sound speed in the water column and in the sediment is allowed to vary with depth, whereas it is supposed to be constant in the half-space.

The numerical technique for solving the depth-dependent Helmholtz or modal equation and its boundary conditions is a finite-difference discretization. The resulting algebraic eigenvalue problem is solved using routines of the well-known EISPACK package to compute the eigenvalues and eigenvectors of a real symmetric tridiagonal matrix in a specified interval.<sup>4</sup> This eigenvalue interval is chosen such that only the modes corresponding to the discrete eigenvalue spectrum are calculated, thereby omitting the continuous spectrum. Loss effects due to volume attenuation in the water column, sediment and half-space are taken into account by first order perturbation theory.<sup>5</sup> Shear in the bottom layers is not accounted for.

Range-dependent ocean environments are handled by using the adiabatic approximation.<sup>6</sup> This is, however, not needed for the present study, as all test cases are range-independent.

For the calibration test case (see Fig. 1) the pressure fields generated by SAFARI have been compared directly with the fields calculated using our normal-mode model.

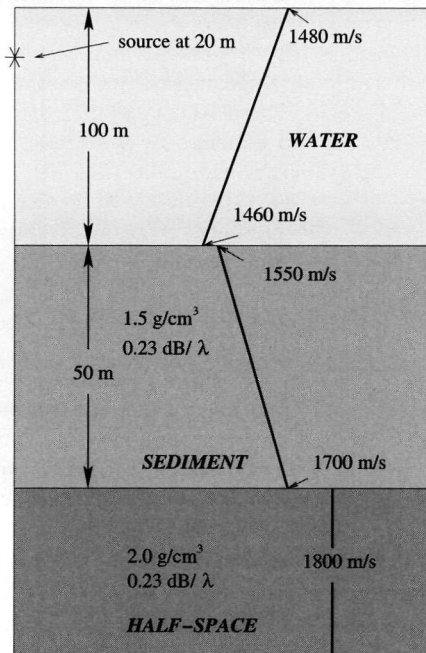


Fig. 1 The calibration test case.

This has been done in the following way: let  $\mathbf{p}_{obs}$  (obs = observed, or true), and  $\mathbf{p}_{calc}$  (calc = calculated) be the pressure fields calculated using SAFARI and the normal-mode model, respectively. When using the data at the fixed ranges (vertical line arrays consisting of 100 hydrophones with 1-m spacing), both  $\mathbf{p}_{obs}$  and  $\mathbf{p}_{calc}$  are complex vectors of length 100. Now, as a measure of the agreement between the two models, we have used an energy function  $E$  based on the single-frequency linear or Bartlett processor<sup>7</sup>, which is given by

$$E = 1 - \left| \mathbf{p}_{obs} \cdot \mathbf{p}_{calc}^* \right|^2 \quad (1)$$

with the suffix \* denoting the complex conjugate. Here it is assumed that  $\mathbf{p}_{obs}$  and  $\mathbf{p}_{calc}$  are normalized, i.e.,  $\|\mathbf{p}_{obs}\|$  and  $\|\mathbf{p}_{calc}\| = 1$ . The difference in propagation convention between SAFARI ( $e^{+i\omega t}$ ) and the normal-mode code ( $e^{-i\omega t}$ ) is accounted for.

$E$  has been calculated as a function of frequency for the data provided at the fixed ranges. The results for the 1-km and 5-km data are presented in Fig. 2. (The curves for the 2, 3 and 4 km data lie in between these two curves).

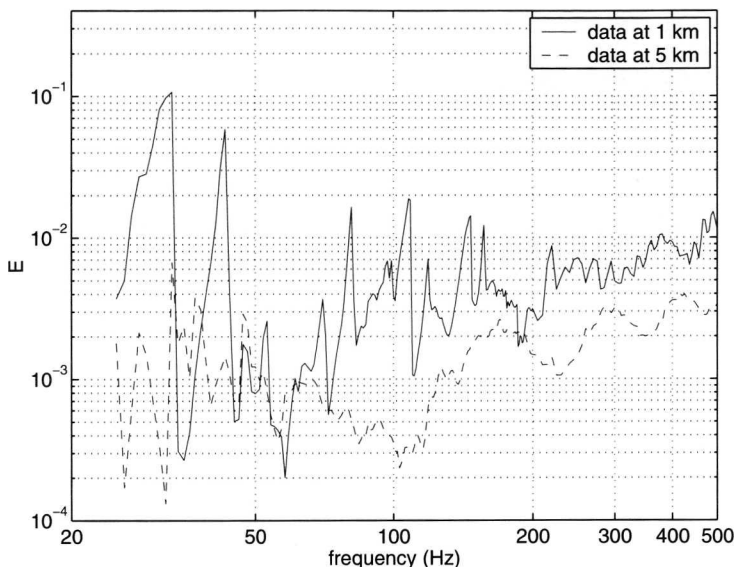


Fig. 2 Agreement between the two models for the calibration test case for the data at 1 and 5 km.

It is observed that the model outputs agree very well as the energy function is quite low for all frequencies and all ranges. For the 1-km data this agreement is slightly worse than that for the data at all other ranges. This is due to the fact that the leaky modes (continuous spectrum), which become more important at shorter ranges, are not taken into account by the normal-mode model.

The generally excellent agreement between the two models for the calibration test case gives much confidence for the inversion work.

### 4.3 The test cases selected for inversion

The normal-mode model used precludes inversion of the data for test case 6 (more than one sediment layer) and test case 7 (elastic layers). For the inversion we have selected the test cases that were denoted AT and WA. From the remaining four test cases that can be handled by our acoustic model these two cases are the most difficult as the number of unknown parameters is largest. Moreover, the two cases selected are quite different: for AT all unknown parameters are geo-acoustic parameters, whereas for WA also geometrical parameters (source location and water depth) are unknown. The selected test cases are depicted schematically in Fig. 3. In this figure the unknown parameters are indicated by squares.

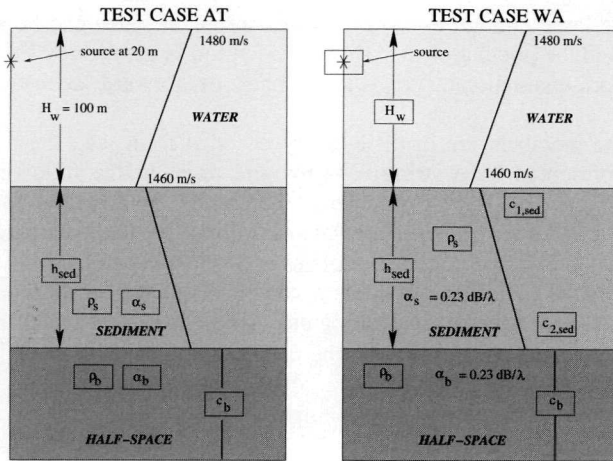


Fig. 3 The test cases called AT and WA. The unknown parameters are those in boxes.

The search bounds for the unknown parameters are given in Table I. The data for all test cases were generated under the constraints

$$c_{1, \text{sed}} < c_{2, \text{sed}} < c_b \quad (2)$$

and

$$\rho_{\text{sed}} < \rho_b \quad (3)$$

These constraints were accounted for in the optimization procedure.

Table I Unknown parameters and their search bounds for test cases AT and WA.

Parameter	Test case	Symbol	Search interval	Unit
Sediment thickness	AT, WA	$h_{\text{sed}}$	[10, 50]	m
Sediment density	AT, WA	$\rho_{\text{sed}}$	[1.4, 1.7]	$\text{g/cm}^3$
Speed at top of sediment	AT, WA	$c_{1, \text{sed}}$	[1500, 1600]	m/s
Speed at bottom of sediment	AT, WA	$c_{2, \text{sed}}$	[1550, 1750]	m/s
Density of half-space	AT, WA	$\rho_b$	[1.6, 2.0]	$\text{g/cm}^3$
Sound speed of half-space	AT, WA	$c_b$	[1600, 1800]	m/s
Sediment attenuation	AT	$\alpha_{\text{sed}}$	[0.05, 0.5]	$\text{dB}/\lambda$
Half-space attenuation	AT	$\alpha_b$	[0.05, 0.5]	$\text{dB}/\lambda$
Source range (5 km data)	WA	$r_s$	[5.0, 5.4]	km
Source depth	WA	$z_s$	[10, 30]	m
Water depth	WA	$H_w$	[100, 120]	m

## 4.4 The genetic algorithm

As mentioned in the introduction we have used a genetic algorithm (GA) as the global search method. The algorithm, which has been developed at TNO-FEL in MATLAB<sup>8</sup>, is described below. Gerstoft was the first to apply GAs to inverse problems in underwater acoustics.<sup>2</sup>

The first step in a genetic algorithm is to create an initial population consisting of  $q$  members. Each member represents a possible parameter value combination, i.e., a possible solution to the optimization problem. This first generation is created randomly. The

population size  $q$  should be large enough to ensure that the problem space can be searched thoroughly. On the other hand the population size should be not too large, thereby limiting the amount of energy function evaluations (i.e., the number of forward acoustic model calculations).

At this creation stage the members are in their binary encoded form, i.e., the parameter value combinations are represented by a string of zeros and ones. In the following these strings are denoted as chromosomes. Each parameter is represented by a certain part of the chromosome. These parts are called genes. The encoded form of the parameter value combinations is needed when applying certain operators as will be explained later.

After decoding, the values for the energy function  $E$  can be calculated for all members of this first population. This is also referred to as assigning a fitness value to each member. When the energy function is normalized ( $0 < E < 1$ ), the fitness  $\phi$  is given by

$$\phi = 1 - E \quad (4)$$

i.e., a low value for the energy function means a high value for the fitness.

The energy function we have selected is based on the incoherent multi-frequency linear or Bartlett processor<sup>7</sup> and is given by

$$E(\mathbf{m}) = 1 - \frac{1}{K} \sum_{k=1}^K \left| \mathbf{p}_{obs}(f_k) \cdot \mathbf{p}_{calc}^*(f_k, \mathbf{m}) \right|^2 \quad (5)$$

with

- $\mathbf{m}$  the vector containing the parameters for which the inversion is performed
- $K$  the number of frequencies
- $\mathbf{p}_{obs}(f_k)$  the (normalized) pressure field at frequency  $f_k$  calculated by SAFARI
- $\mathbf{p}_{calc}(f_k, \mathbf{m})$  the (normalized) pressure field at frequency  $f_k$  calculated by the normal-mode model

We have used the data provided at fixed ranges, thereby inverting the pressure field across a vertical line array consisting of 100 hydrophones with 1-m spacing. From these vertical array data, we have selected the 5-km data. This is a somewhat arbitrary choice as the models agree very well at all ranges, although it is somewhat worse at 1 km (see Fig. 2).

For the creation of the next generation, first a parental population is selected from the initial population. This selection is based on the fitness values obtained for the different chromosomes: a higher fitness implies a larger probability of being selected, thus resulting in a parental population with a higher proportion of fit members. The selection criterion should be such that, on the whole, more opportunities to reproduce are given to the population members that are the most fit. However, at the beginning the selection criterion should not be chosen too strict, as that would force the algorithm to converge to a local minimum. On the other hand a criterion that allows nearly all members to reproduce will result in slow convergence. In our application the probability  $p_j$  for the member  $\mathbf{m}_j$  to be selected is taken as<sup>2</sup>

$$p_j = \frac{e^{-E(\mathbf{m}_j)}}{\sum_{i=1}^q e^{-E(\mathbf{m}_i)}} \quad (6)$$



The temperature  $T$  is chosen equal to the lowest value of the energy function found in the entire current population. This choice results in a flat probability distribution at the beginning, but as the optimization process continues, the temperature will decrease, resulting in a more peaked probability distribution and therefore more emphasis will be put on the most fit members in later generations.

The following step is to create a population of  $q$  children. This is done by applying different operators to the members of the parental population. These operators are crossover and mutation, and they are applied to the members when they are in encoded form. In order to apply crossover the members of the parental population are paired randomly. Crossover results in the exchange of corresponding chromosome parts between the two chromosomes of each set of parents. We have applied multiple point crossover: a crossover point is selected at each gene, i.e., the number of crossover points is equal to the number of parameters for which the optimization is performed.

Consider for example the following two genes, representing different values for the same parameter (encoded using  $N$  bits):

$$(a_0, a_1, \dots, a_{N-1}) \quad \text{and} \quad (b_0, b_1, \dots, b_{N-1}) \quad (7)$$

with  $a_j$  and  $b_j = 0, 1$ . Applying crossover at location  $i$  results in the creation of the following two genes:

$$(a_0, \dots, a_{i-1}, b_i, \dots, b_{N-1}) \quad \text{and} \quad (b_0, \dots, b_{i-1}, a_i, \dots, a_{N-1}) \quad (8)$$

Crossover is applied with crossover probability  $p_c$ . Using a value of  $p_c$  less than one will allow genes to be passed on to the next generation without the disruption of crossover (usually  $0.6 < p_c < 1.0$ ). The crossover point, i.e., the location on the gene at which it is cut, is selected at random.

After crossover another operator called mutation is applied to the chromosomes. Mutation changes each bit of the chromosome with a certain probability  $p_m$ .

Crossover is considered to be a mechanism for rapid exploration of the search space. More crossover points or a higher crossover probability imply a more thorough search, but also more disruption. On the other hand, mutation is a process that provides a small amount of random search, ensuring that no point in the search space has zero probability of being explored. However, the mutation probability should not be chosen too high as then the search becomes effectively random (in general  $p_m < 0.1$ ). At the start of the algorithm (i.e., for the first generations) crossover is the more productive operator, but as the population converges, mutation becomes increasingly important.

A new population (again consisting of  $q$  members) is established by taking at random  $f_r q$  ( $0 < f_r < 1$ ) members of the children population and the  $(1-f_r) q$  most fit members of the original population.  $f_r$  is called the reproduction size. The choice for  $f_r$  is an important research item. For values of  $f_r$  close to one, or even equal to one (generational replacement), convergence of the algorithm to the global minimum might be slow. On the other hand, low values of  $f_r$  might promote the algorithm to converge rapidly to a local minimum. In a recent study<sup>8</sup> we have investigated the performance of a GA for different values for  $f_r$ . It should be noted, however, that such a study is very time consuming and that the performance of a certain value for a GA parameter can be very dependent on the particular values chosen for other GA parameters.

The new population is used as the next generation onto which the same procedure is applied as described above. This process is continued for a certain amount of generations, which should be chosen large enough to allow convergence of the optimization process.

Most of the values for the GA parameters were taken equal to those used in (Gerstoff<sup>2</sup>):

- population size  $q = 64$
- crossover probability  $p_c = 0.8$
- mutation probability  $p_m = 0.05$
- reproduction size  $f_r = 0.5$

The number of generations is taken to be 400, hence the number of forward model calculations per GA run amounts to approximately 13000 per frequency.

A diagram summarizing the different steps in the optimization process using a GA is given in Fig. 4.

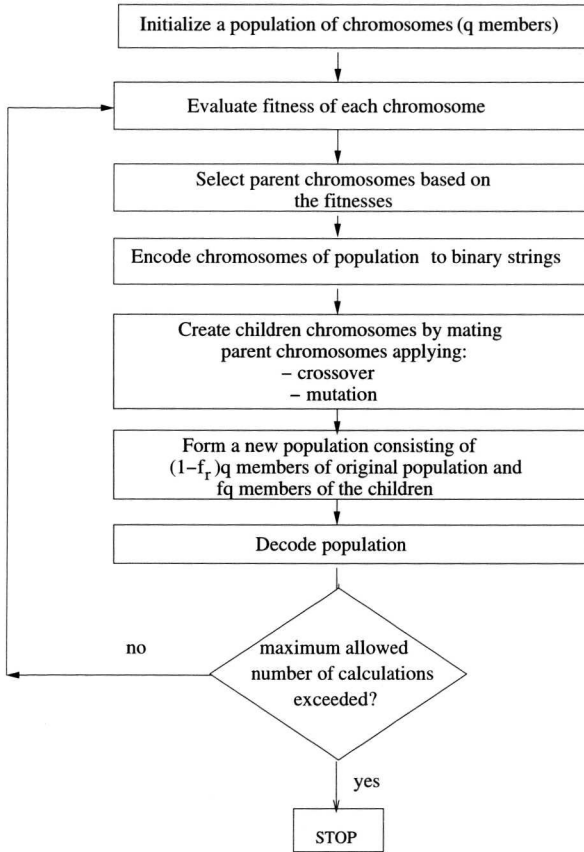


Fig. 4 Flowchart of the optimization process in a genetic algorithm.

## 4.5 Results

From experience<sup>8</sup> we know that broadband processing outperforms single-frequency processing. For this reason we have selected the (incoherent) multi-frequency Bartlett processor (see Section 4.4). It is difficult to know in advance the set of frequencies needed for a successful inversion of shallow water environments in general. For instance, the frequencies required to successfully estimate the half-space parameters will definitely depend on sediment thickness and sediment attenuation. However, in general, one can argue that the high frequencies are useful for the sediment properties near the water/sediment interface, whereas

lower frequencies will be better for probing deeper into the bottom. We have selected the frequencies 25, 30, 50, 100, 200, 400 Hz, thereby exploiting the full frequency band available, still using the data at a limited number of frequencies.

As mentioned previously we have chosen the widely used experimental configuration of a vertical array that spans the whole water column, i.e., the classical approach. We have selected the data at the vertical line array at 5 km using the data provided at all depths.

For the choices made concerning frequencies and experimental configuration, we have performed the inversion for all three realizations of the two test cases selected.

Estimates for the values of the parameters for which the optimization is performed have to be derived from the members of the final GA population. Increasing the probability of finding the global optimum, the GA has been run five times independently for each of the six inversions (two test cases times three realizations). At the same time, the parameter space close to the global optimum is explored more thoroughly, thereby improving the accuracy of the parameter estimates.

As an example, the energy function values for the parameter values in the final populations are shown in Fig. 5 for test case WA, realization (b). The dashed lines denote the true parameter values. The total number of parameter combinations shown in this figure amounts to  $5 \times 64 = 320$ .

Estimates for the unknown parameters can be obtained by simply taking the parameter combination with the lowest energy function value. This solution to the inverse problem is referred to as  $GA_{best}$ .

An alternative method to obtain estimates for the unknown parameters from the final populations is to calculate the so-called *a posteriori* mean values.<sup>2</sup> These are given by

$$\sum_{j=1}^{nq} \mathbf{m}_j \sigma(\mathbf{m}_j) \quad (9)$$

with

$$\sigma(\mathbf{m}_j) = \frac{e^{-E(\mathbf{m}_j)/T'}}{\sum_{i=1}^{nq} e^{-E(\mathbf{m}_i)/T'}} \quad (10)$$

with  $n$  the number of independent GA runs for each inversion (being 5). Following (Gerstoft<sup>2</sup>), the temperature parameter  $T'$  is taken equal to the average value of  $E$  of the 50 best members. This solution to the inverse problem is referred to as  $GA_{mean}$ .

Generally, it is useful to calculate both the  $GA_{best}$  and  $GA_{mean}$  solution, since a significant difference between the two solutions for a particular parameter indicates that the acoustic field is hardly sensitive to corresponding changes in that parameter. This corresponds to a flat or at least ambiguous distribution of energy function values for this parameter, see Fig. 5. (This is only valid for a temperature  $T'$  that is not too low as then both solutions will coincide automatically).

From the final populations it is also possible to calculate the so-called *a posteriori* covariance<sup>2</sup>, which is usually used as an estimate of the uncertainty on the solutions. However, this covariance is not an objective measure for the uncertainty as it will depend on the weighting applied (in this case the value for  $T'$ ) and the type of energy function used.

For all six inversions the GA estimates are compared with the true values in Figs. 6 and 7. Both the  $GA_{best}$  and the  $GA_{mean}$  results are displayed in these figures. It is observed that the

inverted values for the geometric parameters (source location and water depth), the sediment parameters ( $c_{1, sed}$ ,  $\rho_{sed}$  and  $\alpha_{sed}$ ) and the half-space sound speed  $c_b$ , are in excellent agreement with the true values. The agreement between the estimated and true values for the remaining parameters is somewhat worse, but still very good: even for the least sensitive parameter  $\rho_b$  the estimated and true values are highly correlated. Note that for  $\rho_b$  significant differences in the  $GA_{best}$  and  $GA_{mean}$  solution occur indicating that this parameter is less well determined. This is clearly observed from the flat energy function distribution for  $\rho_b$  (see Fig. 5).

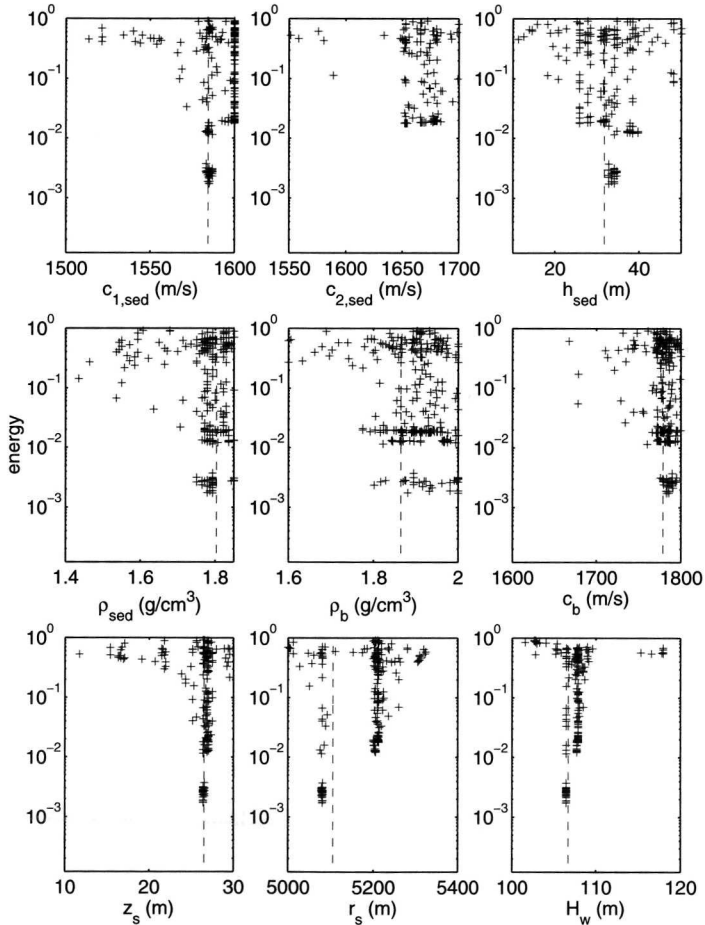


Fig. 5 Energy versus parameter values in the final populations for test case WA, realization (b). The dashed lines indicate the true parameter values.

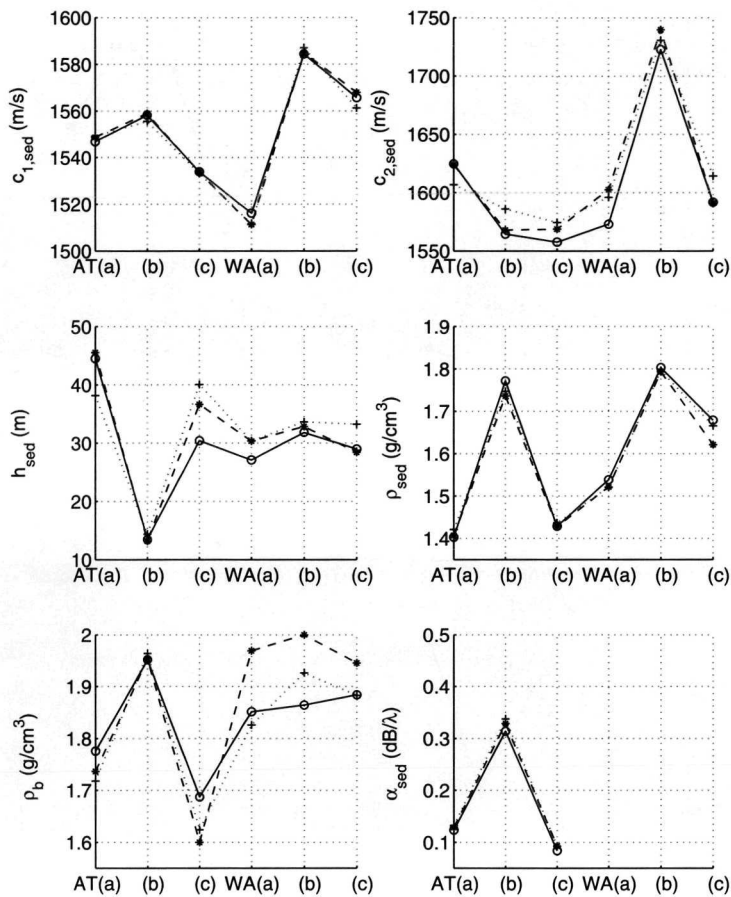


Fig. 6 GA estimates and true parameter values for all six inverted environments. The GA<sub>best</sub> and GA<sub>mean</sub> solutions are denoted by stars and crosses, respectively, whereas the circles denote the true parameter values.

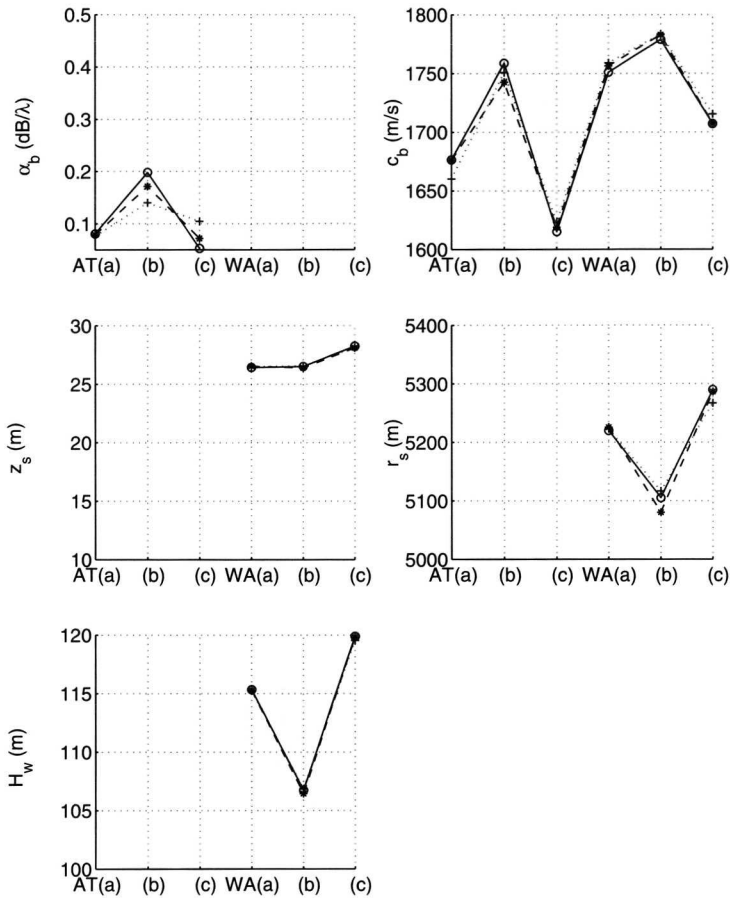


Fig. 7 GA estimates and true parameter values for all six inverted environments. The GA<sub>best</sub> and GA<sub>mean</sub> solutions are denoted by stars and crosses, respectively, whereas the circles denote the true parameter values.

We also investigated the correlation between the different parameters. According to (Gerstoff<sup>9</sup>), correlations can cause problems in finding the global optimum when using search algorithms that are based on perturbing one parameter at a time. This is especially true when in the energy function a long valley exists that is orientated obliquely to the parameter axes. However, our experience is that despite of correlation a genetic algorithm still manages to find the global optimum, probably because it changes all parameters at the same time. Further, we have observed that, in general, the use of multiple frequencies results in much sharper peaks in the energy function, i.e., the parameters are better determined, and hence a considerable reduction in the correlation.

Finally, we have investigated the inversion performance for array configurations with fewer hydrophones than that for the full array (100 hydrophones with a spacing of 1 m). For this investigation we used the 5-km data of test case WA(b). Conventional beamforming

requires the sampling to be done at half-wavelength for the highest frequency, i.e., about 2 m at 400 Hz. Using multiple frequencies probably allows for a larger spacing.

Figure 8 presents the  $GA_{\text{best}}$  and  $GA_{\text{mean}}$  solutions as a function of hydrophone spacing. One observes that the inversion performance does not degrade up to hydrophone spacings of at least 20 m (corresponding to only five hydrophones). Note that the estimates for the geometric parameters ( $z_s$ ,  $r_s$  and  $H_w$ ) do not deviate from the true values for hydrophone spacings as high as 38 m (corresponding to only 2 hydrophones at depths of 37 and 75 m, respectively).

The minimum required hydrophone spacing when using a broadband processor (coherent or incoherent) is subject to further research.

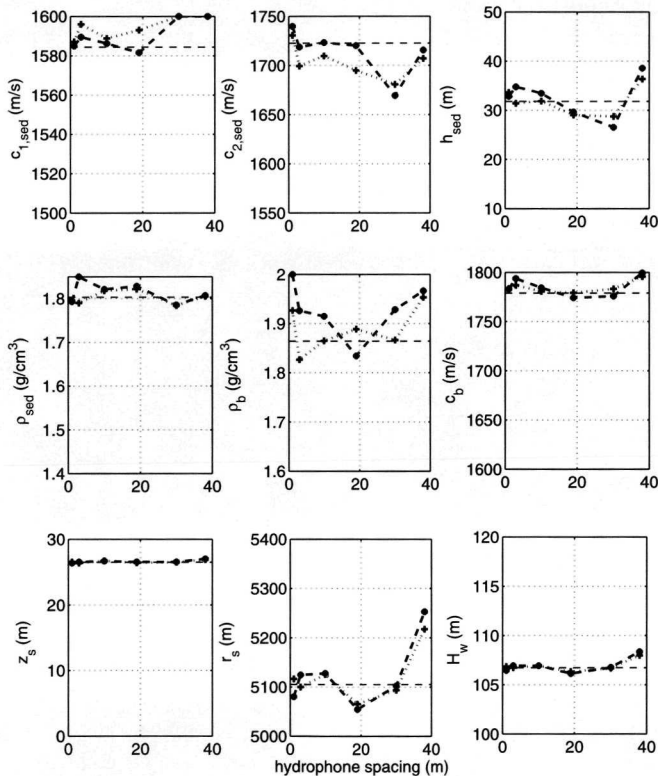


Fig. 8 GA estimates as a function of hydrophone spacing for the test case WA(b). The  $GA_{\text{best}}$  and  $GA_{\text{mean}}$  solutions are denoted by stars and crosses, respectively, whereas the horizontal dashed lines denote the true parameter values.

## 4.6 Summary and conclusions

Matched field inversion has been applied to part of the broadband data of the benchmark exercise to determine geo-acoustic bottom parameters, water depth and source location. Use has been made of a genetic algorithm as optimization method and a standard normal-mode code as forward acoustic model. The geo-acoustic model of the test cases selected consisted

of a single fluid sediment on top of a fluid homogeneous half-space. For these type of range-independent shallow water environments we have clearly demonstrated that all unknown parameters can successfully be inverted when use is made of a vertical line array configuration and a broadband processor. For the latter we have selected the incoherent multi-frequency Bartlett processor using only a few frequencies that are more or less evenly distributed over the band 25-500 Hz.

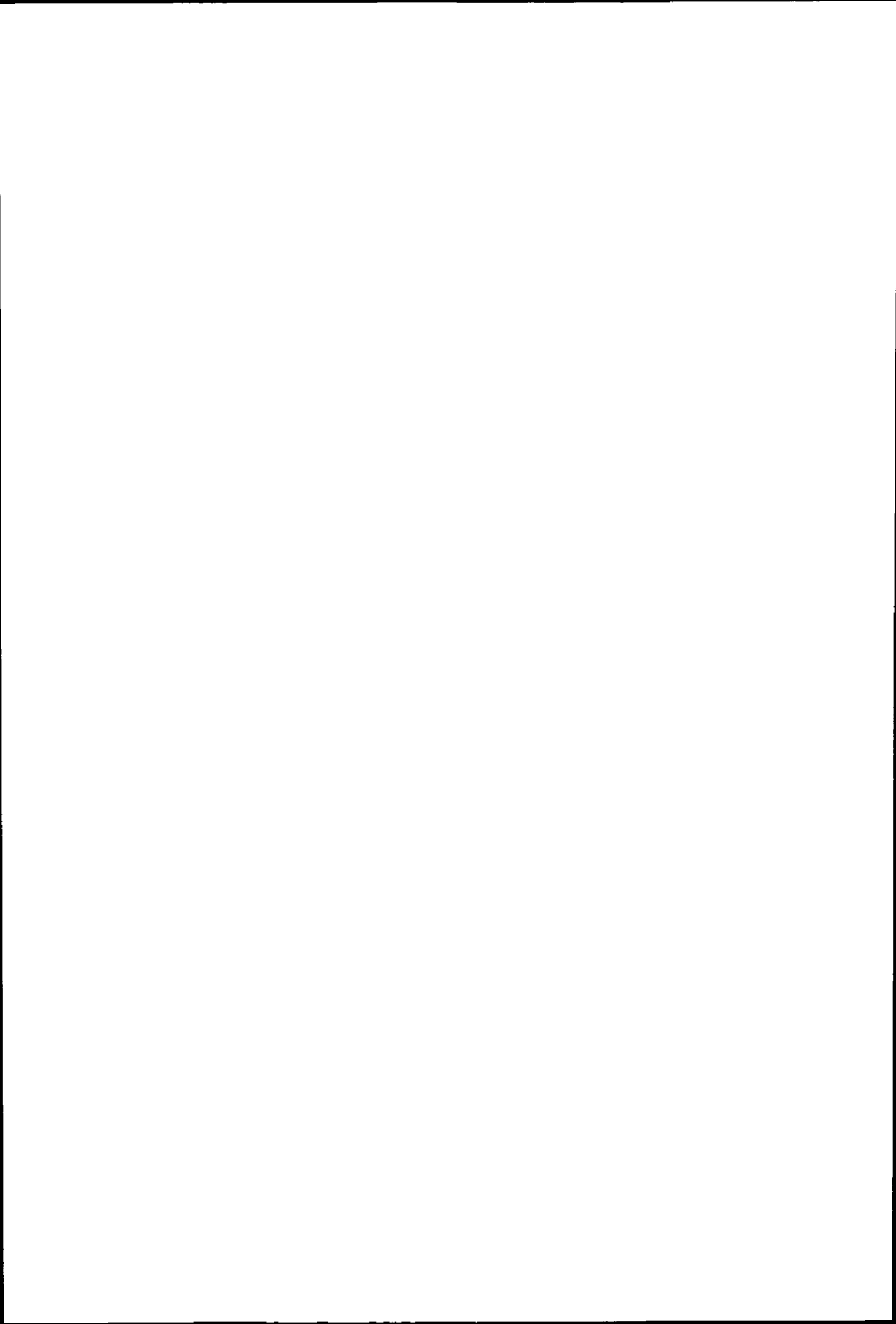
## 4.7 Acknowledgments

This work was funded by the Royal Netherlands Navy and carried out under the auspices of the Directorate of Materiel, Department of Weapon and Communication Systems, Bureau of Underwater Sensors and Acoustic Warfare.



## References

- <sup>1</sup> M. D. Collins, and W. A. Kuperman, "Focalization: Environmental focusing and source localization," *J. Acoust. Soc. Am.* **90** (3), 1410-1422 (1991).
- <sup>2</sup> P. Gerstoft, "Inversion of seismoacoustic data using genetic algorithms and a *posteriori* probability distributions," *J. Acoust. Soc. Am.* **95** (2), 770-782 (1994).
- <sup>3</sup> D.G. Simons and R. Laterveer, *Normal-mode Sound Propagation Modelling for Matched Field Processing*, TNO-report FEL-95-A084, 1995.
- <sup>4</sup> *Lectures Notes in Computer Science 6: Matrix Eigensystem Routines - EISPACK Guide*, Springer-Verlag, 1976.
- <sup>5</sup> C.A. Boyles, *Acoustic Waveguides: Applications to Ocean Science*, John Wiley and Sons, Inc, 1984.
- <sup>6</sup> F.B. Jensen and M.C. Ferla, SNAP: The SACLANTCEN Normal-mode Acoustic Propagation model, SACLANTCEN MEMORANDUM SM-121.
- <sup>7</sup> A. Tolstoy, *Matched field processing for Underwater Acoustics*, World Scientific Publishing Co. Pte. Ltd., 1993.
- <sup>8</sup> M. Snellen and D.G. Simons, *Single-frequency and Multi-frequency Matched Field Inversion using a Genetic Algorithm*, TNO-report FEL-97-A218, 1997.
- <sup>9</sup> M.D. Collins and L. Fishman, "Efficient navigation of parameter landscapes," *J. Acoust. Soc. Am.*, **98** (3), 1637-1644 (1995).



## Chapter 5

# An environmental assessment in the Strait of Sicily: Measurement and analysis techniques for determining bottom and oceanographic properties<sup>B</sup>

### Abstract

In October 1997, the EnVerse 97 shallow-water acoustic experiments were jointly conducted by SACLANT Centre, TNO-FEL and DERA off the coast of Sicily, Italy. The primary goal of the experiments was to determine the seabed properties through inversion of acoustic data. Using a towed source, the inversion method is tested at different source/receiver separations in an area with a range-dependent bottom. The sources transmitted over a broad band of frequencies (90-600 Hz) and the signals were measured on a vertical array of hydrophones. The acoustic data were continuously collected as the range between the source and receiving array varied from 0.5 to 6 km. An extensive seismic survey was conducted along the track providing supporting information about the layered structure of the bottom as well as layer compressional sound speeds. The oceanic conditions were assessed using current meters, satellite remote sensing, wave height measurements, and casts for determining conductivity and temperature as a function of water depth. Geo-acoustic inversion results taken at different source/receiver ranges show seabed properties consistent with the range-dependent features observed in the seismic survey data. These results indicate that shallow-water bottom properties may be estimated over large areas using a towed source fixed receiver configuration.

---

<sup>B</sup> Published in the IEEE Journal of Oceanic Engineering, Volume 25 (3), pp. 364-385 (2000).

## 5.1 Introduction

The strong dependence of shallow-water ocean acoustic propagation on seabed type has led to the development of inversion methods that use measured acoustic transmissions to determine properties of the bottom such as its sound speed, density and attenuation constant. Ocean acoustic inversion methods have been developed based on the technique of matched field processing (MFP).<sup>1-5</sup> For MFP inversions, a propagation code is implemented on a computer to numerically simulate the acoustic field for many hypothetical ocean environments. A search is then performed for the environment that produces the best agreement between measured and simulated data. These inversions assume a geo-acoustic model of the experimental site, which is made up of a number of environmental parameters. The agreement between measured and simulated data, for a particular parameter set, is quantified by an objective (energy) function. Generally the parameter search space is enormous with many local optima. Hence, efficient techniques for solving MFP inversions have been developed, which use global optimization methods such as genetic algorithms and simulated annealing.<sup>2,5,6</sup> Full-field acoustic inversion results, using experimental data, have demonstrated that measurements over a broad band of frequencies improve the bottom parameter estimates.<sup>7-9</sup> A collection of papers describing various full-field inversion methods are presented in (Diachok<sup>10</sup>). The purpose of MFP inversion here is to determine a geo-acoustic model for the Adventure Bank (Strait of Sicily, Mediterranean Sea) experimental site. This geo-acoustic model should be suitable as input to propagation codes which can then predict, for example, acoustic transmission loss, multipath arrival structures and reverberation levels.

Experimental validation of MFP inversion methods have been applied to areas where the seabed was assumed to vary only with depth.<sup>9,11,12</sup> For a practical system, capabilities are needed for estimating seabed properties over large areas which are likely to have range and depth variability. Recently, range- and depth-dependent features of the seabed were determined from transmission loss measurements using a fixed sound source and receivers at five ranges between 8-40 km.<sup>13</sup> Properties of a range- and depth-dependent bottom may also be estimated using fixed receivers and a towed sound source. In this paper, MFP inversion is extended to estimate seabed properties that vary both in range and depth by using measurements from a towed source on a stationary vertical receiving array. In principle, towed source measurements could be used for seabed identification over large shallow-water areas and the research presented in this paper describes the first steps in developing such a system. An added level of complexity is introduced into a towed source MFP inversion as the exact experimental geometry (i.e., relative source and receiver positions) are known with much less precision than for a fixed geometry. Since the source is moving, it is not possible to ensemble average many acoustic realizations to improve data quality (i.e., remove acoustic fluctuations due to changing water volume, changing surface roughness, or ambient noise). Also, to validate the results, 'ground-truth' for the type of seabed needs to be established across the entire acoustic track. Some of the issues which will be addressed are: the feasibility of MFP inversions using a source towed over 3-h periods on two different days, applying the method to determine range-dependent seabed properties, and the dependence of the inversions on frequency band and changing water volume.

Section 5.2 gives an explanation of the acoustic, oceanographic, and seismic data collected. The water sound speed is one of the measured oceanographic quantities that is directly incorporated into the geo-acoustic inversion. The presented ocean current data are important as they have a strong influence on the vertical array position, which indirectly affects the geo-acoustic inversion. Other oceanographic quantities like sea surface temperature and wave

height are presented mainly to provide a full description of the environmental conditions under which the acoustic measurements were made. The seismic data presented in Section 5.2 offer a set of alternative measurements, which help validate the MFP inversion results. The MFP inversion method is outlined in Section 5.3; also in this section, the forward propagation model is described along with the objective function and genetic algorithm optimization routine. In Section 5.4 the results of the MFP geo-acoustic inversion are shown which includes an estimation of the inversion quality.

## 5.2 The EnVerse 97 experiments

The EnVerse 97 experiments considered in this paper were conducted on the south end of Adventure Bank.<sup>14</sup> The location of the measurement systems are indicated in Fig. 1. On October 22-23, 1997, both acoustic and oceanographic measurements were taken and the following sub-sections present the collected data. Details of the acoustic data collection and processing are presented, as these are directly relevant to the MFP inversion. Although most of the oceanographic and seismic data analysis are not required for MFP inversion, they are presented here to fully document the experimental conditions and, where applicable, to provide ground truth for some of the inverted parameters.

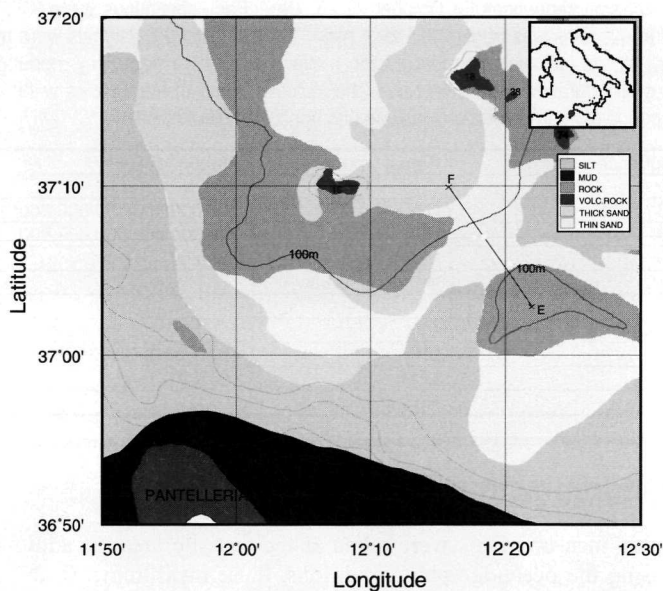


Fig. 1 EnVerse 97 experimental region on Adventure Bank. Acoustic transmissions were made from a sound source towed by HNLMS *Tydeman* between points F and E and received on a moored vertical array of hydrophones (VA, shown as the square). The location of NRV *Alliance* (circle) and the current meter chain (triangle) are also indicated. The seabed types and bottom contours are taken from the SACLANT Centre geographical information system (GIS).<sup>15</sup>

### 5.2.1 Acoustic propagation measurements

Acoustic transmissions were made from a source, towed near 50 m depth by HNLMS *Tydeman* of the Dutch Navy, with speed of  $\approx 2.5$  m/s. The experiments considered here are taken from transmissions between point F and the vertical array (VA) where the range between the source and VA was 0.5-6 km (Fig. 1). The VA was bottom moored close to NRV

*Alliance*; it contained 64 receiving elements, spanned 62 m and was centered near mid-water depth. On October 22, transmissions were made using a 200-800 Hz sound projector, and on October 23, a 50-300 Hz projector was used. These will be referred to as the high-frequency (HF) and low-frequency (LF) sources, respectively. Due to a low signal-to-noise ratio (SNR), only frequencies of 200-600 Hz will be considered for the HF source and 90-300 Hz for the LF source. The received pressure fields were first divided into snapshots of length 0.5 s for the HF data and 1 s for the LF data before fast Fourier transforming into the frequency domain. The length of the snapshots is determined by balancing the requirements of a high SNR and, for inversion modeling, the need to assume a fixed source position. For the inverse modeling described in Section 5.3, many of these snapshots are used which allows for estimating bottom properties and their uncertainty. The transmission sequences are summarized in Table I. These 10-min sequences contained continuous-wave, multi-tone and linearly frequency modulated signals and were repeated as the towed sources moved towards and away from the VA. In this paper, only 1-min multi-tone transmissions, which occurred once in each 10-min sequence, are considered (inversion results using LFM transmissions are, in general, consistent with those using multi-tone data<sup>16</sup>). A total of four of these 1-min transmissions, two LF (at distances of 1.5 and 3.5 km from VA) and two HF (at distances of 0.7 and 2.1 km from VA), are used in the geo-acoustic inversion. During the time it took to complete these 1-min transmissions, the ship had sailed a total distance of about 150 m.

Table I Acoustic transmission sequences for October 22-23, 1997. Each continuous wave (CW) signal at the indicated frequencies was transmitted for 1 min. The multi-tone (MT) signals were transmitted simultaneously at the indicated frequencies for 1 min. Three linear frequency modulated (LFM) signals each of 1-s duration were swept over the indicated band of frequencies within the 1 min interval. The period of no transmission was used to monitor ambient noise.

Date	Sequence time (min)	Signal type	Frequency (Hz)
October 22			
	0-6	CW	200/300/400/500/600/800
	7-8	MT	200,300,400,500,600,800
	8-9	LFM	200-800
	9-10	No transmission	
October 23			
	0-6	CW	40/55/90/130/200/300
	7-8	MT	40,55,90,130,200,300
	8-9	LFM	40-300
	9-10	No transmission	

## 5.2.2 Oceanographic measurements

A series of oceanographic measurements were taken at the test site area. In addition to the inherent value of assessing the oceanographic conditions, these measurements and analyses are useful to determine the effects on both equipment (e.g., array tilt) and acoustic propagation. In the following sub-sections, these measurements are analyzed in conjunction with previous knowledge of this area.

### 5.2.2.1 CTD, XBT and XSV measurements

As changes in the water column (both spatial and temporal) can, in some cases, have a large influence on the sound propagation, as many sound speed measurements as possible were taken. On October 22, from 14:00 to 19:00 the NRV *Alliance* made conductivity, temperature and depth (CTD) casts every 30-50 min while positioned near the VA to receive the radio telemetry. The next day, CTD casts were made at 7:02, 12:41 and 21:17 in approximately the same location. From these, the sound speeds were computed and are presented in Fig. 2. The sparse temporal resolution of these CTD casts does not permit conclusions to be drawn about

the physical processes contributing to the variations; however, the overall structure of the sound speed profiles is clearly represented. The top layer ( $< 20$  m) is homogeneous due to vertical mixing of the water caused by surface wave motion and wind. Below the mixed layer to about 60 m, there is a strong sound speed gradient which is primarily due to the water being warmed in the upper layers and is typical for summer and early fall. For comparison, a sound speed profile measured at a nearby location in October 1986<sup>17</sup> and another one taken from climatology archive (NAVOCEANO GDEM<sup>18</sup>) are also displayed in Fig. 2. In 1986 the sound speed gradient was stronger and the sound speed was about 5 m/s higher in the top 40 m. These differences are primarily due to a higher temperature in 1986. The climatology profile represents averages of temperature and salinity taken over 70 years (all in October). In comparison to both 1986 and 1997, the averaging process has weakened the gradient in the thermocline. Although the climatology sound speed captures the main features, the reduced gradient can have a strong effect on acoustic propagation. The impact of the different sound speed structure shown in Fig. 2 on acoustic propagation and geo-acoustic inversion will be investigated in Section 5.4.2.

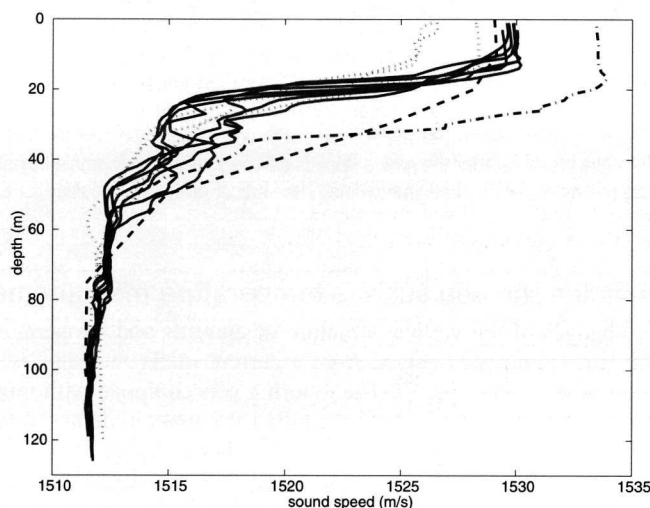


Fig. 2. Sound speed profiles for Adventure Bank. CTD measurements taken from the NRV *Alliance* are shown. Solid lines indicate profiles taken every 30-50 min from 14:00 to 19:00 on October 22. Dotted lines are the profiles taken at 7:02, 12:41 and 21:17 on October 23. The dashed line is taken from the climatology database for October and the dashed-dotted line is a measured profile taken at a location near the experimental site in October 1986.

Between points F and E (Fig. 1), expendable bathythermograph (XBT) probes were deployed from HNLMS *Tydeman* every 5-10 min to determine water temperature, and expendable sound velocity (XSV) probes were cast every 10 min, while the acoustic source was being towed. Using the salinity inferred from the conductivity measurements, taken by *Alliance*, the sound speed was calculated for the XBT casts. In Fig. 3 the sound speed structure along the F-E track is shown with the main feature being the variable structure between the surface and about 40 m depth.

In general, it is unlikely that detailed sound speed profiles will always be available for acoustic forward and inverse modeling. Although useful for determining the extremes at this experimental site, the ocean sound speed was not a large factor in the outcome or quality of the geo-acoustic inversions. This is discussed further in Section 5.4.2.

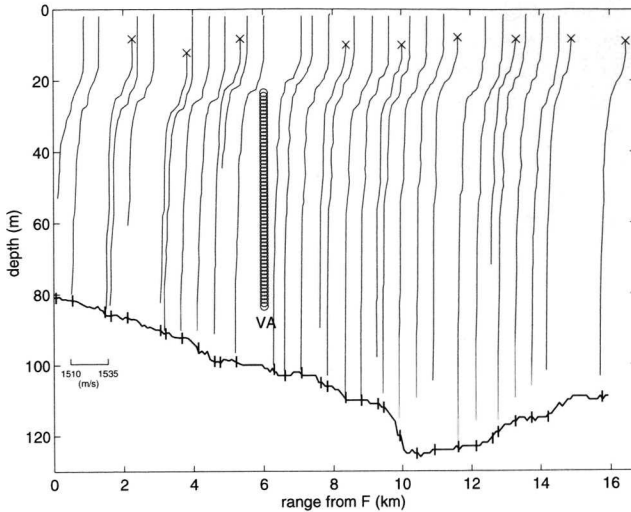


Fig. 3 Sound speed structure along F-E track taken from XBT and XSV probes deployed from HNLMS *Tydeman*. The XSV measurements are indicated with an 'X' on the most shallow point of the profile. The bathymetry is also shown as the solid line with tick marks indicating the location of the XSV or XBT cast. The inset scale for the sound speeds can be applied to all profiles by aligning the left edge with the tick marks on the bathymetry line. The vertical array (VA) position for October 22 is also indicated.

### 5.2.2.2 Current meter and sea surface temperature measurements

Information on temporal changes of the vertical structure of currents and temperature in the immediate vicinity of the vertical structure of currents and temperature in the immediate vicinity of the vertical array is gained from a current meter mooring, which was deployed about 500 m west of the array (Fig. 1). The mooring was equipped with four current meters at nominal depths of 24, 40, 55, and 70 m, recording the magnitude and direction of currents and temperature in 5-min intervals from 13:30 on October 22 to 22:30 on October 23. The time series of currents (Fig. 4) show that at the upper three levels, the meridional component of the current is always negative, i.e., directed to the south. The mean heading at the 70-m level ( $-192^\circ$ ) is also nearly south, but here the fluctuations are stronger than above. The mean speed is steadily decreasing with depth, from 27 cm/s at the 24-m level to 6 cm/s at 20 m. At all levels, both the direction and the current speed are subject to fluctuations exhibiting a high degree of vertical coherence. It is conjectured that these fluctuations are caused by tides, but they could also be due to other physical processes, such as inertial oscillations or traveling meanders. The temperature (bottom panel of Fig. 4) is decreasing with depth and fluctuating at all levels. The fluctuations may either be caused by horizontal advection of different temperature, tides, internal waves, or vertical displacements of the temperature sensors, which cannot be decided here. The fact that the amplitude of the fluctuations at the most shallow level is about three to five times greater than below is due to the larger vertical temperature gradients.

Figure 5 displays the horizontal distribution of currents in an area located about 70 km north of the current meter mooring. Those currents were measured by a ship-mounted Acoustic Doppler Current Profiler (ADCP) on-board the *Alliance* over the period of time from 17:50, October 21, to 20:00, October 25, in 10-min intervals with a vertical resolution of 8 m. In order to reduce the amount of data, the measured profiles were first vertically averaged between 18 and 90 m depth, and then the irregularly spaced data were mapped on a regular horizontal grid with mesh size  $0.01^\circ \times 0.01^\circ$  using two-dimensional (2-D) objective analysis. This technique is widely used in meteorology and oceanography to perform a linear



estimation of a scalar or vector field on a geographical grid from observational data using a minimum error variance method.<sup>19</sup> Figure 5 shows a coherent pattern of strong southward flow extending at least over 10 km in the zonal and about 30 km in meridional direction, and there is good reason to assume that both the currents measured by ADCP and by the mooring farther south are part of a large-scale persistent pattern of southward flow.

The latter is supported by an infrared image of sea surface temperature (SST) taken by the satellite NOAA14 on October 22. Figure 6 shows that SST lies between 22 °C and 23 °C over large parts of the area; however, it is up to 4°C lower off the southwest coast of Sicily. The cold water is found in a stripe parallel to the coast about 20 km wide, a lobe of approximately the same width extending 80 km south from the western tip of Sicily, and in a circular patch of roughly 40 km in diameter centered at about 37.4° N, 12.5° E on the eastern slope of Adventure Bank. Although it is generally impossible to draw conclusions on the horizontal flow field from the SST alone, it is legitimate in this special case, because the situation is similar to those found in previous surveys. According to (Onken<sup>20</sup>) and (Robinson<sup>21</sup>), the eastern slope of Adventure Bank is the favorite site of a quasi-stationary cyclonic (counterclockwise rotating) vortex, which appears as a cold circular patch in SST due to the upward bending of isotherms. Frequently, this cold patch is connected to the western tip of Sicily by a cold ribbon of SST as in the present case. The associated flow pattern is such that the currents are to first order aligned parallel to the iso-lines of SST. Hence, from the SST pattern, one should expect a regime of southward flow between about the Egidian Island archipelago and the site of the vertical array. This is consistent with the measurements.

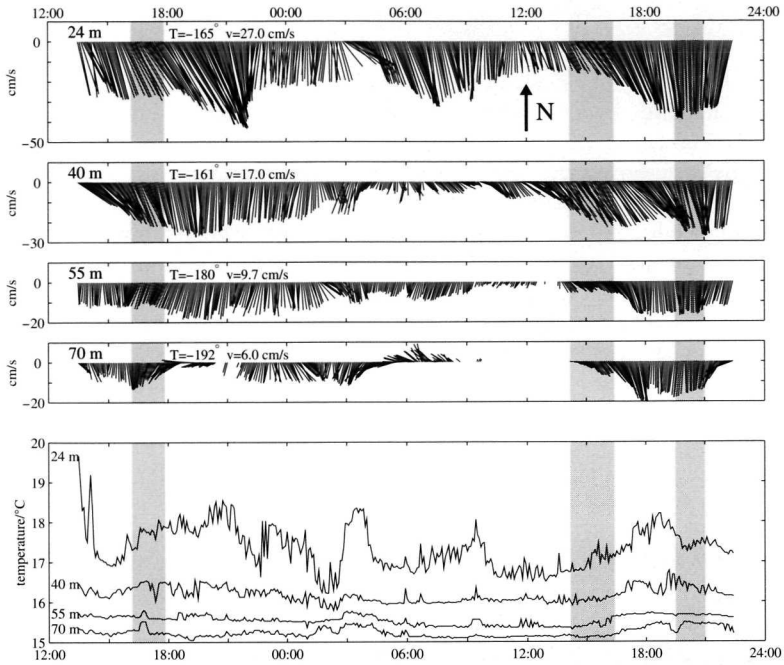


Fig. 4. Time series of currents (top panel) and temperature (bottom) of the current meter mooring positioned in the immediate vicinity of the acoustic vertical array. The nominal instrument depths of 24, 40, 55, and 70 m are indicated in each panel.  $T$  and  $v$  denote the mean direction and speed of the current averaged of the measurement period. The lower and upper limits of the time axis are October 22, 12:00, and October 23, 24:00, respectively. Measurements were taken in 5-min intervals. The shaded bar on the left indicates the time windows of the HF acoustic transmissions and the shaded bar in the center for the LF transmissions (data taken during the time window indicated by the shaded bar on the right are not considered here).

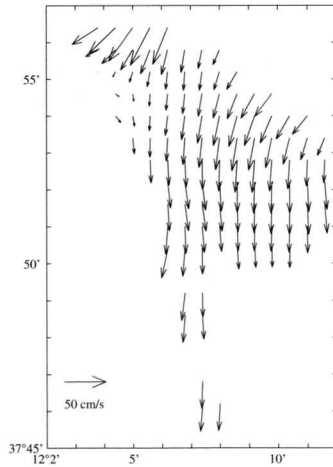


Fig. 5 Vertically averaged currents measured by a ship-mounted ADCP.

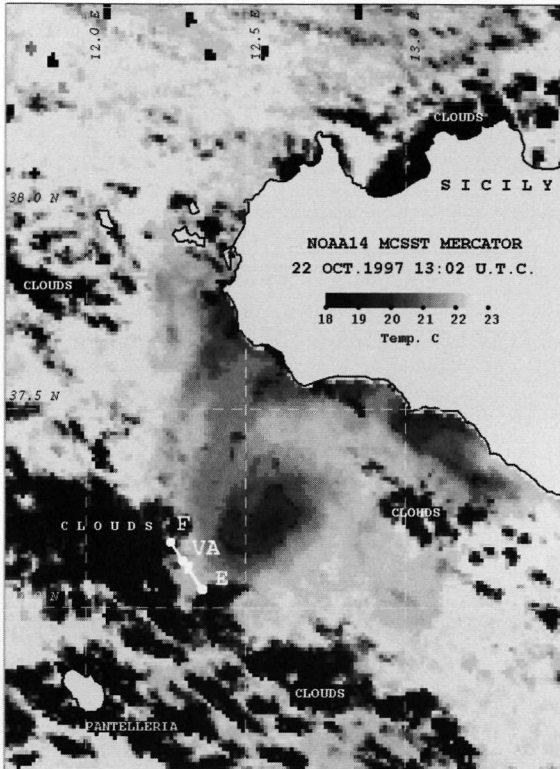


Fig. 6 Sea Surface Temperature near the southwest tip of Sicily. The line on the figure denotes the acoustic transmission track at points F and E with VA showing the vertical receiving array position. Note the circular region of cold temperatures to the northeast of track F-E.

### 5.2.2.3 Waverider measurements

A waverider buoy for recording surface wave heights was positioned about 35 km northwest of the VA where the water depth varies from 80-120 m. Figure 7 shows the spectra obtained using 20 min of data recorded on October 22, 23 and 25. For comparison, the JONSWAP spectrum, typical for shallow waters<sup>22</sup>, and the Pierson-Moskowitz spectrum, typical for deep waters<sup>23</sup>, have been determined from the prevailing wind speeds. Notice, for October 22, there is very good agreement between the spectrum determined from the data and the Pierson-Moskowitz spectrum. The spectrum on October 23 shows several peaks, indicating the presence of different surface wave fields. The high-frequency part of the October 23 spectrum is also well fitted by the Pierson-Moskowitz spectrum. The agreement between these data taken in shallow water and the Pierson-Moskowitz spectrum may be caused by the wave height fields being generated in deeper water off Adventure Bank and propagating toward the measurement area. Other data are well fitted by the JONSWAP spectrum, e.g., the data shown for October 25.

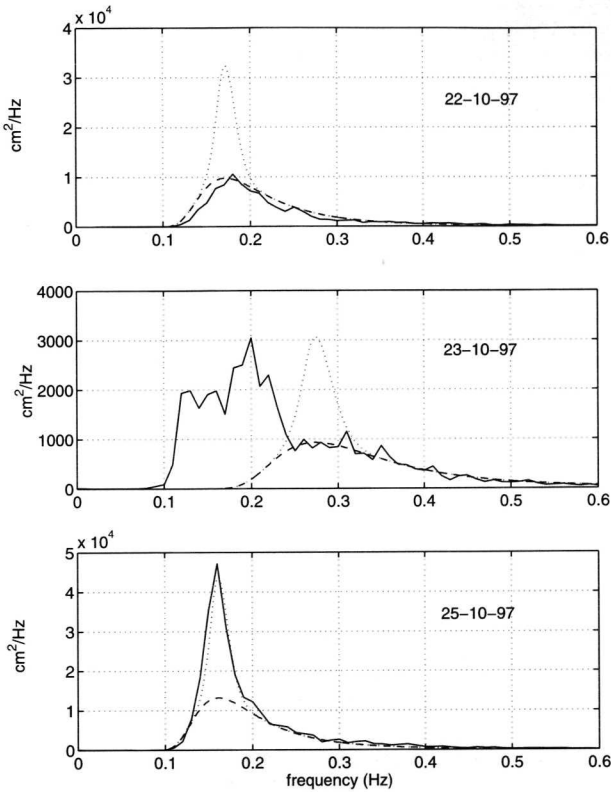


Fig. 7 Sea surface wave spectra (solid lines) as determined from 20 min of data recorded on October 22 (prevailing wind speed of 8 m/s), October 23 (5 m/s) and October 25 (8.5 m/s). Also shown are the JONSWAP spectrum (dotted line) and the Pierson-Moskowitz spectrum (dashed line), calculated from the prevailing wind speeds.

The significant wave height is calculated by taking four times the standard deviation of the waverider time series. The mean wave period  $T_m$  is determined according to

$$T_m = \frac{\int P(f)df}{\int fP(f)df} \quad (1)$$

where  $P(f)$  is the corresponding wave height temporal-frequency spectrum. Figure 8 shows the resulting significant wave heights and the mean wave periods.

Since the significant wave heights are much less than the acoustic wavelengths used during the experiments, this is not expected to greatly impact the acoustic signals. The evolution of the acoustic signals with time on the VA are consistent with the type of changes expected for a towed source and there were no large sudden changes as might be expected if a time-variable sea surface was greatly influencing the acoustic signals or instrumentation. It is also likely that the downward refracting sound speed profile reduced sea surface effects on the acoustics.

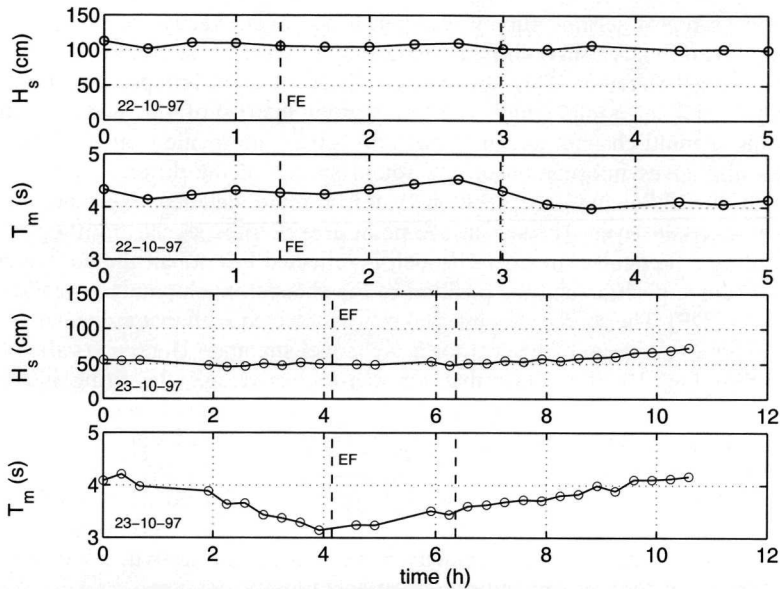


Fig. 8 Significant wave heights  $H_s$  and mean wave periods  $T_m$ , calculated for each 20 min of data on October 22-23. Indicated with vertical dashed lines are the times during which tracks FE (HF transmissions) and EF (LF transmissions) were sailed.

### 5.2.3 Seismic analysis

Seismic profiling was conducted along the acoustic track between points F and E. An impulsive broad-band signal (Uniboom type source, 300 Hz-12 kHz) was transmitted and received on a ten-channel horizontal towed array. The beam-formed output signal was used to produce Fig. 9, which shows the bathymetry and, in colored lines, the strong reflectors due to the layers in the bottom. The layers have variable thickness ranging from 0 to 10 m (assuming a sediment sound speed of 1600 m/s). The squares in Fig. 9 indicate the transmission positions for the two HF multi-tones considered here (0.7 km and 2.1 km from VA) and the locations of LF transmissions are indicated by circles (1.5 km and 3.5 km from VA).

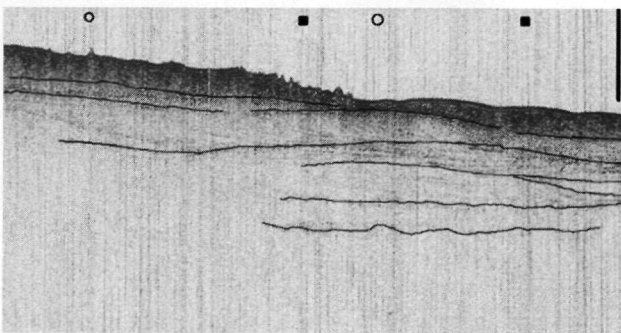


Fig. 9 The results of the seismic analysis up to 4 km northwest of the VA (toward F). The squares indicate the transmission positions for the two HF multi-tone transmissions considered here (0.7 km and 2.1 km from the VA). The locations of LF multi-tone transmissions are indicated by circles (1.5 km and 3.5 km from VA). The vertical line on the right side of the diagram shows the VA position.

### 5.2.3.1 Wide angle reflection analysis

In May 1999, a repeat seismic survey was performed over exactly the same track between points F and E (Fig. 1). A Uniboom-type sound source was used and the signals were received on a multi-channel streamer. This streamer consisted of eight groups of hydrophones, i.e., eight channels, and had a total length of 32 m, a group interval of 4 m, and a group length of 3.8 m. Using a multi-channel streamer not only gives information on the layering in the seabed, but also gives information on the sound speeds of the different layers, as will be explained in the following (see (Hatton<sup>24</sup>) for a more detailed explanation). Consider reflection at a certain layer. The subsurface point at which the signal, from a particular shot and received by a particular streamer channel, is reflected lies at half the horizontal distance between the source position and the position of the channel. Such points are called Common Depth Points (CDP). The source shot interval can be selected such that each CDP is shot more than once, with a maximum of  $n$  shots for a  $n$ -channel streamer. Here,  $n$  is called the fold of the data. From Fig. 10, it is clear that for a  $n$ -fold coverage, the firing interval should correspond to half of the distance between adjacent channels in the streamer.

Ordering the returned signals to CDP, i.e., selecting all returned signals that correspond to a particular CDP (eight in this case), results in reflections that line up along hyperbolae. This hyperbola can be described using an analytical expression, which depends on the differences in travel time from the source to the different receiver groups for the bottom reflected paths. An estimate for layer thickness and velocity is made using the analytical expression for the hyperbola, which relates these quantities to the travel time.

Figure 11 shows the results of this multi-channel seismic analysis. A first reflector is identified over the entire track (at a depth ranging from 5 to 15 m). Comparing Fig. 11 from 0 to 4 km with Fig. 9, it can be seen that the top layers do not vary in thickness as much as indicated with the wide-angle data. This is a consequence of the processing and analysis techniques used to generate these two figures. For Fig. 9, the layers are more easily identified by continuity (and then indicated with lines) once the data are lined up in range. However, with the wide-angle reflection data in Fig. 11, each ping is processed to find a strong reflector and estimate this layer velocity. Unfortunately, this allows for the possibility of a strong lower reflector to sometimes be chosen instead of an upper layer. Although this gives a false impression of the layering, the sound speed estimates are still valid and should be applied as the average sound speed in the layer (in the region above the reflector) as defined by the wide-angle reflection. The mean sound speed in this first sediment layer is 1591 m/s, with a standard deviation of 32 m/s. At the second part of the track, towards point F, a second reflector is found at an average depth of 40 m (but with quite a large standard deviation of  $\pm 10$  m). The second identified layer has an average sound speed of 1710 m/s  $\pm$  70 m/s.

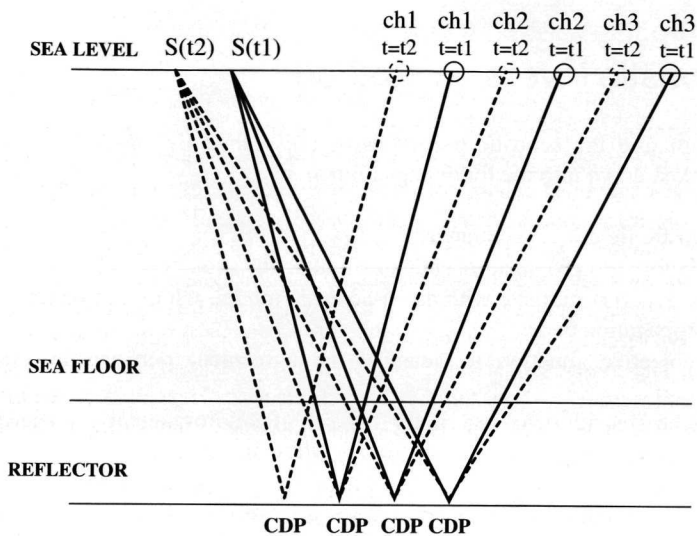


Fig. 10 Multi-channel seismic analysis.  $S(t_1)$  and  $S(t_2)$  are the source positions at times  $t_1$  and  $t_2$ , respectively. The different channels are denoted by  $ch_1$ ,  $ch_2$ , etc., at times  $t_1$  and  $t_2$ .

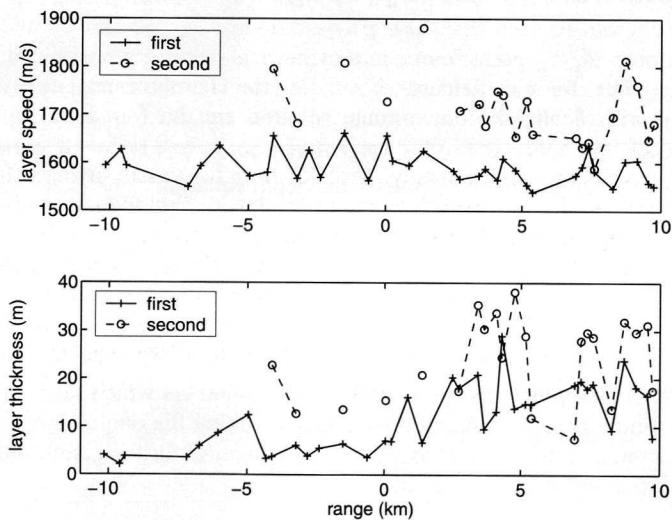


Fig. 11 Multi-channel seismic analysis results: layer speeds and layer thicknesses. The VA is at range 0, positive range values correspond to the northwest of the vertical array (toward point F), and negative range values correspond to the southeast of the vertical array (toward point E). The top panel gives the estimated layer speed in the first and second layers, and the lower panel gives the estimated thickness of the first and second layers.

## 5.3 Acoustic inversion method

The process of estimating the acoustic properties of the seabed by way of matched field inversion can be broken down into the following components:

- Measure the acoustic field in a given area.
- Choose a suitable forward propagation code to simulate the acoustic field.
- Parameterize the experimental site with a geo-acoustic model, which can be implemented in the forward propagation code.
- Determine an objective function to quantify the agreement between measured and simulated data.
- Select an efficient algorithm to search for the set of environmental parameters (e.g., seabed sound speed, density and attenuation), which produces the lowest objective function value.
- After determining the environment giving the lowest objective function value, estimate the quality of the inversion (error analysis).

The previous section described the experimental measurements and the following subsections give details on the rest of the inversion process.

### 5.3.1 The forward acoustic propagation

Assume a time-harmonic  $e^{-i\omega t}$  point source in a cylindrical geometry positioned at range  $r = 0$  and depth  $z = z_s$ . The pressure field  $p(r, z)$  satisfies the Helmholtz equation and, if the medium varies only with depth, the down-range solution can be found by separation of variables. In this case, the normal modes (eigenfunctions),  $\psi_n(z)$ , with corresponding horizontal wavenumbers (eigenvalues),  $k_{r,n}$ , satisfy the depth equation

$$\rho(z) \frac{d}{dz} \left[ \frac{1}{\rho(z)} \frac{d}{dz} \psi_n(z) \right] + \left[ \frac{\omega^2}{c(z)^2} - k_{r,n}^2 \right] \psi_n(z) = 0 \quad (2)$$

where  $\rho(z)$  is the density and  $c(z)$  the total sound speed profile in the water and bottom layers.<sup>25,26</sup> The normal-mode functions and horizontal wavenumbers which satisfy Eq. (2) can be approximated by finite-difference solution techniques. Taking the outgoing solution to the range-separated equation and using the asymptotic approximation for the zeroth-order Hankel function of the first kind, the pressure field reduces to

$$p(r, z) = \frac{e^{i\pi/4}}{\rho(z_s) \sqrt{8\pi r}} \sum_{n=1}^L \frac{1}{\sqrt{\gamma_n}} \psi_n(0, z_s) \psi_n(r, z) e^{i\gamma_n r} \quad (3)$$

Here, the near-field is not of interest, so the summation in Eq. (3) is taken over a finite number of  $L$  discrete modes and the highly lossy continuous spectrum is neglected. To allow for propagation over mildly range-dependent oceanic waveguides, the normal modes in Eq. (3) have been extended to functions of range and depth and  $\gamma_n$  represents the integration of the horizontal wavenumber over range between the source and receiver.<sup>25</sup> This is the so-called adiabatic approximation which asserts that the modes travel independently of each other but



are allowed to modify their shape and phase as they propagate to accommodate changes in the waveguide. When applying the adiabatic approximation, the environment needs to be divided in range sections, each with an appropriate water depth and set of environmental parameters. For this analysis, only the variation of water depth with range is taken into account. A change in water depth of 3 m is the criteria used for introducing a new range section. To account for slight bottom loss, first-order perturbation theory is used; in this case,  $\psi_n(z)$  remains real while a small imaginary term is added to the wavenumbers,  $k_m = k'_m + i\alpha_n$ .

### 5.3.2 The geo-acoustic model for Adventure Bank

Although the seismic profiling discussed in Section 5.2.3 shows a complicated bottom structure, a simple two-layer model is often sufficient to acoustically describe the bottom. Some justification for the two-layer approach can be obtained from solutions to a geo-acoustic benchmarking workshop case.<sup>27,28</sup> In that benchmark case, MFP inversions of simulated data, using a two-layer model, reasonably fit the properties of a multi-layer bottom in a least-squared sense. Therefore, the geo-acoustic model used here for the inversions is that of a single sediment layer overlying a sub-bottom (Fig. 12). The sound speed in the sediment is assumed to vary linearly with depth, whereas it is taken to be depth-independent in the sub-bottom. The density and attenuation are assumed depth-independent through both the sediment and sub-bottom. Some preliminary modeling of this site as well as previous acoustic measurements at a nearby location show shear effects to be small at the frequencies considered here, and it is therefore not included in the geo-acoustic model.<sup>29</sup> Table II lists each inversion parameter and the span of values in the search space.

Table II Inversion parameters, labels and search intervals of the geo-acoustic model. The top six are geo-acoustic parameters and the bottom five are geometrical parameters. Speeds refer to compressional acoustic waves and attenuation is given in units of decibels per wavelength. The distance between the VA and sound source changed for each inversion; therefore an offset distance is required to give the true search interval for  $r_s$ . The HF and LF source range positions at 0.7-HF, 1.5-LF, 2.1-HF and 3.5-LF have corresponding range offsets of 0.0, 0.5, 1.5, and 3 km.

Parameter Description	Label	Search Bounds
Sediment speed at water interface (m/s)	$C_{1, sed}$	1500-1750
Sediment speed at sub-bottom interface (m/s)	$C_{2, sed}$	1500-1800
Sediment thickness (m)	$h_{sed}$	1-50
Sediment and sub-bottom attenuation (dB/ $\lambda$ )	$\alpha$	0.0-1.0
Sediment and sub-bottom density (g/cm <sup>3</sup> )	$\rho$	1.0 - 2.3
Sub-bottom speed (m/s)	$C_b$	1515-1900
Depth of sound source (m)	$z_s$	20-80
Range for sound source-VA separation (+offset m)	$r_s$	0-2000
Water depth change from assumed value ( $\pm$ m)	$\Delta H_w$	10
VA tilt ( $\pm$ degrees)	$\theta$	10
VA vertical translation ( $\pm$ m)	$h_t$	5

A single water sound speed profile was chosen for each of the inversions. After some preliminary investigation, it was determined that the outcome of the geo-acoustic inversion was not greatly dependent on the particular sound speed profile chosen for the water column. Therefore, water sound speed profiles taken at times closest to the acoustic transmissions were used for the inversions.

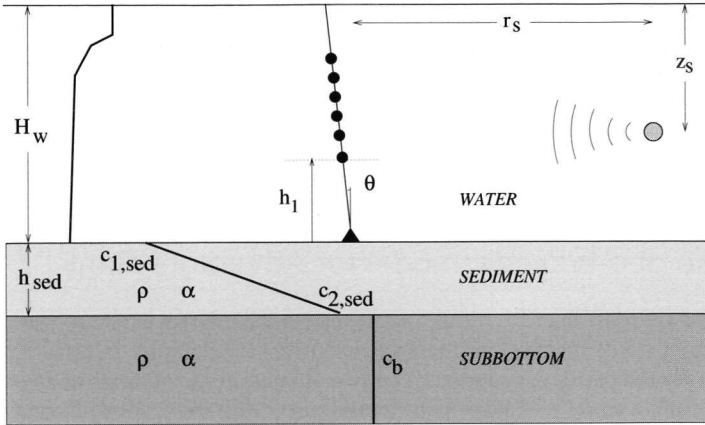


Fig. 12 The Adventure Bank geo-acoustic model and experimental configuration. Thick lines indicate, schematically, the sound speed distribution in the water, in the sediment, and in the sub-bottom. For the nomenclature, see Table II.

### 5.3.3 Matched field objective function

The objective (or energy) function quantifies the agreement between the simulated and measured acoustic fields. The objective function chosen here is based on the incoherent multi-frequency Bartlett processor<sup>30</sup>

$$E(\mathbf{m}) = 1 - \frac{1}{K} \sum_{k=1}^K \left| \mathbf{p}_{obs}(f_k) \cdot \mathbf{p}_{calc}^*(f_k, \mathbf{m}) \right|^2 \quad (4)$$

where, “ $\cdot$ ” indicates an inner product of the pressure vectors (over depth),  $\mathbf{m}$  is the vector containing the parameters over which the inversion is performed,  $K$  is the number of frequencies,  $\mathbf{p}_{obs}(f_k)$  is the measured pressure field vector at frequency  $f_k$ , and  $\mathbf{p}_{calc}^*(f_k, \mathbf{m})$  is the conjugated, simulated pressure field for parameter set  $\mathbf{m}$ . Here,  $K = 4$  (90, 130, 200 and 300 Hz) for the LF band and  $K = 5$  (200, 300, 400, 500 and 600 Hz) for the HF band. To obtain objective function values between 0 and 1, the inner product in (4) is divided by the normalization factor  $\sqrt{\|\mathbf{p}_{obs}(f_k)\|^2 \|\mathbf{p}_{calc}(f_k, \mathbf{m})\|^2}$ . Minimizing this energy function will lead to the parameter set corresponding to a simulated pressure field  $\mathbf{p}_{calc}(f_k, \mathbf{m})$  having a maximum correlation with the measured pressure field  $\mathbf{p}_{obs}(f_k)$ .

### 5.3.4 The Genetic Algorithm

The objective function given by Eq. (4) typically has many local minima. Global search methods such as genetic algorithms or simulated annealing are useful to find the optimum set of parameters corresponding to the true minimum value of Eq. (4).<sup>5,6,31</sup> The basic principle of a genetic algorithm is as follows. First, an initial population of parameter combinations  $\mathbf{m}$  is created randomly: the first generation. Out of the initial population, the most fit members (i.e., those with the lowest objective function value) have the highest probability to be selected as ‘parents’. From the parents, ‘children’ are obtained by the operations of crossover and mutation. The crossover operation can, with probability  $1-p_c$ , duplicate one of the parent’s parameters in  $\mathbf{m}$  and perform crossover. That is, using bit string representations of the parameter values, form the child’s string by taking part from one parent and part from the

other. The mutation operation makes a change, with probability  $p_m$ , of a single bit in the parameter value string to allow for better exploration of the parameter space. Part of the children is then used to replace the least fit members of the initial population creating the next generation. Successive generations become increasingly fit and the process is continued until the optimization process has converged.

### 5.3.5 Quality of the inversion results

Estimates for the optimum values of the parameters can be derived from the members of the final genetic algorithm population. This can be done by taking the parameter combination with the lowest energy function value. This solution to the inverse problem will be referred to as  $GA_{\text{best}}$ . An alternative method is to calculate the so-called *a posteriori* mean values.<sup>5</sup> These are given by

$$GA_{\text{mean}} = \sum_{j=1}^J \mathbf{m}_j \sigma(\mathbf{m}_j) \quad (5)$$

with

$$\sigma(\mathbf{m}_j) = \frac{e^{-\frac{E(\mathbf{m}_j)}{T'}}}{\sum_{i=1}^J e^{-\frac{E(\mathbf{m}_i)}{T'}}} \quad (6)$$

The summations in Eqs. (5) and (6) are over  $J$  solutions from the final GA populations, where,  $J$  is the product of the population size with the number of independent GA runs (here,  $J = 64 \times 5 = 320$ ). Following Ref. (Gerstoft<sup>5</sup>),  $T'$  is set equal to the average of  $E$  over the 50 best members. Generally, it is useful to calculate both  $GA_{\text{best}}$  and  $GA_{\text{mean}}$ , since a significant difference between these two indicates either a flat or ambiguous distribution, and the parameter value is not well determined.

An estimation of the errors can also be obtained by evaluating inversions for several snapshots of the one-minute multi-tone data sets. Although the source was moving during the transmissions, it is assumed that changes in the bottom properties are negligible over this short distance. Therefore, by inverting many snapshots, an estimate of the uncertainty in the results can be made. The mean of the  $GA_{\text{best}}$  solutions taken over snapshots of data is used to estimate the parameter value and the standard deviation to estimate the error. At least nine snapshots were used for each inversion to make these estimates.

## 5.4 Results and analysis

Matched field inversion, using the method outlined in Section 5.3, was used to determine the bottom properties for the Adventure Bank site at the four range positions. Figure 13 shows the inverted geometrical parameter results for the different snapshots of high frequency data (HF) at the 0.7-km range position and Fig. 14 shows the inverted geo-acoustic parameter results. At each of the four range positions (HF-0.7 km, LF-1.5 km, HF-2.1 km, LF-3.5 km), similar sets of inversion results were produced for all the snapshots of data. These results are put in summary form in Table III for the geometrical parameters and Table IV for the geo-acoustic

parameters. Presented in these tables are the average and standard deviation for  $GA_{best}$  values taken over all inverted snapshots of data at each range.

Table III Geometrical parameter estimates for inversions at 0.7, 1.5, 2.1 and 3.5 km. The results are the average and standard deviation for  $GA_{best}$  values taken over all inverted snapshots of data at each range. Differences from the direct measurements of source range ( $r_s$ ), source depth ( $z_s$ ), water depth ( $H_w$ ), array tilt ( $\theta$ ), and array translation ( $h$ ) are indicated as  $\Delta r_s$ ,  $\Delta z_s$ ,  $\Delta H_w$ ,  $\Delta \theta$ , and  $\Delta h$ .

Range-Band	$\Delta r_s$ (m)	$\Delta z_s$ (m)	$\Delta H_w$ (m)	$\Delta \theta$ (deg)	$\Delta h_1$ (m)
0.7 km-HF	$-2.9 \pm 26$	$-2.5 \pm 1.1$	$4.8 \pm 2.4$	$-0.4 \pm 1.2$	$1.2 \pm 1.6$
1.5 km-LF	$58 \pm 72$	$1.8 \pm 1.9$	$0.5 \pm 2.1$	$0.5 \pm 1.1$	$3 \pm 0.8$
2.1 km-HF	$40 \pm 21$	$-4.8 \pm 0.4$	$2.8 \pm 0.8$	$-1.8 \pm 1.1$	$0.5 \pm 1.0$
3.5 km-LF	$105 \pm 280$	$-4.2 \pm 1.3$	$1.7 \pm 5$	$0.1 \pm 1.0$	$2.2 \pm 2.3$

Table IV Geo-acoustic parameter estimates for inversions at 0.7, 1.5, 2.1, and 3.5 km. The results are the average and standard deviation for  $GA_{best}$  values taken over all inverted snapshots of data at each range.

Range-Band	$c_{1, sed}$ (m/s)	$c_{2, sed}$ (m/s)	$c_b$ (m/s)	$h_{sed}$ (m)	$\alpha$ (dB/ $\lambda$ )	$\rho$ (g/cm <sup>3</sup> )
0.7 km-HF	$1580 \pm 32$	$1732 \pm 36$	$1797 \pm 49$	$25 \pm 16$	$0.68 \pm 0.26$	$1.92 \pm 0.29$
1.5 km-LF	$1641 \pm 6$	$1746 \pm 46$	$1813 \pm 51$	$31 \pm 12$	$0.43 \pm 0.16$	$1.46 \pm 0.18$
2.1 km-HF	$1572 \pm 63$	$1733 \pm 44$	$1805 \pm 45$	$5.7 \pm 2$	$0.92 \pm 0.11$	$1.62 \pm 0.13$
3.5 km-LF	$1576 \pm 33$	$1749 \pm 47$	$1840 \pm 62$	$11 \pm 5$	$0.91 \pm 0.08$	$1.28 \pm 0.17$

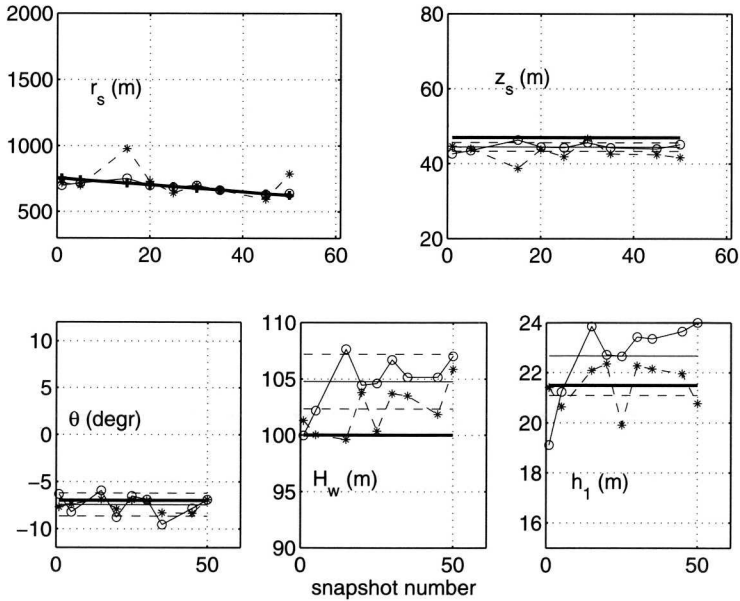


Fig. 13 The inverted geometrical parameter values for the high frequency source (HF) at the 0.7-km range position. Each of the circle/star values represents the result of inverting 0.5 s of data. The circles denote the  $GA_{best}$  solutions, and the stars denote  $GA_{mean}$  results. The solid thin black lines are the mean values of  $GA_{best}$  and the dashed lines indicate the  $GA_{best}$  standard deviation. The solid thick lines show the estimated 'true' values. The y-axes indicate the search bounds, which are listed along with the nomenclature used in Table II.

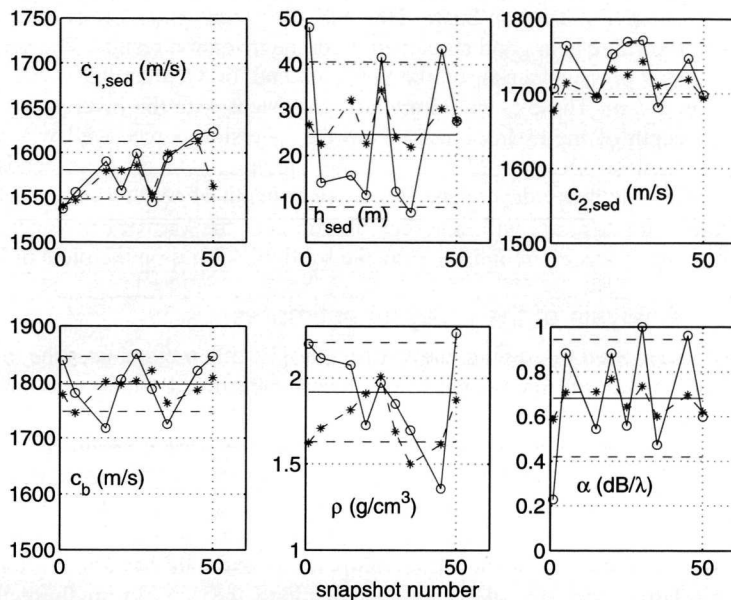


Fig. 14 The inverted geo-acoustic parameter values for the high frequency source (HF) at the 0.7 km range position. Each of the circle/star values represents the result of inverting 0.5 s of data. The circles denote the  $GA_{best}$  solutions, and the stars denote  $GA_{mean}$  results. The solid lines are the mean values of  $GA_{best}$  and the dashed lines indicate the  $GA_{best}$  standard deviation. The y-axes indicate the search bounds, which are listed along with the nomenclature used in Table II.

## 5.4.1 Assessment of the inversion results

A comparison between  $GA_{best}$  and  $GA_{mean}$ , for any single snapshot of data, gives insight into the quality of the inversion. For a given parameter, a large difference between these two indicates a flat or ambiguous distribution of values (i.e., several peaks all with low objective function values), whereas agreement is an indication that there is one sharply peaked minimum. With this criterion, it was ascertained that the geometrical parameters and  $c_{1, sed}$  were well determined for nearly all snapshots. Parameters  $c_{2, sed}$  and  $c_b$  are not as well resolved and  $h_{sed}$ ,  $\alpha$  and  $\rho$  even less so. This essentially gives an indication of the sensitivity of each of the inverted parameters. Lower sensitivity indicates that the parameter value is more difficult to extract and therefore is less significant with respect to acoustic propagation. The standard deviations in Tables III and IV give a more quantitative estimate of the errors associated with each inverted parameter value.

### 5.4.1.1 Analysis of the geometrical parameter estimates

In general, for all inversions, the geometrical parameters ( $r_s$ ,  $z_s$ ,  $H_w$ ,  $\theta$  and  $h_l$ ) are well determined as indicated by the agreement between  $GA_{best}$ ,  $GA_{mean}$ , and their relatively low standard deviations. This is not a surprising result since, typically, altering the geometry causes large changes in the down-range pressure field which consequently impacts Eq. (4). For this reason, the geometrical parameters usually converge quickly. Since the geometry of the experiment is known from direct measurements, comparing this with the inverted geometry is a valuable sanity check of the entire inversion process. For convenience, the differences between measured and inverted geometry values  $\Delta r_s$ ,  $\Delta z_s$ ,  $\Delta H_w$ ,  $\Delta \theta$ , and  $\Delta h_l$  are

listed in Table III. The source range has been estimated using a Differential Global Positioning System (DGPS) on-board HNLMS *Tydeman* (plus offset for the tow cable distance), and the value is in good agreement with the inversion results. The source depth was approximated by a pressure sensor on the tow body and, on October 22, was  $47 \pm 2$  m and on October 23,  $50 \pm 2$  m. These  $z_s$  values are also consistent with the inversion results. The VA position (i.e., depth of the hydrophones) from the inversion agrees well with that measured before deployment on October 22 and 23. The bathymetry taken from echosoundings and presented in Fig. 3 is range-dependent with a water depth of about 100 m near the VA. The inversion results for  $\Delta H_w$  are within acceptable limits of the known bathymetry (i.e.,  $< 5$  m). The estimated 'true' values are indicated by the solid thick lines on the plots in Fig. 13.

#### 5.4.1.2 Analysis of the array tilt estimates

Two methods were used to estimate the VA tilt ( $\theta$ ). The first method uses the matched filtered output of linear frequency-modulated (FM) signals transmitted within one min of the multitones used for inversion. The FM signal was one s in duration and swept the band 200-800 Hz (Table I). On October 22, 1997, in total nine FM sweeps were transmitted at distances of  $\approx 0.5$ , 2, and 3.6 km from the VA. Figure 15 shows, for these three distances, the received signals after matched filtering. The x-axis represents the lag time of the matched filter output and not absolute arrival times. These figures show the time dispersion between different arrivals. Also, from these matched filter outputs, an estimate for array tilt is obtained by considering relative delays in the first arrivals along the VA. From these figures, it was estimated that the top of the VA was tilted  $\sim 7^\circ \pm 1^\circ$  away from the source. This corresponds to about a 7.6 m displacement in range between the top and bottom hydrophones. A similar analysis of the FM data for October 23, 1997, was performed, resulting in an estimate for the tilt of about  $3^\circ \pm 1^\circ$  in the same direction, which corresponds to about a 3.2 m displacement in range between the top and bottom hydrophones. These tilt values agree in both magnitude and direction with the inverted values.

The second method for estimating tilt was by inference of the measured ocean current magnitude and direction near the VA (currents shown in Fig. 4). Here, a hydrostatic model of the VA system is used, considering, among other factors, the VA drag and the buoyancy of the subsurface float.<sup>32</sup> In Fig. 16, the estimated VA shape is shown using measured ocean currents data from October 22-23. These values are slightly lower than those found using the matched filter response and MFP inverted values. The reason could be underestimation of the drag of the VA and mooring. However, the hydrostatic model correctly predicts the direction of tilt and shows the approximate change in tilt between October 22 and 23. The model also gives an impression of the VA shape. The acoustic propagation model always assumes a straight VA even if it is tilted, and, from Fig. 16 it seems a reasonable approximation.

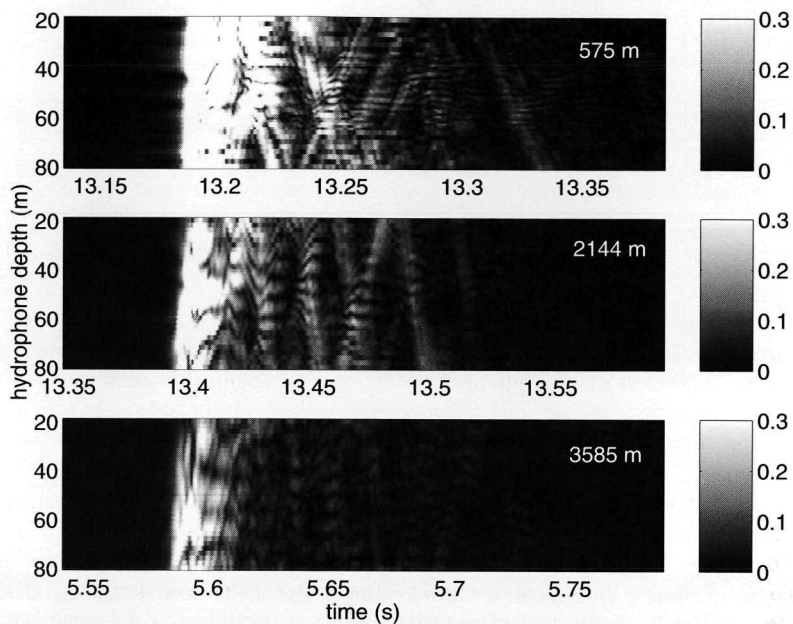
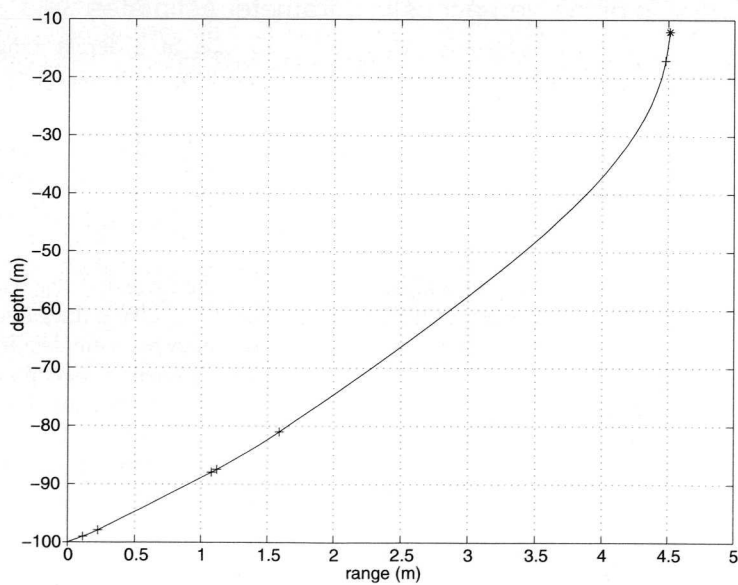


Fig. 15 The matched filter outputs for FM signals transmitted on October 22, 1997, at three different ranges, which are indicated inside each of the panels.



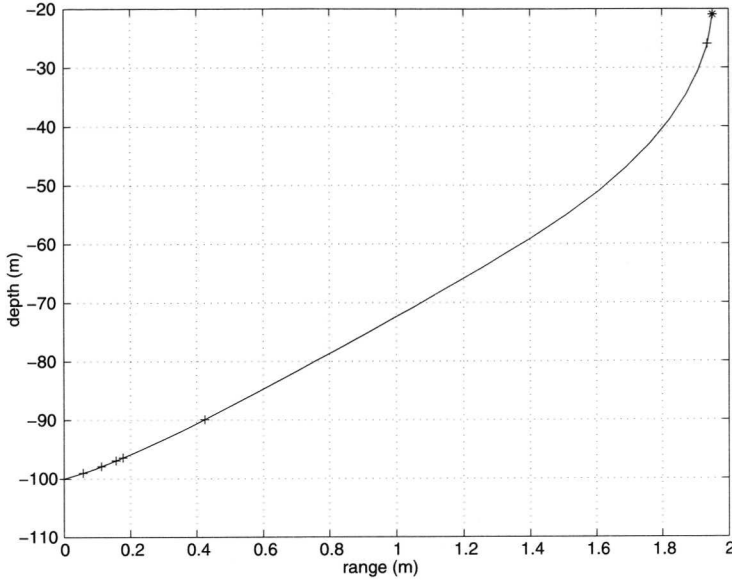


Fig. 16 Estimated VA displacement as a function of depth for October 22 (top) and October 23 (bottom). Star (\*) indicates depth of the subsurface buoy and directly below, the + mark indicates the depth of the shallowest hydrophone and the next + mark indicates the depth of the deepest hydrophone. The lower four + marks indicate link points for VA electronics modules and cables. Note that the x-axis scales differ between top and bottom plot.

### 5.4.1.3 Analysis of the geo-acoustic parameter estimates

The geo-acoustic inversion results (Table IV) taken from data at different ranges and frequencies are not entirely in agreement with each other. Complete agreement between the four inversion results would be inconsistent with the known range-dependence of the track. Note the value for  $c_{l, sed}$  taken from the LF multi-tone signal at 1.5-km range. A much higher sound speed value was found compared with the other inversions. The probable cause is found in the layering of the bottom (refer back to Fig. 9). Near the VA, the first significant layer has a thickness of about 6 m (shown as a gray line in Fig. 9). Moving from the VA along the acoustic track, this surface layer decreases in thickness and then increases again. At about 1.5 km from the VA, the layer nearly disappears. At this point, the inversion results show a marked increase for  $c_{l, sed}$ . Note, however, for the nearby 2.1-km HF inversion the value  $c_{l, sed} = 1580$  m/s along with  $h_{sed} = 5.7$  m. It is likely that the higher frequency acoustic data inversion is capable of resolving the thin surface layer whereas the low frequency inversion is not. Since the shortest wavelength in the LF inversion is 5 m, it is unlikely that this layer has a great influence on acoustic fields at these frequencies. That is, the surface layer is much thicker, with respect to wavelength, for the high frequency signals compared to the LF. At 3.5 km, this surface layer becomes thicker, to nearly 10 m, and the value found from the LF inversion there is  $c_{l, sed} = 1576$  m/s, which is in much better agreement with the 0.7-km HF result of 1580 m/s and the 2.1-km result of 1572 m/s.

Additional support for the inverted values of  $c_{l, sed}$  is given by the wide-angle reflection results in Section 5.2.3.1. With wide-angle reflection, the average sound speed in the top layers is estimated at points where a strong reflector is identified below. Figure 11 identifies two reflectors at the depths indicated and the corresponding velocities within those layers. The values show variability along the track with an average sound speed of 1591 m/s with 32 m/s standard deviation, which is in keeping with the MFP inversions. There are notable points



along the track where the sound speed is as low as 1540 m/s and as high as 1650 m/s. The wide-angle reflection analysis gives the average speed within the layer, which compares well with the MFP results. It is important to note that the wide angle seismic analysis gives layer sound speeds at points along the track. The MFP inversion data may be weighted by the bottom properties near the sound source or the VA, but, because the propagation is over long ranges in comparison to the wide-angle data, it gives a more (range) integrated prediction for the bottom properties.

The inverted values of  $h_{sed}$  should be interpreted carefully. The multi-layer structure of the bottom (and the range-dependence) is not included in the geo-acoustic model. Therefore,  $h_{sed}$  represents a break point, setting a depth in the bottom below which it is considered homogeneous and above which it fits with the sound speed gradient determined by  $c_{1,sed}$  and  $c_{l,sed}$ . At 0.7 km (HF), and at 1.5 km (LF), deeper values are found for  $h_{sed}$  compared to 2.1 km (HF) and 3.5 km (LF). There is evidence from the seismic analysis that the top layer is thinner and there are fewer lower layers at the longer ranges. The regions beyond about 2 km may be adequately approximated by setting the 'basement' at a lower  $h_{sed}$  value. Further analysis of the HF and LF inversion results and the relationship with sediment sound speed and thickness is provided with numerical simulations in Section 5.4.3.

The attenuation is not extremely well resolved in the inversions here, but the results set bounds within 0.4-0.9 dB/ $\lambda$ . Like the sound speeds, the attenuation indicates range-dependent properties of the bottom. The 0.7-km and 3.5-km inversion results tend toward an attenuation constant similar to sand materials which has a typical value of 0.8 dB/ $\lambda$ .<sup>25</sup> The lower attenuation value found at 1.5 km is consistent with harder (faster) materials in accordance with the inversion values for  $c_{l,sed}$ .

The density values do not seem consistent with the range-dependent seismic profiles or the material types. This parameter was not well determined in the inversion. The density has a small influence on the acoustic field and is therefore difficult to determine to high precision with this MFP inversion method. For the same reasons, it usually has little importance for acoustic prediction.

The overall agreement between the direct measurements and MFP inverted parameter values indicates that the inversion is of good quality. It is difficult to establish ground-truth values for all the bottom properties, but the seismic analysis provides supporting evidence that the inverted geo-acoustic parameters are reasonable and consistent. The results indicate bottom properties, which are similar to sand materials over rock. These are in agreement with the results expected from looking at archived data (Fig. 1) and other analyses in the Adventure Bank area.<sup>33</sup>

#### 5.4.1.4 Measured and simulated acoustic field comparison

Another check of the quality of the inversion is the direct comparison of the simulated and measured acoustic fields. Fig. 17 shows measured and simulated transmission loss ( $TL$ ) for one snapshot from each of the 0.7-km and 2.1-km HF multi-tone signals. The simulated  $TL$  is taken using the  $GA_{best}$  environment determined through inversion. Even though the objective function given by Eq. (4) uses normalized complex pressure fields, which is not sensitive to absolute level, the simulated fields compare well with the measured  $TL$ . Presented in Fig. 18 are the measured and simulated pressure fields (normalized magnitudes) taken from LF snapshots at 1.5-km and 3.5-km source ranges. These simulated fields also use the environment determined from the  $GA_{best}$  for that snapshot of data. The LF source did not have adequate calibration data and these fields are therefore normalized and not on an absolute pressure scale (or  $TL$ ).

### 5.4.1.5 Backpropagation ambiguity surfaces

As a final check of the inversion results, matched field ambiguity surfaces are generated.<sup>30</sup> These surfaces are generated by taking hypothetical source positions at all points within a region of the waveguide and simulating the resulting acoustic field on the VA. Each of the fields are correlated with the measured pressure field according to  $1 - E(\mathbf{m}_{ave})$  where  $E$  is taken from Eq. (4) and  $\mathbf{m}_{ave}$  is the averaged environment given in Table IV. This is equivalent to a normalized 'backpropagation' of the measured pressure field from the VA back into the waveguide using the environment found by inversion. Each pixel in the images can take a value between 0 and 1. If the field refocuses at the true source location, i.e., have a region with high pixel values with little or no ambiguity, it is an indication that the environment is well characterized for acoustic propagation at those frequencies. The ambiguity surfaces are shown in Fig. 19. There are extremely well focused fields near the true transmission locations. There is a slightly lower objective function value for the 2.1-km HF transmission but with a maximum near the true source location. There is also more ambiguity (or side lobes) for the 1.5-km and 3.5-km transmissions, which is typical for low frequency data.

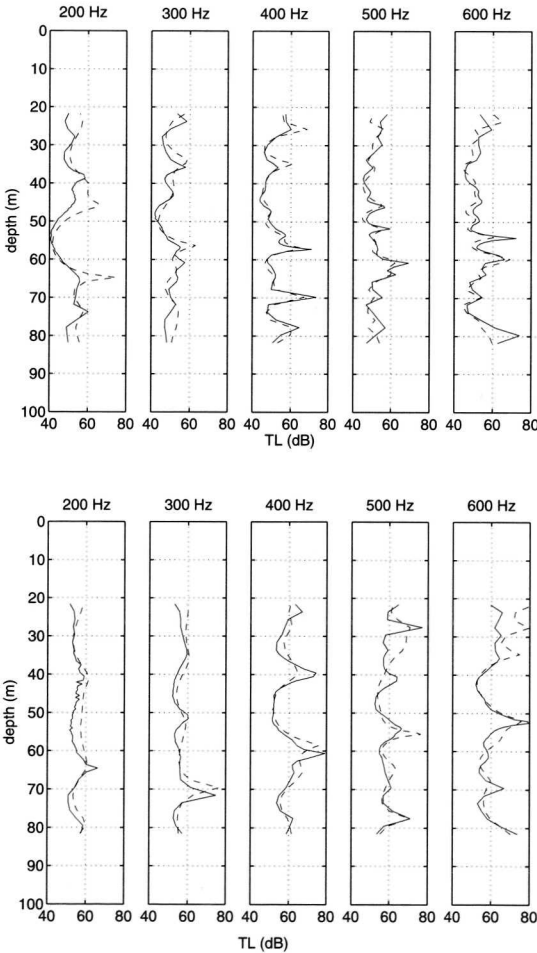


Fig. 17 Experimental (solid lines) and simulated (dashed lines) HF transmission loss data along the VA at the indicated frequencies. Top graph shows results for the 0.7-km source range, bottom graph shows results for the 2.1-km source range.

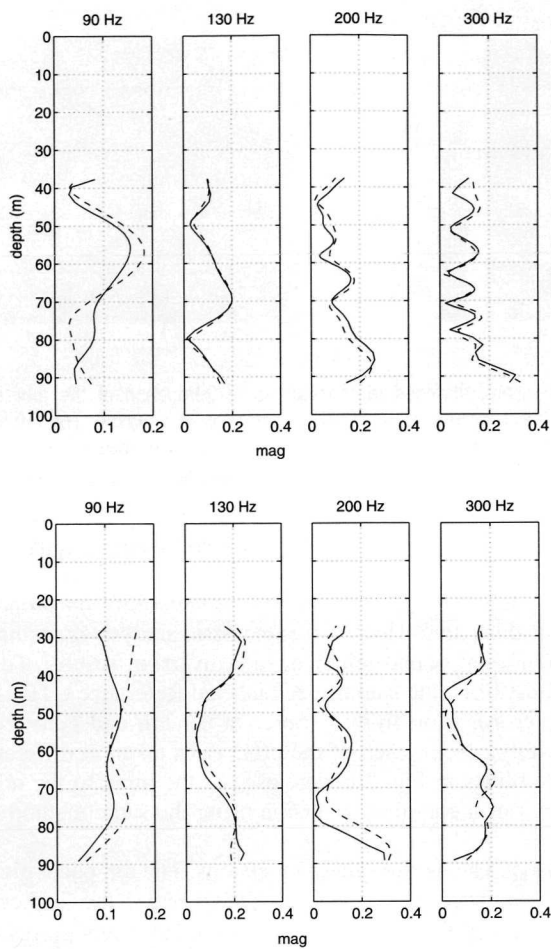
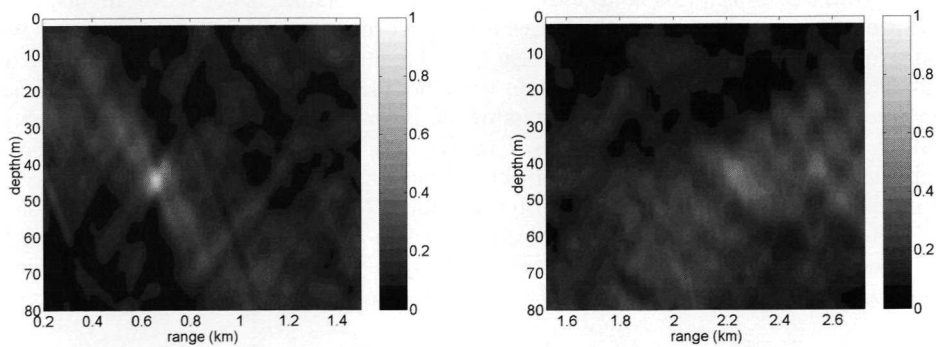


Fig. 18 Experimental (solid lines) and simulated (dashed lines) LF pressure field magnitudes along the VA at the indicated frequencies. Top: 1.5-km source range, bottom: 3.5-km source range.



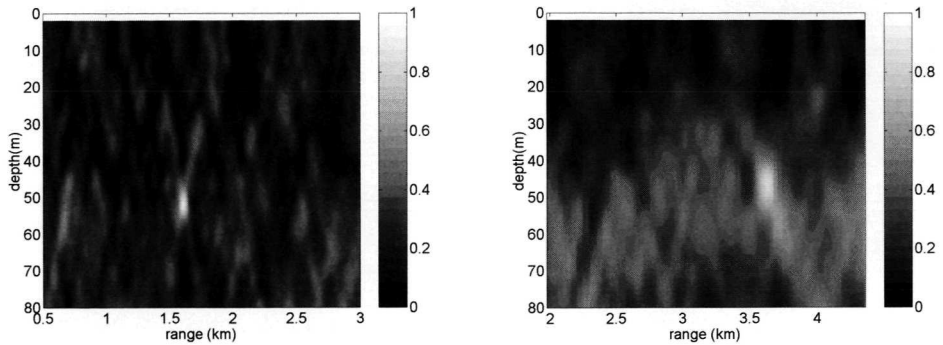


Fig. 19 Ambiguity ('backpropagation') surfaces for one snapshot from each of the four source range positions. Range and depth windows are indicated on the x- and y-axes. Top left: 0.7-km range position HF transmission. Top right: 2.1-km range position HF transmission. Bottom left: 1.5-km range position LF transmission. Bottom right: 3.5-km range position LF transmission

## 5.4.2 Effect of sound speed variability on inversion

Studying all the effects of temporal and spatial sound speed variability on propagation and inversion is beyond the scope of this paper. However, some basic analysis is required to make a conclusion about the importance of sound speed on the inversion results. To make this judgment, a simple test was made. First, the sound speed labeled Reference CTD#1 in Fig. 20 was used to simulate acoustic propagation from a source at 0.7 km and generate reference acoustic data (HF frequencies only). Next, each of the CTD casts taken at different times on that day, and shown with dashed lines in Fig. 20, were used as the input to the normal-mode forward propagation code as part of a complete inversion using the same method as outlined in Section 5.3.

Figure 21 shows the final  $GA_{\text{best}}$  values from these inversions. The top panel gives the final objective function value, Eq. (4), and the lower panels give the errors in the final estimation of  $\Delta r_s$ ,  $\Delta z_s$ , and  $\Delta c_{1,\text{sed}}$ . The solid lines in Fig. 21 are for the simulated inversion results for  $r_s = 0.7$  km and the dashed line is the same for  $r_s = 2.1$  km.

Consider the first seven profiles, which are all taken within 4 h of the Reference sound speed. These inversion results give final parameter estimates that are within acceptable limits of the known true value. This holds even for the inverted parameters not shown in this figure. As expected, the first inversion, which uses the correct sound speed, finds all parameters with little error and the objective function is near zero. For subsequent inversions (2-7), there is a slight degradation of the objective function value but the inverted parameters are found near their true values. Consider now the results of the inversions using the climatology and the October 1986 profiles (numbers 8 and 9 in Fig. 21). The final parameter estimates are significantly worse. Note that the final objective function value is nearly the same for the 2.1-km inversion using profile 7, in comparison with the 0.7-km inversion using the climatology profile 8. Even with almost identical objective function values, the inversion results are, for  $c_{1,\text{sed}}$ , much worse when the climatology profile is used. This suggests how difficult it can be to only use the objective function value for estimating the quality of the inversion results.

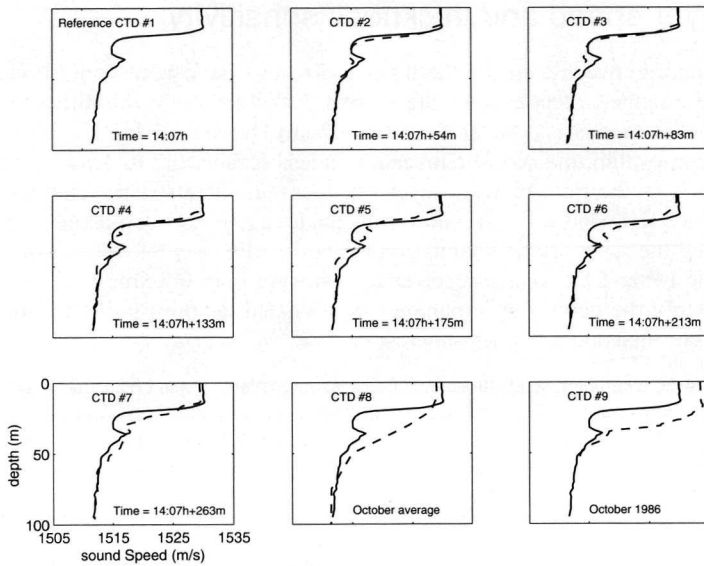


Fig. 20 Sound speeds for Adventure Bank. Top left: the reference profile taken at 14:07 on October 22, 1997 and is shown as a solid line in each of the 9 panels. Sound speeds taken from subsequent CTD casts are shown as dashed lines with times given as minutes after the reference. The archived sound speed taken from the climatology database and profile from October 1986 are also shown as dashed lines in the two right panels in the bottom row.

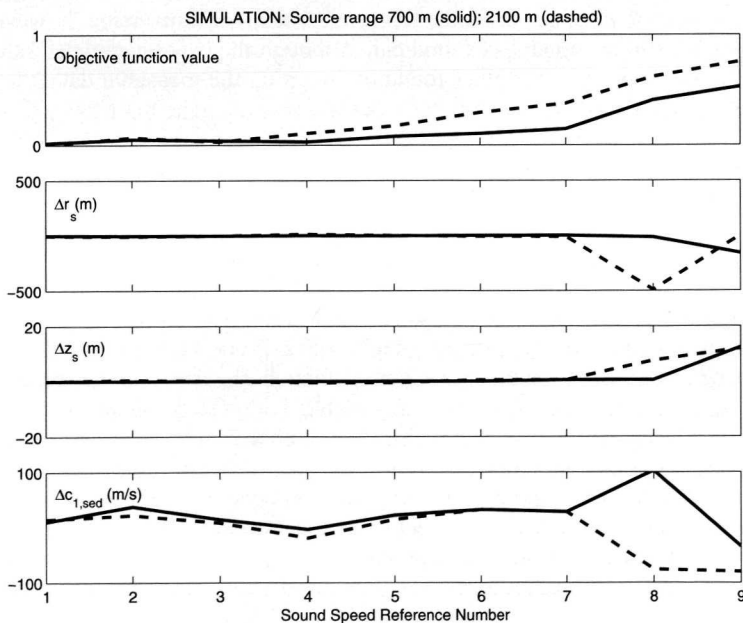


Fig. 21 Final ( $GA_{best}$ ) values from the inversion. The x-axis indicates the sound speed profile Reference number (from Fig. 20) used in the inversion. The top panel gives the final objective function values and below are the errors in estimating  $r_s$ ,  $z_s$ , and  $C_{1, sed}$ . The solid line is taken from simulated inversion results taken for  $r_s = 0.7$  km and the dashed line for  $r_s = 2.1$  km.

### 5.4.3 Layer speed and thickness sensitivity

The differences found between some of the inversion results have been conjectured here as primarily due to the range-dependence of the seabed. Consider again the differences in the inversion results for parameter  $c_{l, sed}$  taken from the 0.7-km HF and 1.5-km LF data sets. As a sediment layer becomes thin, the acoustic inversion is less sensitive to it. This is exaggerated at lower frequencies, as the ratio between layer thickness and acoustic wavelength becomes smaller. A simulated HF and LF inversion was made using the geo-acoustic model of Adventure Bank and the same search bounds and method outlined in Section 5.3. In this case, for comparison, the LF and HF source-receiver ranges were both 0.7 km. Table V gives the inversion results. Only the geo-acoustic parameters are listed, as the geometrical parameters were very well determined and are of less interest here.

Table V Geo-acoustic parameter values taken from  $GA_{best}$  for simulated HF and LF inversions at 0.7 km.

Range-Band	$c_{l, sed}$ (m/s)	$c_{2, sed}$ (m/s)	$c_b$ (m/s)	$h_{sed}$ (m)	$\alpha$ (dB/ $\lambda$ )	$\rho$ (g/cm <sup>3</sup> )
Ground-truth	1572	1790	1812	8.0	0.74	1.43
0.7 km, HF	1595	1771	1799	8.3	0.74	1.44
0.7 km, LF	1675	1752	1864	9.1	0.98	1.42

Some observations can be made from these simulations. If the sediment layer becomes thin, especially when there is a large sound speed gradient, there can be significant differences in sound speed estimates between HF and LF inversions. However, significant differences between HF and LF inversions as shown in Table V were eliminated when  $h_{sed}$  was increased to 20 m (not shown in Table V). It is likely that, with the measured data inversions, something similar to these simulations is occurring. Recall in Fig. 9 at range near 1.5 km from the VA the top sediment layer thins to a few meters, and the reported value for  $c_{l, sed}$  and  $h_{sed}$  seem to indicate the LF inversion does not sense the top layer. The 2.1-km inversion, however, shows a 5.7-m layer with a strong sound speed gradient. Although the exact parameter values differ between these simulations and the values found by inverting the measured data, the behavior is similar.

## 5.5 Conclusions

The EnVerse 97 towed source experiments demonstrated the technique of using acoustic data taken at various source/receiver separations to estimate properties of the seabed. These estimates change as the distance between source and receiver changes in a way consistent with the actual geo-acoustic properties. Both high-(HF 200-600 Hz) and low-frequency (LF 90-300 Hz) bands were used in the inversion. Although the HF and LF data sets were collected on separate days and there was a variable bathymetry, which required range-dependent forward propagation modeling, these did not pose problems for the inversion. The measured acoustic signals down-range are from propagation over a range-dependent bottom, but the MFP inverted bottom properties are range-independent and represent the result of this averaging process. The results are consistent with the bottom layering and sound speeds estimated using standard geophysical measurements and existing knowledge of the area. A wide-angle seismic reflection experiment was conducted using a towed horizontal array to estimate sediment sound speed along the acoustic track. These values agreed with the MFP inversion results. A striking feature in the MFP inversion results was  $c_{l, sed}$ , the sediment sound speed at the water-sediment interface. This parameter changed along the track according to the appearance and disappearance of the surface sediment layer. The jump from 1580 m/s for the HF inversion at 0.7 km to 1641 m/s for the LF inversion at 1.5 km was probably due to a combination of effects. Likely causes are both the thinning layer and the

reduced ability to extract the sediment properties due to the lower frequency signals. The combination would act together to increase the sound speed estimate. This calls attention to an important issue in the geo-acoustic inversion: the parameters found which make up the geo-acoustic model are those, which can be sensed at the frequencies transmitted. Applying the geo-acoustic parameters to other frequencies may result in erroneous results. Ideally, inverted acoustic data would contain the entire frequency band of interest.

The inverted parameters for the Adventure Bank site were used to simulate acoustic fields, which were in excellent agreement with the measured fields. Using the averaged inverted geo-acoustic model, the 'backpropagated' fields correctly localized the position of the source. The genetic algorithm converged and the parameter estimates are reasonably consistent over many snapshots. Also, the final inverted geo-acoustic model is consistent with the seismic survey data. Together this indicates that the towed source MFP inversion is a promising method for determining geo-acoustic properties over large areas. It was asserted that a relatively recent sound speed profile taken in the vicinity of the experiment should be adequate for the MFP inversion. This likely would not hold for longer range propagation or higher frequency signals. In addition, it was shown that archived sound speed profiles did not perform well for either localization or geo-acoustic inversion. Determining the effects on MFP inversion of stronger range-dependence in the water volume and seabed are important areas of future research.

## 5.6 Acknowledgments

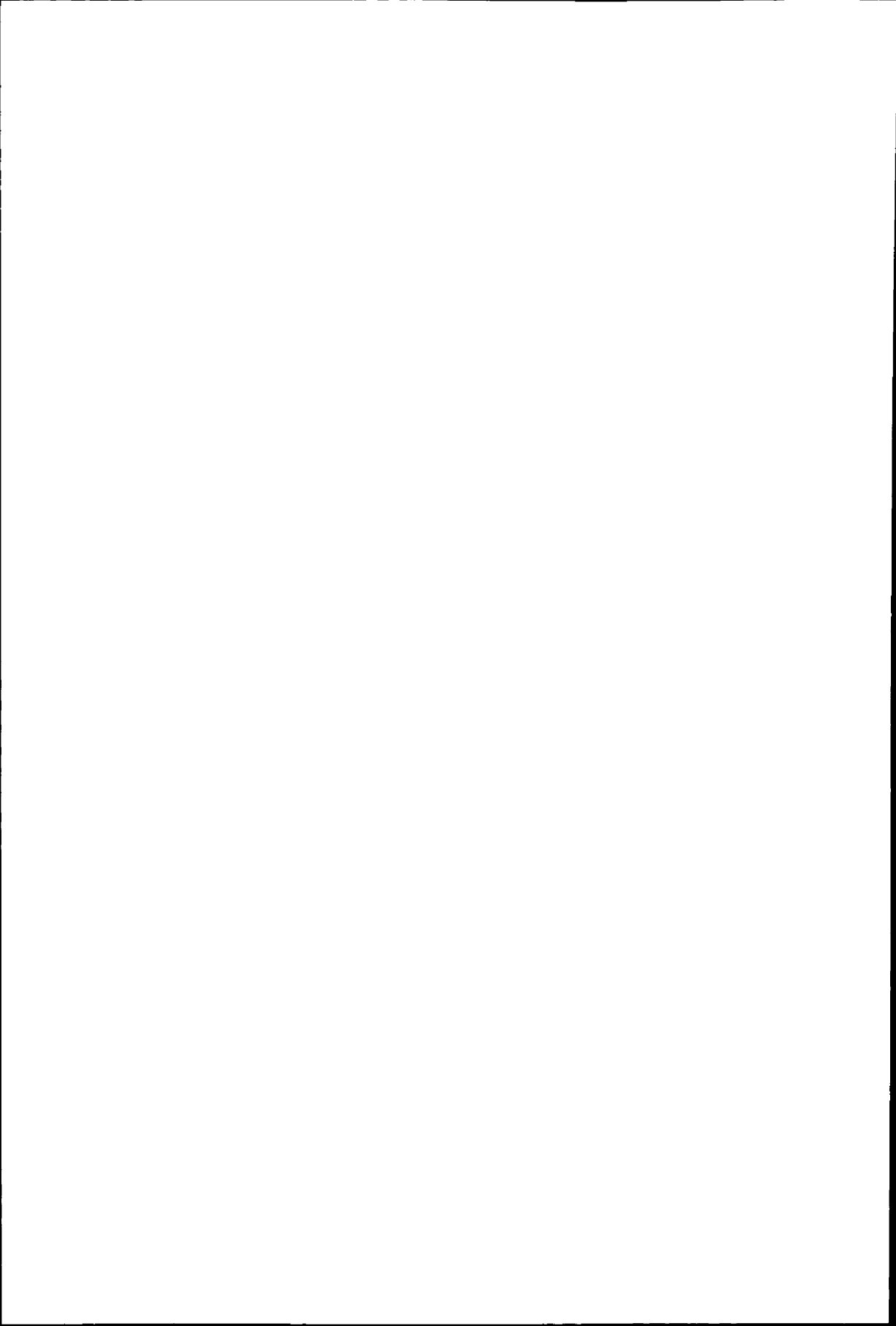
The authors wish to thank all the members who participated in EnVerse 97, in particular from SACLANT Centre, J. P. Hermand, E. Michelozzi, P. Boni and F. Spina. From TNO-FEL: E. van Ballegooijen, J. Kromjongh. From DERA: M. Galpin, and S. Holt. Thanks are also due to the crews of NRV *Alliance* and HNLMS *Tydeman*. The authors would also like to gratefully acknowledge contributions from C. Mesdag and P. Frantsen from TNO-NIAG.

## References

- 1 M. D. Collins, and W. A. Kuperman, "Focalization: Environmental focusing and source localization," *J. Acoust. Soc. Am.* **90** (3), 1410-1422 (1991).
- 2 M. D. Collins, W. A. Kuperman, and H. Schmidt, "Nonlinear inversion for ocean bottom properties," *J. Acoust. Soc. Am.*, **92** (5), 2770-2783 (1992).
- 3 C. E. Lindsay and N. R. Chapman, "Matched field inversion for geophysical parameters using adaptive simulated annealing," *IEEE J. Ocean. Eng.* **18** (3), 224-231 (1993).
- 4 S. E. Dosso, M. L. Jeremy, J. M. Ozard, and N. R. Chapman, "Estimation of ocean bottom properties by matched-field inversion of acoustic field data," *IEEE J. Ocean. Eng.* **18** (3), 232-239 (1993).
- 5 P. Gerstoft, "Inversion of seismoacoustic data using genetic algorithms and a *posteriori* probability distributions," *J. Acoust. Soc. Am.*, **95** (2), 770-782 (1994).
- 6 P. Gerstoft, "SAGA Users manual 2.0, an inversion software package," Tech. Rep. SM-333, SACLANT Undersea Research Centre, La Spezia, Italy, 1997.
- 7 P. Gerstoft and D. F. Gingras, "Parameter estimation using multi-frequency range-dependent acoustic data in shallow water," *J. Acoust. Soc. Am.*, **99**, 2839-2850 (1996).
- 8 G. Haralabus and P. Gerstoft, "Source localization in shallow water using multi-frequency processing of shot data," Tech. Rep. SR-253, SACLANT Undersea Research Centre, La Spezia, Italy, 1996.
- 9 J. P. Hermand and P. Gerstoft, "Inversion of broadband multi-tone acoustic data from the Yellow Shark summer experiments," *IEEE J. Ocean. Eng.* **21** (4), 324-346 (1996).
- 10 O. Diachok, A. Caiti, P. Gerstoft, and H. Schmidt, Eds., *Full field inversion methods in ocean and seismo-acoustics*, Kluwer Academic Publishers, Dordrecht, The Netherlands, 1995.
- 11 N. R. Chapman and C. E. Lindsay, "Matched-field inversion for geoacoustic model parameters in shallow water," *IEEE J. Oceanic Eng.* **21** (4), 347-354 (1996).
- 12 A. Tolstoy, "Using matched-field processing to estimate shallow-water bottom properties from shot data taken in the Mediterranean Sea," *IEEE J. Oceanic Eng.* **21** (4), 471-479 (1996).
- 13 M. Siderius and J. P. Hermand, "Yellow shark spring 1995: Inversion results from sparse broadband acoustic measurements over a highly range-dependent soft clay layer," *J. Acoust. Soc. Am.*, **106** (2), 637-651 (1999).
- 14 M. Siderius, D. G. Simons, M. Snellen, J. P. Hermand, and E. van Ballegooijen, "Inversion results from the Enverse 97 shallow water experiments," in *Proceedings of the fourth European conference on underwater acoustics*, Istituto di Acustica, Rome, Italy, 1998, pp. 517-522, Italian National Research Council.
- 15 M. Max, N. Portunato, and F. Spina, "Digital map and linked data (DMap) implementation at SACLANTCEN as an aid to sea-going research," SM-291, SACLANT Undersea Research Centre, La Spezia, Italy, 1995.
- 16 M. Siderius, P. L. Nielsen, and F. B. Jensen, "Geo-acoustic inversion of experimental data from two shallow water sites," in *Oceans '99*, New York, NY, 1999, IEEE.
- 17 Medatlas Project, "Medatlas Mediterranean Hydrological Atlas," CD-ROM, BP 70, 29280 Plouzane, France, 1997.
- 18 W. J. Teague, M. J. Carron, and P. J. Hogan, "A comparison between the Generalized Digital Environmental Model and Levitus climatologies," *J. Geophys. Res.*, vol. 95, no. C5, pp. 7167-7183, 1990.
- 19 F. P. Bretherton, R. E. Davis, and C. B. Fandry, "A technique for objective analysis and design of oceanographic experiments applied to MODE-73," *Deep-Sea Res.*, vol. 23, no. 7, pp. 559-582, 1976.
- 20 R. Onken and J. Sellschopp, "Seasonal variability of flow instabilities in the Strait of Sicily," *J. Geophys. Res.*, vol. 103, no. C11, pp. 24799-24820, 1998.
- 21 A. R. Robinson, J. Sellschopp, A. Warn-Varnas, W. G. Leslie, C. J. Lozano, P. J. Haley Jr., L. A. Anderson, and P. F. J. Lermusiaux, "The Atlantic Ionian Stream," *J. Mar. Systems*, vol. 20, pp. 129-156, 1999.
- 22 W. J. Pierson and L. Moskowitz, "A proposed spectral form for fully developed wind seas based on the similarity theory of S. A. Kitaigorodskii," *J. Geophys. Res.*, vol. 69, no. 24, pp. 5181-5190, 1964.
- 23 D. J. C. Carter, "Prediction of wave height and period for a constant wind velocity using the JONSWAP results," *Ocean Engineering*, vol. 9, pp. 17-33, 1982.
- 24 L. Hatton, M.H. Worthington, and J. Makin, Eds., *Seismic Data Processing, Theory and Practice*, Blackwell Science Ltd., 1986.
- 25 F. B. Jensen, W. A. Kuperman, M. B. Porter, and Henrik Schmidt, *Computational Ocean Acoustics*, American Institute of Physics, Inc., New York, 1994.
- 26 C. A. Boyles, *Acoustic Waveguides Applications to Oceanic Science*, John Wiley and Sons, Inc., New York, 1984.



- <sup>27</sup> M. Siderius, P. Gerstoft, and P. Nielsen, "Broadband geoacoustic inversion from sparse data using genetic algorithms," *J. Comp. Acoust.*, vol. 6, no. 1&2, pp. 117-134, 1998.
- <sup>28</sup> A. Tolstoy, N. R. Chapman, and G. Brooke, "Workshop '97: Benchmarking for geoacoustic inversion in shallow water," *J. Comp. Acoust.*, vol. 6, no. 1&2, pp. 1-28, 1998.
- <sup>29</sup> A. Caiti, F. Ingenito, A. Kristensen, and M. D. Max, *Measurements of bottom parameters and transmission loss at two sites in the Sicilian channel*, SR-228, SACLANT Undersea Research Centre, La Spezia, Italy, 1994.
- <sup>30</sup> A. Tolstoy, *Matched Field Processing for Underwater Acoustics*, World Scientific Pub. Co., River Edge, New Jersey, 1993.
- <sup>31</sup> D. G. Simons and M. Snellen, "Multi-frequency matched-field inversion of benchmark data using a genetic algorithm," *J. Comp. Acoust.*, vol. 6, no. 1&2, pp. 135-150, 1998.
- <sup>32</sup> L. Troiano, *ETD Cablesim program*, Personal communication, June 1999.
- <sup>33</sup> A. Caiti, S. M. Jesus, and A. Kristensen, "Geoacoustic seafloor exploration with a towed array in a shallow water area of the Strait of Sicily," *IEEE J. Oceanic Eng.* 21 (4), 355-366 (1996).



## Chapter 6

# An evaluation of the accuracy of shallow water matched field inversion results<sup>C</sup>

### Abstract

In this paper the accuracy of geo-acoustic and geometric parameter estimates obtained through matched field inversion (MFI) was assessed. Multi-frequency MFI was applied to multi-tone data (200-600 Hz) received at a 2 km source/receiver range. The acoustic source was fixed and the signals were received at a vertical array. Simultaneously with the acoustic transmissions, a CTD (conductivity, temperature and depth) -chain was towed along the acoustic track. A genetic algorithm was used for the global optimization, whereas a normal-mode model was applied for the forward acoustic calculations. Acoustic data received at consecutive times were inverted and the stability of the inverted parameters was determined. Also, the parameter estimates were compared with independent measurements, such as multi-channel seismic surveys (for geo-acoustic parameters). The obtained uncertainty in the inversion results was assumed to have two distinct origins. The first origin is the inversion method itself, since each optimization will come up with some solution close to the exact optimum. Parameter coupling and the fact that some parameters hardly influence the acoustic propagation further contribute to this uncertainty. The second is due to oceanographic variability. Both contributions were evaluated through simulation. The contribution of oceanographic variability was evaluated through synthetic inversions that account for the actual sound speed variations as measured by the towed CTD-chain.

---

<sup>C</sup> Published in the Journal of the Acoustical Society of America, Volume 109 (2), pp. 514-527 (2001).

## 6.1 Introduction

Matched field inversion (MFI) is a technique for obtaining information on unknown parameters that influence the propagation of sound underwater. When employing MFI, a measured acoustic field is compared with acoustic fields that are calculated by a propagation model for many sets of unknown parameters. Since the number of possible parameter combinations is huge and there are many local optima, global optimization methods are needed for guiding the search for the set of unknown parameters that gives the optimum match between measured and calculated acoustic fields. An important application of MFI is geo-acoustic seabed parameter estimation.

An important issue to be addressed is the accuracy of the parameter estimates. In general, performing several independent inversions for the same acoustic field can result in different estimates for the unknown parameters. This uncertainty in parameter estimates is partly due to the optimization method, as global optimization methods often do not determine the exact optimum, but a solution close to it. The resulting variation in parameter estimates is dependent on their influence on the acoustic propagation. For the parameters that hardly influence the acoustic propagation the variation in parameter estimates will comprise a large part of the parameter search space, whereas for the parameters that have a strong influence on the acoustic propagation the variation will be small. Also the fact that there can be correlations between the unknown parameters contributes to the uncertainty. These two above-mentioned factors can result in optimized parameter values that deviate from the actual parameter values. However, the agreement between optimized and measured acoustic fields can still be high. By adapting the optimization method the uncertainties due to the above-mentioned factors can be reduced. For example, a local search method can be applied after convergence of the global search.<sup>1</sup> In the following we will denote the uncertainties in parameter estimates that result from these two mechanisms as the uncertainties caused by the method itself.

When inverting for unknown parameters and using experimental acoustic fields that were measured at different times, the temporal variability of the oceanographic conditions can result in additional uncertainties in parameter estimates.<sup>2</sup> If the sound speed profile in the water column varies with time and if one does not account for these variations in the inverse modeling, this can result in parameter estimates that also vary with time. In this case, the optimized parameter value is such that it corrects for the difference between the actual sound speed profile and the sound speed profile that is used for the forward model calculations. The effects of the varying oceanographic conditions can directly be seen in the acoustic data, as these variations result in changes in the propagation conditions and consequently varying (in time) received signals. This contribution to the uncertainty can, at least in principle, be eliminated when the sound speed structure between source and receiver is known exactly at the time of each transmission. However, under practical experimental conditions this is rather cumbersome.

Matched field inversion results are presented for experimental data that are obtained during the ADVENT99 sea trial. This sea trial was conducted by SACLANT Centre and TNO-FEL on the Adventure Bank, south of Sicily, in April/May 1999.<sup>3</sup> Several experiments were carried out during ADVENT99. The analysis presented in this paper deals with data that were acquired during experiments with both the source and the receiver at a fixed position. The goal of these experiments was to obtain data for a fixed geometry over an extensive period of time. During these experiments also many measurements were carried out to obtain information on the ocean environment. These environmental measurements included conductivity, temperature and depth (CTD) casts and waverider measurements. Further, a CTD-chain was towed along the acoustic track, giving more detailed information on the

sound speed structure. Also, an extensive seismic survey was carried out, thereby obtaining independent geophysical information on the seabed. For the survey use was made of a multi-channel streamer, which allows for the estimation of, in addition to the ocean bottom layering, the sound speeds of the layers.

The main goal of this paper is to assess the uncertainties in parameter estimates obtained through MFI using experimental data. The uncertainty that is due to the method itself is estimated by simulation, i.e., by performing inversions of synthetic data, and it is demonstrated that for some parameters the uncertainty can thus largely be explained. The CTD-chain data are used to show that the remaining uncertainties originate from oceanographic variations in the water column.

This paper is organized as follows: in Section 6.2 the ADVENT99 sea trial is presented and an overview of the acoustic and environmental data is provided. The inversion problem, comprising the forward acoustic model and the optimization method, is described in Section 6.3. In Section 6.4 the inversion results are presented and the parameter estimates and their uncertainties assessed.

## 6.2 The ADVENT99 experiment

### 6.2.1 Acoustic measurements

A large part of the ADVENT99 sea trial comprised acoustic experiments with both the source and the receiver at a fixed position. These fixed geometry experiments were conducted for source/receiver ranges of 2, 5 and 10 km.

In this paper we only consider data of the 2 km experiment. The position of the source during this experiment was  $37^{\circ} 17.966'$  N,  $12^{\circ} 15.588'$  E. The receiving system was positioned at  $37^{\circ} 17.883'$  N,  $12^{\circ} 14.207'$  E. This experiment took place on May 2 1999 from 12:37 to 20:17 UTC time.

The source used for the acoustic transmissions was mounted on a tower that was moored on the sea bottom for keeping it at a fixed position. The Nato Research Vessel (NRV) *Alliance* was connected to the source by a power supply cable and therefore had to remain close to the source, but at a sufficient distance (a few hundred meters) to reduce risk of damage. Consequently, CTD casts could not be carried out very close to the source. The receiving system consisted of a vertical array (VA), containing 64 elements and spanning 62 meters of the water column. The signals received on the VA were sent directly to the data acquisition system on board NRV *Alliance* by radio link. In Fig. 1 a schematic of the experimental configuration is shown.

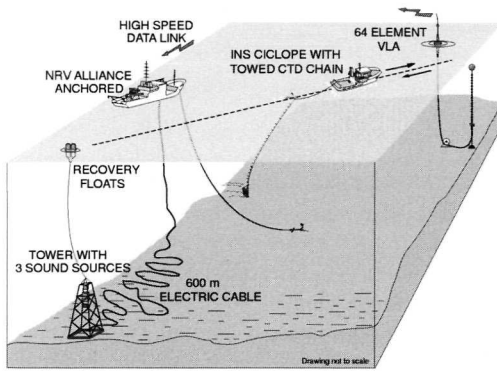


Fig. 1 The configuration of the fixed geometry experiments.

Both low-frequency (200-700 Hz) and high-frequency (800-1600 Hz) multi-tones and LFM sweeps were transmitted. In this paper only the low-frequency multi-tones are considered. Snapshots of 2 seconds were selected from the received time series and were fast Fourier transformed into the frequency domain. The resulting complex pressures as a function of depth are further referred to as 'pressure fields'. The magnitudes of 41 pressure fields are displayed in Fig. 2 for the frequencies 200, 300, 400 and 600 Hz. These 41 pressure fields were used in the inversions. The corresponding data were transmitted at 15 minutes interval, spanning the total duration of the 2 km experiment (about 8 hours). The figure clearly shows the variability in the received acoustic fields. The set of data considered in this paper is thus suitable for the purpose of investigating the contribution of water column variability to uncertainties in the parameter estimates. Note that the variability in the received signals increases with increasing frequency.

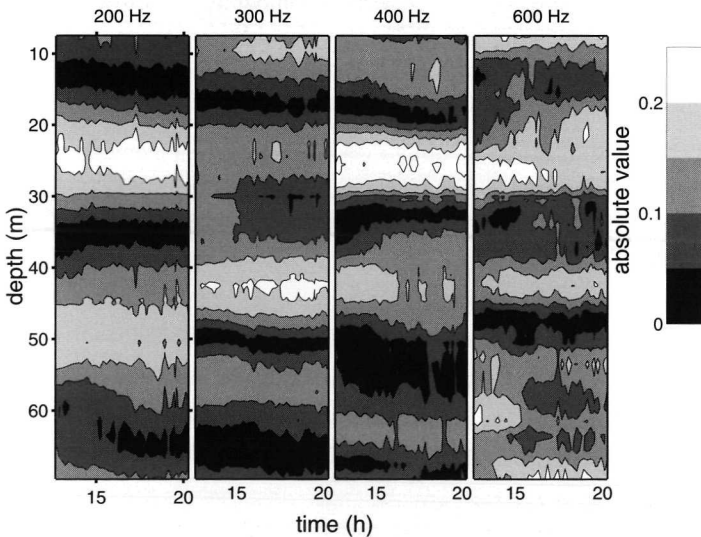


Fig. 2 Absolute values of the measured pressure fields as a function of UTC time for the frequencies 200, 300, 400 and 600 Hz.

Also illustrative is to determine a quantitative measure for the variability in the received signals. For this quantitative measure  $M_{ij}$  we have used the correlation between pressure fields  $\mathbf{p}_j$  and  $\mathbf{p}_i$

$$M_{ij} = \left| \mathbf{p}_i \cdot \mathbf{p}_j^* \right| \quad (1)$$

with “ $\cdot$ ” indicating the inner product and “ $*$ ” denoting the complex conjugate. The pressure fields  $\mathbf{p}_j$  and  $\mathbf{p}_i$  are normalized such that their norm equals one, i.e.,  $\|\mathbf{p}_i\| = \|\mathbf{p}_j\| = 1$ . Figure 3 shows, for the four frequencies, the correlation for all possible combinations of received pressure fields. Note that along the diagonal a pressure field is correlated with itself, resulting in a value of one for the correlation. Moving away from the diagonal shows, on the whole, a decrease in correlation, as moving away from the diagonal corresponds to an increase in time span between two transmissions. As with Fig. 2, also Fig. 3 clearly shows increasing variability with increasing frequency. Since the signal to noise ratio was high (at least 20 dB), the structure seen in Fig. 3 at 300 Hz and higher must be due to variations in oceanographic conditions and possible variations in the tilt of the vertical array (see Section 6.4.1.3).

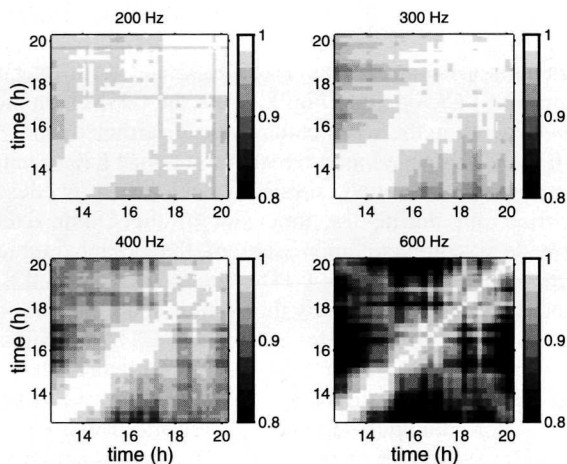


Fig. 3 The quantitative measure  $M_{ij}$  (Eq. (1)) for the variability in received signals for the 4 frequencies.

## 6.2.2 Ocean environmental measurements

### 6.2.2.1 CTD measurements

From the NRV *Alliance* a few CTD casts were taken. Figure 4 shows the corresponding sound speed profiles (ssp). From this figure it can be seen that there is a minor sound speed variation over the water depth (1509-1513 m/s). The ssp plotted as a solid line corresponds to the CTD taken 17 minutes prior to the 2 km fixed geometry experiment. No further CTD casts were carried out from *Alliance* during this experiment.

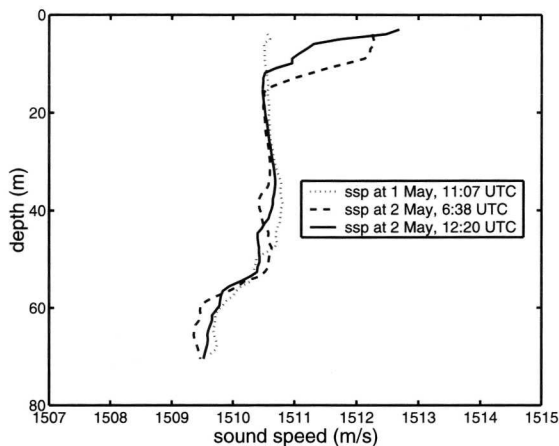


Fig. 4 Sound speed profiles as derived from the CTD casts from NRV *Alliance*.

#### 6.2.2.2 CTD-chain measurements

During the acoustic experiments a CTD-chain was towed back and forth over the acoustic track by the Italian Navy Ship (INS) *Ciclope*, see Fig. 1. From the CTD-chain measurements the sound speed as a function of depth in the water column was determined along the acoustic track. The tracks along which the CTD-chain measurements were done have a length of about 8.8 km. Figure 5 presents the water sound speeds, calculated from the CTD-chain measurements that were carried out during the time slot of the 2 km fixed geometry experiment. In order to provide a complete impression of the oceanographic variability encountered during the experiment, we present the CTD-chain data for the full 8.8 km track. The 2 km acoustic track is indicated in the figures by the vertical solid lines. As the tow ship is moving, both time and position are different for succeeding CTD-chain measurements. Hence, these figures do not represent time frozen sound speed structures that can be used directly as input to a (range-dependent) acoustic model. They are indicative of the amount of sound speed variability in the water column. Sound speed realizations will be selected from these CTD-chain data to simulate the effect of this oceanographic variability on inversion results (see Section 6.4.2).



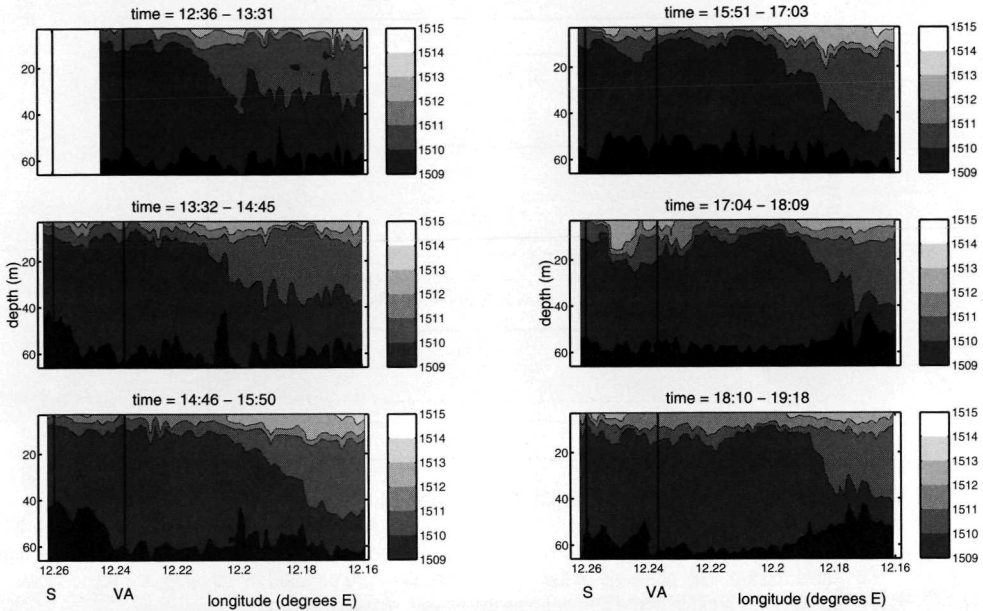


Fig. 5 Sound speed (in m/s) as a function of longitude and time as derived from the CTD-chain measurements made during the 2 km fixed geometry experiment. The vertical lines indicate the position of the source (S) and the vertical array (VA) for this experiment. The total horizontal axis corresponds to about 8.8 km.

### 6.2.2.3 Seismic measurements

A seismic survey was carried out at the experimental site. In total 5 tracks were covered in the area around the acoustic track. Figure 6 shows the tracks that were sailed during the survey. As can be seen, the seismic survey covers the full acoustic track (up to 10 km source/receiver distance). The survey was carried out prior to the acoustic measurements and covers an area of 12 by 2 km. Within this area we have selected the acoustic track such that the range-dependence in both bathymetry and bottom properties (as derived from the seismic measurements) is minimal. This is because the main scientific issue of this paper is to assess the influence of variability in the water column on the geo-acoustic parameter estimates. In the figure also the position of the VA for the different experiments, the source position and the position of the waverider are indicated.

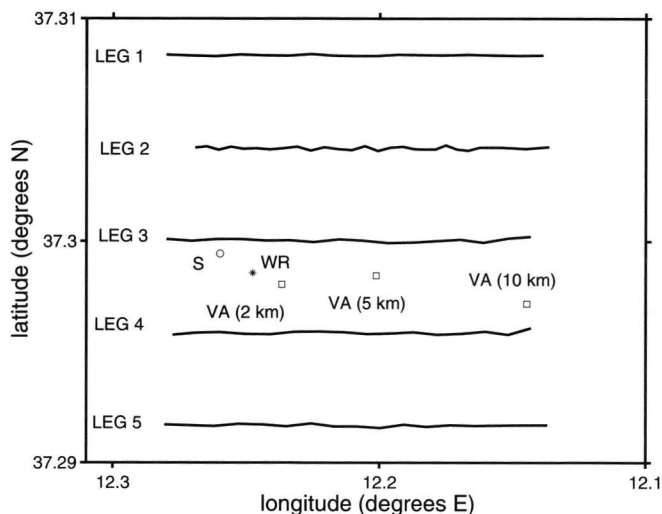


Fig. 6 The tracks sailed during the seismic survey. Note that the vertical distance between the five legs is only 0.5 km. The positions of the vertical array (VA) are denoted by squares, the source tower (S) position by a circle and a star denotes the waverider (WR) position.

Use was made of a boomer type sound source and the signals were received on a multi-channel seismic streamer. The streamer comprised eight groups of hydrophones, i.e., eight channels, and had a total length of 32 m, a group interval of 4 m and a group length of 3.8 m. Using a multi-channel receiving array allows for estimating both the layering of the seabed and the sound speeds of the layers.<sup>4</sup> This is a classical seismic technique, which is based on differences in travel time from reflectors in the bottom towards the various channels in the streamer.<sup>5</sup>

Figure 7 shows the layering on parts of leg 3 and leg 4 as obtained from the seismic measurements. Some internal structures within the sedimentary cover can be seen. This structure consists of a series of sub-horizontally layers, i.e., the sedimentary deposits are at a small angle with the horizontal. In these seismic data there is no clear definition of the basement.<sup>6</sup>

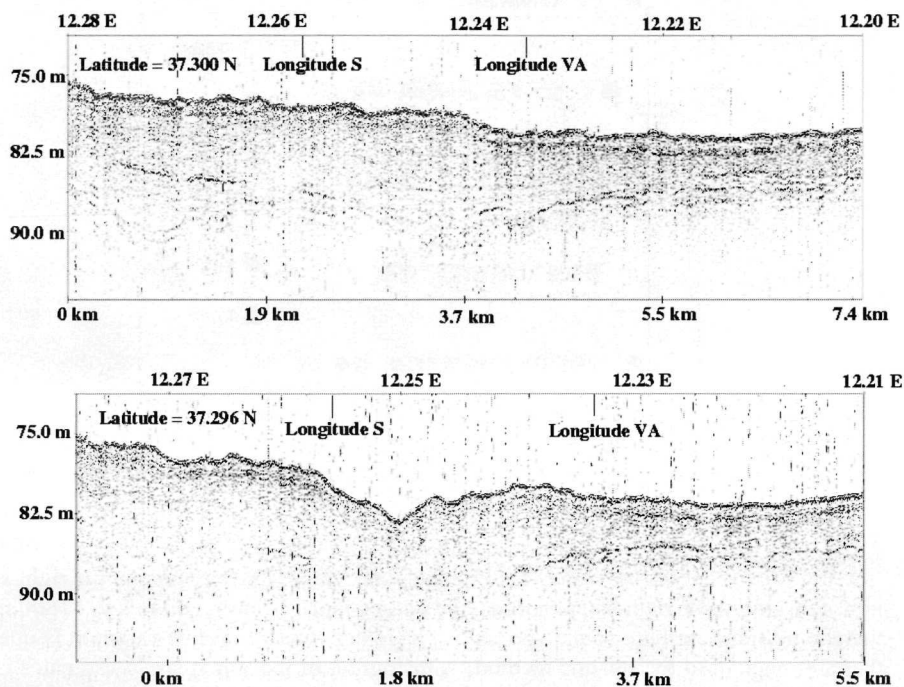


Fig. 7 Bottom layering as derived from seismic measurements on part of leg 3 (upper plot) and part of leg 4 (lower plot). The variable along the y-axis is depth in meters, whereas position is along the x-axis. For reference also the longitudes of the source (S) and vertical array (VA) positions are indicated.

When estimating sound speeds from the seismic data use is made of reflections that correspond to a strong reflector. If there are several strong reflectors in the bottom, then the sound speed as a function of depth can be estimated.<sup>5</sup> However, with the seismic data presented here, only one strong reflector could be identified for the majority of the data. Therefore, we only consider layer thicknesses and sound speeds that are estimated for this one reflector. This reflector does not necessarily correspond to the upper layer. Note that the estimated sound speeds represent a value averaged over the layer thickness.

Figures 8 and 9 show the thin layer thicknesses and corresponding thin layer sound speeds as a function of geographical position for the full area of the seismic survey. The results for the full area are presented here as then possible systematic changes in bottom properties can be seen. However, no trends in thin layer thickness are visible. In the area surrounding the source and the vertical array, the thin layer thickness ranges from  $\sim 2$  m to  $\sim 10$  m, i.e.,  $(6 \pm 4)$  m/s.

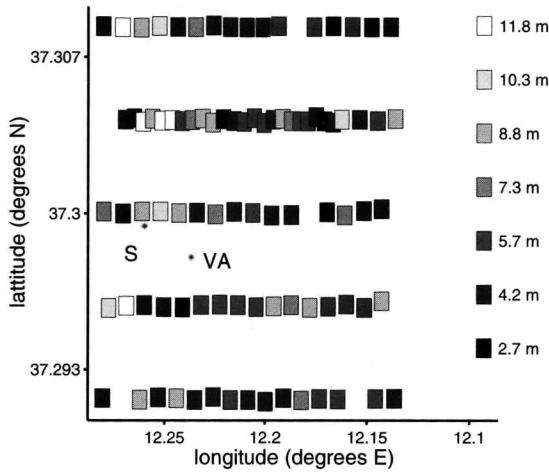


Fig. 8 Thin layer thickness as a function of geographical position. Stars are used for indicating the source (S) and vertical array (VA) position.

As with the thin layer thickness, no trends can be identified in the thin layer sound speeds (see Fig. 9), except for the somewhat higher sound speeds ( $> 1620$  m/s) at the right side of the plot. Ignoring these high sound speeds, the values range from  $\sim 1500$  m/s to  $\sim 1600$  m/s. Since there is no trend in these sound speeds, we have concluded that this variation is due to errors that are inherent to the seismic method. A histogram of the sound speed estimates is given in Fig. 10, thereby treating the sound speeds as independent observations of the same quantity. The histogram contains all sound speed estimates except those higher than 1620 m/s. A Gaussian fit is applied to these data. The mean and standard deviation of the Gaussian curve is 1552 and 31 m/s, respectively.

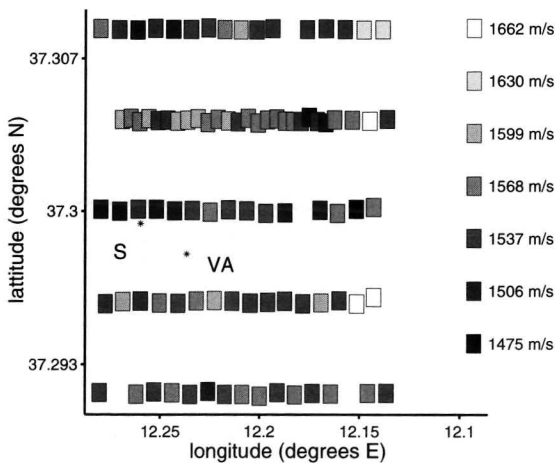


Fig. 9 Thin layer sound speed as a function of geographical position. Stars are used for indicating source (S) and vertical array (VA) positions.

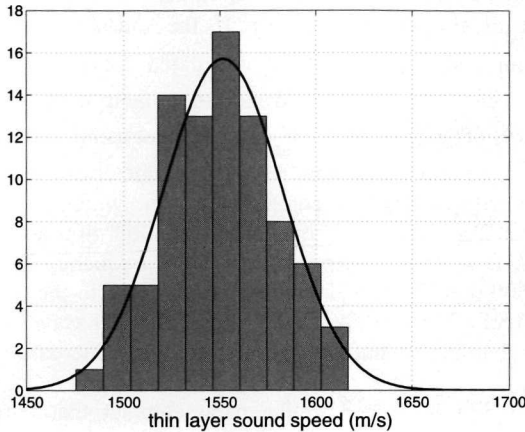


Fig. 10 A histogram of the thin layer sound speeds as estimated from the multi-channel seismic analysis. The black line indicates a Gaussian fit to the histogram.

#### 6.2.2.4 Additional ocean environmental measurements

In addition to the environmental measurements described above, also bathymetry measurements, waverider measurements and Acoustic Doppler Current Profiler (ADCP) measurements were carried out.

The bathymetry of the trial area was measured with the echosounder of *Alliance*. There was virtually no variation in water depth along the 2 km track with a depth of 77 m at the source position and 79 m at the VA position.

The sea surface wave height spectrum was measured by a waverider. The root-mean-squared wave height during the 2 km experiment was 0.15 m.

The ADCP measurements were collected by two bottom-moored ADCP's and a ship mounted ADCP. The bottom-moored ADCP's were put close to the positions of the VA. Tidal oscillations are found to be the dominant current signals. The ADCP current data are used for validation of the VA tilt estimates (see Section 6.4.1.3).

## 6.3 Acoustic inversion method

For the forward acoustic model we have applied the standard normal-mode technique.<sup>7,8</sup> The sediment layer and the sub-bottom are treated as fluid layers and the high loss continuous eigenvalue spectrum is ignored. In Section 6.3.1 the objective function to be minimized is described. In Section 6.3.2 we present details on the applied global optimization method, and in Section 6.3.3 we describe the acoustic problem.

### 6.3.1 The objective function

The objective (or energy) function gives a quantitative measure for the agreement between the calculated and measured acoustic fields. We have selected the following objective function  $E$ , which is based on the incoherent multi-frequency Bartlett processor<sup>8,9</sup>

$$E(\mathbf{m}) = 1 - \frac{1}{K} \sum_{k=1}^K \left| \mathbf{p}_{obs}(f_k) \cdot \mathbf{p}_{calc}^*(f_k, \mathbf{m}) \right|^2 \quad (2)$$

with  $\mathbf{m}$  the vector containing the unknown parameters,  $K$  the number of frequencies, “.” indicating the inner product of the vectors  $\mathbf{p}_{obs}(f_k)$ , the measured pressure field at frequency  $f_k$ , and  $\mathbf{p}_{calc}(f_k, \mathbf{m})$ , the pressure field calculated for parameter set  $\mathbf{m}$  and frequency  $f_k$ . Both pressure vectors are normalized such that their norm equals one, i.e.,  $\|\mathbf{p}_{obs}\| = \|\mathbf{p}_{calc}\| = 1$ . From previous experience<sup>8,10</sup> it is known that using multiple frequencies for the inversion results in more accurate and more realistic parameter estimates compared to single-frequency inversion. In order to limit the computation time, which increases quadratic with frequency, we have selected a subset of frequencies (200, 300, 400 and 600 Hz) to be used for the inversions, i.e.,  $K$  is 4. This covers sufficiently the frequency band transmitted: for a water sound speed of 1500 m/s, the wavelengths corresponding to the frequency subset range from 7.5 m to 2.5 m. Including 700 Hz would give a shortest wavelength of 2.1 m, which is only slightly smaller than 2.5 m, but would result in a large increase in computation time.

Minimizing the energy function will lead to the parameter set that corresponds to a simulated pressure field  $\mathbf{p}_{calc}(f_k, \mathbf{m})$  having maximum similarity with the measured pressure field  $\mathbf{p}_{obs}(f_k)$ .

### 6.3.2 The genetic algorithm

The objective function given in the previous section is a function of many unknown variables, usually in the order of 10, and with many local optima. Finding the global optimum of such a function requires global optimization methods such as simulated annealing and genetic algorithms. We have applied a genetic algorithm (GA) for finding the minimum of the objective function. The application of a GA in underwater acoustics was introduced by Gerstoft.<sup>11</sup> Specifics about the GA applied here can be found in previous work.<sup>8</sup> The basic principle of a GA is summarized below.

First an initial population, consisting of  $q$  possible solutions to the problem, is created randomly. This population is the so-called first generation. Out of this initial population elements are selected for establishing a parental population. The selection is such that the most fit members of the initial population, i.e., those with the lowest value for the objective function, have the highest probability of being selected. The elements of the parental population are converted to encoded form such that the numerical values are represented by a string of zeros and ones (bits). This string is called a chromosome and the different parts on the chromosome, that all represent a particular parameter, are called the genes. By applying the operators crossover and mutation to the elements of the parental population, a new population, denoted by children population, is created. The crossover operator results, for each gene, in an exchange between two parents of a (random) fragment of the gene. Crossover occurs with crossover probability  $p_c$ . Mutation results in a change of a single bit and occurs with mutation probability  $p_m$ .

A next generation is created by replacing the  $f_r q$  least fit members of the first generation by  $f_r q$  members of the children population. The latter are selected at random.  $f_r$  is called the reproduction size ( $0 < f_r < 1$ ) and is an important parameter of the GA to be set.<sup>8</sup> We have taken  $q = 64$ ,  $f_r = 0.5$ ,  $p_c = 0.8$  and  $p_m = 0.05$ .

By repeating the above-described process, the successive generations become increasingly fit. This process is continued until the optimization process has converged. Convergence is established by taking at least 400 generations, resulting in 12832 forward acoustic model runs per frequency. For better exploitation of the search space around the global optimum and for diminishing the risk of ending up in a local minimum, 5 independent GA runs are carried out (i.e.,  $12832 \times 5 \times 4 = 256640$  forward runs per pressure field). As we have selected a population size  $q$  of 64, each set of 5 GA runs ends up with 320 parameter sets. From these parameter

sets, the one that corresponds to the lowest energy function value is selected. This parameter set is denoted by  $GA_{\text{best}}$  and is taken to be the solution of the optimization.

### 6.3.3 The acoustic problem

As mentioned in the introduction an important application of MFI is geo-acoustic parameter estimation. However, in general, other parameters also need to be optimized as they have an important influence on the propagation, but are not known accurately enough. In this section the parameters included in the inversion are discussed.

Since the bathymetry along the 2 km acoustic track was found to be fairly range-independent (Section 6.2.2.4) we assume a constant water depth. Due to slight variations in water depth and offsets in the echosounder measurements the water depth  $H_w$  is not known exactly and has to be included in the optimization.

The geo-acoustic model selected consists of a single sediment layer with thickness  $h_{\text{sed}}$ , overlying a homogeneous sub-bottom. Justification for the single sediment layer assumption is obtained from literature.<sup>12</sup> Here it was found that inversions of synthetic data, calculated for a multi-layer bottom, and using a two-layer model for the forward calculations, resulted in properties of the two-layer bottom that fitted the properties of the actual multi-layer model reasonably well.

The sediment compressional wave speed is assumed to vary linearly with depth from  $c_{1,\text{sed}}$  at the top of the sediment to  $c_{2,\text{sed}}$  at the bottom of the sediment, and to have a constant value  $c_b$  in the sub-bottom. The attenuation constant  $\alpha$  and density  $\rho$  are taken depth-independent through both the sediment and the sub-bottom. Shear is not taken into account. Shear speed effects and the justification for not including it in the inversion are discussed in Section 6.4.1.1.

Due to irregularities at the sea bottom the depth of the array is not known precisely. Further, currents can result in a tilt of the array in some direction. Assuming that the effect of a tilt in the azimuth direction can be accounted for by an effective tilt  $\theta$  in the plane of propagation, the array configuration is completely defined by estimating  $h_1$ , which is the distance of the deepest hydrophone to the bottom, and the array tilt  $\theta$ .

The source range,  $r_s$ , and the source depth, here defined by the distance from the source to the bottom  $\Delta$ , have a large influence on the acoustic propagation and are not known to the required accuracy. The baseline values of  $r_s$ ,  $\Delta$  and  $h_1$  are 2040, 4 and 9.5 m, respectively.

In Fig. 11 the resulting parameterization for the ocean environment and the 11 unknown parameters are shown. The sound speed profile used for the inversions is the sound speed profile that corresponds to the CTD taken from the NRV *Alliance* on May 2, 12:20 UTC, i.e., 17 minutes prior to the execution of the experiment (see Fig. 4).

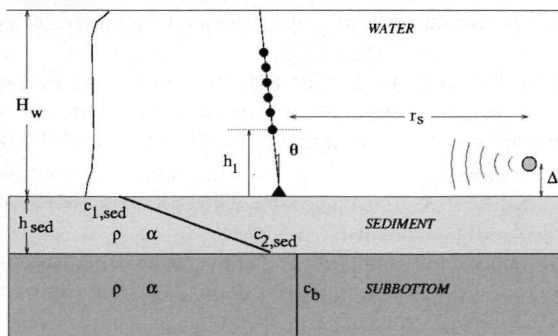


Fig. 11 The parameters to be optimized.

Table I lists the unknown parameters and their search bounds.

Table I The unknown parameters, their symbols and search bounds.

Parameter	Symbol	Search bounds
Upper sediment sound speed (m/s)	$c_{1, sed}$	[1475 1700]
Sediment thickness (m)	$h_{sed}$	[1 25]
Lower sediment sound speed (m/s)	$c_{2, sed}$	[1475 1800]
Sub-bottom sound speed (m/s)	$c_b$	[1515 1900]
Density ( $g/cm^3$ )	$\rho$	[1 2.3]
Attenuation constant (dB/ $\lambda$ )	$\alpha$	[0 1]
Source range (m)	$r_s$	[1700 2500]
Distance source to bottom (m)	$\Delta$	[0 10]
Tilt (degr)	$\theta$	[-10 10]
Water depth (m)	$H_w$	[75 85]
Distance lowest hydrophone to bottom (m)	$h_1$	[7.5 12.5]

## 6.4 Results and discussion

The inversion was carried out for 41 pressure fields. These pressure fields were determined from 2-second snapshots of acoustic data differing in transmission time by approximately 15 minutes and spanning the entire 2 km experiment (about 8 hours). The absolute values of the selected pressure fields are plotted in Fig. 2.

Figure 12 presents the results of the inversions. For each parameter a plot of the 41 succeeding  $GA_{best}$  estimates is given. The lower right subplot shows the corresponding energy function values. The y-axes ranges of the plots are equal to the search bounds for the unknown parameters. The variable along the x-axes is UTC time. Note the behavior of the  $GA_{best}$  energy function  $E$  as a function of time. This must be due to temporal oceanographic variations, which are not taken into account in the inversions as we use a single sound speed profile for the forward calculations in all inversions.

Since the experimental configuration is stationary, all unknown parameters (except for the tilt, which might vary due to varying currents) should be constant with time. Therefore, the inversion results can be used for determining the mean and standard deviations for each parameter. Assuming statistically independent observations, also the uncertainty (or error) on the mean ( $\sigma_{mean}$ ) and the uncertainty (or error) on the standard deviation ( $\sigma_{std}$ ) can be determined by

$$\sigma_{mean} = \frac{std}{\sqrt{N}} \quad (3)$$

$$\sigma_{std} = \frac{std}{\sqrt{2N}}$$

with  $N$  the number of observations (here equal to 41), and  $std$  the standard deviation of the  $N$  observations. The errors on the mean and standard deviation must be accounted for, since the number of observations  $N$  is quite small (see Section 6.4.1.1).

In Table II the values for the means and standard deviations, and their uncertainties, are listed. Hereafter we further assess the estimates for the different parameters.



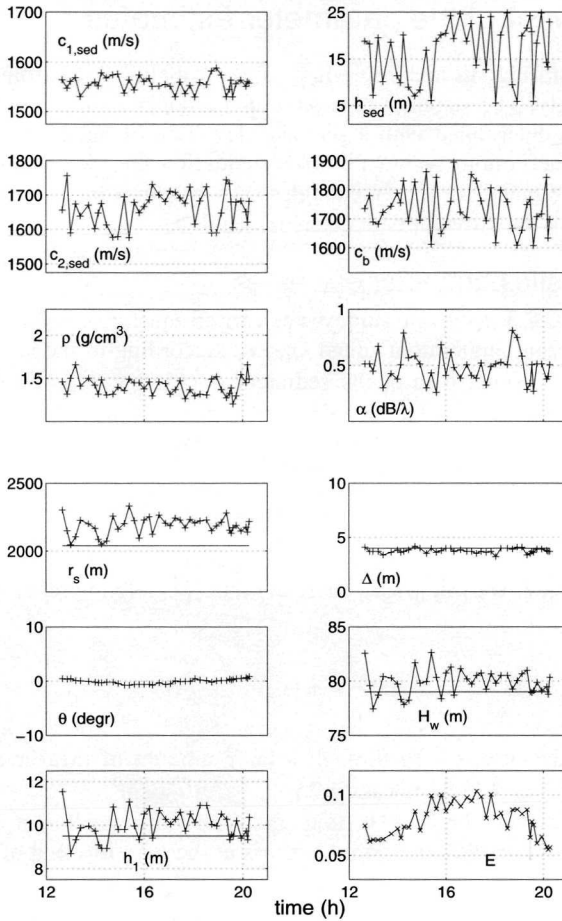


Fig. 12 Parameter estimates ( $GA_{best}$ ) and corresponding energy function values as obtained from inversions of the experimental data. The horizontal solid lines in 4 of the subplots indicate measured values, where for the water depth the depth at the vertical array position (79 m) is used.

Table II The means and standard deviations (and their uncertainties) of the inversion results of Fig. 12. The last column lists for the geometrical parameters the true measured values.

Parameter	Mean ( $\sigma_{mean}$ )	Std ( $\sigma_{std}$ )	True measured values
$c_{1, sed}$ (m/s)	1556.3 (2.3)	14.8 (1.6)	
$h_{sed}$ (m)	16.49 (0.99)	6.36 (0.70)	
$c_{2, sed}$ (m/s)	1663.1 (7.6)	48.8 (5.4)	
$c_b$ (m/s)	1734.6 (11.9)	75.9 (8.4)	
$\rho$ (g/cm <sup>3</sup> )	1.405 (0.016)	0.101 (0.011)	
$\alpha$ (dB/ $\lambda$ )	0.482 (0.021)	0.134 (0.015)	
$r_s$ (m)	2186 (10)	65.3 (7.2)	2040
$\Delta$ (m)	3.772 (0.034)	0.215 (0.024)	4.0
$H_w$ (m)	79.89 (0.18)	1.16 (0.13)	77-79
$h_1$ (m)	10.00 (0.10)	0.646 (0.071)	9.5

## 6.4.1 Assessment of the parameter estimates

From the results presented in Fig. 12 and Table II it can be concluded that some parameters are estimated very accurately. The standard deviation of the upper sediment sound speed is only 15 m/s, the density is determined with a standard deviation of only 0.1 g/cm<sup>3</sup> and the distance of the source to the bottom within 0.2 m. Considering the tilt estimates it can be concluded that the tilt is estimated accurately enough to resolve for a trend. In the following we examine the estimates for the different parameters in detail.

### 6.4.1.1 Geo-acoustic parameter estimates

As mentioned in Section 6.2.2.3 a seismic survey was carried out for obtaining independent information on bottom layering and bottom sound speeds. According to the seismic analysis the mean sound speed in the upper 6 m of the sediment is (1552 ± 31) m/s. The inverted values for  $c_{1, sed}$  (1556 m/s),  $h_{sed}$  (16 m) and  $c_{2, sed}$  (1663 m/s) give a mean sound speed value of 1576 m/s over the upper 6 m of sediment. It can thus be concluded that this inversion result is in very good agreement with the seismic measurements.

Considering its large search interval (1.0-2.3 g/cm<sup>3</sup>), the density is reasonably well resolved within 0.1 g/cm<sup>3</sup> (in agreement with other findings<sup>11,12</sup>). In Fig. 13 sediment sound speed and density values are plotted for different types of continental shelf sediment. In this figure also an empirical curve is shown, giving the relation between (compressional) sediment sound speed  $c_p$  and density  $\rho$

$$c_p = 2330.4 - 1257 \cdot \rho + 487.7 \cdot \rho^2 \pm 33 \text{ m/s} \quad (4)$$

This expression has been derived as a fit through a large amount of measurements.<sup>13</sup> The expression is valid for  $1520 < c_p < 1840$  m/s and  $1.25 < \rho < 2.10$  g/cm<sup>3</sup>.

The inverted sediment density ( $1.41 \pm 0.10$  g/cm<sup>3</sup>) and upper sediment sound speed (1556.3 m/s) values satisfy the above expression, but it is at the very low end of the brackets (see star in Fig. 13). We feel confident about our estimation of sediment sound speed as it is in agreement with independent seismic measurements and therefore we think the error is on the density. From the expression given above, and taking into account the error of 33 m/s, the inverted sediment sound speed should correspond to a density of  $1.56 \pm 0.12$  g/cm<sup>3</sup>, instead of the optimized density of 1.41 g/cm<sup>3</sup>.

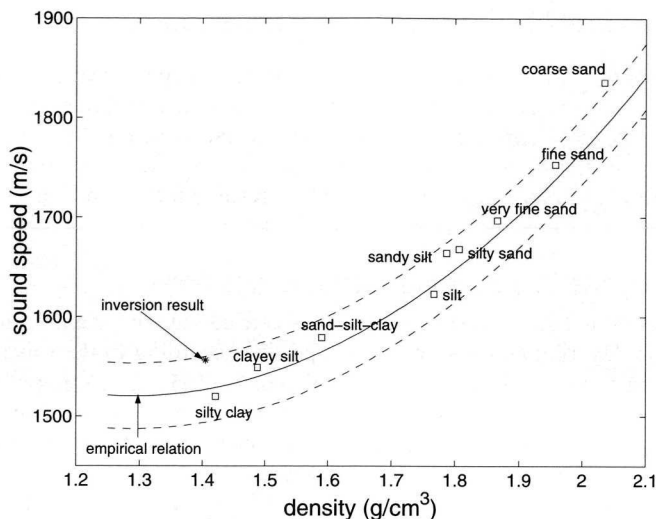


Fig. 13 Sound speeds and densities for continental shelf sediments. Also plotted is an empirical curve that gives the relation between sediment sound speed and density.<sup>13</sup> The star indicates the inversion result.

This deviation can be an indication for the presence of shear waves, as neglecting the effect of shear is accounted for by an effective density.<sup>14,15</sup> This is expressed through the following relation between actual density  $\rho$ , shear speed  $c_s$  and an effective density  $\rho_{eff}$

$$\rho_{eff} = \rho \left[ 1 - 2 \left( \frac{c_s}{c_w} \right)^2 \right]^2 \quad (5)$$

with  $c_w$  the sound speed in the water. Employing this expression, a sediment density of  $1.56 \pm 0.12 \text{ g/cm}^3$  and an effective sediment density of  $1.405 \pm 0.101 \text{ g/cm}^3$  are found to correspond to a shear speed of  $241 \pm 121 \text{ m/s}$ . This basically means that shear cannot be inverted for as the presence of shear results in an effective density. This is illustrated in Figs. 14 - 15 where the complex reflection coefficient<sup>7</sup> is plotted as a function of incident grazing angle for homogeneous bottoms with a compressional wave speed of  $1556.3 \text{ m/s}$  and attenuation constant of  $0.5 \text{ dB}/\lambda$  and with values for the density and the shear speed as listed below.

- BOTTOM1:  $\rho = 1.56 \text{ g/cm}^3$ ,  $c_s = 0 \text{ m/s}$
- BOTTOM2:  $\rho = 1.56 \text{ g/cm}^3$ ,  $c_s = 241 \text{ m/s}$
- BOTTOM3:  $\rho = 1.41 \text{ g/cm}^3$ ,  $c_s = 0 \text{ m/s}$

BOTTOM1 is included for illustration: comparing the results for BOTTOM1 and BOTTOM2 shows the influence of shear speeds. The reflection coefficient for BOTTOM2 and BOTTOM3 (both the absolute value and the phase shift) virtually coincide, which demonstrates that the effect of shear is compensated by a decrease in density as given by Eq. (5).

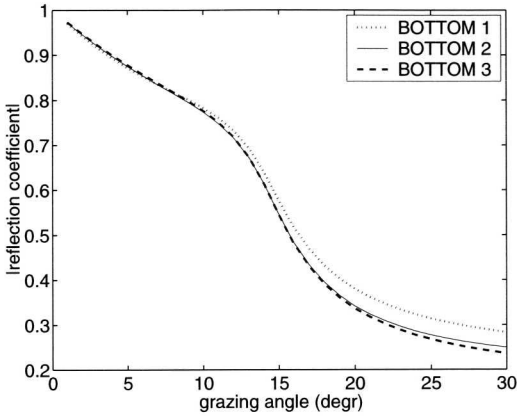


Fig. 14 Magnitude of the reflection coefficient versus angle for BOTTOM1, BOTTOM2 and BOTTOM3. Note that the curves for BOTTOM2 and BOTTOM3 virtually coincide.

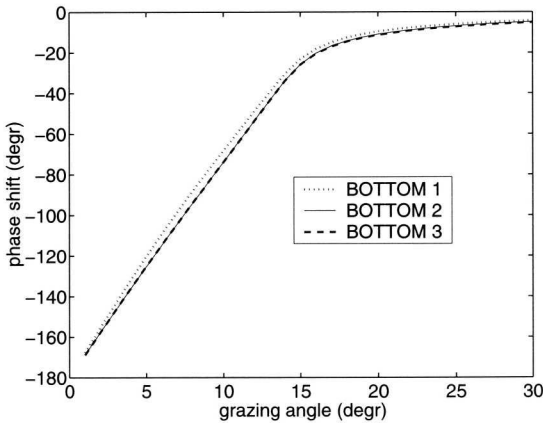


Fig. 15 Phase shift of the reflection coefficient versus angle for BOTTOM1, BOTTOM2 and BOTTOM3. Note that the curves for BOTTOM2 and BOTTOM3 virtually coincide.

Another method for estimating shear speeds is to apply the following regression equation<sup>16</sup>, relating shear speed  $c_s$  (in m/s) to compressional wave speed  $c_p$  (also in m/s)

$$c_s = 1.137 \cdot c_p - 1485 \tag{6}$$

This equation is valid for  $1555 < c_p < 1650$  m/s.

From this equation a shear speed value of  $285 \pm 17$  m/s is calculated for a compressional wave speed of  $(1556.3 \pm 14.8)$  m/s. The two derived values for the shear speed, viz.  $241 \pm 121$  m/s and  $285 \pm 17$  m/s, are in agreement and are therefore considered to be reliable indicative estimates for the sediment shear speed. Note that due to their similar effects on the reflection coefficient, it will not be possible to unambiguously estimate both the density and the shear speed simultaneously through inversion.

The sediment attenuation constant is not well resolved, but remains within the bounds of  $0.25 \text{ dB}/\lambda$  and  $0.81 \text{ dB}/\lambda$ , corresponding roughly to the values for clay and sand.<sup>7</sup>

Parameter  $h_{sed}$  should be interpreted carefully. The multi-layer structure of the bottom is not included in the geo-acoustic model. However, from the seismic data analysis we know that, in reality, the sediment has some internal layering and is not made up of a single layer (see Fig. 7). Also, the layer's thicknesses are not independent of range (as assumed in the inversions).  $h_{sed}$  represents a breakpoint, setting a depth in the bottom below which the bottom is considered homogeneous and above which it fits the sound speed gradient determined by  $c_{1, sed}$  and  $c_{2, sed}$ . No independent measurements are available for the sediment thickness  $h_{sed}$  since from the seismic data no clear reflector that marks the boundary between sediment and sub-bottom could be identified. The parameter is highly undetermined, as the optimized values for  $h_{sed}$  comprise nearly the entire search space. From the inversion results we found the two parameters  $h_{sed}$  and  $c_{2, sed}$  to be strongly correlated. This indicates that these parameters do have an influence on the propagation, but that they cannot be estimated separately. Parameter correlation is illustrated in Fig. 16 in which the 41 final parameter estimates are plotted against each other. Ten parameter combinations with strong coupling are shown here.

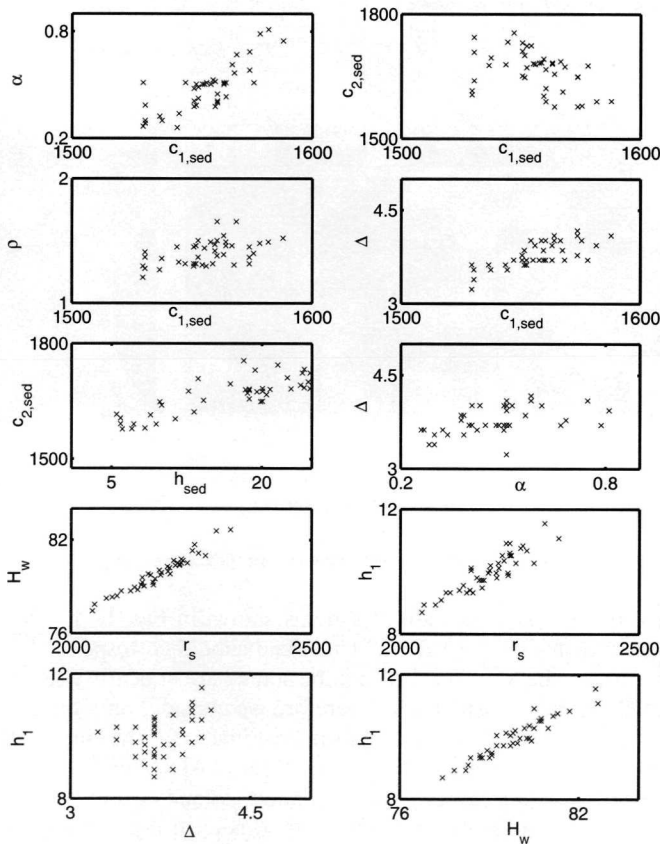


Fig. 16 Final parameter estimates plotted against each other for 10 parameter combinations with strong coupling.

It is clearly observed from this figure that some parameters, such as  $h_{sed}$  and  $c_{2, sed}$ , are highly correlated. Avoiding parameter coupling possibly requires a completely different parameterization of the environment<sup>11,17,18,19</sup> (e.g. inverting for the sediment sound speed

gradient and  $h_{sed}$ , instead of  $h_{sed}$  and  $c_{2,sed}$ ). The full parameter coupling of the inversion problem is illustrated in Fig. 17, which shows the magnitude of the linear correlation coefficient calculated for all combinations of parameter estimates. It is emphasized that these calculated values for the linear correlation coefficient are based on a fairly limited number of data pairs (41), i.e., also the statistical significance of each of the correlation coefficient values was determined. The stars in Fig. 17 indicate for which parameter combination the confidence of the calculated correlation coefficient exceeds 95%.<sup>20</sup> For instance, the correlation coefficient between  $\Delta$  and  $H_w$  is 0.34 with a confidence of 96.9%, i.e., there is a probability of 3.1% that the observed correlation can occur between two random (uncorrelated) data sequences of length 41. Correlation coefficients greater than 0.5 have a confidence of at least 99.98%. The advantage of re-parameterization of the environment in this specific inversion problem is subject to further research.

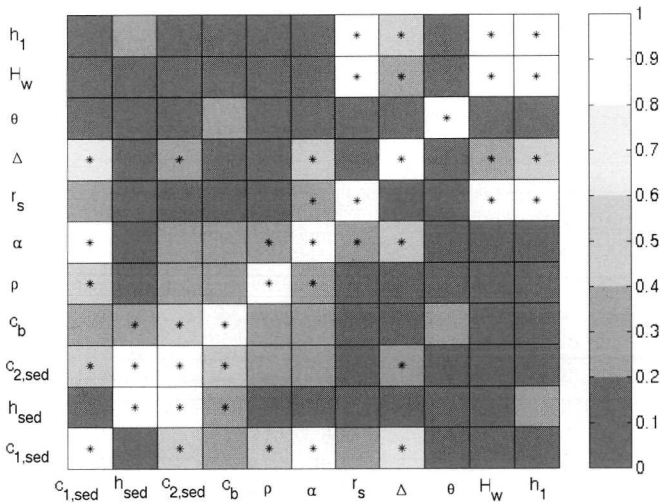


Fig. 17 The correlation coefficient for all parameter combinations.

#### 6.4.1.2 Array tilt estimates

From the parameter estimates as a function of time as shown in Fig. 12 it can be seen that there is a trend in the estimates for the VA tilt. This trend should correspond to some similar trend in the currents close to the VA. The VA and the source are at nearly equal latitudes and we consider array tilt along the acoustic track. Therefore we consider only the east/westwards directed currents. In Fig. 18 we have plotted both the estimates for the tilt and the eastward component of the currents as measured by the bottom moored ADCP at a depth of 27 m. The tilt is positive in eastward direction (towards the tower source) and negative westwards (away from the tower source). This also holds for the currents. It is clear that the current and the tilt are in excellent agreement as they show a very similar trend. This indicates that the inverted tilt estimates are reliable.

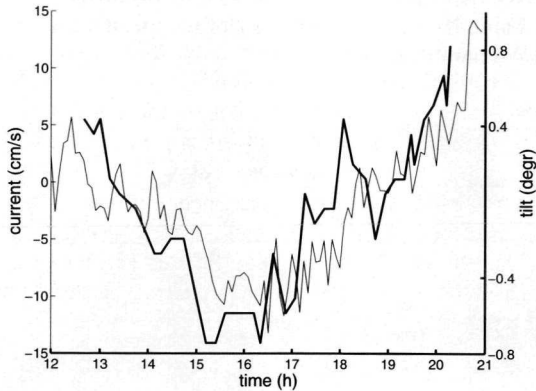


Fig. 18 Eastward current (thin solid line) and tilt estimates (thick solid line) as a function of UTC time.

### 6.4.1.3 Geometrical parameter estimates

From Fig. 12 and Table II it can be seen that for the geometrical parameters, i.e.,  $r_s$ ,  $\Delta$ ,  $H_w$  and  $h_l$ , the inverted values are in good agreement with the true values, especially when considering the uncertainty (standard deviation) in these parameter estimates. The true range, being 2040 m as calculated from the navigation data, slightly deviates from the mean inversion result. This can be partly ascribed to a difference between the DGPS positions of the ship at the time of source and VA deployment and the final source and VA position.

The water depth, the source range and the distance of the deepest hydrophone to the bottom are strongly correlated (see Fig. 17). This can explain the minor differences between true and inverted values. Neglecting the variations in water depth over the acoustic track in the inversions will result in an effective water depth. It is known that there is a small variation in water depth over the 2 km acoustic track (from 77 at the source to 79 m at the VA). Therefore, the estimates for the geometrical parameters that correspond to the resulting effective water depth might deviate from their actual values. In the next section it is shown that also oceanographic variability can result in a shift of geometrical parameter values.

### 6.4.2 Assessment of the parameter uncertainties

As mentioned before, there are two main origins for the variations in the parameter estimates. The first origin is the method itself. The second is oceanographic variability. The contribution of both is determined through simulation and is presented and discussed in this section. Other contributions to the uncertainty can be due to a low signal to noise ratio, e.g. due to noise of passing ships, and wrong parameterization. As the signal to noise ratio was very high its contribution to the uncertainty is negligible. We will demonstrate that the above-mentioned two main origins can fully explain the obtained parameter uncertainties. Wrong parameterization will not be considered here.

The contribution of the method to the parameter uncertainty was determined through the repetitive inversion (41 times) of a simulated pressure field, i.e., 41 optimization runs were performed on the same synthetic pressure field. As a genetic algorithm is a Monte Carlo search method, this approach requires the use of a different random seed for each of these 41 optimization runs. The parameters used for creating this synthetic field are values close to the mean parameter values obtained from inversion of the experimental data. This simulation is further denoted as SIM1. The results of these inversions can be found in Fig. 19. Also shown are the true values (solid horizontal lines) and the means of the inversion results (dashed

horizontal lines). For all parameters, except for  $h_{sed}$ ,  $c_{2, sed}$  and  $c_b$ , the mean values virtually coincide with the true values. In Table III the deviation  $\delta_{mean}$  of the mean values from the true values is listed together with the standard deviations.

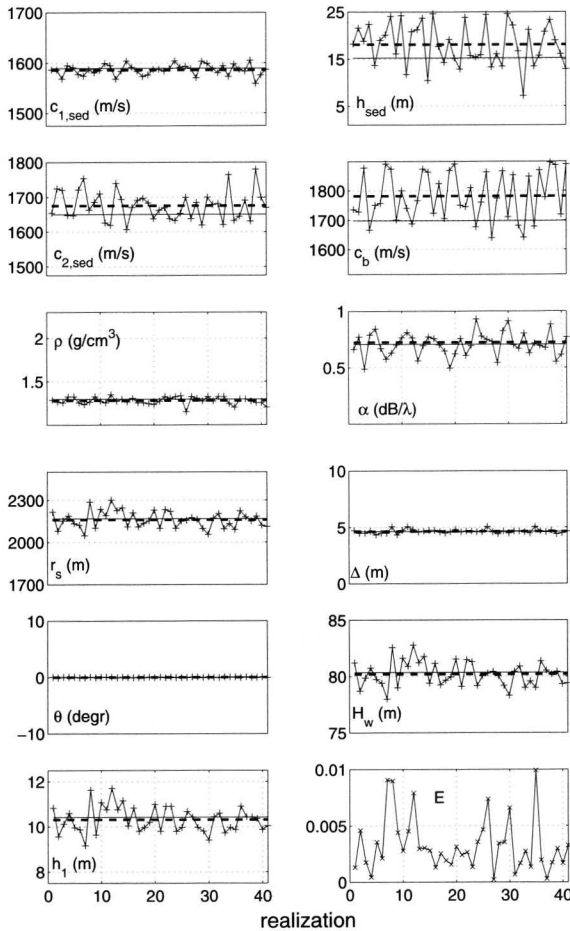


Fig. 19 Parameter estimates and corresponding values for the energy function (lowest, most right subplot) as obtained from inversions of synthetic data (SIM1). The dashed horizontal lines are the mean values, whereas the solid horizontal lines indicate the true values.

In Fig. 20 the standard deviations of the parameter estimates ( $std$ ) are plotted, both for the experimental data inversion results and the simulation. The uncertainties in the standard deviation ( $\sigma_{std}$ ), representing the statistical error, are also plotted in the figure as error bars. By dividing both by the appropriate search bounds a direct comparison between parameter uncertainties can be made. The parameter tilt is not considered as in the experimental configuration the tilt varies, whereas it is constant in the simulation. In the figure also the relative standard deviation for uniformly distributed parameter values (being equal to  $1/\sqrt{12}$ ) is plotted (horizontal dashed line). Parameters whose standard deviation divided by the search bound approach this value are badly determined: they have a uniform distribution over the entire search area. From Fig. 20 it can be seen that this is the case for the sediment thickness as determined from the experimental data. It can be concluded that for  $c_{2, sed}$ ,  $c_b$ ,  $r_s$  and  $\Delta$ ,  $H_w$  and  $h_1$ , the uncertainties in the inversion results for the experimental and the synthetic data



coincide within the statistical error. Hence, for these parameters the uncertainties can be completely ascribed to the method itself. For the remaining parameters the additional uncertainty should be caused by oceanographic variability. Note, however, that also for these parameters a significant part of the uncertainty stems from the method itself.

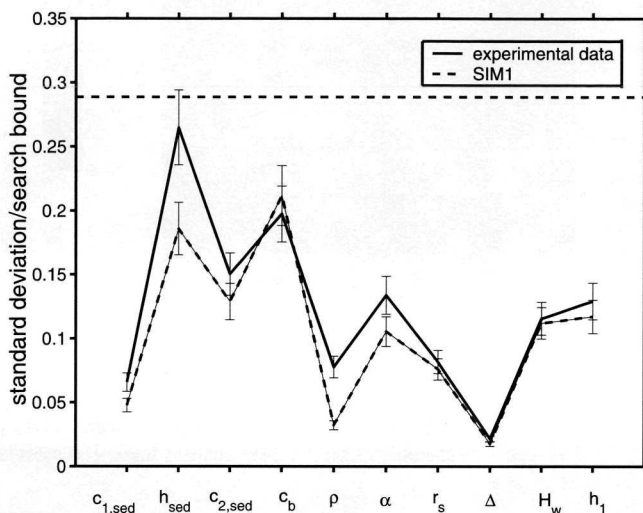


Fig. 20 The standard deviations and their statistical errors divided by the appropriate search bounds, for all parameters except for the tilt, for both the experimental data and simulated data. The horizontal dashed line indicates the relative standard deviation for a uniform distribution ( $1/\sqrt{12}$ ).

From the CTD-chain measurements it is known that the sound speed profile varies with time (and range). For investigating the effect of these variations on the inversion results we have proceeded as follows: 41 sound speed profiles measured by the CTD-chain were selected on the 2 km acoustic track, i.e., in between  $12^\circ 15.588' E$  (source position) and  $12^\circ 14.207' E$  (VA position). The selected profiles, plotted in Fig. 21, represent realistic oceanographic variations on the 2-km acoustic track. For these 41 sound speed profiles, the corresponding pressure fields were calculated (for the 4 frequencies). For the unknown parameters we have taken the same values as those for SIM1. The spatial structure of the sound velocity field between source and receiver is not exactly accounted for in these calculations, as each of the 41 calculations is still range-independent.

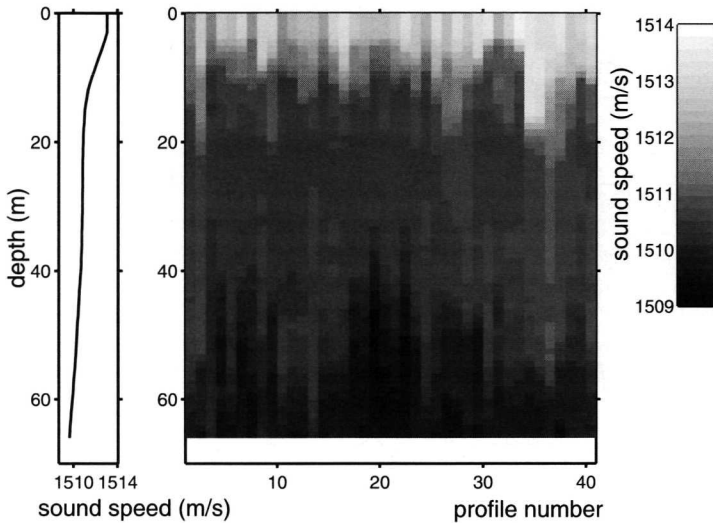


Fig. 21 The sound speed profiles for which synthetic pressure fields were calculated. The data are obtained from the CTD-chain measurements on the 2-km acoustic track. The most left plot shows the mean sound speed profile.

The resulting pressure fields were subsequently inverted. The sound speed profile used for the forward calculations is the mean of all profiles from the CTD-chain data as given in Fig. 5. This mean profile, also shown in Fig. 21, is obtained by simply taking the mean of all sound speeds at each depth. This simulation is further denoted as SIM2.

In Fig. 22 the resulting parameter estimates can be found. Also plotted are the true values (solid lines) and the means of all 41 estimates (dashed lines). The bottom, most right subplot shows the corresponding lowest energy function values. As for SIM1, Table III lists the deviation  $\delta_{\text{mean}}$  of the mean parameter estimates from the true values. Also given are the standard deviations.

From the results presented in Fig. 22 and Table III several conclusions can be drawn. Introducing oceanographic variability can result in a shift of parameter estimates. A more important effect of the oceanographic variability is an increase in the standard deviation for some parameters. This is illustrated in Fig. 23. Variability in the water column has resulted in a statistically significant increase of the standard deviation for the parameters  $c_{l, \text{sed}}$ ,  $\rho$  and  $\Delta$  (compare with Fig. 20). From this figure it can also be seen that now we have almost completely explained the uncertainty for all parameters. For  $h_{\text{sed}}$  and  $\rho$  the experimental data still show a statistically significant larger standard deviation compared to the simulations. This might be due to mismatch: in SIM2 the geo-acoustic model assumed is per definition correct. This is not true for the inversions of experimental data as, for example, we have assumed a single layer sediment. Further we have assumed the density and attenuation to be constant throughout the bottom, which is probably not true in reality.

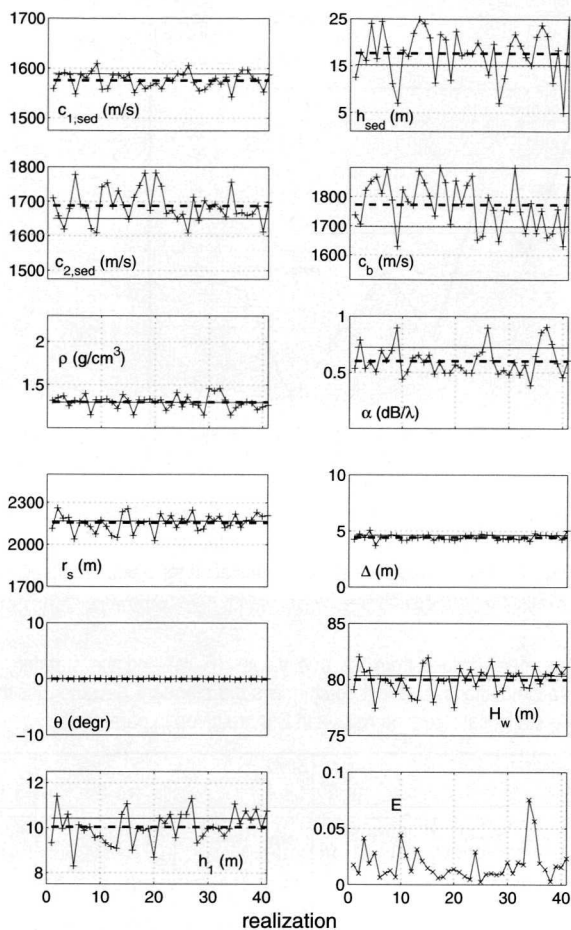


Fig. 22 SIM2 results: Parameter estimates and corresponding values for the energy function (lowest, most right subplot). Plotted as dashed lines are the means of the parameter values. The solid lines indicate the true values.

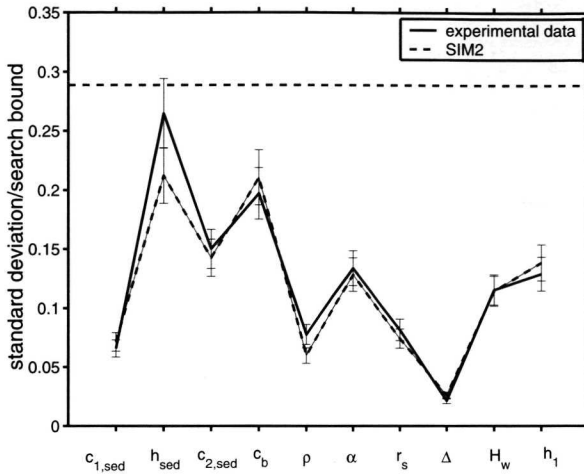


Fig. 23 The standard deviations and their statistical errors divided by the appropriate search bounds, for all parameters except for the tilt, for both the experimental data and for simulation SIM2. The horizontal dashed line indicates the relative standard deviation for a uniform distribution ( $1/\sqrt{12}$ ).

Table III The deviation of the mean values from the true values ( $\delta_{\text{mean}}$ ) and the standard deviation (Std) obtained for the two simulations. The last column lists the standard deviation for the experimental data inversions. The statistical errors on  $\delta_{\text{mean}}$  and Std are given in parentheses.

Parameter	True	SIM1		SIM2		EXP
		$\delta_{\text{mean}}$ ( $\sigma_{\text{mean}}$ )	Std ( $\sigma_{\text{std}}$ )	$\delta_{\text{mean}}$ ( $\sigma_{\text{mean}}$ )	Std ( $\sigma_{\text{std}}$ )	Std ( $\sigma_{\text{std}}$ )
$c_{1,\text{sed}}$ (m/s)	1588.9	-2.8 (1.7)	10.7 (1.2)	-12.9 (2.5)	16.0 (1.8)	14.8 (1.6)
$h_{\text{sed}}$ (m)	15.2	2.88 (0.70)	4.46 (0.49)	2.49 (0.80)	5.09 (0.56)	6.36 (0.70)
$c_{2,\text{sed}}$ (m/s)	1650.4	24.9 (6.5)	41.8 (4.6)	36.9 (7.2)	46.4 (5.1)	48.8 (5.4)
$c_b$ (m/s)	1698	84 (13)	81.4 (9.0)	75 (13)	81.2 (9.0)	75.9 (8.4)
$\rho$	1.292	-0.0154 (0.0065)	0.0418 (0.0046)	0.004 (0.012)	0.0777 (0.0086)	0.101 (0.011)
$\alpha$ (dB/ $\lambda$ )	0.724	-0.018 (0.016)	0.105 (0.012)	-0.123 (0.020)	0.128 (0.014)	0.134 (0.015)
$r_s$ (m)	2168	-7.4 (9.5)	60.7 (6.7)	-11.3 (9.3)	59.3 (6.6)	65.3 (7.2)
$\Delta$ (m)	4.63	-0.004 (0.028)	0.177 (0.020)	-0.190 (0.041)	0.260 (0.029)	0.215 (0.024)
$\theta$ (degr)	0.024	-0.0250 (0.0062)	0.0397 (0.0044)	-0.0192 (0.0078)	0.0498 (0.0055)	0.419 (0.046)
$H_w$ (m)	80.35	-0.16 (0.17)	1.12 (0.12)	-0.36 (0.18)	1.15 (0.13)	1.16 (0.13)
$h_t$ (m)	10.42	-0.104 (0.091)	0.585 (0.065)	-0.39 (0.11)	0.693 (0.077)	0.646 (0.071)

## 6.5 Summary and conclusions

In this paper we reported matched field inversion (MFI) results of multi-tone shallow water acoustic data that were obtained during the ADVENT99 sea trial. The multi-tone data were collected during an experiment with both the source and the receiver at a fixed position. The range between source and receiver was 2 km. In order to be able to assess the influence of oceanographic variability, the experiment was continued for as long as 8 hours. A genetic algorithm was applied as the global optimization method, whereas a normal-mode model was used for the forward propagation calculations. The parameters to be inverted, i.e., the unknown parameters, comprise both geo-acoustic and geometric parameters.

Many measurements were carried out for determining parameters of the ocean environment. These parameters are needed as input for the forward acoustic model and to obtain independent information about the unknown parameters (e.g. multi-channel seismic measurements for obtaining estimates of sediment thickness and sediment speed). The third objective of these environmental measurements is to monitor oceanographic variability. For this, a CTD-chain was towed back and forth over the acoustic track, thereby measuring sound speeds as a function of time and position. It was found that many of the unknown parameters could be estimated very accurately through inversion and that they are in good agreement with the independent measurements.

An important item addressed in this paper is the uncertainty of the parameter estimates. It is shown through simulation that the main part of this uncertainty stems from the method itself, as the optimization does not locate the exact global optimum and many of the parameters are correlated. Simulations including the water column variability, as determined from the CTD-chain measurements, show that for nearly all parameters the remaining uncertainties can be ascribed to this oceanographic variability.

## 6.6 Acknowledgements

The authors would like to thank all participants of the ADVENT99 sea trial, E. Michelozzi and P. Boni from SACLANT Centre in particular. Thanks are also due to the crews of NRV *Alliance* and INS *Ciclope*. The fruitful collaboration with Dr. M. Ainslie from CORDA is especially acknowledged. The authors further thank C. Mesdag and P. Frantsen from TNO-NIAG for performing the seismic experiments and subsequent seismic data analysis.

## References

- 1 P. Gerstoft, "Inversions of acoustic data using a combination of genetic algorithms and the Gauss-Newton approach," *J. Acoust. Soc. Am.*, **97** (4), 2181-2190 (1995).
- 2 F. Gingras and P. Gerstoft, "Inversion for geometric and geoacoustic parameters in shallow water: Experimental results," SR-229, SACLANT Undersea Research Centre, La Spezia, Italy (1994).
- 3 J. Sellschopp, M. Siderius and P. Nielsen, "ADVENT99, pre-processed acoustic and environmental cruise data," CD-35, SACLANT Undersea Research Centre, La Spezia, Italy (2000).
- 4 T. M. Siderius, M. Snellen, D.G. Simons and R. Onken, "An environmental assessment in the Strait of Sicily: Measurement and analysis techniques for determining bottom and oceanographic properties," *IEEE J. Ocean. Eng.* **25** (3), 364-387 (2000).
- 5 L. Hatton, M.H. Worthington, and J. Makin, *Seismic Data Processing, Theory and Practice* (Blackwell Science Ltd., 1986).
- 6 C.S. Mesdag and T.A.M. de Groot, *Seismic survey in the Strait of Sicily, part of the ADVENT99 cruise* (TNO-NIAG report, NITG 99-233-C, 1998).
- 7 F.B. Jensen, W.A. Kuperman, M.B. Porter and H. Schmidt, *Computational ocean acoustics* (American Institute of Physics, Inc., New York, 1994).
- 8 D.G. Simons and M. Snellen, "Multi-frequency matched-field inversion of benchmark data using a genetic algorithm," *J. Comp. Acoust.*, **6** (1&2), 135-150 (1998).
- 9 A. Tolstoy, *Matched Field Processing for Underwater Acoustics* (World Scientific Pub. Co., River Edge, New Jersey, 1993).
- 10 G. Haralabus and P. Gerstoft, "Variability of multi-frequency parameter estimates in shallow water," in Third European Conference on Underwater Acoustics, edited by J.S. Papadakis (Heraklion, Crete, 1996), Vol. I, pp. 355-360.
- 11 P. Gerstoft, "Inversion of seismoacoustic data using genetic algorithms and a *posteriori* probability distributions," *J. Acoust. Soc. Am.*, **95** (2), 770-782 (1994).
- 12 M. Siderius, P. Gerstoft and P. Nielsen, "Broadband geoacoustic inversion from sparse data using genetic algorithms," *J. Comp. Acoust.*, **6** (1&2), 117-134 (1998).
- 13 E. L. Hamilton and R. T. Bachman, "Sound velocity and related properties of marine sediments," *J. Acoust. Soc. Am.*, **72** (6), 1891-1904 (1982).
- 14 D. M.F. Chapman, P. D. Ward and D. D. Ellis, "The effective depth of a Pekeris ocean waveguide, including shear effects," *J. Acoust. Soc. Am.*, **85** (2), 648-653 (1989).
- 15 Z.Y. Zhang and C.T. Tindle, "Improved equivalent fluid approximations for a low shear speed ocean bottom," *J. Acoust. Soc. Am.*, **98** (6), 3391-3396 (1995).
- 16 E. L. Hamilton, " $V_p/V_s$  and Poisson's ratios in marine sediments and rocks," *J. Acoust. Soc. Am.*, **66** (4), 1093-1101 (1979).
- 17 P. Gerstoft, "Global inversion by genetic algorithms for both source position and environmental parameters," *J. Comp. Acoust.*, **2**, 251-266 (1994).
- 18 M.D. Collins and L. Fishman, "Efficient navigation of parameter landscapes," *J. Acoust. Soc. Am.*, **98** (3), 1637-1644 (1995).
- 19 C.A. Zala and J.M. Ozard, "Estimation of geoacoustic parameters from narrowband data using a search-optimization technique", *J. Comp. Acoust.*, **6** (1&2), 223-243 (1998).
- 20 J.S. Bendat and A.G. Pierson, *Random data: analysis and measurement procedures* (John-Wiley & Sons (1971)), 125-129.

## Chapter 7

# Application of the downhill simplex algorithm to reduce the uncertainty in matched field inversion results<sup>D</sup>

## Abstract

In this paper an assessment of the accuracy of unknown geo-acoustic and geometric parameter estimates, obtained through matched field inversion, is presented. This work is a sequel of work presented earlier [J. Acoust. Soc. Am. **109** (2), 514-527 (2001)], where use was made of a genetic algorithm for the inversion of multi-frequency experimental data. The inverted signals were transmitted by a fixed source and received on a vertical array at a distance of 2 km from the source. The parameter uncertainties are assumed to originate from several distinct causes, i.e., the imperfect optimization method, temporal oceanographic variability, and noise in the data. The influence of the first two causes is evaluated through simulations comprising sets of synthetic data. It is shown that through the additional use of the downhill simplex method as a local optimization method, the parameter uncertainties are reduced significantly compared to that when applying a genetic algorithm only. At the same time, applying the downhill simplex method reveals that the temporal oceanographic variability cannot account for all uncertainty. The Cramer-Rao lower bounds are calculated in order to determine the theoretical lower bounds on the parameter uncertainty.

## 7.1 Introduction

Matched field inversion (MFI) is a technique for determining unknown parameters of the ocean environment. The unknown parameters are estimated by minimizing an energy function that provides a measure for the differences between a measured acoustic field and acoustic

---

<sup>D</sup> Submitted to the Journal of the Acoustical Society of America.

fields that are calculated by a propagation model. One important application of MFI is geo-acoustic seabed parameter estimation.

Since the number of possible parameter combinations is huge, and since there are many local optima, global optimization methods are needed for guiding the search for the set of unknown parameters that gives the optimum match between measured and calculated acoustic fields. The two most widely used global inversion methods are genetic algorithms (GA) and simulated annealing (SA). The drawback of using global optimization methods for matched field inversion problems is that these methods are not suited for determining the exact global optimum. They provide a solution in the neighborhood of the global optimum, resulting in an uncertainty in parameter estimates. This uncertainty can be reduced, or even eliminated, through the additional use of a local optimization method. The optimization method itself, however, is not the only cause for the uncertainty in the parameter estimates. Variability in the ocean environment<sup>1</sup> and noise in the data further contribute to the uncertainty.

In this paper the accuracy of the parameter estimates is quantitatively assessed by considering the contributions of each of the above-mentioned causes. Use is made of acoustic data that have been obtained during the ADVENT99 sea trial.<sup>1,2</sup> In (Snellen<sup>1</sup>) results of inversions of these data are presented. The inverted parameter values were found to be in very good agreement with independent measurements, which comprise DGPS measurements for the source/receiver range, and current meter measurements for the array tilt. A seismic survey was carried out for obtaining information on the sediment layer thicknesses and layer sound speeds. In this paper we will extend the analysis of (Snellen<sup>1</sup>).

In general, when using a global optimization method for finding the optimum, and performing several independent inversions for the same acoustic data, each inversion will result in (slightly) different estimates for the unknown parameters. As already mentioned above, this stems from the fact that global optimization methods are suitable methods for locating the global optimum, but are inefficient in finding the exact global optimum. Local methods are usually able to more efficiently descend towards a local minimum. However, they easily get trapped in local minima. Therefore, a logical approach seems to use a combination of a global and a local optimization method. In the literature several approaches are presented.<sup>3-8</sup> We combined a GA with the downhill simplex (DHS) method as a local method, in such a way that GA and DHS were applied sequentially, i.e., DHS was applied after the GA has converged.

The way the variability in the ocean environment influences the accuracy of parameter estimates is illustrated in the following. Consider inversions of experimental acoustic fields that were measured at different times, which is the situation here. In practical situations the sound speed profile in the water column will vary with time to a certain extent. If one does not account for this variability in the inverse modeling, this can result in mismatch between the actual sound speed structure between source and receiver and the sound speed structure that is used for the forward model calculations. Therefore, the parameter estimates will also vary with time in such a way that it corrects for this mismatch. The corresponding contribution to the uncertainty can, at least in principle, be eliminated when the sound speed structure is known exactly at the time of each transmission. Under practical experimental circumstances, however, this is virtually impossible. In (Snellen<sup>1</sup>) and in this work we assess the influence of the oceanographic variability by performing inversions for synthetic data that account for the mismatch due to this variability.

Noise in the data results in a contamination of the energy function. Minima can get less pronounced, or might even disappear.<sup>3</sup> This also contributes to the uncertainty in the parameter estimates.

The results presented here provide an additional analysis of that given in (Snellen<sup>1</sup>). This paper differs from (Snellen<sup>1</sup>) in the following: to reduce the uncertainty due to the method, the DHS method is applied after the GA. Also, the Cramer-Rao lower bounds are calculated in order to estimate the maximally attainable accuracy.



The paper is organized as follows:

In Section 7.2 the ADVENT99 experiment is briefly summarized. In Section 7.3 details on the acoustic inversion method are presented. In Section 7.4 results of the inversions are given, illustrating the effect of the additional application of the local optimization method. Section 7.5 presents the Cramer-Rao lower bounds for the acoustic problem.

## 7.2 The ADVENT99 experiment

A detailed description of the ADVENT99 experiments, jointly conducted by SACLANT Centre and TNO-FEL, is given in (Snellen<sup>1</sup>) and (Siderius<sup>2</sup>). A large part of the ADVENT99 sea trial comprised acoustic experiments with both the source and the receiver at a fixed position. These fixed geometry experiments were conducted in a shallow water area on the Adventure Bank (water depth 80 m) for source/receiver ranges of 2, 5 and 10 km. As in (Snellen<sup>1</sup>) we only consider data of the 2-km experiment. The 2-km experiment took place on May 2 1999 from 12:37 to 20:17 UTC time. The source used for the acoustic transmissions was mounted on a tower that was moored on the sea bottom for keeping it at a fixed position. The receiving system consisted of a vertical array (VA), containing 64 elements and spanning 62 meters of the water column. As in (Snellen<sup>1</sup>) we consider the multi-tone signals transmitted in the band (200-700 Hz). 41 snapshots of 2-s data were selected from the received time series and were fast Fourier transformed into the frequency domain. We have selected the frequencies 200, 300, 400 and 600 Hz. The resulting complex pressures as a function of depth are further referred to as 'pressure fields'. These 41 pressure fields were used in the inversions, and correspond to data transmitted at 15 minutes interval, spanning the total duration of the 2-km experiment (about 8 hours). A CTD-chain was towed by INS *Ciclope* back and forth along the acoustic track, providing information on the sound speed structure of the water column. These data are used for simulating the effect of oceanographic variability on the parameter uncertainty.

## 7.3 Acoustic inversion method

For the forward acoustic model we have applied the standard normal-mode technique.<sup>10</sup> The sediment layer and the sub-bottom are treated as fluid layers and the high loss continuous eigenvalue spectrum is ignored.

In Section 7.3.1 the objective function to be minimized is described. In Section 7.3.2 we present details on the applied global optimization method, whereas in Section 7.3.3 the applied local optimization method is presented. In Section 7.3.4 the acoustic problem is briefly described.

### 7.3.1 The objective function

The objective (or energy) function gives a quantitative measure for the agreement between the calculated and measured acoustic fields. We have selected the following objective function  $E$ , which is based on the incoherent multi-frequency Bartlett processor<sup>11,12</sup>

$$E(\mathbf{m}) = 1 - \frac{1}{K} \sum_{k=1}^K |\mathbf{p}_{obs}(f_k) \cdot \mathbf{p}_{calc}^*(f_k, \mathbf{m})|^2 \quad (1)$$

with  $\mathbf{m}$  the vector containing the unknown parameters, the "\*" denoting the complex conjugate transposed, "." indicating the inner product of the vectors  $\mathbf{p}_{obs}(f_k)$ , the measured

pressure field at frequency  $f_k$ , and  $\mathbf{p}_{calc}(f_k, \mathbf{m})$ , the pressure field calculated for parameter set  $\mathbf{m}$  and frequency  $f_k$ . Both pressure vectors are normalized such that their norm equals one, i.e.,  $\|\mathbf{p}_{obs}\| = \|\mathbf{p}_{calc}\| = 1$ . The number of frequencies  $K$  is 4, see previous section.

### 7.3.2 Global optimization: the genetic algorithm

We have applied a genetic algorithm (GA)<sup>13</sup> for finding the minimum of the objective function, Eq. (1). A description of the GA applied can be found in previous work.<sup>12</sup> The settings of the GA are: population size  $q = 64$ , reproduction size  $f_r = 0.5$ , crossover probability  $p_c = 0.8$  and mutation probability  $p_m = 0.05$ . Convergence of the GA is established by taking 400 generations, resulting in 12832 forward acoustic model runs per frequency. For better exploitation of the search space around the global optimum and for diminishing the risk of ending up in a local minimum, 5 independent GA runs are carried out for each pressure field. This results in  $12832 \times 5 \times 4 = 256640$  forward runs per pressure field. As we have selected a population size  $q$  of 64, each set of 5 GA runs results in 320 estimates for each parameter. From these parameter sets, the one that corresponds to the lowest energy function value was selected.<sup>12</sup> This parameter set is denoted by  $\text{GA}_{best}$  and is taken to be the solution of the optimization.

### 7.3.3 Local optimization: The downhill simplex method

In the literature a variety of combinations of global and local methods is presented.<sup>3-8</sup> Since in this paper the goal is to assess uncertainties in parameter estimates, and since for this use is made of the results presented in (Snellen<sup>1</sup>), we select the following straightforward approach. The results presented in (Snellen<sup>1</sup>) were obtained using a GA. Here we assume that the global optimum has been correctly located, and that all solutions are somewhere in the neighborhood of the global optimum. To reduce the inherent uncertainty in parameter estimates, we apply a local method after the global GA search using the  $\text{GA}_{best}$  parameter set as a starting point. The chosen local method is the downhill simplex (DHS) method.<sup>5-8</sup> In Appendix D another local optimization method, being the Levenberg-Marquardt method, is considered and its performance is compared to that of the DHS method for the acoustic problem.

DHS is not very efficient in the amount of function evaluations that it requires, but has the important advantage that it does not require the calculation of derivatives. It is based on an intuitive geometric scheme for minimizing the energy function in the parameter search space, such that it makes its way downhill through the complexity of an  $M$ -dimensional topography, until it ends up in a (local) minimum. For  $M$  unknowns, DHS works with  $M+1$  parameter sets. The geometrical figure that consists of these  $M+1$  parameter sets and all interconnecting line segments is called the simplex. In two dimensions ( $M = 2$ ), the simplex is a triangle; in three dimensions it is a tetrahedron ( $M = 3$ ). For finding parameter sets with lower values of the energy function the simplex undergoes a series of transformations, illustrated in Fig. 1 for  $M = 3$ . One of these transformations is reflection, where the point of the simplex with the highest energy is moved through the opposite face of the simplex, with the intention to thereby obtain a solution with a lower energy. In case the new point has an energy function value lower than that of any of the simplex points, the simplex is expanded in this direction for further exploring this new area. If reflection (and expansion) do not result in a decrease of the energy, contraction away from the point with the highest energy is carried out. The algorithm is repeated if it encounters an improvement in the energy function during any of these three operations. If no decrease in the energy function value is obtained, a multiple contraction in all dimensions towards the parameter set with the lowest value for the energy function is performed. As a consequence of all these operations, DHS has the ability to explore the

parameter space within and around itself to some extent and eventually contract to a local minimum if allowed to run long enough.

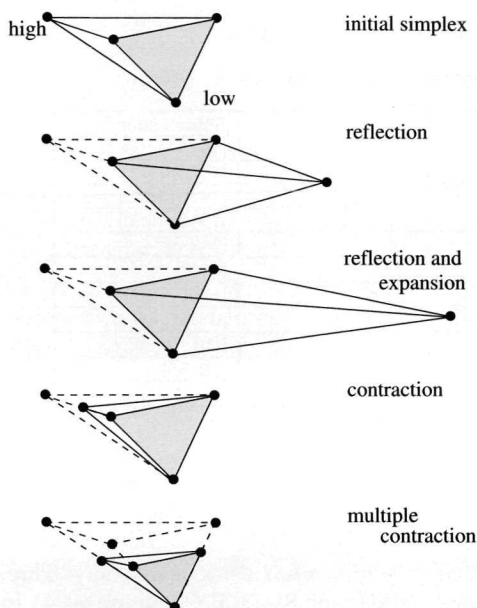


Fig. 1 Steps taken during the DHS optimization.

We use the DHS algorithm as described by (Nelder<sup>14</sup>). An extensive set of test runs showed that the best results are obtained when the DHS algorithm is restarted several times until this does not result in a further improvement. This is done in such a way that the resulting parameter set of the current DHS run is used as one of the elements of the initial simplex of the next DHS run, while each DHS run is carried out for a limited set of iterations. This approach ensures that the simplex keeps a certain volume, thereby providing a better exploration of the area around the minimum.

### 7.3.4 The acoustic problem

The 11 parameters included in the inversion are extensively discussed in (Snellen<sup>1</sup>) and are briefly summarized below.

The bathymetry along the 2 km acoustic track was found to be fairly range-independent (2-m depth variation over the 2 km) and therefore we assume a constant water depth  $H_w$ . The geo-acoustic model consists of a single sediment layer with thickness  $h_{sed}$ , overlying a homogeneous sub-bottom. The sediment compressional wave speed is assumed to vary linearly with depth from  $c_{1, sed}$  at the top of the sediment to  $c_{2, sed}$  at the bottom of the sediment, and to have a constant value  $c_b$  in the sub-bottom. The attenuation constant  $\alpha$  and the density  $\rho$  in the sea bottom are taken to be depth independent and are assumed to be equal in the sediment and the sub-bottom. The array configuration is defined by estimating  $h_I$ , the distance of the deepest hydrophone to the bottom, and the effective array tilt  $\theta$  in the plane of propagation. The source range,  $r_s$ , and the source depth, here defined by the distance from the source to the bottom  $\Delta$ , have a large influence on the acoustic propagation and are not known to the required accuracy. The baseline values of  $r_s$ ,  $\Delta$  and  $h_I$  are 2040, 4 and 9.5 m, respectively.

The sound speed profile used for the inversions is the sound speed profile that corresponds to the CTD taken from the NRV *Alliance* on May 2, 12:20 UTC, i.e., 17 minutes prior to the execution of the experiment.

Table I lists the unknown parameters and their search bounds.

Table I The unknown parameters, their symbols and search bounds.

Parameter	Symbol	Search bounds
Upper sediment sound speed (m/s)	$c_{1, sed}$	[1475 1700]
Sediment thickness (m)	$h_{sed}$	[1 25]
Lower sediment sound speed (m/s)	$c_{2, sed}$	[1475 1800]
Sub-bottom sound speed (m/s)	$c_b$	[1515 1900]
Density ( $g/cm^3$ )	$\rho$	[1 2.3]
Attenuation constant (dB/ $\lambda$ )	$\alpha$	[0 1]
Source range (m)	$r_s$	[1700 2500]
Distance source to bottom (m)	$\Delta$	[0 10]
Tilt (deg)	$\theta$	[-10 10]
Water depth (m)	$H_w$	[75 85]
Distance lowest hydrophone to bottom (m)	$h_1$	[7.5 12.5]

## 7.4 Inversion results

The inversion results presented in (Snellen<sup>1</sup>) were obtained using a GA only. Three sets of inversions were carried out, denoted by EXP, SIM1, and SIM2. EXP comprises 41 inversions of measured data. The 41 snapshots used for these inversions were transmitted at approximately 15-min intervals, and span the entire 2-km experiment, which lasted for over eight hours. SIM1 consists of 41 independent inversions, each for the same synthetic pressure fields. The results of the SIM1 inversions can be used for assessing the contribution of the optimization method itself to the uncertainty in the parameter estimates, and its ability to locate the correct solution. Finally, SIM2 comprises inversions of 41 synthetic pressure fields calculated using 41 different sound speed profiles. These profiles were measured along the acoustic track by the towed CTD-chain, and, therefore, are indicative of the actual temporal sound speed variability as encountered during the experiment. By using a single averaged sound speed profile for all replica pressure fields, SIM2 provides a simulation of the effect of temporal oceanographic variability on the parameter uncertainty. SIM1, SIM2 and EXP are all multi-frequency inversions using the frequencies (200, 300, 400 and 600 Hz) and assume the environment to be range-independent.

From the three sets of inversions it was found in (Snellen<sup>1</sup>) that a large part of the uncertainty in the inverted parameters is caused by the optimization method itself (SIM1). In the present work the aim is to get a more accurate optimization by applying DHS as a local method after the GA. DHS is applied to all results of the three sets of inversions, using the  $GA_{best}$  parameter set as one of the elements of the initial simplexes.

### 7.4.1 Applying DHS to SIM1 inversions

Figure 2 shows for three of the unknown parameters,  $c_{1, sed}$ ,  $\rho$ , and  $r_s$ , the values as obtained by GA only, and by GA followed by DHS. (Plots for the remaining parameters can be found in Appendix D, Fig. 12). The solid black horizontal lines indicate the true parameter values, which are, of course, known exactly for these simulations. The true geo-acoustic parameter values are chosen such that they correspond to a clayey silt sediment.<sup>1</sup> It can be concluded that applying DHS after GA is a suitable method for determining the correct solution.

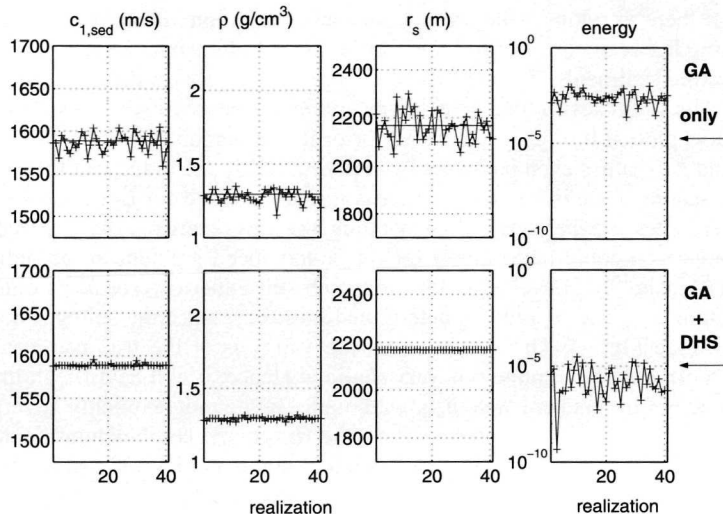


Fig. 2  $c_{1, \text{sed}}$ ,  $\rho$ , and  $r_s$  estimates for the SIM1 inversions using the GA only (upper subplots), and GA followed by DHS (lower subplots). The two right-most subplots show the corresponding energy values. The upper plots are from (Snellen<sup>1</sup>).

As a measure of the parameter uncertainty we present the standard deviations of the 41 estimates for each parameter in Table II. Since the number of observations (i.e., 41) is relatively small we also determined the statistical uncertainty or error on the standard deviations.<sup>1</sup> These are also given in Table II. It is seen that due to the additional application of the local method, the contribution of the optimization method to the uncertainty is reduced significantly, except for  $h_{\text{sed}}$ ,  $c_{2, \text{sed}}$ , and  $c_b$ . For these three parameters the standard deviation actually increases. They are less well determined due to parameter coupling and because some of these parameters have only a minor influence on the acoustic propagation. This is illustrated in Fig. 3 showing energy as a function of  $c_{2, \text{sed}}$  and  $h_{\text{sed}}$ , while having the remaining 9 parameters at their correct values.

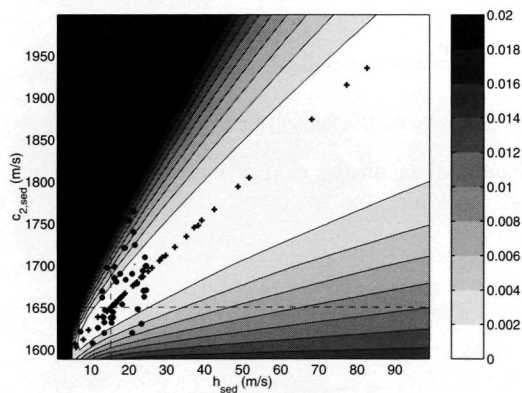


Fig. 3 Energy as a function of  $c_{2, \text{sed}}$ , and  $h_{\text{sed}}$ , while keeping the remaining parameters at their correct values. Also shown are the  $c_{2, \text{sed}}$  estimates plotted against  $h_{\text{sed}}$  estimates as obtained from GA inversions only (indicated by circles) and by also applying DHS (indicated by the crosses). The dashed lines indicate the true  $h_{\text{sed}}$  and  $c_{2, \text{sed}}$  values.

It appears that there is a long valley with low energy function values indicating a strong parameter coupling between  $c_{2, sed}$  and  $h_{sed}$ , i.e., the acoustic field is only sensitive to the sound speed gradient in the sediment. This explains the large uncertainty on the estimates for these two parameters. The estimates for  $c_{2, sed}$  and  $h_{sed}$  as obtained from the inversions (GA only and GA+DHS) are also plotted in Fig. 3 and are all on or in the neighborhood of the valley. The spread in  $c_{2, sed}$  and  $h_{sed}$  values even increases by applying DHS, due to the fact that for the GA optimization the search space is bounded, whereas it is unbounded for DHS. However, these  $c_{2, sed}$  and  $h_{sed}$  estimates are perfectly aligned along the low energy valley. Based on this knowledge, an approach could be to invert for the sound speed gradient in the sediment (as demonstrated in (Ainslie<sup>15</sup>)). However, in this approach still either  $c_{2, sed}$  or  $h_{sed}$  would have to be determined. Both  $c_{2, sed}$  and  $h_{sed}$  can be determined in theory, since the valley is not equally deep everywhere (see Fig. 4). The minimum of the valley is at the true parameter values (1650 m/s and 15 m), but this minimum is very shallow. Hence, it will be difficult to estimate  $h_{sed}$  when optimizing for gradient and  $h_{sed}$ . Although we do not explicitly invert for the sediment gradient, its value can be inferred from the  $(h_{sed}, c_{2, sed})$  combinations found by the DHS inversions plotted in Fig. 3. The inverted gradient amounts to  $4.0 \text{ s}^{-1}$ , which is equal to the true gradient.

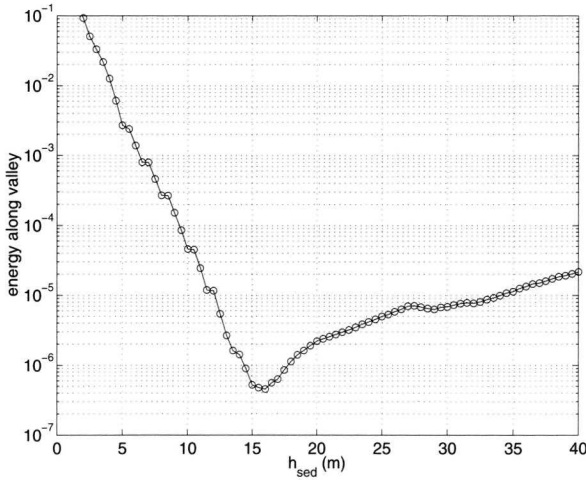


Fig. 4 Energy as function of  $h_{sed}$  along the low energy valley of Fig. 3. (Note that in this figure a varying  $h_{sed}$  implies a varying  $c_{2, sed}$  according to the line through the crosses of Fig. 3).

In Fig. 5 we compare the influence of  $c_b$  on the energy with that of  $h_{sed}$  and  $c_{2, sed}$ . The minor influence of  $c_b$  on the energy explains the large spread in its optimized values, see Table II.

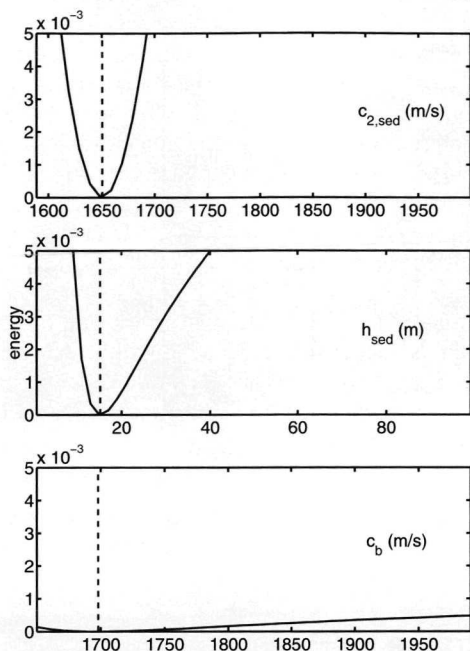


Fig. 5 Energy plotted as function of  $c_{2, sed}$ ,  $h_{ sed}$ , and  $c_b$ . The dashed vertical lines show the true values. The plots for  $h_{ sed}$  and  $c_{2, sed}$  correspond to cross-sections in the energy surface of Fig. 3 along the dashed lines indicated in this figure.

## 7.4.2 Applying DHS to the SIM2 inversion results

For the SIM2 inversions, Fig. 6 shows the estimates for  $c_{l, sed}$ ,  $\rho$ , and  $r_s$  as obtained by GA only, and by GA followed by DHS. The solid horizontal lines indicate the true parameter values. As can be seen in Table II the standard deviations corresponding to the inversion results are considerably reduced by the additional application of DHS. The difference between SIM2 and SIM1 is that SIM2 includes the effect of temporal oceanographic variability by using different sound speed profiles for each of the 41 realizations, whereas for SIM1 the same profile is repeated 41 times. Due to this oceanographic variability the parameter estimates show a larger spread than those obtained for the SIM1 inversions. Also shown in Fig. 6 is the optimized energy, both obtained after applying GA only, and obtained after also applying DHS. The decrease in energy obtained through the additional application of DHS is smaller than that for the SIM1 inversions.

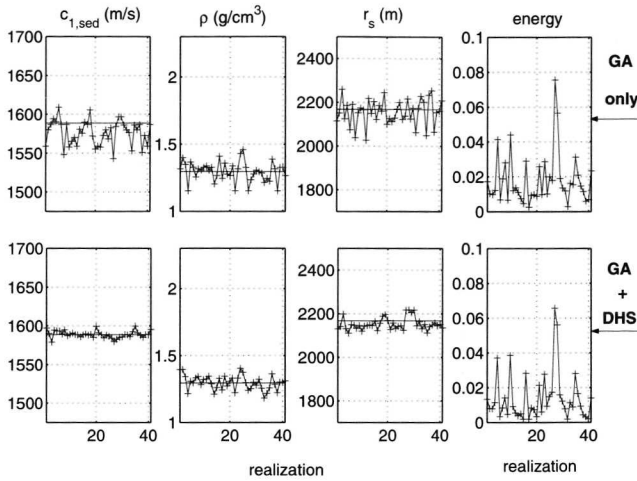


Fig. 6  $c_{1, sed}$ ,  $\rho$ , and  $r_s$  estimates for the SIM2 inversions using the GA only (upper subplots), and GA followed by DHS (lower subplots). The two right-most subplots show the corresponding energy values. The upper plots are from (Snellen<sup>1</sup>).

### 7.4.3 Applying DHS to the EXP results

Figure 7 shows the estimates for  $c_{1, sed}$ ,  $\rho$ , and  $r_s$  as obtained by GA only, and by GA followed by DHS for the experimental data. Clearly, the parameter uncertainty is reduced by using the DHS and this can be seen also from Table II. As for the SIM2 inversions, the decrease in energy is less than that obtained for the SIM1 inversions.

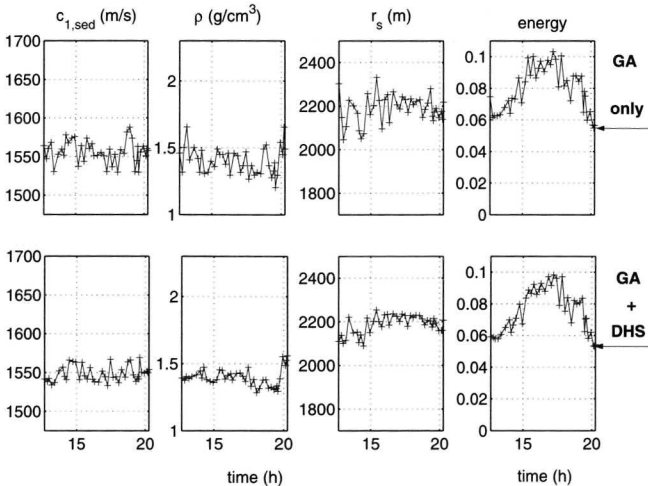


Fig. 7  $c_{1, sed}$ ,  $\rho$ , and  $r_s$  estimates obtained after inversions of the EXP data using the GA only (upper subplots), and GA followed by DHS (lower subplots). The two right-most subplots show the corresponding energy values. The upper plots are from (Snellen<sup>1</sup>).



## 7.4.4 Discussion

Table II summarizes the standard deviations of the parameter estimates for the three sets of inversions. Since a limited amount of runs is considered (41), the statistical error on the standard deviation must also be considered in order to judge whether the observed improvement in the accuracy in the parameter estimates is statistically significant.<sup>1</sup> It can be seen that the standard deviation for all parameters, except for  $h_{sed}$ ,  $c_{2,sed}$  and  $c_b$ , is indeed reduced by the additional application of DHS.

Table II Standard deviations for the 41 parameter estimates of the SIM1, SIM2 and EXP inversions. Also given is the statistical error on each standard deviation. The last row gives the result for the sound speed gradient in the sediment, determined from  $c_{1,sed}$ ,  $c_{2,sed}$ , and  $h_{sed}$ .

Parameter symbol	SIM1		SIM2		EXP	
	GA only	GA + DHS	GA only	GA + DHS	GA only	GA + DHS
$c_{1,sed}$ (m/s)	11 ± 1	1.6±0.2	16±2	4.5±0.5	15±2	10 ± 1
$h_{sed}$ (m)	4.5 ± 0.5	18±2	5.1±0.6	47±5	6.4±0.7	8.1 ± 0.9
$c_{2,sed}$ (m/s)	42 ± 5	76±8	46±5	198±22	49±5	71 ± 8
$c_b$ (m/s)	81±9	208±23	81±9	378±42	76±8	168 ± 19
$\rho$ (g/cm <sup>3</sup> )	0.042 ±0.005	0.011 ±0.001	0.078 ±0.009	0.054 ±0.006	0.10 ±0.01	0.065 ±0.007
$\alpha$ (dB/λ)	0.11 ±0.01	0.020 ±0.002	0.13 ±0.01	0.061 ±0.007	0.13 ±0.01	0.070 ±0.008
$r_s$ (m)	61±7	0.75±0.08	59±7	28±3	65±7	43±5
$\Delta$ (m)	0.18 ±0.02	0.0056 ±0.0006	0.26 ±0.03	0.09 2±0.010	0.22 ±0.02	0.1 8±0.02
$H_w$ (m)	1.1±0.1	0.017 ±0.002	1.2±0.1	0.50±0.06	1.2±0.1	0.72±0.08
$h_1$ (m)	0.59±0.06	0.009 ±0.001	0.69±0.08	0.42±0.05	0.65±0.07	0.47±0.05
gradient (s <sup>-1</sup> )	2±5 0.3	0.59±0.06	3.9±0.4	1.5±0.2	3.5±0.4	3.1±0.3

Figure 8 shows the standard deviations (and their statistical errors) of the SIM1, SIM2 and EXP inversion results. In order to facilitate inter-parameter comparisons, here the standard deviations are normalized by dividing by the search bounds applied in the GA. The upper plot shows the standard deviations of the inversion results obtained by GA only<sup>1</sup>, whereas the lower plot shows the effect of the additional application of DHS. The standard deviations on  $h_{sed}$ ,  $c_{2,sed}$  and  $c_b$  are not shown, since these parameters estimates are highly uncertain: the application of DHS actually degrades the accuracy for these parameters. Also array tilt is not shown, since the tilt is known to vary deterministically with time for the experimental data (see Fig. 18 of (Snellen<sup>1</sup>)). In (Snellen<sup>1</sup>) it was concluded, based on the results shown in the upper plot of Fig. 8, that oceanographic variability and errors due to the method could completely explain the uncertainty in the parameter estimates. From the lower plot it is seen that by applying DHS after GA, the influence of the optimization method on the uncertainty is almost eliminated. At the same time this reveals a gap between the SIM2 and EXP accuracy (see Section 7.6).

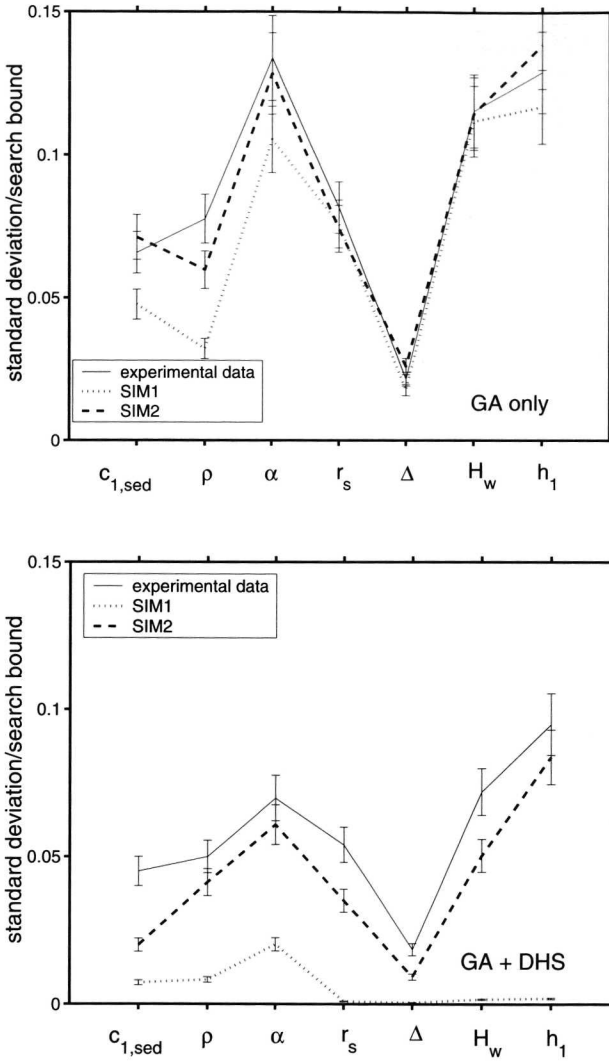


Fig. 8 Standard deviations (normalized by the GA search bounds) of the SIM1, SIM2 and EXP inversion results. The upper plot corresponds to results obtained by GA only<sup>1</sup>, whereas the lower plot corresponds to the application of GA followed by DHS. The error bars indicate the statistical errors on the standard deviations.

## 7.5 Cramer-Rao bounds

The theoretical lower limit on the parameter uncertainties is assessed by determining the Cramer-Rao bounds (CRB).<sup>9,16-18</sup> They are determined by the amount of noise in the data and the sensitivity of the propagation to each of the parameters. Parameters that highly influence the propagation, i.e., those parameters that are well estimated, have a lower susceptibility to the noise (and vice versa).

The Cramer-Rao bounds are calculated from the Fisher information matrix  $\mathbf{J}$ , the entries of which are<sup>9</sup>

$$J_{ij} = \text{Tr} \left( \mathbf{K}^{-1}(\mathbf{m}) \frac{\partial \mathbf{K}(\mathbf{m})}{\partial m_i} \mathbf{K}^{-1}(\mathbf{m}) \frac{\partial \mathbf{K}(\mathbf{m})}{\partial m_j} \right) \quad (2)$$

with  $\mathbf{m}$  the vector containing the unknown parameters,  $\mathbf{K}(\mathbf{m})$  the covariance matrix of the received signal, i.e., signal and noise, and  $\text{Tr}$  denoting the trace of the matrix. The mean square errors or parameter uncertainties are bounded from below by the diagonal terms of the inverse of  $\mathbf{J}$ , i.e., considering the uncertainty for the  $i^{\text{th}}$  parameter  $\sigma_i$ , the following relation applies

$$\sigma_i^2 \geq [\mathbf{J}^{-1}]_{ii} \quad (3)$$

The covariance matrix  $\mathbf{K}$  consists of both a noise and a signal contribution:

$$\mathbf{K}(\mathbf{m}) = \mathbf{K}_n(\mathbf{m}) + \mathbf{K}_s(\mathbf{m}) \quad (4)$$

with  $\mathbf{K}_n$  the noise covariance matrix, and  $\mathbf{K}_s$  the signal covariance matrix, which both depend on  $\mathbf{m}$ .

An approach for calculating the CRB would be to use the real measured data for  $\mathbf{K}$ , which contains both the signal and noise contribution. Acoustic models must then be used for calculating the partial derivatives  $\frac{\partial \mathbf{K}_s(\mathbf{m})}{\partial m_i}$  and  $\frac{\partial \mathbf{K}_n(\mathbf{m})}{\partial m_i}$ . However, the difficulty of this approach is that the parameter set  $\mathbf{m}$  used in the calculation of the partial derivatives consists of estimates for the true ocean environmental parameters, whereas  $\mathbf{K}$  as obtained from the measurements corresponds to the true ocean environmental parameters. Consequently, the partial derivatives are determined for a parameter set  $\mathbf{m}$  that will in practice differ from the parameter set that corresponds to  $\mathbf{K}$ . Since there is no way to interpret these results, a different approach is selected as described below.

First, the total covariance matrix is normalized by  $\text{Tr}(\mathbf{K}_s)$

$$\mathbf{K} = \frac{\mathbf{K}_s}{\text{Tr}(\mathbf{K}_s)} + \frac{1}{\text{SNR}} \frac{\mathbf{K}_n}{\text{Tr}(\mathbf{K}_n)} \quad (5)$$

where the signal-to-noise ratio  $\text{SNR}$  is given by

$$SNR = \frac{Tr(\mathbf{K}_s)}{Tr(\mathbf{K}_n)} \quad (6)$$

which equals the averaged intensity  $SNR$  at the hydrophone level.

The signal covariance matrix  $\mathbf{K}_s$  is determined theoretically according to

$$\mathbf{K}_s(\mathbf{m}) = \mathbf{p}_{calc}^*(\mathbf{m})\mathbf{p}_{calc}(\mathbf{m}) \quad (7)$$

with  $\mathbf{p}_{calc}$  a row vector containing the calculated acoustic pressures for parameter set  $\mathbf{m}$  calculated by the normal-mode model.

Noise is known to originate from several distinct mechanisms, i.e., surface-generated ambient noise, discrete interfering sources, and, equipment noise. Since dedicated noise experiments were also carried out, we have used this measured noise for determining  $\mathbf{K}_n$ :

$$\mathbf{K}_n = \langle \mathbf{p}_n^* \mathbf{p}_n \rangle \quad (8)$$

with  $\mathbf{p}_n$  the measured pressure field containing noise only, and  $\langle \rangle$  indicating the mean. Since the noise conditions varied with time, noise recorded at relevant times during the experiment is considered.

A problem when using measured noise data for determining  $\mathbf{K}_n$  is that its partial derivatives are unknown. The  $\frac{\partial \mathbf{K}_n(\mathbf{m})}{\partial m_i}$ -contribution to  $\frac{\partial \mathbf{K}(\mathbf{m})}{\partial m_i}$  is assessed through simulations using an ambient noise model based on normal modes.<sup>9</sup> It is found that including  $\frac{\partial \mathbf{K}_n(\mathbf{m})}{\partial m_i}$  in Eq. (2) results in a small reduction of the CRB. We neglect the noise contribution to  $\frac{\partial \mathbf{K}(\mathbf{m})}{\partial m_i}$ , and keep in mind that the real CRB are somewhat lower.

Since there are no analytical expressions for  $\frac{\partial \mathbf{K}_s(\mathbf{m})}{\partial m_i}$ , these are calculated numerically.

Appropriate values for the derivatives were obtained by subsequently decreasing the increments  $\partial m_i$ , which assures the CRB to stabilize.

Equation (2) is the CRB for a single frequency, for which we select 400 Hz.

For determining the  $SNR$  in Eq. (5) we have to account for the fact that during the 2-km experiment the noise level varied significantly with time due to the presence of INS *Ciclope*, which was sailing back and forth along the acoustic track. The  $SNR$  was estimated from 41 noise data snapshots that were recorded at times close to the 41 data snapshots used for the EXP inversions. The resulting  $SNR$  is plotted in Fig. 9 together with the distance of the INS *Ciclope* to the VA. The strong correlation between  $SNR$  and distance shows that noise radiated by INS *Ciclope* dominates, i.e., the interfering noise is originating from a discrete source. Note that the  $SNR$  always exceeds  $\sim 10^3$  ( $> 30$  dB).

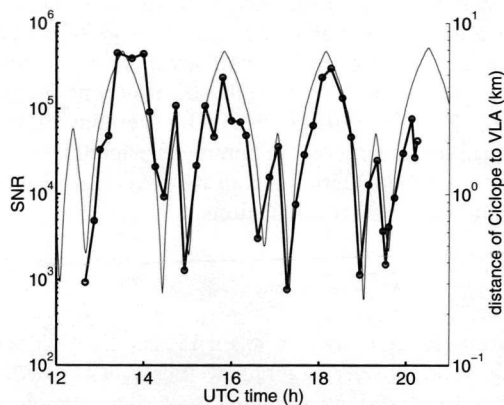


Fig. 9 SNR for 400 Hz, and distance of INS *Ciclope* from the VA.

The influence of INS *Ciclope* on the noise signal can also be observed from the noise covariance matrices. These are shown in Fig. 10 for INS *Ciclope* 'far away' from the VA (distance  $\sim 7$  km), and INS *Ciclope* very close to the VA (distance few 100 m), respectively. Also presented in this figure are noise covariance matrices for a single interfering noise source and for sea surface noise. The latter is calculated using the above-mentioned ambient noise model. The structure of the measured covariance matrices strongly resembles that of the discrete noise source instead of that of the 'sheet' noise source (i.e., the sea surface).

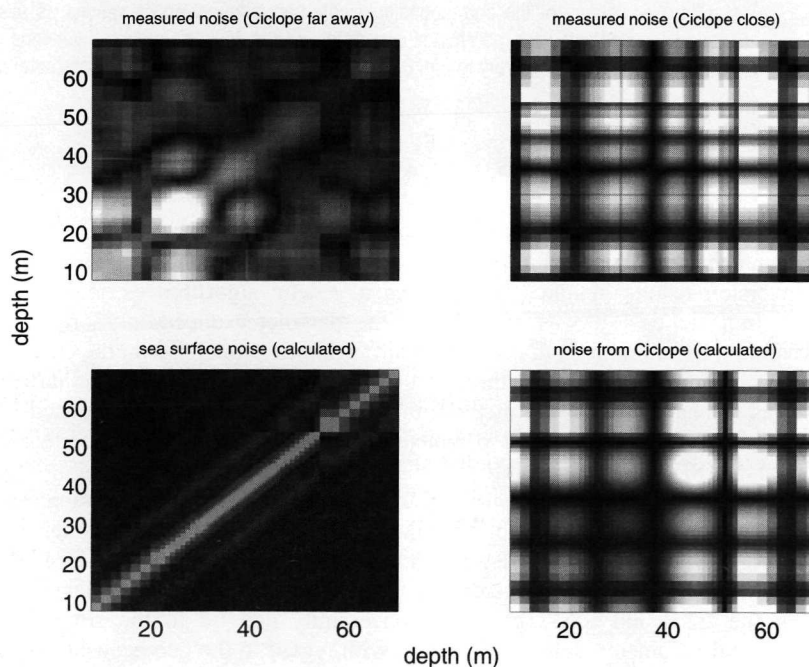


Fig. 10 Top panels: Absolute values of measured noise covariance matrices (at 400 Hz) for INS *Ciclope* 'far away' (distance to VA 7 km) and 'close by' (distance to VA few 100 m). Lower panels: Absolute values of modeled noise covariance matrices (at 400 Hz) for a discrete interfering noise source and for sea surface noise (i.e., a 'sheet' source).

Figure 11 shows the resulting CRB for the highest and the lowest SNR encountered. For comparison, also the parameter uncertainty corresponding to EXP inversions using 400-Hz data only are shown, together with the standard deviations corresponding to the inversions using the four frequencies. These are somewhat lower than those corresponding to the 400-Hz inversions. The CRB are far below ( $\sim 2$  orders of magnitude) the uncertainty in the parameter estimates, and therefore the theoretical lower limit on the parameter uncertainties is by far not reached. The similarity in shape between the uncertainties in the inversion results and in the CRB, however, demonstrates the value of the CRB calculations.

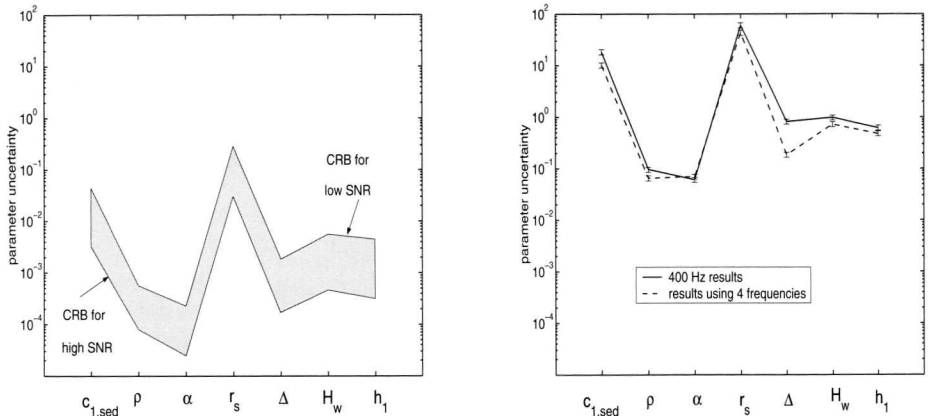


Fig. 11 Left plot: Cramer-Rao bounds for 400 Hz (shaded area). For comparison the right plot shows the standard deviations of the corresponding single-frequency inversion results as a solid line. The dashed line indicates the parameter uncertainty of the multi-frequency inversions (i.e., the EXP inversions). Note that contrary to Fig. 8, no normalization is applied to the parameter uncertainty.

## 7.6 Conclusions

In this paper we present an assessment of the uncertainty of the parameter estimates obtained through matched field inversion of real acoustic data. In (Snellen<sup>1</sup>), we discussed matched field inversion results obtained by applying a genetic algorithm as a global optimization method. In (Snellen<sup>1</sup>) it was argued that the parameter uncertainty originates from the imperfect optimization method, oceanographic variability, and noise in the data. In the current paper it is definitely shown that through the additional application of the downhill simplex method as a local optimization method, the parameter uncertainty is reduced considerably. Figure 8 shows that the residual parameter uncertainty due to the imperfect optimization method alone (SIM1) is negligible.

The observed parameter uncertainty of the multi-frequency EXP inversions can largely be explained by oceanographic variability (SIM2 inversions, see Fig. 8), although a gap between the EXP and SIM2 accuracy exists. Although the SNR was found to be high, noise is a possible contributor to the parameter uncertainty. Another possible explanation for the gap between the EXP and SIM2 parameter uncertainty can lie in the simplification of the environmental parameterization, particularly with regard to the geo-acoustic model of the sea floor. Other possible sources of temporal variability that can contribute to the parameter uncertainty, and that are not modeled, include sea surface wave interaction, internal wave interactions, the spatial variability in the water column sound speed and tidal effects.

## 7.7 Acknowledgements

The authors would like to thank all participants of the ADVENT99 sea trial, M. Siderius, J. Sellschopp, E. Michelozzi and P. Boni from SACLANT Centre in particular. Thanks are also due to the crews of NRV *Alliance* and INS *Ciclope*.

## References

- 1 Mirjam Snellen, Dick G. Simons, Martin Siderius, Jürgen Sellschopp and Peter L. Nielsen, "An evaluation of the accuracy of shallow water Matched Field Inversion results," *J. Acoust. Soc. Am.*, 109 (2), 514-527 (2001).
- 2 Martin Siderius, Peter L. Nielsen, Jürgen Sellschopp, Mirjam Snellen and Dick G. Simons, "Experimental study of geo-acoustic inversion uncertainty due to ocean sound-speed fluctuations," *J. Acoust. Soc. Am.* 110 (2), 769-781 (2001).
- 3 Peter Gerstoft, "Inversion of acoustic data using a combination of genetic algorithms and the Gauss-Newton approach," *J. Acoust. Soc. Am.* 97 (4), 2181-2190 (1995).
- 4 Gopu R. Potty, James H. Miller James F. Lynch and Kevin B. Smith, "Tomographic inversion for sediment parameters in shallow water," *J. Acoust. Soc. Am.* 108 (3), 973-986 (2000).
- 5 Mark R. Fallat and Stan E. Dosso, "Geoacoustic inversion via local, global, and hybrid algorithms," *J. Acoust. Soc. Am.* 105 (6), 3219-3230 (1999).
- 6 Mark R. Fallat, Peter L. Nielsen and Stan E. Dosso, "Hybrid geoacoustic inversion of broadband Mediterranean Sea data," *J. Acoust. Soc. Am.* 107 (4), 1967-1977 (2000).
- 7 Martin Musil, Michael J. Wilmut and N. Ross Chapman, "A Hybrid Simplex Genetic Algorithm for Estimating Geoacoustic Parameters Using Matched-Field Inversion," *IEEE J. Oceanic Eng.* 24 (3), 358-369 (1999).
- 8 Martin Musil, N. Ross Chapman and Michael J. Wilmut, "Range-dependent matched-field inversion of SwellEX-96 data using the downhill simplex algorithm," *J. Acoust. Soc. Am.* 106 (6), 3270-3281 (1999).
- 9 A. B. Baggeroer, W. A. Kuperman and H. Schmidt, "Matched field processing: Source localization in correlated noise as an optimum parameter estimation problem," *J. Acoust. Soc. Am.*, 83 (2), 571-587 (1988).
- 10 F.B. Jensen, W.A. Kuperman, M.B. Porter and H. Schmidt, *Computational ocean acoustics*, American Institute of Physics, Inc., New York (1994).
- 11 A. Tolstoy, *Matched Field Processing for Underwater Acoustics*, World Scientific Pub. Co., River Edge, New Jersey (1993).
- 12 D.G. Simons and M. Snellen, "Multi-frequency matched-field inversion of benchmark data using a genetic algorithm," *J. Comp. Acoust.*, 6 (1&2), 135-150 (1998).
- 13 P. Gerstoft, "Inversion of seismoacoustic data using genetic algorithms and a *posteriori* probability distributions," *J. Acoust. Soc. Am.*, 95 (2), 770-782 (1994).
- 14 J. A. Nelder and R. Mead, "A simplex method for function minimization," *The computer journal*, 7, 308-313 (1965).
- 15 M.A. Ainslie, R.M. Hamson, G.D. Horsley, A.R. James, R.A. Laker, M.A. Lee, D.A. Miles and S.D. Richards, "Deductive multi-tone inversion of sea bed parameters," *J. Comp. Acoust.*, 8 (2), 271-284 (2000).
- 16 A. B. Baggeroer and H. Schmidt, "Parameter estimation bounds and the accuracy of full field inversions," in *Full Field Inversion methods in Ocean and Seismo Acoustics*, edited by O. Diachok, A. Caiti, P. Gerstoft, and H. Schmidt, Kluwer, Dordrecht, 79-84 (1995).
- 17 H. Schmidt and A. B. Baggeroer, "Physics-imposed resolution and robustness issues in seismo-acoustic parameter inversion," in *Full Field Inversion methods in Ocean and Seismo Acoustics*, edited by O. Diachok, A. Caiti, P. Gerstoft, and H. Schmidt, Kluwer, Dordrecht, 85-90 (1995).
- 18 N.C. Makris, G.S. Perkins, S.P. Heckel and J. Catipovic, "Optimizing environmental parameterization and experimental design for shallow water sound speed inversion," in *Full Field Inversion methods in Ocean and Seismo Acoustics*, edited by O. Diachok, A. Caiti, P. Gerstoft, and H. Schmidt, Kluwer, Dordrecht, 115-120 (1995).
- 19 W.H. Press, B.P. Flannery, S.A.T. Teukolsky and W.T. Vetterling, "Numerical recipes in C," Cambridge University Press, 543-544 (1988).



## Chapter 8

# Inversion for geo-acoustic bottom parameters and the water column sound speed profile<sup>E</sup>

### Abstract

This paper discusses estimates for geo-acoustic bottom parameters and sound speeds in the water column obtained through matched field inversion (MFI) of shallow water acoustic data. In MFI measured acoustic fields are compared with acoustic fields calculated by a propagation model for many sets of parameter combinations. A genetic algorithm was used for solving this optimization problem. The sound speed profile in the water column was represented using empirical orthogonal functions. MFI was applied to multi-tone data (200-600 Hz) received at a vertical hydrophone array. The acoustic source was fixed at a range of 2 km. For obtaining independent measurements, a CTD-chain was towed along the acoustic track simultaneously with the acoustic transmissions to monitor oceanographic variations. Many snapshots of acoustic data received within a period of 8 hours were inverted. The resulting parameter estimates compare well with the independent measurements, i.e., a seismic survey for the geo-acoustic parameters and the CTD-chain data for the inverted water column profiles.

## 8.1 Introduction

Matched field inversion (MFI) is a technique for obtaining information on unknown parameters that influence the propagation of sound under water. When employing MFI, a measured acoustic field is compared with acoustic fields that are calculated by a propagation model for many sets of unknown parameters. Since the amount of possible parameter combinations is huge and there are many local optima, global optimization methods are

---

<sup>E</sup> The work described in this chapter was presented in "Inversion for geo-acoustic bottom parameters and the water column sound speed profile using broadband shallow water data," Proceedings of the Undersea Defence Technology Conference, Hamburg, 26-28 June, 2001

needed for guiding the search for the set of unknown parameters that results in an optimum match between both acoustic fields. An important application of MFI is geo-acoustic seabed parameter estimation. Another application of MFI lies in the field of ocean acoustic tomography, where the goal is to obtain information on the sound speeds in the water column.<sup>1,2,3</sup>

The analysis presented in this paper deals with acoustic data that were acquired during the ADVENT99 MFI sea trial.<sup>4,5</sup> This sea trial has been jointly conducted by SACLANT Centre and TNO-FEL on the Adventure Bank, south of Sicily, in April/May 1999. In (Snellen<sup>4</sup>) results of inversions of the ADVENT99 acoustic data for both geo-acoustic and geometric parameters are presented. The majority of the unknown parameters could be estimated very accurately through inversion and were in good agreement with the independent measurements. The main objective of the analysis presented in this paper is to investigate whether MFI techniques can also be applied to the ADVENT99 acoustic data for tomographic purposes, i.e., for obtaining information on the sound speeds in the water column. To this end, the sound speed profiles are constructed through the use of empirical orthogonal functions (EOFs) that are efficient basis functions for describing a set of water column sound speed profiles. For investigating how many of the EOFs are needed for a sufficient representation of the water column sound speed profiles, the effect of employing an increasing amount of EOFs in the inversions is investigated.

## 8.2 The ADVENT99 experiment

In this paper we consider data for which the range between source and receiver was about 2 km. The position of the source during this experiment was 37° 17.966' N, 12° 15.588' E. The receiving system was positioned at 37° 17.883' N, 12° 14.207' E. This experiment took place on May 2 1999 from 12:37 to 20:17 UTC time.

The source used for the acoustic transmissions was mounted on a tower construction that was moored on the sea bottom for keeping it at a fixed position. The receiving system consisted of a vertical array (VA), containing 64 elements and spanning 62 meters of the water column. Both low-frequency (200-800 Hz) and high-frequency (800-1600 Hz) multi-tones and LFM sweeps have been transmitted. In this paper only the low-frequency multi-tones are considered.

During the experiment also many non-acoustic measurements have been carried out to obtain information on the ocean environment. These environmental measurements include CTD casts and waverider measurements. The bathymetry of the trial's area was measured with the ship's echosounder, showing virtually no variation in water depth along the 2-km track (depth 77-79 m). Further, a CTD-chain was towed back and forth along the acoustic track. From the CTD-chain measurements the sound speed as a function of depth in the water column can be determined along the acoustic track. Since the tow ship was moving, both time and position are different for the succeeding CTD-chain measurements. Also, an extensive seismic survey was carried out, thereby obtaining independent geophysical information on the seabed. Use was made of a boomer type sound source and the signals were received on a multi-channel seismic streamer. Using a multi-channel receiving array allows for estimating, besides the layering of the seabed, also the sound speeds of the different layers.<sup>6</sup> The multi-channel seismic data analysis indicated a strong reflector at approximately 6 m depth. The sound speed in this thin layer amounts to  $(1554 \pm 35)$  m/s.<sup>4</sup>

### 8.3 Empirical orthogonal functions

In the field of oceanography a technique has been developed for deriving efficient basis functions that completely describe large sets of sound speed profiles.<sup>1</sup> These basis functions are called empirical orthogonal functions (EOFs).

The sound speed profiles used for the current EOF analysis are the CTD-chain measurements. Since the tow ship was sailing back and forth along the acoustic track several sets (7 in total) of CTD-chain measurements were obtained. For illustration purposes, Fig. 1 shows the measurements along six of these tracks.

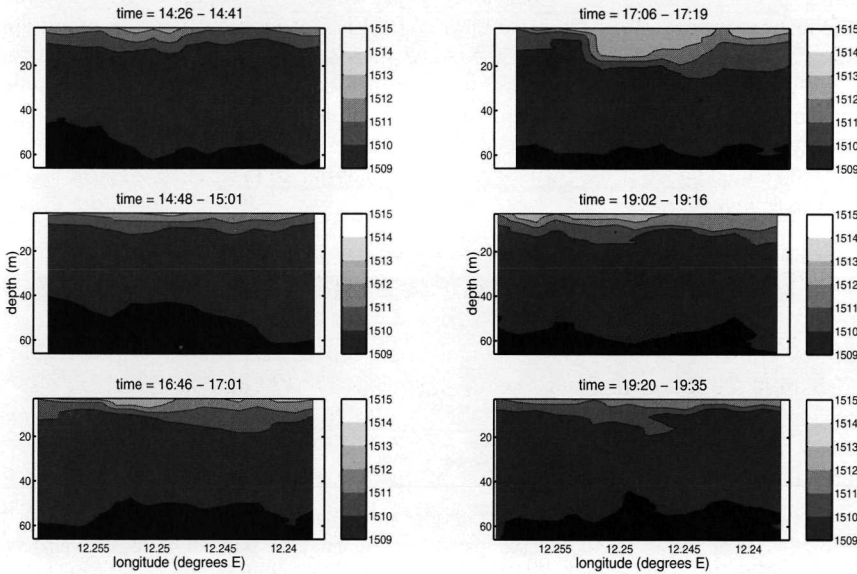


Fig. 1 Sound speed (in m/s) as a function of longitude and depth and time (UTC) as derived from the CTD-chain measurements. The horizontal axes range from the source position to the vertical array position.

The EOFs are the eigenvectors  $\mathbf{v}_k$  of the covariance matrix  $\mathbf{R}$  of  $N$  sound speed profiles  $\mathbf{c}_n$  ( $n = 1 : N$ ), calculated through

$$\mathbf{R} = \frac{1}{N} \sum_{n=1}^N [\mathbf{c}_n - \bar{\mathbf{c}}] \cdot [\mathbf{c}_n - \bar{\mathbf{c}}]^T = \frac{1}{N} \sum_{n=1}^N \begin{bmatrix} \Delta c_n(z_1)^2 & \cdots & \Delta c_n(z_1)\Delta c_n(z_K) \\ \vdots & \ddots & \vdots \\ \Delta c_n(z_K)\Delta c_n(z_1) & \cdots & \Delta c_n(z_K)^2 \end{bmatrix} \quad (1)$$

with  $[\mathbf{c}_n - \bar{\mathbf{c}}]$  a column vector.  $K$  is the amount of depth points in the sound speed profiles and  $z_k$  ( $k = 1 : K$ ) denotes the depth in the water. Superscript  $T$  indicates the transposed.  $\bar{\mathbf{c}}$  is the mean water column sound speed profile, obtained by taking the mean of all sound speeds at each depth.  $\Delta c_n(z_k)$  is the deviation from the mean of sound speed profile  $\mathbf{c}_n$  at depth  $z_k$ .

The first subplot of Fig. 2 shows the eigenvalues of  $\mathbf{R}$  (divided by the largest eigenvalue). Since the mean sound speed profile was subtracted from the measured profiles in the calculation of  $\mathbf{R}$ , its eigenvalues are measures for the amount of variability that is accounted for by the corresponding EOFs. It is seen that the first three eigenvalues are large compared to the remaining eigenvalues. To further investigate this, the cumulative sum of eigenvalues is calculated. The result is shown in the second subplot of Fig. 2 as the cumulative percentage of the total sum of eigenvalues. For the CTD-chain data, the first three eigenvalues are seen to account for 90 % of the variability. This means that 90 % of the variability in the sound speed profiles is represented by the first three EOFs, thereby clearly demonstrating the efficiency of the EOFs as basis functions.

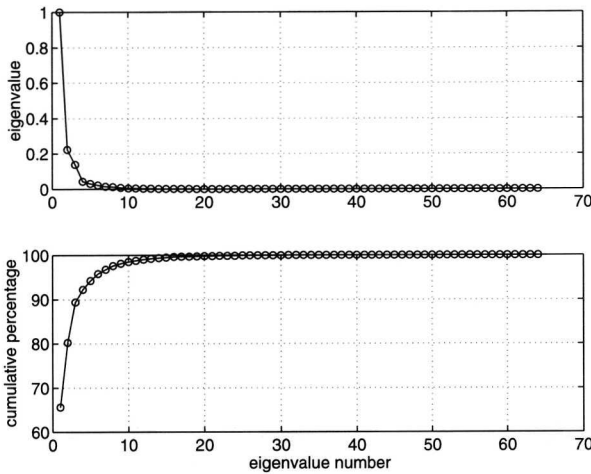


Fig. 2 Eigenvalues of the covariance matrix  $\mathbf{R}$ , divided by the largest eigenvalue (upper subplot). The lower subplot shows the cumulative percentage of the total sum for increasing amount of eigenvalues.

Figure 3 shows the EOFs corresponding to the four highest eigenvalues. The EOFs are normalized such that their norm equals 1.

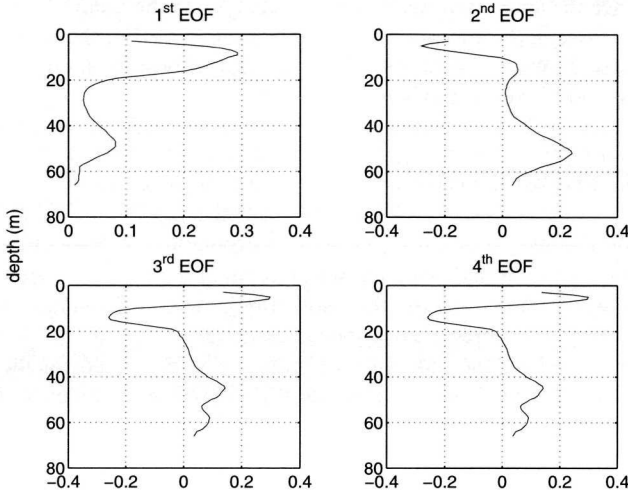


Fig. 3 The EOFs corresponding to the four highest eigenvalues. The EOFs are normalized such that their norm equals 1.

Each of the measured sound speed profiles can be written as a sum over the EOFs  $\mathbf{v}_k$

$$\mathbf{c}_n = \bar{\mathbf{c}} + \sum_{k=1}^K \alpha_{k,n} \mathbf{v}_k \quad (2)$$

This can also be written as

$$\mathbf{c}_n = \bar{\mathbf{c}} + \mathbf{V} \boldsymbol{\alpha}_n \quad (3)$$

with  $\boldsymbol{\alpha}_n$  the  $n^{\text{th}}$  column of the  $(K \times N)$  matrix that contains the EOF coefficients  $\alpha_{k,n}$ , and  $\mathbf{V}$  the  $(K \times K)$  matrix containing the EOFs  $\mathbf{v}_k$  as columns. The EOF coefficients can then be found according to

$$\boldsymbol{\alpha}_n = \mathbf{V}^{-1} [\mathbf{c}_n - \bar{\mathbf{c}}] \quad (4)$$

In Eqs. (3) and (4) we have used all EOFs, thereby completely reproducing the original sound speed profiles. However, from Fig. 2 it was concluded that the major part of the variability is contained in only a few EOFs. It is therefore legitimate to approximate the sound speed profiles by accounting only for the EOFs that correspond to the large eigenvalues. The  $n^{\text{th}}$  profile is then estimated according to

$$\tilde{\mathbf{c}}_n = \bar{\mathbf{c}} + \sum_{k=1}^G \alpha_{k,n} \mathbf{v}_k \quad (5)$$

$\tilde{\mathbf{c}}_n$  is the approximation for the  $n^{\text{th}}$  sound speed profile  $\mathbf{c}_n$  and  $\mathbf{v}_k$  ( $k = 1 : G$ ) are the EOFs that correspond to the  $G$  largest eigenvalues.

By accounting only for the EOFs that correspond to the large eigenvalues, we can optimize for only a few EOF coefficients, instead of having to optimize for all depth points of the

sound speed profile. Since the amount of depth points usually is in the order of a hundred, this implies a significant decrease in the amount of unknown parameters. For the forward acoustic calculations in the inversions we will represent the sound speed profile employing only 1, 2, and 3 EOFs, i.e.,  $G = 1, 2$  and  $3$ , respectively.

## 8.4 The inversion method

For the forward acoustic model calculations a normal-mode model has been applied. Range-independent calculations are performed since the water depth along the 2-km acoustic track is virtually constant, and we further assumed that both the geo-acoustic parameters and the sound speed profile can be taken constant along the acoustic track.

A genetic algorithm is used for the global optimization. The data used for the inversions were transmitted at 15-min intervals and spanned the total duration of the experiment (8 h). The resulting 41 snapshots of 2 seconds of acoustic data were selected from the received time series and were fast Fourier transformed into the frequency domain. The energy function to be minimized is based on the incoherent multi-frequency Bartlett processor<sup>7</sup>, employing the data at the frequencies 200, 300, 400 and 600 Hz.

In (Snellen<sup>4</sup>) results of inversions of the same acoustic data are presented. These inversions have been carried out for in total 11 unknown geo-acoustic and geometric parameters. Figure 4 shows the model for the ocean environment and the 11 unknown parameters.

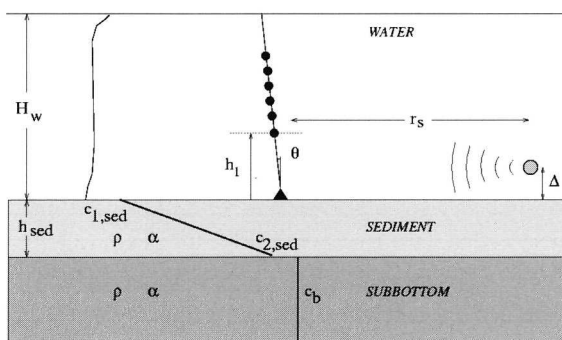


Fig. 4 The unknown parameters to be inverted.

For the current analysis we have inverted for the same 11 unknown parameters, plus the unknown parameters of the water column sound speed profile. As mentioned in the previous section, the sound speed profile used for the forward acoustic calculations is represented using 1, 2 and 3 EOFs, respectively. These are the EOFs corresponding to the three highest eigenvalues and together they account for 90 % of the variation in the sound speed profiles. The coefficients of these EOFs are the unknowns that have to be determined through inversion. This gives a total of 12, 13, and 14 unknown parameters, respectively. In the following we will denote the unknown EOF coefficients as  $a_1$ ,  $a_2$  and  $a_3$ . For example, when representing the water column sound speed profile by 3 EOFs, the water column sound speed profile  $\mathbf{c}$  is then calculated as

$$\mathbf{c} = \bar{\mathbf{c}} + a_1 \mathbf{v}_1 + a_2 \mathbf{v}_2 + a_3 \mathbf{v}_3 \quad (6)$$

## 8.5 Results

As mentioned in the previous section we have done inversions for 11 geo-acoustic and geometric parameters, and up to three EOF coefficients.

Figure 5 shows for 8 of the geo-acoustic and geometric parameters the inversion results as a function of geo-time. We have not shown the results for the remaining 3 geo-acoustic parameters, viz., lower sediment sound speed ( $c_{2, sed}$ ), sub-bottom sound speed ( $c_b$ ) and sediment thickness ( $h_{sed}$ ), since these could not be determined (see (Snellen<sup>4</sup>) for details). Figure 6 shows the estimates for  $a_1$  as a function of time, employing 1, 2 and 3 EOF coefficients as unknowns, respectively. Figure 7 shows the estimates for  $a_2$  and  $a_3$ . The ranges of the  $y$ -axis of these 3 figures correspond to the parameter search bounds.

The results shown in Fig. 5 are obtained from inversions where only the first EOF coefficient was used as the unknown water column sound speed parameter, i.e., the sound speed profile used for the forward calculations is represented only by the EOF that corresponds to the highest eigenvalue. The results of the inversions where the sound speed profile was represented using 2 and 3 EOFs are similar and are therefore not shown.

Since the experimental configuration is stationary, all unknown parameters (except for the EOF coefficients and the array tilt  $\theta$ , which might vary due to varying currents) should be constant with time. Therefore the inversion results can be used for determining the mean and standard deviation of the 41 estimates for each parameter. Assuming statistically independent observations, also the standard deviation of the mean ( $\sigma_{mean}$ ) can be determined according to

$$\sigma_{mean} = \frac{std}{\sqrt{M}} \quad (7)$$

with  $M$  the number of observations (here equal to 41), and  $std$  the standard deviation of the  $M$  observations. In Table I at the end of this section, the means of the 41 inversion results and their corresponding uncertainties are presented. This uncertainty is taken as 2 times  $\sigma_{mean}$ . In Table I also the means and their uncertainties obtained from the inversions presented in (Snellen<sup>4</sup>) are presented for each parameter. Since these results were found to be in good agreement with independent measurements, such as the seismic measurements, we will use them for comparison with the current results. For all parameters, except for the density, the means obtained from inversions with and without including EOF coefficients fall together within the uncertainty. The estimates for the array tilt obtained from the 2 sets of inversions coincide. It can be concluded that the inclusion of water column sound speed parameters in the inversion does not have a statistically significant influence on the estimates for the geo-acoustic and geometric parameters, except for the bottom density for which a somewhat higher, though significant, value is obtained. Simulations show that this is not caused by the change in sound speed profile in a direct way. The increase in density must therefore be caused by a shift in the optimum values of the other parameters. However, as mentioned above, the inclusion of water column sound speed parameters in the inversion did not have a statistically significant influence on the estimates for the other parameters. Therefore, the shift in the value for the bottom density must be due to a significant shift in a certain combination of parameters. We have not identified the particular combination of parameters that causes the shift.

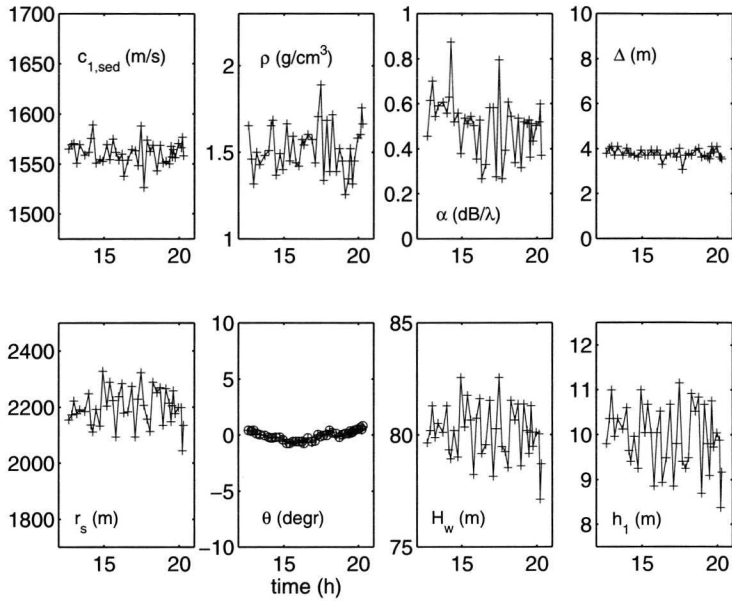


Fig. 5 Parameter estimates as a function of time obtained from inversions employing 11 geo-acoustic and geometric parameters and 1 EOF coefficient as unknowns.

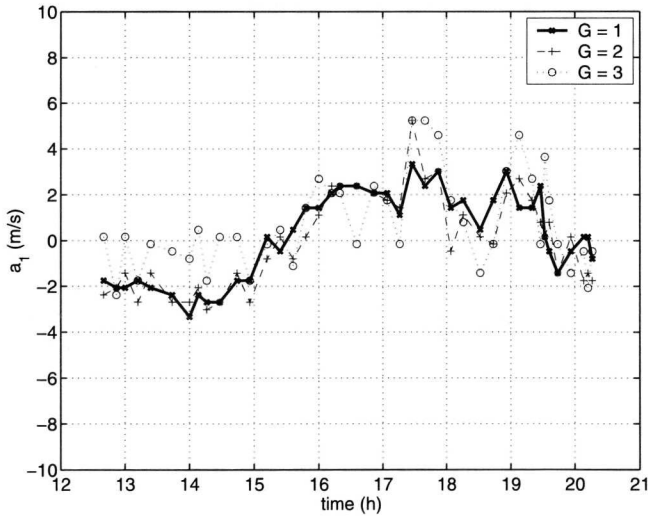


Fig. 6 Estimates for the coefficient of the first EOF ( $a_1$ ) as a function of time, representing the sound speed profile using 1, 2 and 3 EOFs, respectively.



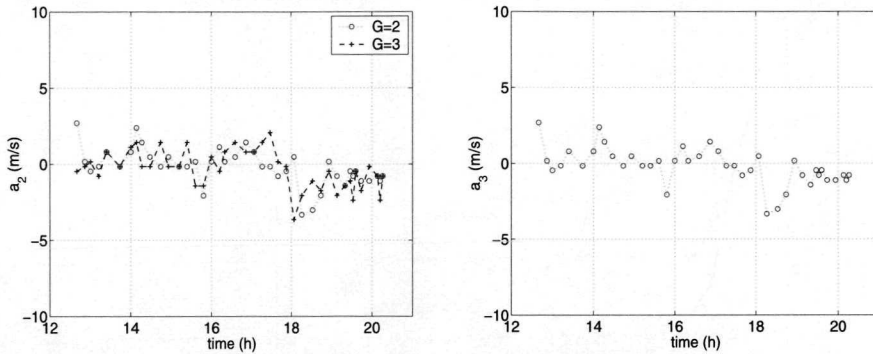


Fig. 7 Estimates for the coefficients of the second ( $a_2$ ) and third EOF ( $a_3$ ).

In order to determine how many EOFs are needed to represent the sound speed profile, we have investigated whether a trend is present in the estimates for the EOF coefficients as a function of time. This trend then reflects variations with time of the sound speed structure along the acoustic track. Although there is a difference in the exact behavior of  $a_1$  as a function of time, a similar trend in the  $a_1$  estimates can be seen for the 3 different inversions by visual appraisal of Fig. 6. No trend appears to be present in the estimates for  $a_2$  and  $a_3$ . To further investigate the existence of trends in the EOF coefficient estimates we have applied a strict mathematical test to the results of Figs. 6 and 7. The basic principle behind this test is to fit the data with a polynomial of increasing degree  $m$ . For these polynomials, that are fitted to the data in a least squared sense, the measure  $D$  for the deviation between fit and data is calculated<sup>8</sup>

$$D = \sqrt{\sum_{i=1}^M \frac{(a_g(t_i) - F_m(t_i))^2}{(M - m)}} \quad (8)$$

with  $a_g(t_i)$  ( $g = 1:G$ ) the  $i^{\text{th}}$  estimate (out of  $M$  (41)) for the  $g^{\text{th}}$  EOF coefficient and  $F_m(t_i)$  the value of the polynomial of degree  $m$  at time  $t_i$ . If a trend is present in the data, employing polynomials of increasing degree will result in a decrease of  $D$ , up to a certain value of  $m$ . Using a polynomial fit of a higher degree will fit to the noise on the data, but will not result in a further decrease of  $D$ . The resulting plateau value for  $D$  is the standard deviation of the noise, viz., arbitrary fluctuations, in the data.

Figures 8 and 9 show  $D$  as a function of polynomial degree. From Fig. 8 it can be seen that indeed a trend is present in the estimates for  $a_1$ . This trend becomes less pronounced when inverting for more EOF coefficients. This can be due to the increased amount of unknowns, making it more difficult to find the global optimum. It can also be the result of correlations between the EOF coefficients. As can be seen from Fig. 9 no trends are present in the estimates for  $a_2$  and  $a_3$ , i.e.,  $D$  starts at the plateau value of the standard deviation of the noise on the data. It is therefore concluded that it is sufficient to represent the sound speed profile using the first EOF only. Another indication that a single EOF is sufficient for representing the sound speed profile is that the energy function values obtained after the inversion do not decrease when inverting for more coefficients (not shown here). Including more EOF coefficients results in more ambiguity and therefore less pronounced trends, but does not enable a better fit to the data.

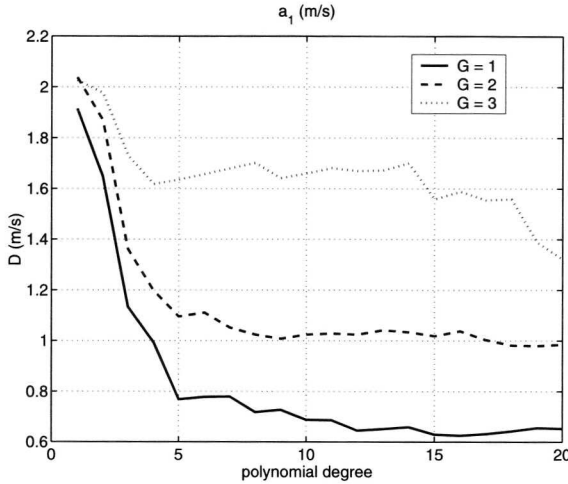


Fig. 8  $D$  as a function of polynomial degree used for the fit of the  $a_1$  estimates.

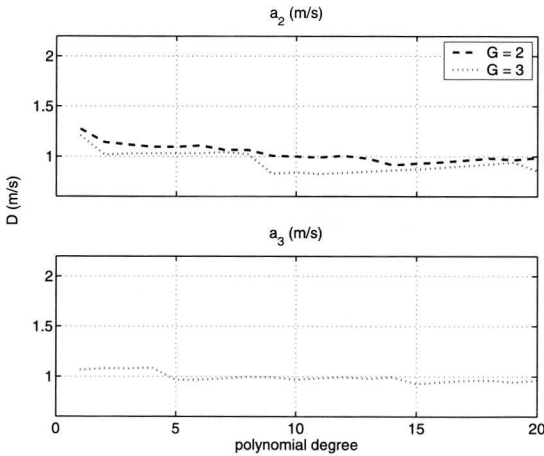


Fig. 9  $D$  as a function of polynomial degree used in the fit of the  $a_2$  and  $a_3$  estimates.

In Fig. 10 the water column sound speed profiles that result from the inversions of the 41 snapshots of data are shown. These profiles  $\mathbf{c}(t_i)$  are determined using Eq. (6), but now employing only the first EOF

$$\mathbf{c}(t_i) = \bar{\mathbf{c}} + a_1(t_i)\mathbf{v}_1 \quad (9)$$

As expected, since the  $a_1$  coefficient shows a trend, also these inverted sound speed profiles clearly exhibit a trend. For investigating whether this corresponds to an actual variation with time of the sound speed structure along the acoustic track, a comparison with measurements has to be made. For these measurements we have used the 7 means of the CTD-chain measurements carried out along the 2-km acoustic track, which are shown in Fig. 11. Clearly similar trends are seen in both the inverted and measured sound speed profiles.

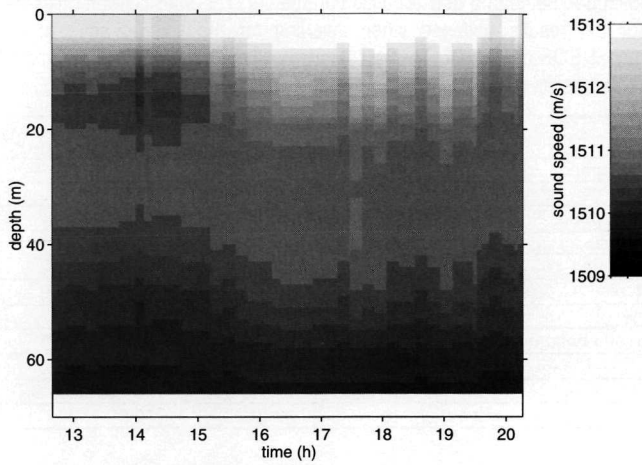


Fig. 10 Inverted water column sound speed profiles.

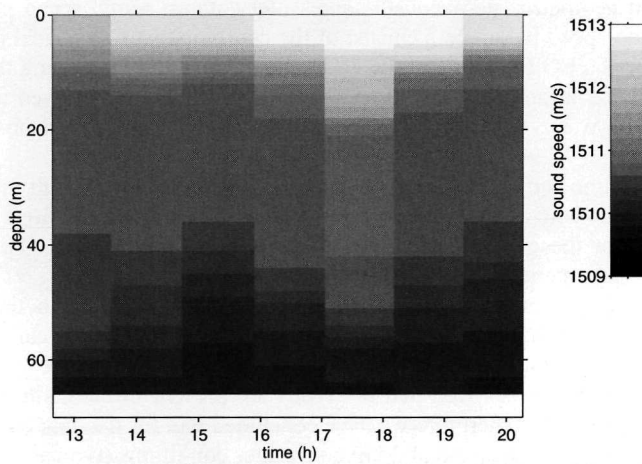


Fig. 11 Measured water column sound speed profiles. These are the mean values of CTD-measurements along the 2-km acoustic track.

Table 1 The 11 unknown geometric and geo-acoustic parameters. The third column gives the means and uncertainty for the results obtained when inverting for the 11 geo-acoustic and geometric parameters, and 1 EOF coefficient. The last (fourth) column gives the means and corresponding uncertainty for the results presented in (Snellen<sup>4</sup>) (no EOF coefficients included).

Parameter	Symbol	mean ( $2\sigma_{mean}$ )	mean ( $2\sigma_{mean}$ ) <sup>4</sup>
Upper sediment sound speed	$C_{1, sed}$	1561.1 (3.8)	1556.3 (4.6)
Sediment thickness	$h_{sed}$	18.2 (1.8)	16.5 (2.0)
Lower sediment sound speed	$C_{2, sed}$	1662 (15)	1663 (15)
Sub-bottom sound speed	$C_b$	1759 (24)	1735 (24)
Density	$\rho$	1.520 (0.043)	1.405 (0.032)
Attenuation constant	$\alpha$	0.505 (0.041)	0.482 (0.042)
Source/receiver range	$r_s$	2198 (20)	2186 (20)
Distance of source to sea bottom	$\Delta$	3.766 (0.066)	3.772 (0.067)
Tilt angle	$\theta$	-	-
Water depth	$H_w$	80.12 (0.38)	79.89 (0.36)
Distance of deepest hydrophone to sea bottom	$h_1$	9.92 (0.22)	10.00 (0.20)

## 8.6 Summary and conclusions

In this paper we have presented matched field inversion results where the unknown parameters comprise of geometric, geo-acoustic, and water column sound speed parameters. The water column sound speed parameters consist of the coefficients of empirical orthogonal functions (EOFs). Since the EOF analysis of the CTD-chain data showed the first three EOFs to describe 90 % of the variation in the sound speed profiles, we have employed up to three EOFs for calculating the water column sound speeds used for the forward acoustic model calculations.

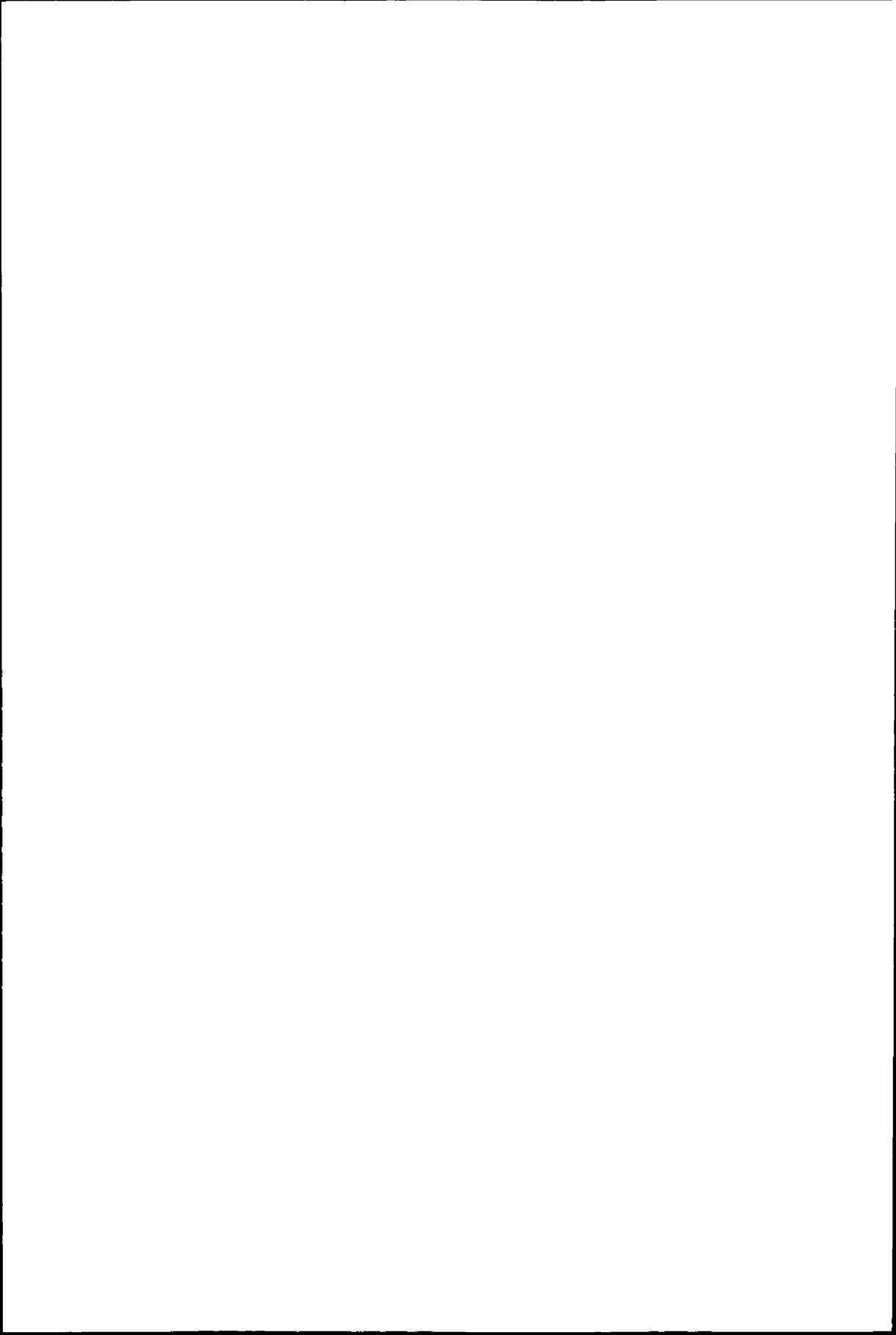
Inclusion of water column sound speed parameters as unknowns did not result in a shift for the majority of the geo-acoustic and geometric parameters compared to inversions where the optimization was done for these geo-acoustic and geometric parameters only. The inverted parameters are in good agreement with independent measurements.

The inversions including 1 and 2 EOF coefficients showed a trend (with time) in the estimates for the coefficient  $a_1$  of the first EOF. Employing a strict mathematical test clearly revealed this trend in  $a_1$  estimates. The trend in  $a_1$  estimates becomes debatable when employing 3 EOFs. The test also showed that no trends are present in the estimates for the second and third EOF coefficient. Therefore we have concluded that for the data considered in this paper, with a source/receiver distance of 2 km and winter conditions (typical variations of  $\sim 4$  m/s in sound speed over the water depth), representing the water column sound speed by the first EOF only is sufficient for describing temporal variations in the water column sound speed profile.

For investigating whether the trend in  $a_1$  corresponds to an actual trend in the sound speed structure along the acoustic track, the inverted sound speed profiles have been compared to measured sound speed profiles. Although the measured sound speed profiles comprise of a very limited set, the measured and inverted profiles show a similar behavior with time. It can therefore be concluded that matched field inversion techniques can be applied for estimating water column sound speeds.

## References

- 1 A. Tolstoy and O. Diachok, "Acoustic tomography via matched field processing", *J. Acoust. Soc. Am.*, 89 (3), 1119 – 1127 (1991).
- 2 Gopu R. Potty and James H. Miller, "Tomographic inversion for sediment parameters in shallow water," *J. Acoust. Soc. Am.*, 108 (3), 973 – 986 (2000).
- 3 Michael Taroudakis and Maria G. Markaki, "On the use of matched-field processing and hybrid algorithms for vertical slice tomography," *J. Acoust. Soc. Am.*, 102 (2), 85 – 895 (1997).
- 4 Mirjam Snellen, Dick G. Simons, Martin Siderius, Jürgen Sellschopp and Peter L. Nielsen, "An evaluation of the accuracy of shallow water Matched Field Inversion results," *J. Acoust. Soc. Am.*, 109 (2), 514 – 527 (2001).
- 5 Martin Siderius, Peter L. Nielsen, Jürgen Sellschopp, Mirjam Snellen and Dick G. Simons, "Experimental study of geo-acoustic inversion uncertainty due to ocean sound-speed fluctuations," *J. Acoust. Soc. Am.* 110 (2), 769-781 (2001).
- 6 Martin Siderius, Mirjam Snellen, Dick Simons and Reiner Onken, "An environmental assessment in the Strait of Sicily: Measurement and analysis techniques for determining bottom and oceanographic properties," *IEEE J. Oceanic Eng.* 25 (3), 364-387 (2000) .
- 7 D.G. Simons and M. Snellen, "Multi-frequency matched-field inversion of benchmark data using a genetic algorithm," *J. Comp. Acoust.*, 6 (1&2), 135-150 (1998).
- 8 William H. Press, Brian P. Flannery, Saul A. Teukolsky, William T. Vetterling, "Numerical recipes in C," Cambridge University Press, 1988, 521-553.



## Chapter 9

# Bottom classification capabilities of matched field inversion

### 9.1 Introduction

In the previous chapters the matched field inversion (MFI) technique has been applied to obtain geo-acoustic bottom parameters. Two environments have been considered, being the area north of Elba (Chapter 5), and the Adventure bank (Chapter 6 to Chapter 8). In this chapter we will apply MFI to a new set of data in order to investigate whether it is an appropriate method for estimating seabed parameters for a range of bottom types. In Chapter 1, one of the applications of MFI was said to be bottom classification, and the work presented here can be seen as a demonstration of the MFI bottom classification capabilities. Use is made of data obtained during the MAPEX trial as carried out by SACLANT Centre in November/December 2000. (MAPEX is an acronym for 'Malta Plateau Experiments').

Several sets of experiments were carried out during MAPEX. The experiments considered here are dedicated MFI experiments using the vertical line array (VA) as the receiving system. In order to obtain sets of data in environments with different bottom types, the array has been deployed at several sites. The availability of data recorded at different sites with different bottom types allows for assessing the robustness of MFI with respect to bottom type. In Section 9.2 the MAPEX sites, three in total, are summarized and a brief description of information available on these sites, obtained from literature, is presented. This information is used as 'groundtruth', necessary when assessing the performance of MFI as a bottom classification technique.

In Section 9.3 the inversion method is briefly described. Section 9.4 presents the results of the inversions. Section 9.5 provides an overview of the inversion results, together with a comparison of the results with the information obtained from literature. Finally, Section 9.6 illustrates the need for accurate bottom information by means of two applications, viz., source localization and sonar performance prediction models.

### 9.2 The MAPEX experiments

A summary of the VA deployments of the MFI experiments is given in Table I. The sound source was towed by NRV *Alliance* at mid-water depths. The source transmitted, amongst other signals, multi-tones comprising the frequencies 200, 275, 350, 425, 500 and 575 Hz. Use is made of these multi-tones only.

Figure 1 shows the area of the experiment. Circles indicate the VA deployment positions. Also indicated are the array positions of two previous experiments, i.e., EnVerse 97 and ADVENT99.

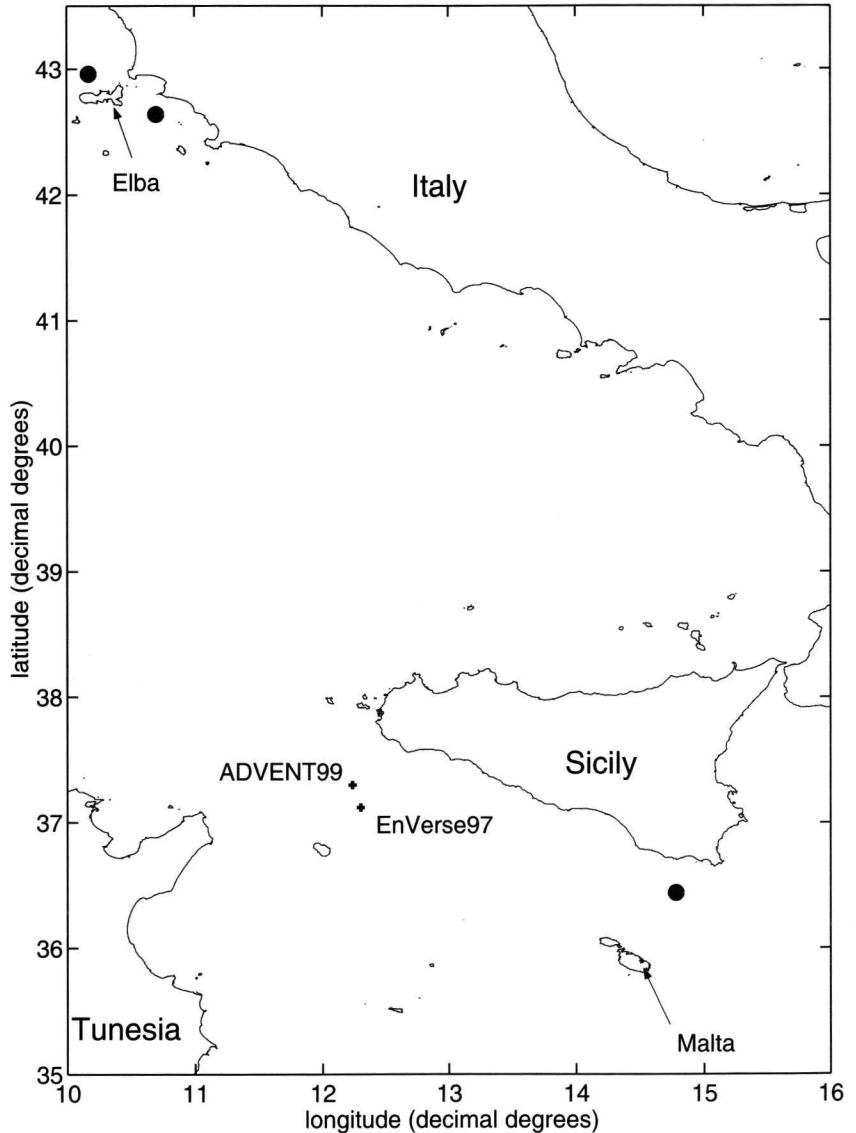


Fig. 1 Area of MAPEX experiments. Circles indicate the MAPEX VA deployment positions. Also indicated are the VA deployment positions (+) of two previous experiments, carried out on the Adventure Bank, viz., EnVerse 97 and ADVENT99.



Table I Relevant VA deployments during the MAPEX trial.

Site	Date	Julian day	VA latitude (degr)	VA longitude (degr)	Water depth (m)
Malta plateau	22 November 2000	327	36.44455	14.776	130
North Elba	29 November 2000	334	42.95755	10.165	121
Southeast Elba	30 November 2000	335	42.63712	10.699	126

A limited literature survey on available geo-acoustic information for the shallow water sites mentioned above has been carried out. A total of 7 independent open sources of information were considered (see Table II). It should be noted that the geographical positions corresponding to the geo-acoustic information presented in these references do not exactly coincide with VA deployment positions given in Table I.

Table II Summary of the literature considered.

Reference	Area	Positions	Method
1	Malta plateau		Cores/grabs/seismic survey
2	Malta plateau	36° 17.7' N, 14° 42.6' E (core 255) 36° 18.0' N, 14° 53.3' E (core 257) 36° 24.8' N, 14° 38.4' E (core 258)	Cores
3	North Elba	43° 10' N, 10° 7' E	Cores
4	North Elba	43° 2.86' N, 10° 10.01' E	Inversion result
5	North Elba	43° 2.86' N, 10° 10.01' E	Inversion result
6	Southeast Elba	42° 38.5' N, 10° 47' E (core 8) 42° 36' N, 10° 53' E (core 9)	Core
7	Southeast Elba	42° 37.5' N, 10° 42' E	Inversion result

Appendix E provides the detailed results of the literature survey. A summary is presented in Table III, and gives an overview of the upper sediment (0-3 m into the sediment) sound speed values encountered. The reason for considering the upper sediment sound speeds is that, in general, these can be used for bottom classification purposes. For the Malta Plateau a large spread of values for the sediment sound speed is found. Note, however, that the cores from which this information is partly derived (see Table II) are taken at large distances apart.

Table III Summary of the different areas at which experiments have been carried out, the bottom type, and the range of sediment sound speeds for each of the areas as obtained from literature.

Site	range of sediment sound speeds (m/s)
Malta Plateau	1500-1700
North of Elba	1450-1580
Southeast of Elba	1457-1485

## 9.3 Acoustic inversion method

For the forward calculations the normal-mode model has been applied. The environment was taken to be range-independent. The model for the ocean environment is taken equal to that of the previous chapters (see e.g. Fig. 12 of Chapter 5), and results in 11 unknown parameters.

The sound speed profile used in the inversions was measured by NRV *Alliance* while she was towing the source at times close to the time of the transmissions. The energy function that is minimized in the optimization is based on the multi-frequency Bartlett processor (see e.g. Chapter 3), employing three frequencies, being 200, 275 and 425 Hz. The pressure fields at these frequencies were obtained by fast Fourier transformation of 0.5 seconds of data into the frequency domain. The snapshot length of 0.5 seconds was selected such that the effect of the

source displacement on the received signals can be neglected. Data transmitted at 2-km range from the receiver has been used for the inversion. The optimization is carried out using the genetic algorithm (GA), followed by the downhill simplex algorithm (DHS). DHS was applied, using the best parameter set found by GA as input. The DHS algorithm was restarted three times.

A difference with the inversions of the ADVENT99 data is that now only a relatively small amount of inversions were carried out. Instead of the five independent runs, here the amount of independent runs was increased until repeatability of, and thereby confidence in, the solution was obtained. This approach was selected in view of the bottom classification application, where one is interested in obtaining a quick estimate for the bottom properties.

## 9.4 Results

### 9.4.1 Malta Plateau

Data transmitted at 2-km distance of the VA, were used for the inversions. Three independent inversions have been carried out. Table IV presents the inversion results, i.e., the parameter estimates obtained after applying both the GA and DHS. Also the corresponding values for the energy function are given.

Table IV Estimates for the unknown parameters obtained from the three independent runs after applying both GA and DHS, and the corresponding values for the energy function (last row).

	#1	#2	#3
$C_{1, \text{sed}}$ (m/s)	1556	1556	1547
$h_{\text{sed}}$ (m)	23	24	21
$C_{2, \text{sed}}$ (m/s)	1563	1565	1551
$C_b$ (m/s)	1704	1636	1766
$\rho$ (g/cm <sup>3</sup> )	1.88	2.30	2.23
$\alpha$ (dB/ $\lambda$ )	0.10	0.26	0.08
$r_s$ (m)	2137	2096	2067
$z_s$ (m)	55	55	54
$\theta$ (degr)	-0.2	-0.4	-0.4
$H_w$ (m)	127	125	124
$h_l$ (m)	13	13	12
$E$	0.16	0.18	0.17

In order to get an indication of the accuracy of the parameters estimates, one could look for each parameter at the deviation between the three estimates #1, #2, and #3. A large deviation implies that the parameter either has only a minor influence on the propagation, or that there are several values for that parameter that correspond to low values for the energy function, i.e., there are local minima. However, this approach provides no overview of the parameter landscape, and therefore we look at the *a posteriori* distributions. These show for each parameter the values obtained after the optimization, weighted by the corresponding energy function value, and thereby give an overview of all parameter values (in the search domain) that correspond to low values for the energy function. The weighting is applied according to the Boltzmann distribution, equal to the weighting applied in the GA optimization. Detailed information on these *a posteriori* distributions is provided in Chapter 3.

Figure 2 shows the *a posteriori* distributions corresponding to all GA inversion results. These comprise all elements of the final populations for the three independent inversions, i.e., they are determined by accounting for  $3 \times 128 = 384$  parameter combinations. The weighting was chosen similar to that of Chapter 3, viz.,  $T$  in Eq. (12) of Chapter 3 is taken as the lowest energy function value. The  $x$ -axes of Fig. 2 indicate the search areas. It is seen that the upper

sediment sound speed is quite well determined, with values ranging from about 1530-1560 m/s. Also the lower sediment sound speed shows a small spread. The sub-bottom sound speed and the density are not determined accurately. However, nearly all values are higher than  $1.5 \text{ g/cm}^3$ . For the attenuation most values are below  $0.5 \text{ dB}/\lambda$ . Source depth and tilt are determined unambiguously. In the estimates for range and water depth two peaks are seen. The peaks at  $\sim 2040 \text{ m}$  source/receiver range and  $\sim 123 \text{ m}$  water depth correspond to higher values for the energy function than the peaks at  $\sim 2120 \text{ m}$  range and  $\sim 126 \text{ m}$  depth, which are in agreement with the DGPS and echosounder measurements.

As in Chapter 7 also the sound speed gradient in the sediments has been determined. The lowest, most right subplot shows the sound speed gradient in the sediment as obtained from the inversions. The gradient is not obtained directly, but is calculated from the optimized sediment sound speeds and sediment thickness. The range of the  $x$ -axis for this parameter was selected such that it shows the majority of all results. The peak at the lowest gradient values corresponds to the lowest energy function values. The minimum in energy belongs to a sediment sound speed gradient of  $0.33 \text{ s}^{-1}$ .

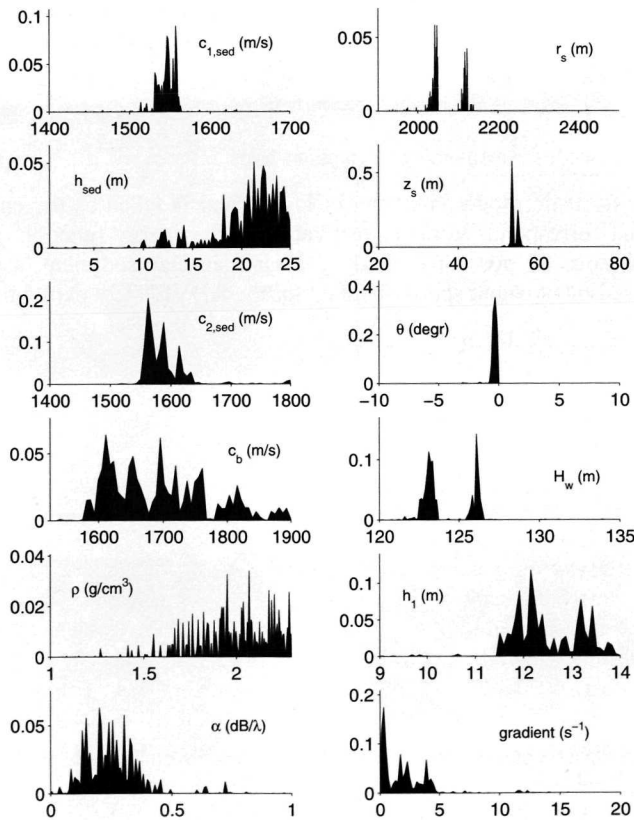


Fig. 2 *A posteriori* distributions of GA solutions.

As a further assessment of the quality of the inversion results, Fig. 3 shows the optimized and measured pressure fields. The optimized pressure fields are calculated for the parameter

set that corresponds to the lowest energy function value obtained, i.e., the #1 parameter set of Table IV. Clearly the optimization is capable of finding a parameter set that corresponds to pressure fields that show good similarity with the measured pressure fields.

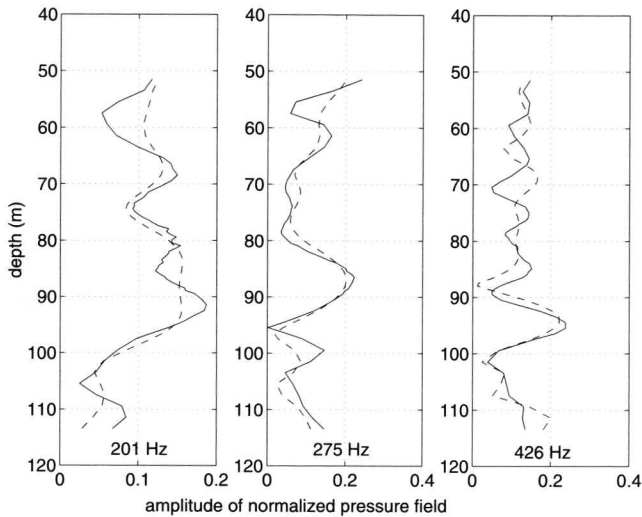


Fig. 3 Optimized (dashed) and measured (solid) pressure fields.

The resulting geo-acoustic model is shown in Fig. 4, and is taken as the environment of that parameter set that corresponds to the lowest value for the energy function (parameter set #1 of Table IV). The sound speed corresponds to a sand-silt-clay sediment (see Chapter 2), and is similar to the sediment sound speed obtained for the ADVENT99 experiments.

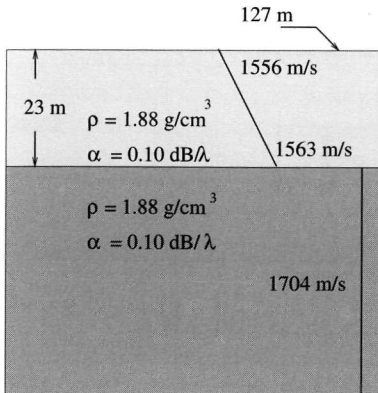


Fig. 4 Geo-acoustic model obtained for the site visited during MAPEX on the Malta plateau.

## 9.4.2 North of Elba

In this section inversion results of data recorded in the area north of Elba are presented.

Data transmitted at 2-km distance, at both sides from the VA, have been used in the inversions. Five independent inversions have been carried out for each of the two positions. The two snapshots selected were transmitted when NRV *Alliance* was at 1.926 km south of

the array, sailing towards it, when *Alliance* was at 1.911 km north of the array, sailing away from it.

Table V presents the GA+DHS results. Considering the first five columns, it is concluded that the last two of these (S#4 and S#5) correspond to a local minimum, with a smaller sediment thickness, a lower density, a higher attenuation, a larger water depth, and higher energy function values. Considering the results that correspond to inversion results for the snapshot that was transmitted north of the array (N), there also appears to be a local minimum (N#2 and N#5), now with a larger sediment thickness, a higher density, a lower attenuation, and higher energy function values.

Table V GA+DHS results of 5 independent inversions for the two data snapshots, transmitted at 12:29 UTC, i.e., south (S) of the VA, and at 13:00 UTC, i.e., north (N) of the VA.

	S#1	S#2	S#3		N#1		N#3	N#4
$C_{1, \text{sed}}$ (m/s)	1530	1525	1526		1520		1523	1519
$h_{\text{sed}}$ (m)	21	26	26		6.5		6.7	6.7
$C_{2, \text{sed}}$ (m/s)	1625	1655	1650		1635		1633	1641
$C_b$ (m/s)	1713	1855	1679		1842		1872	1864
$\rho$ (g/cm <sup>3</sup> )	1.8	1.7	1.7		1.7		1.8	1.8
$\alpha$ (dB/ $\lambda$ )	0.20	0.16	0.16		0.86		0.89	0.91
$r_s$ (m)	2015	2031	2031		1606		1594	1589
$z_s$ (m)	69	69	69		63		63	63
$\theta$ (degr)	1.0	1.0	1.0		-0.9		-0.9	-0.9
$H_w$ (m)	121	121	121		120		120	120
$h_l$ (m)	14	13	13		14		14	14
$E$	0.14	0.14	0.14		0.18		0.18	0.18

Figs. 5 and 6 show the *a posteriori* distributions corresponding to the GA inversion results of the snapshot transmitted south (S) of the array and the snapshot transmitted north (N) of the array, respectively. The local minima mentioned above can also be seen in these figures. From Fig. 5 it is seen that for the south side of the array the upper sediment sound speed is determined quite accurately, with values in between 1510 and 1530 m/s. The sediment thickness shows two peaks, of which the peak at a sediment thickness of ~10 m corresponds to a higher energy, see Table V. Lower sediment sound speeds are in between 1620 and 1680 m/s. Density shows a large spread, with values  $> 1.5 \text{ g/cm}^3$  corresponding to lower values for the energy function than the densities  $< 1.5 \text{ g/cm}^3$ . The attenuation shows two peaks with the attenuation constant of ~0.25 dB/ $\lambda$  corresponding to the lowest energy. Source depth and tilt are determined unambiguously, whereas the *a posteriori* distribution for source/receiver range and water depth show two peaks. The peaks at the highest values for these two parameters correspond to the lowest values for the energy. The lowest, right-most subplot shows the *a posteriori* distribution for the sediment sound speed gradient that was calculated from the inverted sediment sound speeds and the sediment thickness. For the area south of the array, the minimum in energy is encountered for a sediment sound speed gradient of  $4.4 \text{ s}^{-1}$ . The corresponding sediment thickness is ~22 m. The peaks in the *a posteriori* distribution for the sediment sound speed gradient at gradients  $> 10 \text{ s}^{-1}$  correspond to sediment thicknesses of ~10 m, i.e., a local minimum.

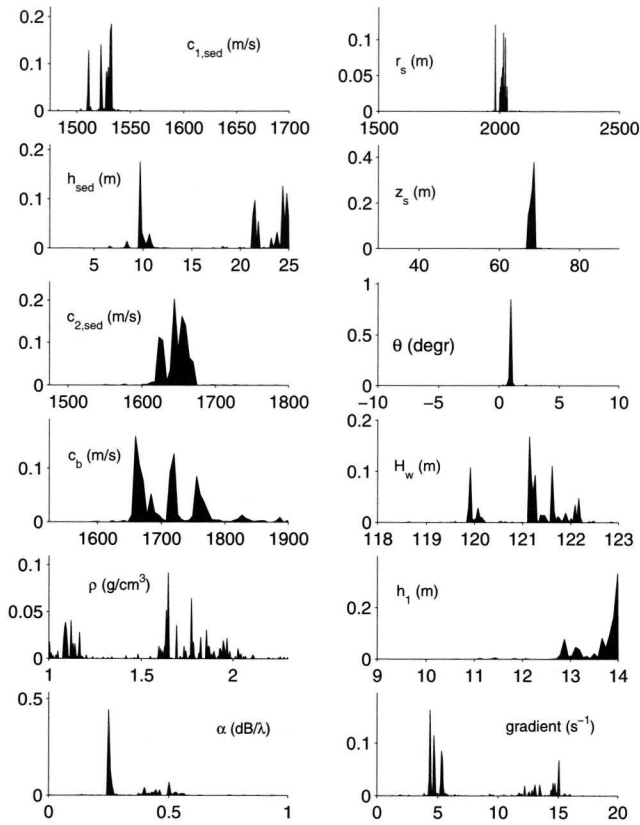


Fig. 5 *A posteriori* distributions of GA solutions obtained for the snapshot that was transmitted south of the array.

Figure 6 shows that for many parameters resulting from inversions of data transmitted at the north side of the array a distribution similar to that at the south side of the array is obtained. However, for the attenuation somewhat higher values are found. In Fig. 6 three peaks are present in the plot showing the *a posteriori* distribution of the lower sediment sound speed. Analysis (not shown here) indicates that each of these peaks correspond to one of the peaks in the sediment thickness. This results in the relatively peaked distribution for the sediment sound speed gradient. The sediment sound speed gradient corresponding to the lowest energy amounts to 19 s<sup>-1</sup>.

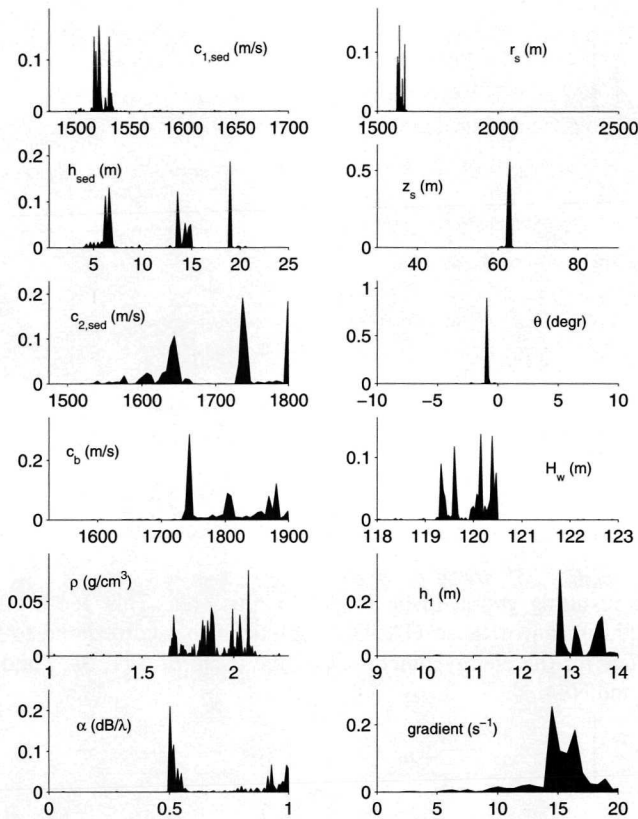


Fig. 6 *A posteriori* distributions of GA solutions obtained for the snapshot transmitted north of the array.

Figure 7 shows for the frequencies used in the inversions, the pressure fields as measured south of the array and the S#3 optimized pressure fields. Clearly the inversion has provided a parameter set that results in an acceptable match between the two sets pressure fields. The agreement between measured and optimized pressure fields north of the array is similar, and is therefore not shown here.

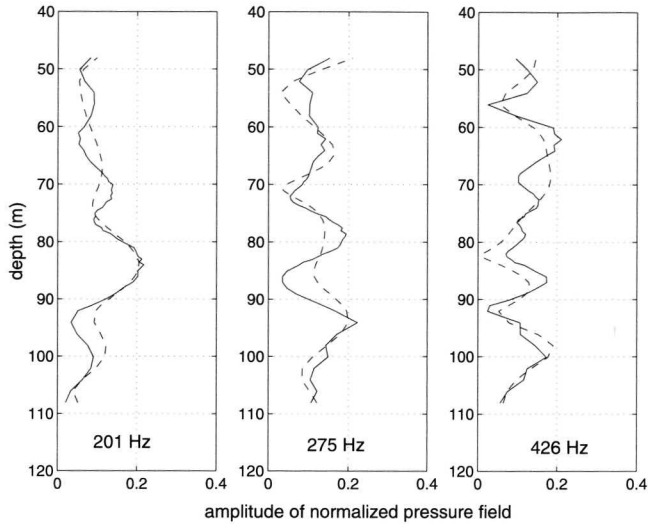


Fig. 7 Pressure fields as measured south of the array (solid) and corresponding optimized pressure fields (dashed).

Figure 8 shows the resulting geo-acoustic model for this area. This geo-acoustic model is obtained by taking the mean of those GA+DHS solutions that correspond to the minimum with the lowest values for the energy function, i.e., the mean of S#1, S#2, and S#3, and the mean of N#1, N#3, and N#4.

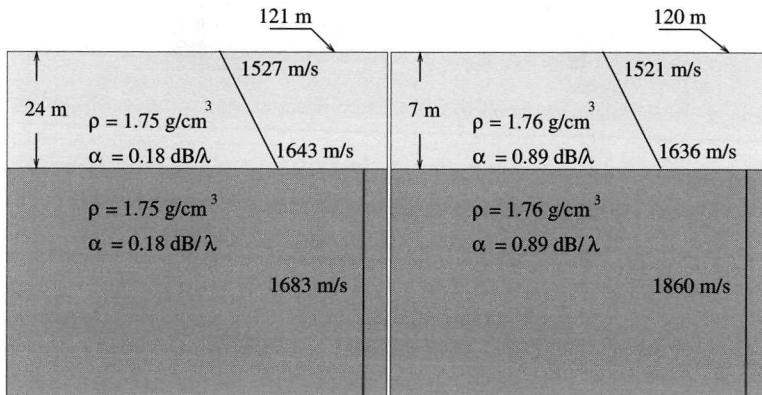


Fig. 8 Geo-acoustic model obtained from inversions of data transmitted at 2 km south of the array (left plot), and 2 km north of the array (right plot).

### 9.4.3 Southeast of Elba

Data transmitted at 2.01 km distance have been used for the inversions.

In Table VI the inversion results are presented. Clearly, a low sound speed sediment is found. Considering the results corresponding to the lowest values of the energy function, i.e., columns #1 - #3, and #5, the values for the upper sediment sound speed range from 1422 to 1444 m/s.



Table VI GA+DHS results of 7 independent inversions for the data snapshot transmitted at 10:51 UTC, i.e., at the left side of the VA.

	#1	#2	#3	#4	#5	#6	#7
$c_{i, \text{sed}}$ (m/s)	1434	1422	1427	1437	1444	1395	1459
$h_{\text{sed}}$ (m)	11	8.2	11	8.2	8.8	8.1	25
$c_{2, \text{sed}}$ (m/s)	1477	1428	1487	1437	1444	1439	1659
$c_b$ (m/s)	1610	1608	1589	1606	1592	1631	1659
$\rho$ (g/cm <sup>3</sup> )	2.3	2.0	2.2	1.5	1.9	2.2	1.1
$\alpha$ (dB/ $\lambda$ )	0.43	0.37	0.16	0.43	0.26	0.59	0.11
$r_s$ (m)	1542	1527	1593	1576	1574	1484	1844
$z_s$ (m)	31	31	31	31	31	30	31
$\theta$ (degr)	0.091	-0.082	0.075	0.45	-0.43	0.38	1.0
$H_w$ (m)	121	121	122	124	123	120	121
$h_l$ (m)	11	11	11	12	12	11	13
$E$	0.21	0.19	0.22	0.28	0.20	0.23	0.32

Figure 9 shows the *a posteriori* distributions, employing all inversion results. All upper sediment sound speed values are less than 1500 m/s, indicating a clayey silt (or mud) bottom, see Chapter 2. Both the sediment thickness and the lower sediment sound speed show two peaks. Analysis shows that these two peaks correspond to each other, such that a smaller sediment thickness corresponds to a lower sound speed at the bottom of the sediment. However, this coupling does not result in one value for the sediment sound speed gradient. The small thickness, low sediment sound speed at the bottom of the sediment combination results in a gradient of  $\sim 2 \text{ s}^{-1}$ , whereas the thick sediment with a higher sound speed at the bottom of the sediment corresponds to a gradient of  $\sim 12 \text{ s}^{-1}$ . The sediment sound speed gradient corresponding to the minimum energy amounts to  $2 \text{ s}^{-1}$ . Both the density and the attenuation show a large spread. Therefore, the values presented in the table above should be interpreted with care.

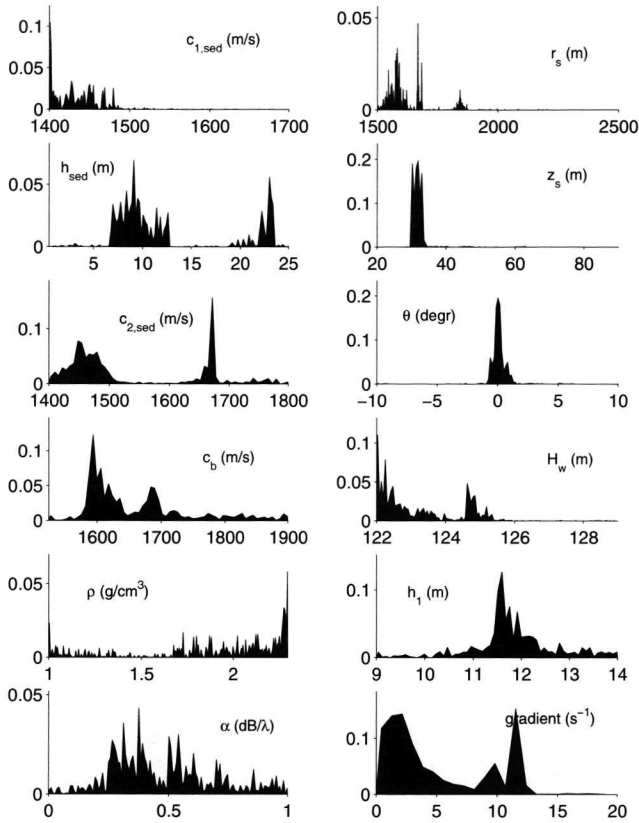


Fig. 9 *A posteriori* distributions of GA solutions obtained for Julian day 335.

Figure 10 shows for the frequencies used in the inversions, the measured pressure fields and the optimized pressure fields. The optimized pressure fields are calculated for the parameter set that correspond to the lowest energy.

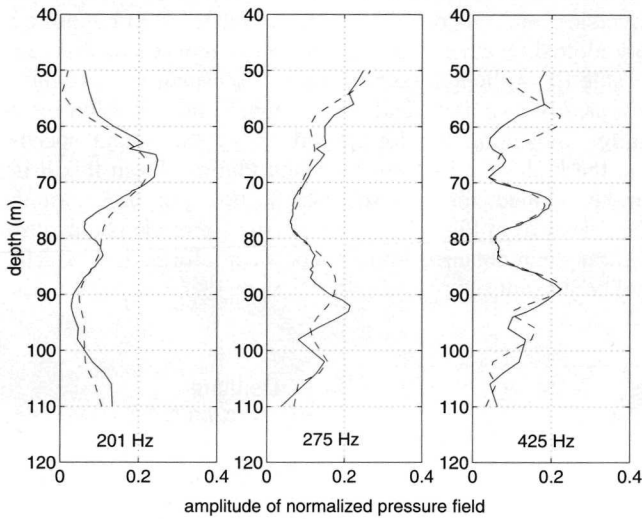


Fig. 10 Optimized (dashed) and measured (solid) pressure fields.

Figure 11 shows the resulting geo-acoustic model, taking into account results #1 to #3 and #5, since these correspond to the lowest values for the energy function.

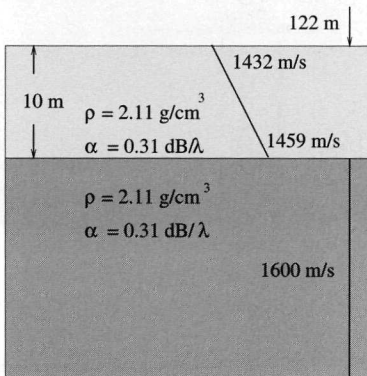


Fig. 11 Geo-acoustic model obtained from inversions of data transmitted at 2 km from the array.

Clearly the sound speed is low, in accordance with the results of the literature survey, presented in Section E.3. The density, and also, but to a lesser extent, the attenuation are too high for a mud sediment. However, from Fig. 9 it is seen that these two parameters are not well determined.

## 9.5 Assessment of the inversion results

As mentioned in the introduction, the goal of the analysis presented in this chapter is to demonstrate the applicability of MFI for bottom classification purposes. Clearly the inversions come up with different results for the three different areas that were surveyed during MAPEX. To see whether these differences are also present in the independent measurements, the inversion results are compared with the results obtained from the literature survey, see Section 9.2. For this comparison we have selected the sound speed at the top of

the sediment, because experience has learned that this parameter can be determined quite accurately through inversion, and this parameter directly relates with bottom type. In Fig. 12 these sound speeds are plotted together with the range of sediment sound speed values found in the literature, see Table III. Although, no independent information was available exactly at the MAPEX positions, clearly a similar trend is seen both in the inversion results, and in the independent information, indicating the lowest values for the sound speeds in the area southeast of Elba, and the highest values on the Malta Plateau. From this it is inferred that MFI techniques can be applied for bottom classification purposes. Another important conclusion that can be drawn from Fig. 12 is that inversions provide geo-acoustic parameters significantly more accurate than obtained from independent information, which in the current case consists mainly of core results.

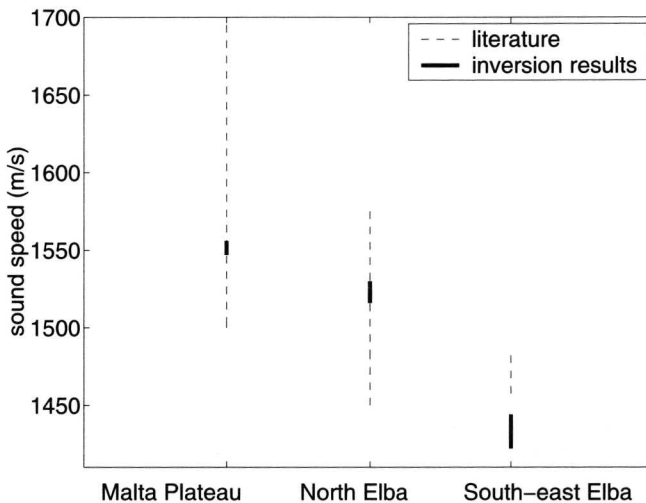


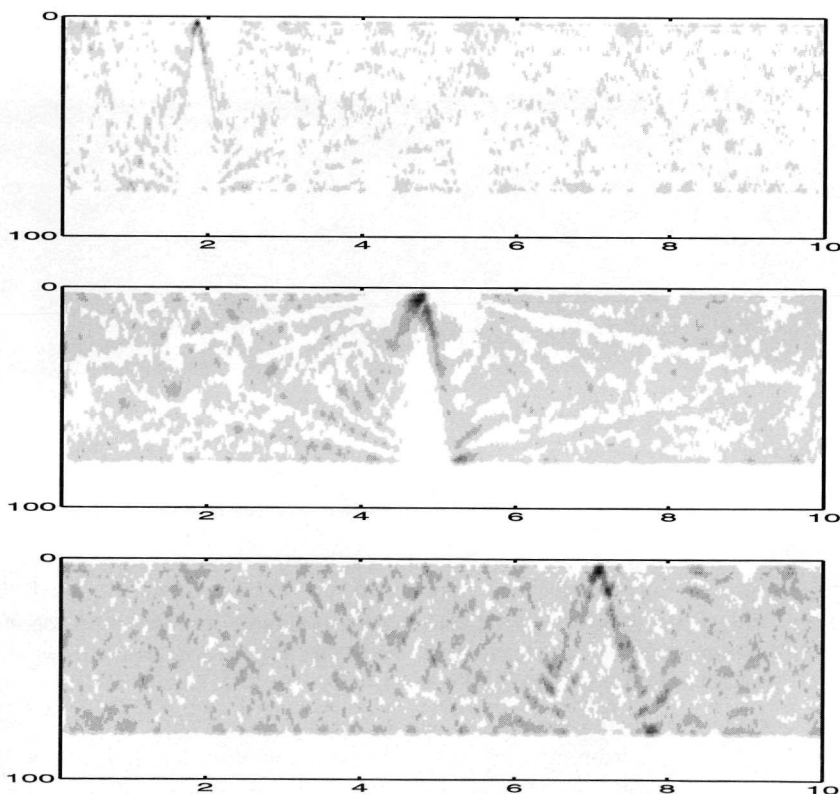
Fig. 12 Sound speed values as found in literature and those obtained from the inversions for the three areas surveyed during MAPEX.

## 9.6 Applications

In this section the importance of having available a bottom classification technique is demonstrated by two applications, being the source localization problem and the use of sonar performance prediction models.

We start of with the problem of localizing a source in both range and depth. It should be mentioned that conventional active sonar systems are capable of localizing a source, or a target, in range and in bearing, whereas conventional passive sonar systems can localize sources in bearing only. In all previous chapters a search was performed for a (large) set of unknown parameters. When this set of unknowns is decreased to two, being the source depth and the source range, the technique is no longer denoted by MFI, but by matched field processing (MFP). MFP, therefore, allows for passively localizing a source in both range and depth. The MFP results are presented as so-called 'range-depth ambiguity surfaces' in which the match, or similarity, between measured and calculated signals is presented as a function of range and depth. Note that thereby the target is also classified as being either a surface ship, or a submarine. Experience has learned that for applying the MFP technique the environment needs to be known accurately. In the preceding chapters the applicability of MFI for this

problem was demonstrated. For source localization in unknown areas the approach might therefore be to first use MFI for obtaining information on the geo-acoustics and on the geometry, and to then apply MFP for localizing sources in the area. For illustrating this approach we use data acquired during the ADVENT99 experiment, see Chapter 6. In Chapter 6 results of inversions are presented for data that were collected during experiments with the source at a 2-km distance from the vertical receiving array. During these experiments the Italian navy ship (INS) *Ciclope* was sailing back and forth along the acoustic track, collecting CTD-chain data. The aim now is to localize with MFP the INS *Ciclope* by its radiated noise. The geo-acoustic model employed in the forward model calculations consists of the above-mentioned Chapter 6 inversion results. Several snapshots of noise data in the band 550-650 Hz, radiated by INS *Ciclope* were selected, spanning the total period needed for INS *Ciclope* to sail back and forth along the acoustic track. It should be noted that the geo-acoustic (and geometric) parameters were estimated using acoustic data that were collected for a source/received distance of 2 km. Figure 13 shows the resulting range-depth ambiguity surfaces, showing the position of the INS *Ciclope* along the track. These results clearly illustrate that the estimates for the unknown parameters, as obtained through MFI, are also accurate enough for localizing sources at those positions of the track of which no data were used in the inversions, i.e., at distances larger than 2 km.



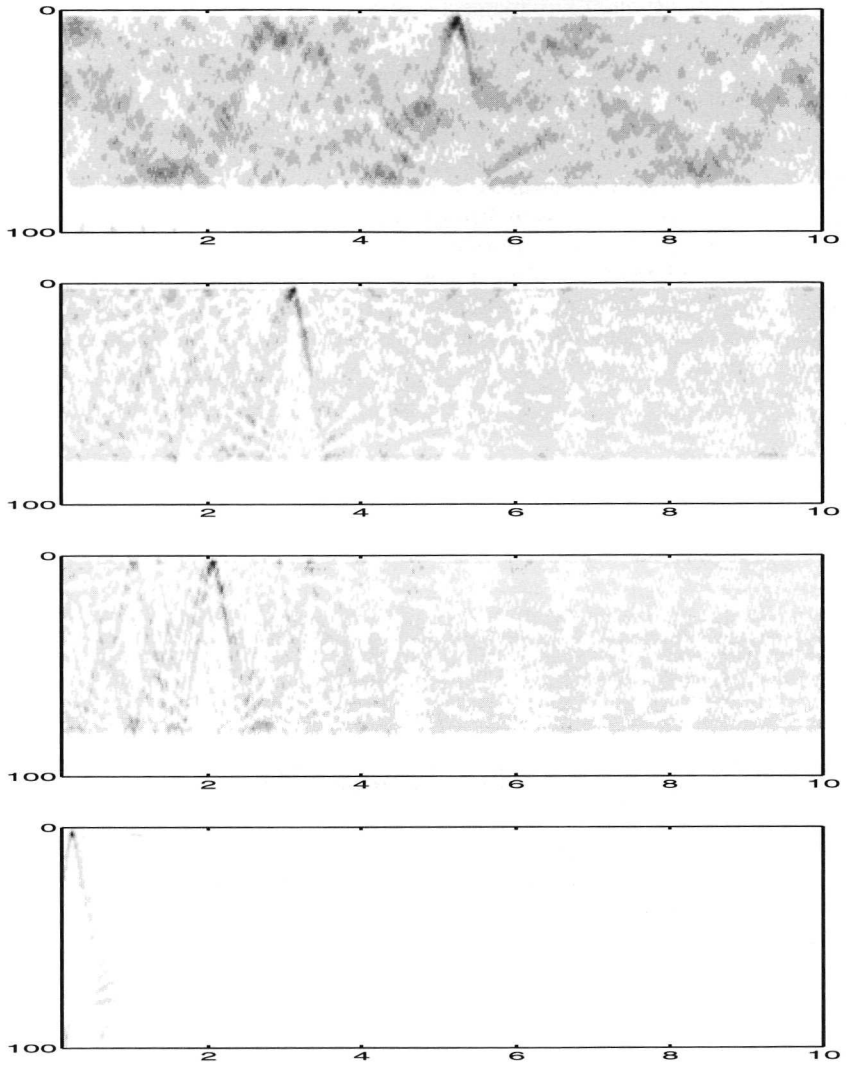


Fig. 13 Range-depth ambiguity surfaces, with range along the  $x$ -axis (in km) and depth along the  $y$ -axis (in m). Note the difference in scale between the  $x$ - and  $y$ -axis, with the total depth span being only 100 m, and the total range span 10 km.

As a second example, illustrating the need for accurate information on bottom parameters, we consider the sonar performance prediction models as used on board of navy vessels.<sup>9</sup> The situation is that of passive detection in a narrow band, also called 'line detection', and we consider the detection probability for the two environments of Chapter 2. The two environments differ with respect to their bottom type, viz., a sand-silt-clay bottom, and a mud bottom. Sonar performance prediction models solve the 'sonar equations', and estimate the probability on detection of a signal against noise. The sonar equation for passive sonar and an omnidirectional-hydrophone can be written as

$$SL - TL - NL = DT \quad (1)$$

with  $SL$  the source level,  $TL$  transmission loss,  $NL$  the noise level and  $DT$  the detection threshold. All terms are in dB. Based on  $DT$ , which is actually signal-to-noise-ratio, the probability of detection is calculated. Figure 14 shows for the two environments the probability of detection, as a function of target range and depth, for a receiving omnidirectional hydrophone at 20 m depth. In this example, the model calculates the environmentally dependent noise level  $NL$  for a wind speed of 8 m/s. The source level  $SL$  of the line to be detected, for which we selected 500 Hz, amounted to 130 dB. Note the striking difference in detection range for the two bottoms. For the sand-silt-clay bottom the detection probability is 100 % up to 8-9 km, whereas it is close to zero after 5 km range for the mud bottom. Again, the importance of having available detailed information about the seabed is illustrated.

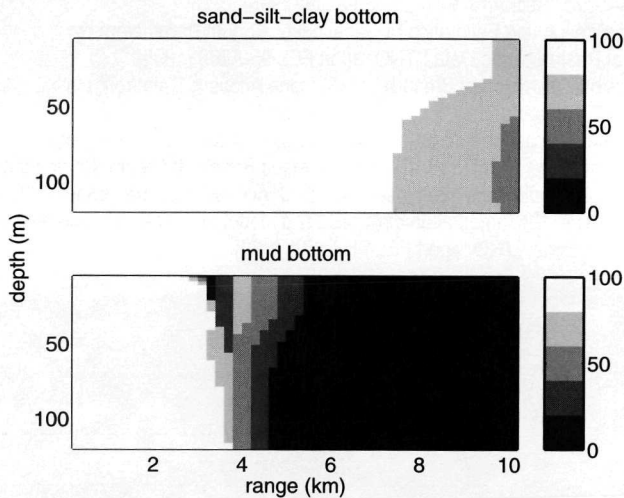


Fig. 14 Probability of detection as a function of target position for the two environments of Chapter 2 (sand-silt-clay bottom and mud bottom) as calculated by the sonar performance prediction model.

## References

- <sup>1</sup> J. Sellschopp, M. Siderius, and P. Nielsen, "ADVENT99, pre-processed acoustic and environmental cruise data," CD-35, SACLANT Undersea Research Centre, La Spezia, Italy (2000).
- <sup>2</sup> B. Tonarelli, F. Turgutcan, M.D. Max, and T. Akal, "A comparison of shallow sediment properties in four locations on the Sicilian-Tunisian platform," SM-267, SACLANT Undersea Research Centre, La Spezia, Italy (1993).
- <sup>3</sup> J. C. Osler, L. Gualdesi, E. Michelozzi, and B. Tonarelli, "Piston coring capabilities at SACLANTCEN: minimizing and assessing core disturbance," SR-321, SACLANT Undersea Research Centre, La Spezia, Italy (2000).
- <sup>4</sup> D.F. Gingras, and P. Gerstoft, "Inversion for geometric and geoacoustic parameters in shallow water: Experimental results," *J. Acoust. Soc. Am.*, **97** (6), 3589-3598 (1995).
- <sup>5</sup> D.G. Simons, "Source localization and Estimation of Geoacoustic Bottom Parameters by Matched Field Inversion of Real Acoustic Data," TNO report FEL-95-A260 (1995).
- <sup>6</sup> J.P. Hermand, and P. Gerstoft, "Inversion of Broad-band Multitone Acoustic Data from the YELLOW SHARK Summer Experiments," *IEEE J. Ocean. Eng.* **21** (4), 324-346 (1996).
- <sup>7</sup> M.R. Fallat, P.L. Nielsen, and F.B. Jensen, "Geo-acoustic inversion of the PROSIM' 97 experimental data using simplex simulated annealing," SM-332, SACLANT Undersea Research Centre, La Spezia, Italy (2000).
- <sup>8</sup> E.L. Hamilton, "Sound velocity gradients in marine sediments," *J. Acoust. Soc. Am.*, **65** (4), 909-922 (1978).
- <sup>9</sup> P. Schippers, and S.P. Beerens, "Documentation of ALMOST, a model for range dependent propagation and sonar performance predictions," TNO report FEL-98-A126 (1999).



## Chapter 10

# Summary and conclusions

In this thesis the bottom classification technique 'matched field inversion' (MFI) has been investigated. MFI can be applied for determining unknown sea bottom parameters, such as sediment density and sediment sound speed, and other parameters that influence the propagation of sound under water. The applications requiring bottom information are manifold. They include topics such as mine hunting, both with regards to the effectiveness of mine hunting operations and the extent to which mines get buried in the sea bottom. Other topics include source localization, employing sonar performance models, dredging, fisheries, and off-shore applications. This is illustrated at the end of the previous chapter for the source localization and sonar performance model application.

With MFI the unknown parameter values are estimated by maximizing the match between measured under water acoustic signals and modeled acoustic signals. The latter are a function of the unknown parameters. Since the amount of unknown parameters is often large (in the order of at least ten) and since there can be local optima, a global optimization method is required for finding the set of unknown parameters corresponding to the maximum match. For this application, two global optimization methods have been considered, being the genetic algorithm and simulated annealing. The two methods have been applied to a typical underwater acoustic inversion problem, favoring the genetic algorithm with regards to its performance in rapidly finding the global optimum with a high success rate. As a second step for assessing the optimization method, an internationally recognized benchmark problem is used for comparing the resulting matched field inversion tool with other approaches, clearly indicating its good performance.

Several experiments have been carried out with the goal to further assess and validate the technique. It is clearly demonstrated that also in the case of practical situations the technique is capable of determining the unknown parameters, as long as they indeed influence the acoustic propagation. Parameters that are strongly correlated can not be determined themselves. Employing data at multiple frequencies is found to result in more accurate and realistic parameter estimates. However, since the scales of features influencing the acoustic propagation depend on the frequency, results obtained at one frequency are not always applicable at other frequencies.

An important item when searching for the unknown parameter values is the accuracy of the resulting parameter estimates. A dedicated experiment has been conducted for investigating the different origins of the parameter uncertainty. These origins comprise the optimization method itself, the influence of variations in the water column sound speed profile as a function of time, resulting from e.g. internal waves, and the noise in the data. The global optimization method itself was found to be a large contributor to the parameter uncertainty. By applying a local optimization method after the global search the influence of the optimization method could, however, be almost completely eliminated. Two local optimization methods are considered, being both the downhill simplex methods, and the Levenberg-Marquardt method. Downhill simplex is more robust, but time consuming.

Levenberg-Marquardt is efficient in locating the optimum. However, contrary to the downhill simplex method, Levenberg-Marquardt does not always result in an optimized parameter estimate. In addition to the optimization method also the oceanographic variability was found to give a large contribution to the uncertainty in the parameter estimates.

Besides geo-acoustic parameters, matched field inversion has also been applied for determining parameters of the water column sound speed. The sound speed profile was not determined directly, but through the use of empirical orthogonal functions, thereby limiting the amount of unknowns. In addition to this tomographic application, where the goal is to estimate parameters of the water column, the ability to estimate parameters of the water column sound speed profile can also be used for reducing the influence of the oceanographic variability on the uncertainty of the parameter estimates: When also estimating the water column sound speed as a function of time, the effect of the variation of the water column sound speed on the other parameter estimates is eliminated. Since this effect is not seen in the results presented in this thesis more research is needed. A reason for this might be that also the range-dependency of the water column sound speed profile has to be accounted for.

MFI has been applied for estimating bottom parameters for a wide range of bottom types, ranging from clay to sand-silt types of bottom. For all these bottom type, the method was found to be capable of accurately predicting the bottom type over large areas. The effect of bottom type on the accuracy of the inversion results has not been investigated. However, it is expected that for longer ranges, due to the attenuation of the sound, it is more difficult to estimate bottom properties for clay type bottoms, than for sand type bottoms. It should be noted that no rock bottoms have been considered. It is expected that when applying matched field inversion for these types of bottoms, additional parameters, such as scattering strengths, have to be included in the inversion. On the other hand, probably any bottom layering can be neglected.

The standard bottom classification technique that is currently operationally available is to take samples of the sea bottom, a costly and time-consuming operation as information over large areas is normally required. MFI is shown to be an accurate alternative for obtaining bottom information over large areas (several km). It requires a sound source and a receiving system. For the work described in the thesis the receiving system consists of a sonar array of hydrophones, placed vertically in the water column. Since this system is not very easily handled in operational circumstances, future research is needed for developing approaches that allow for the application of MFI using operational sonar systems, such as drifting air-deployed sonobuoys, containing a single hydrophone, and horizontally towed arrays. This latter system is typically available on board of navy frigates.

## Appendix A

### A numerical solution to the modal equation

For applying finite-difference discretization, each layer (water column, sediment, sub-bottom) is divided into equally spaced (per layer) intervals. When dividing the water column into  $N$  intervals  $h_w$ , the mesh in the water column is

$$z_j = jh_w \quad j = 1, 2, \dots, N \quad (1)$$

with

$$H_w = Nh_w \quad (2)$$

The mesh in the sediment ( $M$  intervals) and the mesh in the sub-bottom ( $K$  intervals) are

$$z_j = H_w + (j - N)h_s \quad j = N + 1, N + 2, \dots, N + M \quad (3)$$

$$z_j = H_w + H_s + (j - N - M)h_b \quad (4)$$

$$j = N + M + 1, N + M + 2, \dots, N + M + K - 1$$

Figure 1 illustrates the finite-difference discretization.

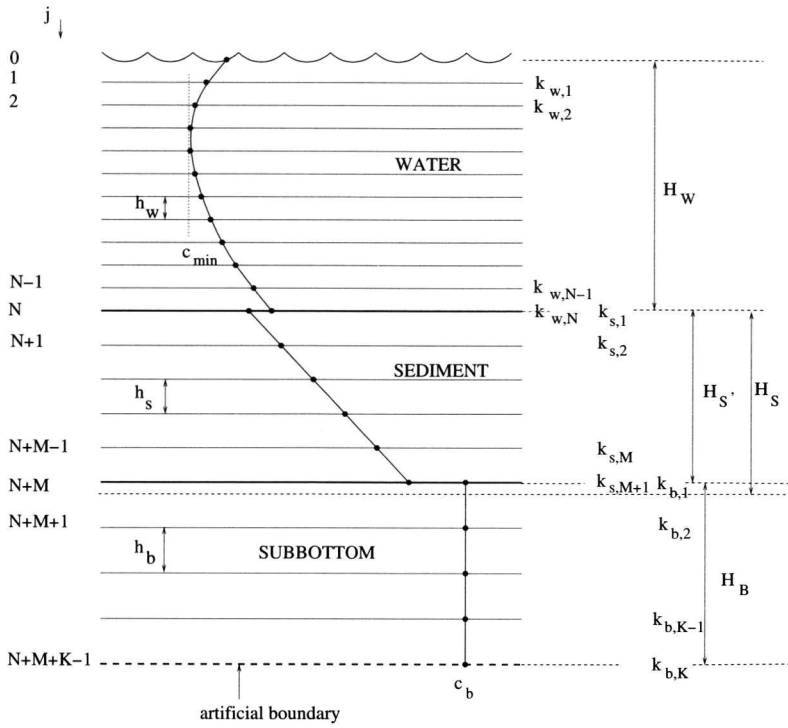


Fig. 1 Discretization of the ocean environment.

As mentioned before  $H_b$  must be taken sufficiently large to represent ‘half-infinite’. All three intervals  $h_w$ ,  $h_s$ , and  $h_b$  are different. It should also be noted that a small correction is applied to  $H_s$ . It will be shown in the remainder of this section that by using the finite-difference discretization the problem can be written as

$$A\Psi = \mu\Psi \tag{5}$$

with

$$\Psi = \begin{pmatrix} \psi_1 \\ \psi_2 \\ \vdots \\ \psi_{S-1} \\ \psi_S \end{pmatrix} \tag{6}$$

with  $\mu$  the eigenvalue,  $\Psi(z_j) = \psi_j$ , and  $S = N+M+K-1$ .

## A.1 The finite-difference equations

From the forward and the backward Taylor series expansion the forward and backward  $O(h)$  approximation of the first derivative is obtained

$$\psi_j' = \frac{\psi_{j+1} - \psi_j}{h} \quad (7)$$

$$\psi_j' = \frac{\psi_j - \psi_{j-1}}{h} \quad (8)$$

Since in each layer, the density is assumed to be constant, the modal equation (Eq. (8) of Chapter 2) for mode  $n$  becomes

$$\frac{d^2 \Psi_n}{dz^2} + (k(z)^2 - k_n^2) \Psi_n = 0 \quad (9)$$

with  $k(z)$  the total wavenumber and the eigenvalue  $k_n$  the horizontal wavenumber of the  $n^{\text{th}}$  mode. Employing this expression, the following  $O(h^2)$  approximations for the first derivatives are obtained

$$\psi_j' = \frac{\psi_{j+1} - \psi_j}{h} + (k(z)^2 - \mu) \psi_j \frac{h}{2} \quad (10)$$

$$\psi_j' = \frac{\psi_j - \psi_{j-1}}{h} - (k(z)^2 - \mu) \psi_j \frac{h}{2} \quad (11)$$

Further, by adding the forward and backward Taylor series expansion, the  $O(h^2)$  approximation for the second derivative becomes

$$\psi_j'' = \frac{\psi_{j+1} - 2\psi_j + \psi_{j-1}}{h^2} \quad (12)$$

Now the modal Eq. (9) becomes

$$\frac{\psi_{j+1} - 2\psi_j + \psi_{j-1}}{h^2} + (k(z_j)^2 - \mu) \psi_j = 0 \quad (13)$$

or, for the water column ( $h = h_w$ )

$$\frac{\psi_{j-1}}{h_w^2} + \left[ \frac{-2}{h_w^2} + k_{w,j}^2 \right] \psi_j + \frac{\psi_{j+1}}{h_w^2} = \mu \psi_j \quad (14)$$

for  $j = 1, 2, \dots, N-1$  and  $j' = 1, 2, \dots, N-1$ . Similarly the modal equation for the sediment ( $h_s$ ) and the sub-bottom ( $h_b$ ) layer can be obtained

$$\frac{\Psi_{j-1}}{h_s^2} + \left[ \frac{-2}{h_s^2} + k_{s,j'}^2 \right] \Psi_j + \frac{\Psi_{j+1}}{h_s^2} = \mu \Psi_j \quad (15)$$

for  $j = N+1, N+2, \dots, N+M-1$  and  $j' = 2, 3, \dots, M$ .

$$\frac{\Psi_{j-1}}{h_b^2} + \left[ \frac{-2}{h_b^2} + k_{b,j'}^2 \right] \Psi_j + \frac{\Psi_{j+1}}{h_b^2} = \mu \Psi_j \quad (16)$$

for  $j = N+M+1, N+M+2, \dots, N+M+K-1$  and  $j' = 2, 3, \dots, K$ .

## A.2 Treatment of boundaries and interfaces

Since the sea surface is a pressure release surface ( $\psi_0 = 0$ ) Eq. (14) reduces for  $j=1$  to

$$\left[ \frac{-2}{h_w^2} + k_{w,1}^2 \right] \Psi_1 + \frac{\Psi_2}{h_w^2} = \mu \Psi_1 \quad (17)$$

At  $z = Ht = H_w + H_s + H_b$ , a rigid boundary is assumed, i.e.,  $\psi_j'$  for  $j = N+M+K-1$ . Using the  $O(h)$  forward approximation for the first derivative

$$\Psi_{N+M+K-1}' = \frac{\Psi_{N+M+K} - \Psi_{N+M+K-1}}{h_b} \quad (18)$$

one obtains

$$\frac{\Psi_{N+M+K-2}}{h_b^2} + \left[ \frac{-1}{h_b^2} + k_{b,K}^2 \right] \Psi_{N+M+K-1} = \mu \Psi_{N+M+K-1} \quad (19)$$

At the water/sediment interface ( $j=N$ ) and the sediment/sub-bottom interface ( $j=N+M$ ) the situation is more complicated. The finite-difference equations at these interfaces can be obtained by imposing that both the pressure and the particle velocity must be continuous. Continuity of pressure is imposed implicitly by assigning a unique value to  $\psi$  at the interface. Continuity of the particle velocity implies

$$\frac{\Psi'(z \uparrow H_w)}{\rho_w} = \frac{\Psi'(z \downarrow H_w)}{\rho_s} \quad (20)$$

Using the  $O(h^2)$  approximations for the backward and forward first derivatives this becomes

$$\frac{\psi_N - \psi_{N-1}}{h_w \rho_w} - (k_{w,N}^2 - \mu) \psi_N \frac{h_w}{2\rho_w} = \frac{\psi_{N+1} - \psi_N}{h_s \rho_s} - (k_{s,1}^2 - \mu) \psi_N \frac{h_s}{2\rho_s} \quad (21)$$

In order to allow for the use of efficient numerical methods, the matrix  $\mathbf{A}$  of Eq. (5) has to be symmetrical. This can be accomplished by choosing  $h_s$  according to

$$h_s = h_w \frac{\rho_s}{\rho_w} \quad (22)$$

Then

$$\frac{\psi_{N-1}}{h_w^2} + \left[ -\frac{1}{h_w^2} - \frac{1}{h_s^2} + \frac{k_{w,N}^2 + k_{s,1}^2}{2} \right] \psi_N + \frac{\psi_{N+1}}{h_s^2} = \mu \psi_N \quad (23)$$

Similarly by taking

$$h_b = h_w \frac{\rho_b}{\rho_w} \quad (24)$$

the finite-difference equation for the sediment/sub-bottom interface becomes

$$\frac{\psi_{N+M-1}}{h_s^2} + \left[ -\frac{1}{h_s^2} - \frac{1}{h_b^2} + \frac{k_{s,M+1}^2 + k_{b,1}^2}{2} \right] \psi_{N+M} + \frac{\psi_{N+M+1}}{h_b^2} = \mu \psi_{N+M} \quad (25)$$

With the finite-difference equations given above the matrix  $\mathbf{A}$  has the following form

$$\mathbf{A} = \begin{pmatrix} d_1 & e_1 & 0 & \cdots & \cdots & \cdots & 0 \\ e_1 & d_2 & e_2 & 0 & \cdots & \cdots & 0 \\ 0 & e_2 & d_3 & e_3 & 0 & & \vdots \\ \vdots & 0 & \ddots & \ddots & \ddots & & \vdots \\ \vdots & & \ddots & \ddots & \ddots & \ddots & 0 \\ \vdots & & & 0 & e_{s-2} & d_{s-1} & e_{s-1} \\ 0 & \cdots & \cdots & \cdots & 0 & e_{s-1} & e_s \end{pmatrix} \quad (26)$$

with

$$\mathbf{d} = \begin{pmatrix} -\frac{2}{h_w^2} + k_{w,1}^2 \\ -\frac{2}{h_w^2} + k_{w,2}^2 \\ \vdots \\ -\frac{2}{h_w^2} + k_{w,N=1}^2 \\ \frac{1}{h_w^2} - \frac{1}{h_s^2} + \frac{k_{w,N}^2 + k_{s,1}^2}{2} \\ -\frac{2}{h_s^2} + k_{s,2}^2 \\ \vdots \\ -\frac{2}{h_s^2} + k_{s,M}^2 \\ \frac{1}{h_s^2} - \frac{1}{h_b^2} + \frac{k_{s,M+1}^2 + k_{b,1}^2}{2} \\ -\frac{2}{h_b^2} + k_{b,2}^2 \\ \vdots \\ -\frac{2}{h_b^2} + k_{b,K-1}^2 \\ -\frac{1}{h_b^2} + k_{b,K}^2 \end{pmatrix}, \quad \mathbf{e} = \begin{pmatrix} 1/h_w^2 \\ 1/h_w^2 \\ \vdots \\ 1/h_w^2 \\ 1/h_s^2 \\ 1/h_s^2 \\ \vdots \\ 1/h_s^2 \\ 1/h_b^2 \\ 1/h_b^2 \\ \vdots \\ 1/h_b^2 \end{pmatrix} \quad (27)$$

The eigenvalue problem, Eq. (5), is solved by using EISPACK routines that determine the eigenvalues and eigenvectors (or eigenfunctions) for the real symmetric tridiagonal matrix  $\mathbf{A}$  in the specified interval  $\left(\frac{\omega}{c_b}\right)^2 < \mu < \left(\frac{\omega}{c_{\min}}\right)^2$ .



## Appendix B

### The vertical sonar array as receiving system

In the majority of the chapters of this thesis use is made of experimentally obtained data. In these chapters only a brief discussion of the equipment is presented. Therefore, more details on the experimental equipment are provided here. During all experiments considered, the receiving system consisted of a vertical array (VA), owned by the NATO institute Saclant Undersea Research Centre.<sup>1</sup> The array used during the experiment described in Chapter 3 contains 48 hydrophones with a spacing of 2-m. The array used during the Enverse 97 (Chapter 5), the ADVENT99 (Chapter 6 - Chapter 8), and the MAPEX200bis experiments (Chapter 9), is a nested array (spacings of 2 m, 1 m and 0.5 m) containing 64 hydrophones.

Figure 2 gives a schematic of the mechanical configuration of the VA. It is fixed at the bottom by a weight, and kept in a vertical position by the subsurface float. The received signals are sent, via the radio buoy, to the NRV *Alliance* by telemetry. The data acquisition system is located on board of the NRV *Alliance*.

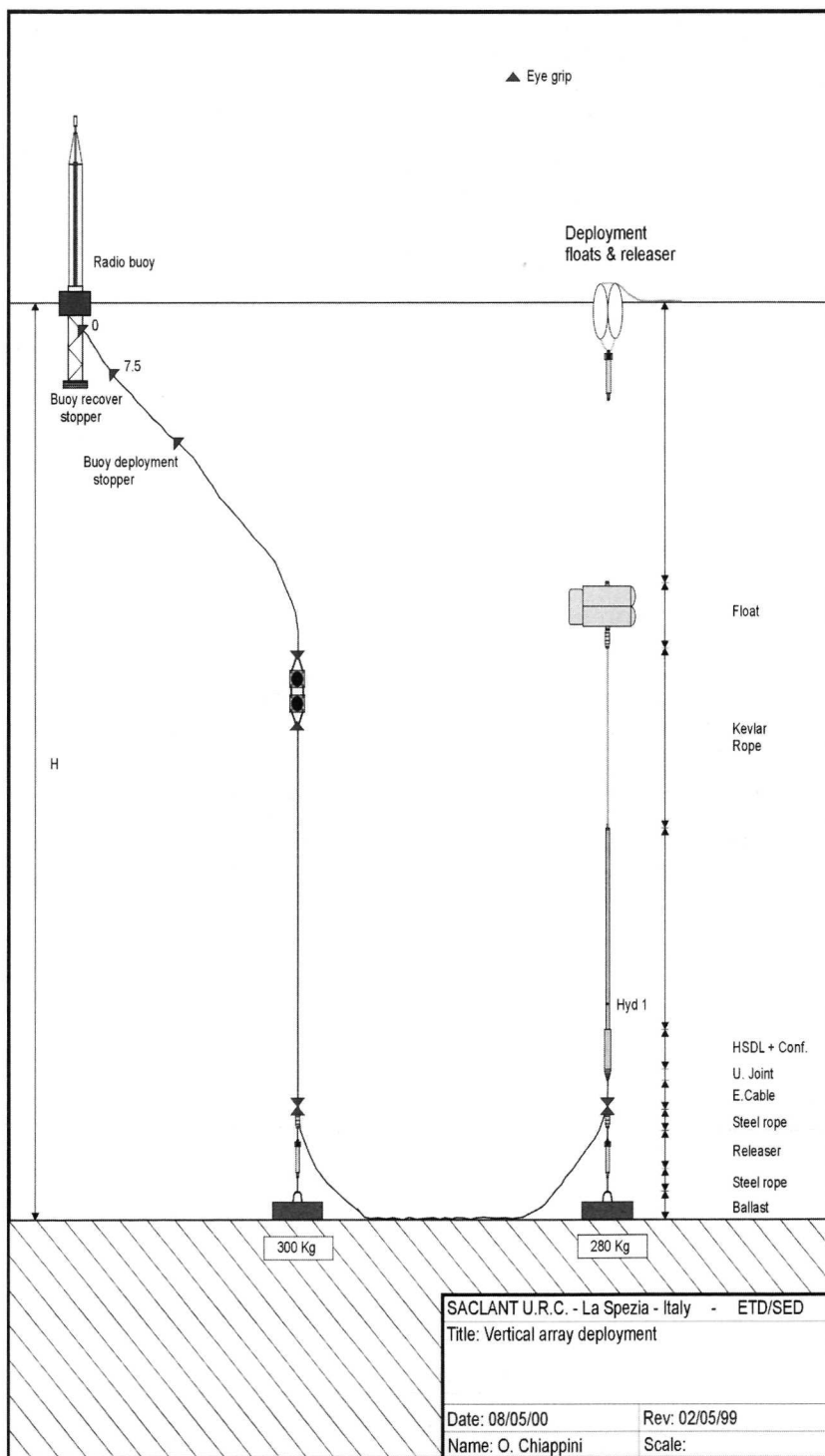


Fig. 1 The vertical array configuration.

A block diagram of the data acquisition system on board is given in Fig. 2. It consists of an acoustic section (hydrophone + pre-amplifier), attached to a separate module, which provides programmable signal conditioning, digitization, and serialization of the hydrophone signals. The latter section is denoted by the high-speed data link (HSDL). The sample frequencies applied amount to 3 and 6 kHz. The corresponding cut-off frequencies of the anti-alias filter are 1 and 2 kHz, respectively.

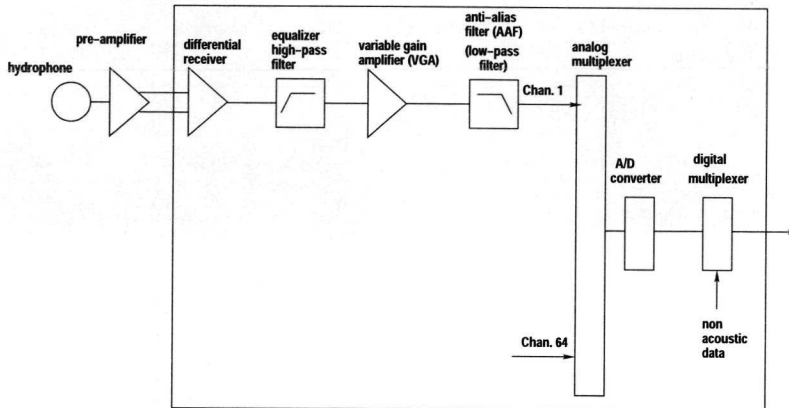


Fig. 2 Block diagram of the vertical array data acquisition system.

Finally, Fig. 3 shows the set-up for a typical matched field inversion experiment. During the ADVENT99 experiment this set-up was slightly different, with a source mounted on a tower construction to keep it fixed at the bottom.

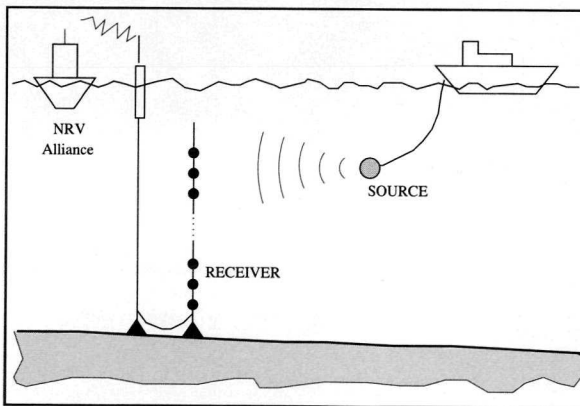


Fig. 3 Set-up of a typical matched field inversion experiment.

## Reference

- <sup>1</sup> L. Troiano, P. Guerrine and A. Barbagelata, "SACLANTCEN towed and vertical array system characteristics," SACLANTCEN report M-117 (1995).

## Appendix C

# Global optimization of a test function

In this appendix the performance of the GA as a function of its setting is assessed through the use of a test function. It should be noted that to perform a similar study for the real acoustic problem is not feasible, since in this case the function evaluation is too slow.

The test function used has the following form<sup>1,2</sup>

$$\begin{aligned}
 z = & [4.8 + x_1^2 + 5x_2^2 + 0.1x_3^2 + 0.05x_4^2 + x_5^2 + x_6^2 + \dots \\
 & - 0.3 \cos(\pi(x_1 - x_2)) - 1.4 \cos(\pi(x_1 + x_2)) - 0.5 \cos(10\pi(0.05x_4 - 0.1x_3)) + \dots \\
 & - 1.0 \cos(10\pi(0.05x_4 + 0.1x_3)) - 0.25 \cos(2\pi(x_5 - x_6)) - 1.35 \cos(2\pi(x_5 + x_6))] / 20
 \end{aligned}$$

The features of this function include: a reasonable number of parameters (6 in total), local minima, parameter correlations and varying sensitivity of  $z$ . The minimum of this function is at  $x_i = 0$ , ( $i = 1, \dots, 6$ ). Figure 1 shows 1-D and 2-D cross-sections of  $z$ . Parameters that are not varied are kept at their value at the global minimum, i.e., zero.

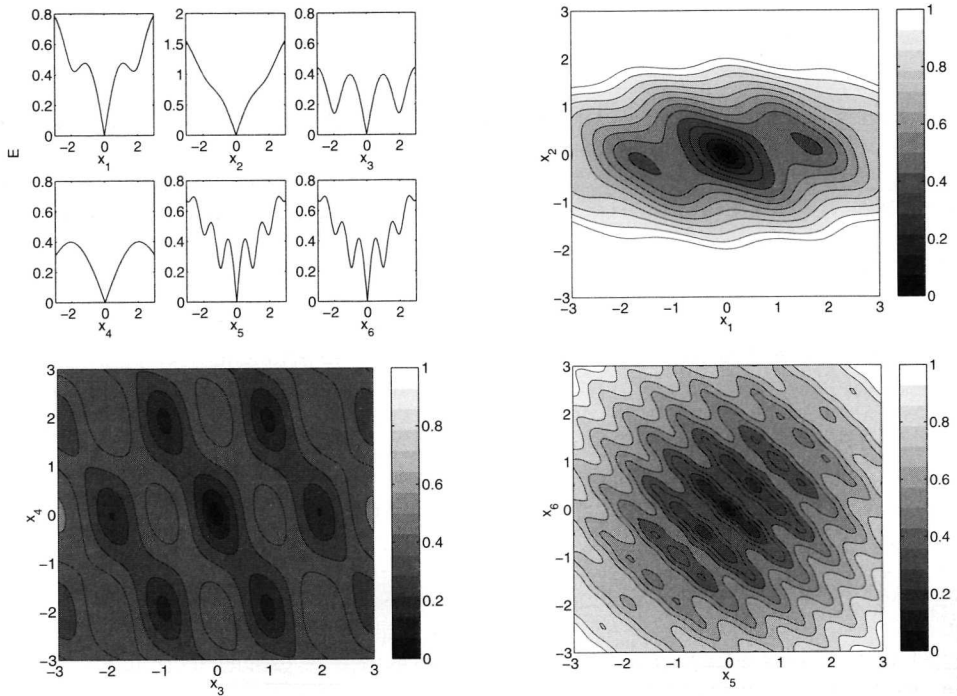


Fig. 1 1-D and 2-D cross-sections of  $z$ .

This function is very suitable for investigating the performance of the genetic algorithm in finding the global optimum of the function  $z$ , since the computational effort for calculating  $z$  is small. In the following we will consider the influence of several of the GA-parameters on the performance of the genetic algorithm to find the global optimum of  $z$ .

## C.1 GA performance as a function of its setting

For investigating the performance of the GA, 1000 independent GA runs have been carried out for various settings of the genetic algorithm, i.e., for various values of the different GA-parameters. The GA-parameters and their default settings are:

- Number of generations: 601;
- The number of bits used for the coding of the parameters: 10 for each parameter. Together with the search bounds of  $[-3 \ 3]$ , this results in steps of  $\frac{3+3}{(2^{10}-1)} = 0.0059$ ;
- Reproduction size, i.e., the fraction of the population that is replaced by randomly selected children each generation  $f_r$ : 0.5;
- Population size  $q$ : 64;
- Crossover rate  $p_c$ : 0.8;
- Mutation rate  $p_m$ : 0.05.

When considering the performance of the GA, two measures can be considered. These are 1) the percentage of the runs that have located the global optimum, and 2) the time that was

needed to accomplish this. Some preliminary runs were carried out to estimate a criterion for determining whether the global optimum has been located. The requirement that all six unknown parameters should be in between  $-0.2$  and  $+0.2$ , was found to be a suitable criterion, since it excludes all surrounding local minima.

To determine the percentage of converged runs, for each run the parameter set that corresponds to the lowest energy function found in the final population was considered. The run is converged if this parameter set satisfies the above-mentioned requirement. In order to allow for comparison of the GA performance for different setting, also the uncertainty on the percentage of converged runs has to be taken into account. The situation considered here, comprising a set of independent events, each with a certain probability on success, typically corresponds to a binomial distribution. Then, denoting the amount of converged runs by  $N_c$ , the fraction of the total amount of runs ( $N_r$ ) that has converged by  $f_c$ , and assuming this fraction to be the probability on convergence, the standard deviation of the amount of converged runs,  $\sigma_{N_c}$ , is

$$\sigma_{N_c} = \sqrt{f_c(1-f_c)N_r}$$

For determining the rate of convergence one approach would be to estimate for each converged GA the amount of calculations that were carried out up to the point at which the convergence criterion was satisfied. However, another approach was selected, since it was found to give a good overview of the general convergence behavior of the GA run. For this approach, the lowest energy found in each population was considered as a function of generation. By now taking the mean of all these curves that correspond to converged runs, an idea of the rate of convergence is obtained.

In the following the influence of the different GA-parameters is considered. No significant difference in GA performance was found when varying the amount of bits used for encoding the parameters, and therefore this GA-parameter is not considered in the following. This is also the case for the amount of generations.

### C.1.1 Influence of reproduction size

To ensure that good solutions do not get lost during the GA run, part of a current population is put directly into the succeeding population. The parameter controlling this process is called the reproduction size. The reproduction size,  $f_r$ , is defined here as that fraction of the population that is renewed when creating the population of a new generation. Thus, for low values of  $f_r$ , only a few elements of the populations corresponding to two succeeding generations are different. For high values of  $f_r$ , the populations of two succeeding generations will differ a lot. Employing higher  $f_r$  values is thought to result in a higher percentage of converged runs, since there is more exploration of the search space. Lower  $f_r$  values should result in a faster convergence, since there is more exploitation of promising solutions.

Figure 2 shows the percentage of converged runs as a function of  $f_r$ . The remaining parameters were kept at their default values. Employing a value of zero for  $f_r$  is not considered here, since for this situation all populations of succeeding generations are equal to the initial population. The standard deviations are plotted as dashed lines in Fig. 2. As expected, the amount of converged runs increases with increasing  $f_r$ , although there seems to be an area of  $f_r$  values (0.2-0.7), where there is no significant influence of  $f_r$  on the percentage of converged GA runs. Note also the large decrease in converged runs when employing a value of 1 for  $f_r$ . This setting is denoted by generational replacement, i.e., no elements of a current population are put directly into the next population. For this setting one of the mechanisms that guide the search towards good solutions is excluded. The result is that good results can get lost during the optimization. The remaining mechanism forcing the algorithm towards good solutions is

the selection of elements for the parental population. This selection is such that good solutions have a larger probability to get selected.

Figure 3 shows the curves representing the mean rate of convergence. Increasing  $f_r$  results in an increase in the amount of forward runs needed for obtaining a certain level of the mean energy, but also, in general, in an increase of the amount of converged runs as shown in Fig. 2. Also with regards to the rate of convergence, employing a value of 1 for  $f_r$ , shows a clearly different behavior. For this setting, the decrease in the energy for succeeding populations is caused solely by the mechanism of selecting elements for the parental population based on their fitness.

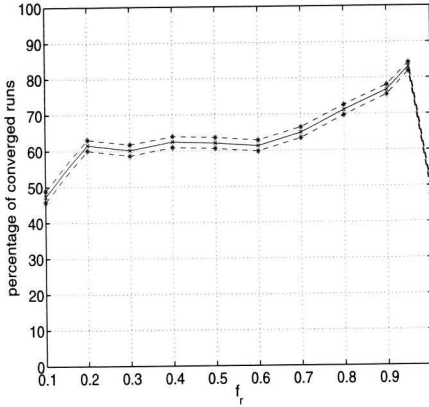


Fig. 2 Percentage of converged runs as a function of  $f_r$ .

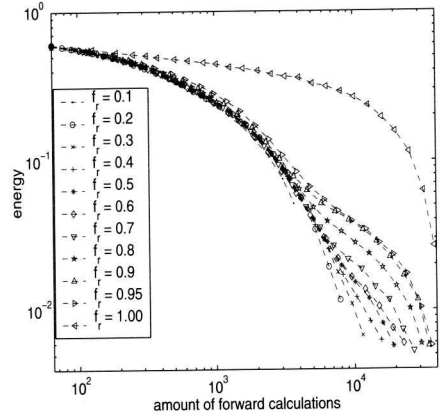


Fig. 3 Curves representing the mean rate of convergence for different  $f_r$  values.

The cause for the change in the slope of the curves shown in Fig. 3 is illustrated in Fig. 4, showing the distribution of the energy of all converged runs as a function of generation, and results from solutions going from some local to the global minimum.



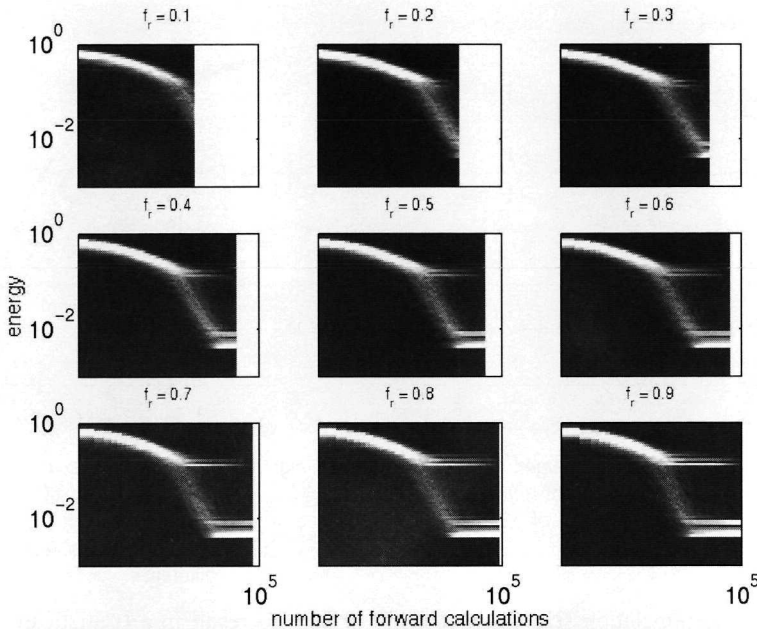


Fig. 4 Distribution of energy corresponding to the converged runs as a function of generation. White corresponds to a high level in the distribution, whereas black corresponds to a low level. All scales are equal for all subplots.

It can be concluded that the influence of  $f_r$  is limited. For values  $f_r$  values from 0.2-0.7, employing different values of  $f_r$  does not result in a statistically significant change in the percentage of converged runs. For values of 0.8, 0.9 the percentage of converged runs increases from  $64.9 \pm 1.5$  % for  $f_r = 0.7$ , to  $76.7 \pm 1.3$  % for  $f_r = 0.9$ , i.e., about 10 %. Up to 2000/3000 forward calculations the rate of convergence is hardly influenced a lot by  $f_r$ . Beyond this point, the curves corresponding to different values of  $f_r$  start to deviate, such that for higher values of  $f_r$  the amount of forward calculations to obtain a certain value for the mean energy is much larger than for low  $f_r$  values.

### C.1.2 Influence of population size

To investigate the influence of the population size, population sizes of 32 and 128 have been employed. Fig. 5 shows the percentage of converged runs as a function of  $f_r$  for the three population sizes  $q$ . Clearly the amount of converged runs increases with increasing  $q$ , due to the increased exploration of the search space. Figure 6 shows the mean energy of all converged runs as a function of the amount of forward calculations for the three population sizes and for the different  $f_r$ . At an equal amount of forward calculations, the mean energy decreases with decreasing population size (at the cost of a smaller percentage of converged runs, see Fig. 5).

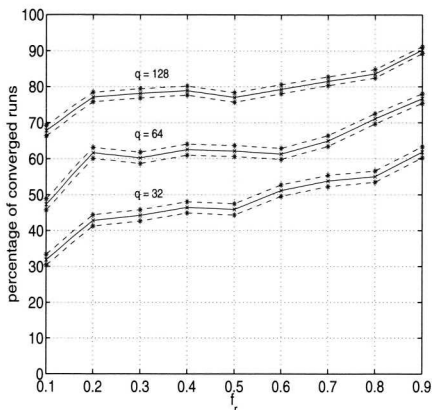


Fig. 5 Percentage of converged runs as a function of  $f_r$  for the three population sizes ( $q$ ) of 32, 64 and 128, respectively.

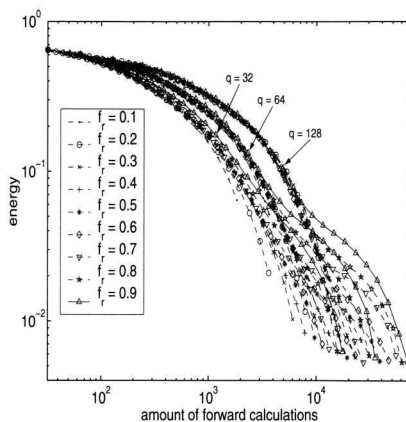


Fig. 6 Mean energy as a function of the amount of forward calculations for the three population sizes and for the different  $f_r$ .

Making the population size twice as large is seen to result in a (statistically significant) increase of about 15 % in the increase of the amount of converged runs. However, this increase is obtained at the cost of slower convergence.

### C.1.3 Influence of the crossover rate and mutation rate

In this section the influence of the mutation and the crossover rates are considered. Mutation and crossover are the two mechanisms through which children are created from the parental population. If for both a value of zero is selected, the populations of each succeeding generation are equal to the initial population.

Figures 7 and 8 show the percentage of converged runs and the mean rate of convergence for four values of  $p_m$ . Employing values for the mutation rate of zero and 0.2 is seen to result in a small percentage of converged runs. Employing a value of 0.1 gives in general the best results with respect to the amount of converged runs. The sudden decrease in the percentage of converged runs for  $f_r = 0.1$  probably will disappear when more generations, i.e., more forward calculations are considered. Similarly it is expected that by increasing the amount of forward calculations, the amount of runs that converge for  $p_m = 0.2$  will increase.

Increasing the mutation rate is seen to result in slower convergence. This is expected since increasing  $p_m$  introduces more and more randomness in the search. The plateau in the rate of convergence that is reached for  $p_m = 0$ , corresponds to that part of the search where the population has converged. At that stage mutation is the only mechanism that results in children that are different from their parents.

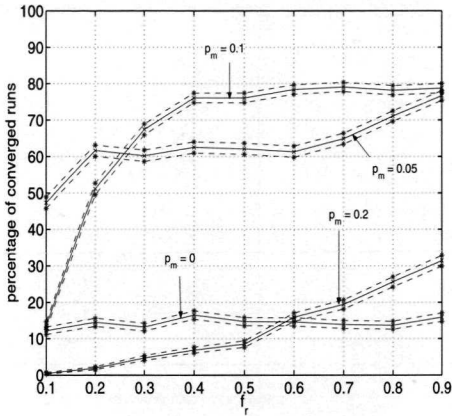


Fig. 7 Percentage of converged runs as a function of  $f_r$  for the four values of  $p_m$ , respectively.

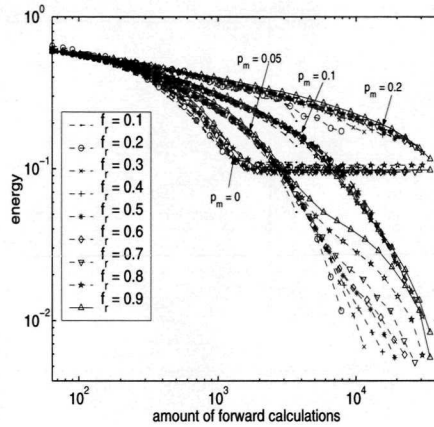


Fig. 8 Mean energy as a function of the amount of forward calculations for the four values of  $p_m$  and for different  $f_r$ .

The influence of the crossover rate  $p_c$  on the behavior of the GA is much less pronounced than that of the mutation probability. Employing a value of zero for the crossover rate, i.e., the children are created from the parental distribution through mutation only, results in less exploitation of promising solutions. Consequently, this setting was found to result in a statistically significant lower percentage of converged runs for the lower values of  $f_r$  ( $<0.4$ ) and slower convergence. Also a value of 0.5 and one for  $p_c$  has been considered. No significant change in behavior compared to the default setting was found for these two settings. It can be concluded that the influence of the crossover rate is limited.

## C.2 The optimal setting

In the previous section, a large number of settings for the GA have been assessed with regards to the amount of the converged runs, and the rate of convergence. It is found that when selecting a setting, a trade-off needs to be made between the probability on convergence, and the amount of forward calculations. The percentage of converged runs increased with increasing reproduction size  $f_r$ , increasing population size  $q$ , and increasing mutation probability  $p_m$ . However, this desirable result is obtained at the cost of a slower rate of convergence, i.e., more forward calculations are needed. The highest percentage of converged runs of all settings considered, was obtained for a population size of 128, a reproduction size of 0.9, and default values for the remaining GA parameters. For this setting  $90 \pm 1\%$  of the runs had converged. From the results presented in Figs. 7 and 8, it is expected that a similar result can be obtained for a mutation rate of 0.1, a population size of 128, a reproduction size of 0.5, and all remaining GA parameters at their default values. This setting was found to result in  $92 \pm 1\%$  converged runs, which indeed is comparable to the  $90 \pm 1\%$  converged runs. Figure 9 shows the mean energy.

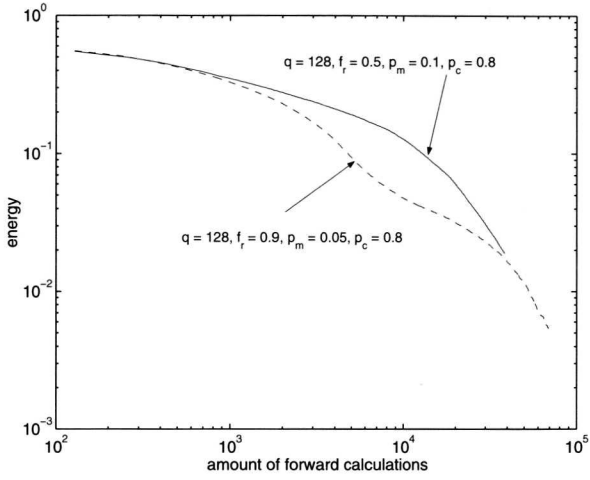
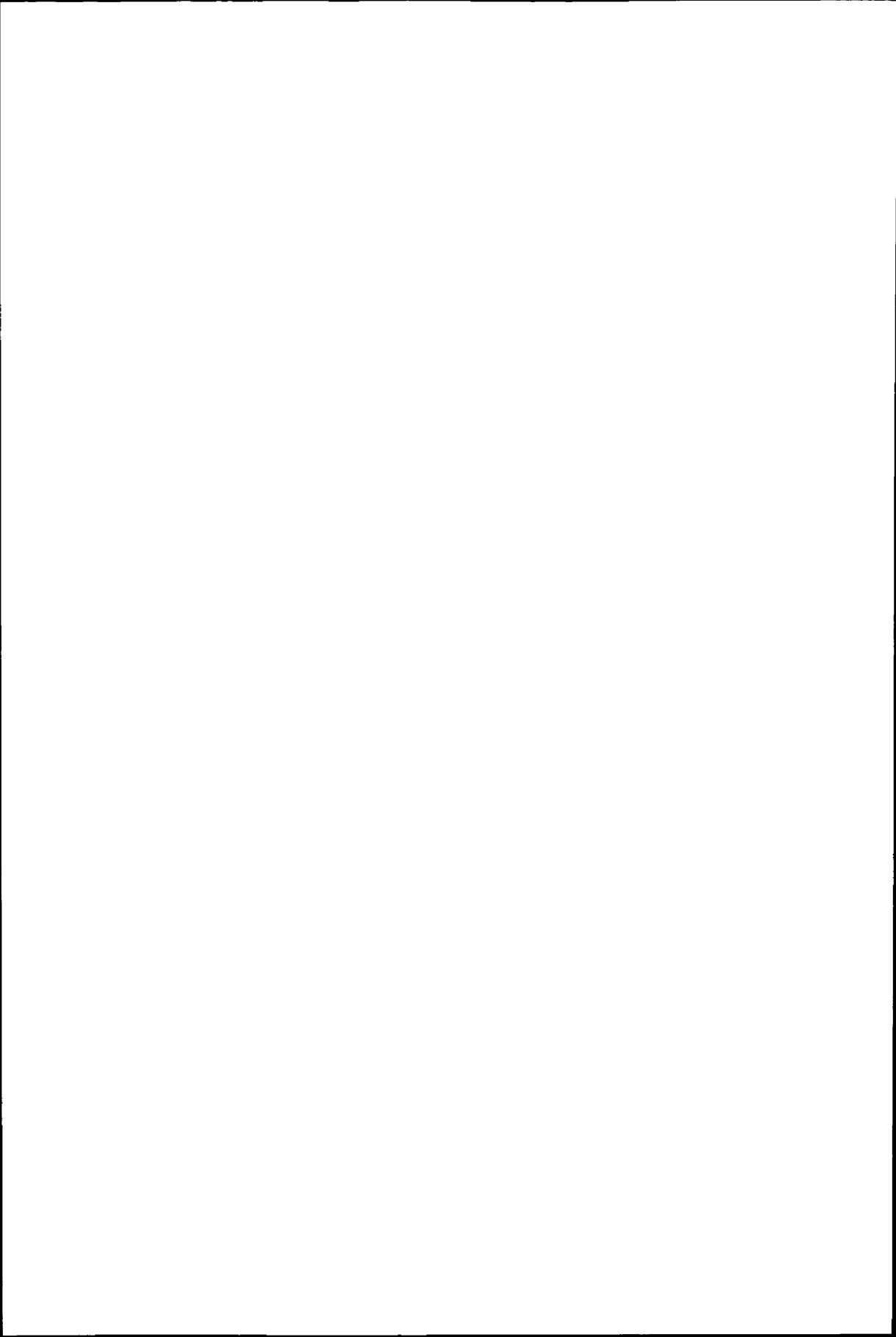


Fig. 9 Mean energy as a function of the amount of forward calculations the two settings corresponding to the highest percentage of converged runs.

## References

- <sup>1</sup> Mark R. Fallat, and Stan E. Dosso, "Geoacoustic inversion via local, global, and hybrid algorithms," *J. Acoust. Soc. Am.* **105** (6), 3219-3230 (1999).
- <sup>2</sup> Martin Musil, Michael J. Wilmut, and N. Ross Chapman, "A Hybrid Simplex Genetic Algorithm for Estimating Geoacoustic Parameters Using Matched-Field Inversion," *IEEE J. Ocean. Eng.* **24** (3), 358-369 (1999).



## Appendix D

# Applying Levenberg-marquardt as a local optimization method

In this appendix the downhill simplex method (DHS) and the Levenberg-Marquardt method (LM) are applied to the matched field inversion problem, and the performance of both methods in finding the global optimum is compared. For this comparison use is made of the SIM1 simulations of Chapter 6 and Chapter 7.

### D.1 Levenberg-Marquardt

For applying the Levenberg-Marquardt (LM) algorithm, an energy function based on the quadratic deviation is required. For example, the following energy function can be used for the acoustic problem

$$\tilde{E}(\mathbf{m}) = [\mathbf{d}_{obs} - \mathbf{d}_{calc}(\mathbf{m})] \cdot [\mathbf{d}_{obs} - \mathbf{d}_{calc}(\mathbf{m})]^T = \mathbf{e} \cdot \mathbf{e}^T \quad (1)$$

with superscript  $T$  denoting the transposed. Symbol  $\mathbf{d}_{obs}$  denotes the absolute values of the measured complex pressures at the vertical receiving array (row vector) and  $\mathbf{d}_{calc}$  denotes the absolute values of the calculated complex pressures at the vertical array (row vector). The amount of hydrophones is denoted by  $N_h$ , and  $\mathbf{d}_{obs}$  and  $\mathbf{d}_{calc}$  have size  $(1 \times N_h)$ . The symbol  $\mathbf{m}$  denotes the vector of unknown parameters. The number of unknowns is denoted by  $M$ .

A Taylor expansion with terms up to the second order is carried out for determining the value of  $\tilde{E}$  for a model perturbation  $\delta\mathbf{m} (M \times 1)^1$

$$\tilde{E}(\mathbf{m} + \delta\mathbf{m}) = \tilde{E}(\mathbf{m}) + \mathbf{g}^T \delta\mathbf{m} + \frac{1}{2} \delta\mathbf{m}^T \mathbf{H} \delta\mathbf{m} \quad (2)$$

with  $\mathbf{g}$  the  $(M \times 1)$  vector containing the first derivatives of  $\tilde{E}$  to the unknown parameters

$$\mathbf{g} = 2\mathbf{J}^T \mathbf{e}^T \quad (3)$$

and  $\mathbf{J}$  the Jacobian matrix written as

$$J_{ij} = -\frac{\partial d_{calc,i}(\mathbf{m})}{\partial m_j} \quad (4)$$

with  $d_{calc,i}$  the absolute value of the calculated complex pressure at the  $i^{\text{th}}$  hydrophone.  $\mathbf{H}$  is the  $(M \times M)$  Hessian of the object function

$$\mathbf{H} = 2\mathbf{J}^T \mathbf{J} + 2[\nabla \mathbf{J}]^T \mathbf{e}^T \approx 2\mathbf{J}^T \mathbf{J} \quad (5)$$

Neglecting the last term in Eq. (5) corresponds to assuming  $\mathbf{e}$  to be linear with respect to the unknown parameters.

The  $\delta \mathbf{m}$  for which the minimum of Eq. (2) is obtained is given by

$$\mathbf{H} \delta \mathbf{m} = -\mathbf{g} \quad \text{or} \quad \mathbf{J}^T \mathbf{J} \delta \mathbf{m} = -\mathbf{J}^T \mathbf{e}^T \quad (6)$$

However, if Eq. (2) is not a good approximation, the only thing that can be done is to step down the gradient

$$\delta \mathbf{m} = -C \mathbf{g} \quad \text{or} \quad \delta \mathbf{m} = -C \mathbf{J}^T \mathbf{e}^T \quad (7)$$

with  $C$  a constant, small enough to not exhaust the downhill direction.

LM varies between Eq. (6), the inverse Hessian method, and Eq. (7), the steepest descent method. The steepest descent method is used far away from the minimum, whereas the inverse Hessian method is used in the area close to the minimum. It can be written as

$$\mathbf{H}(1 + \lambda \mathbf{I}) \delta \mathbf{m} = -\mathbf{g} \quad \text{or} \quad \mathbf{J}^T \mathbf{J}(1 + \lambda \mathbf{I}) \delta \mathbf{m} = -\mathbf{J}^T \mathbf{e}^T \quad (8)$$

For very small  $\lambda$  Eq. (8) is equal to Eq.(6), i.e., the Hessian method. For large  $\lambda$ , Eq. (8) can be written as  $\delta m_j = \frac{1}{\lambda h_{jj}} g_j$ , i.e., Eq. (7) with the constant  $C$  having a value of  $\frac{1}{\lambda h_{jj}}$ .

The use of derivatives is one of the disadvantages of LM. For the acoustic problem considered, these derivatives cannot be calculated analytically, and therefore have to be calculated numerically. This is inefficient and often not accurate. Another disadvantage is the requirement that the energy function is based on quadratic differences, which is not always the most favorable measure for the similarity. Also, LM requires the tuning of several magic parameters, such as  $\lambda$  (see Eq. (8)). The final drawback of LM is that it assumes linear behavior of  $\mathbf{e}$  with respect to the unknown parameters, which might not always be the situation. The advantage of LM lies in its efficiency in locating the global optimum.

## D.2 Applying LM for local minimization of GA results

For applying LM the complex pressures at 4 frequencies ([200.0 300.3 400.3 600.2] Hz) have been used. Letting  $f_k$  ( $k = 1, \dots, 4$ ) denote the different frequencies and  $\mathbf{d}'_{obs}(f_k)$ ,  $\mathbf{d}'_{calc}(f_k)$  the absolute values of the pressure fields (row vectors) at frequency  $f_k$ , then

$$\begin{aligned} \mathbf{d}'_{obs} &= [\mathbf{d}'_{obs}(f_1) \mathbf{d}'_{obs}(f_2) \mathbf{d}'_{obs}(f_3) \mathbf{d}'_{obs}(f_4)], \\ \mathbf{d}'_{calc} &= [\mathbf{d}'_{calc}(f_1) \mathbf{d}'_{calc}(f_2) \mathbf{d}'_{calc}(f_3) \mathbf{d}'_{calc}(f_4)] \end{aligned}$$

Since the LM optimization has to be started close to the global optimum, 41 standard genetic algorithm runs have been carried out using the energy function of Eq. (1). The



situation considered is that of the SIM1 simulations. The results are shown in Fig. 1 for all optimized parameters.

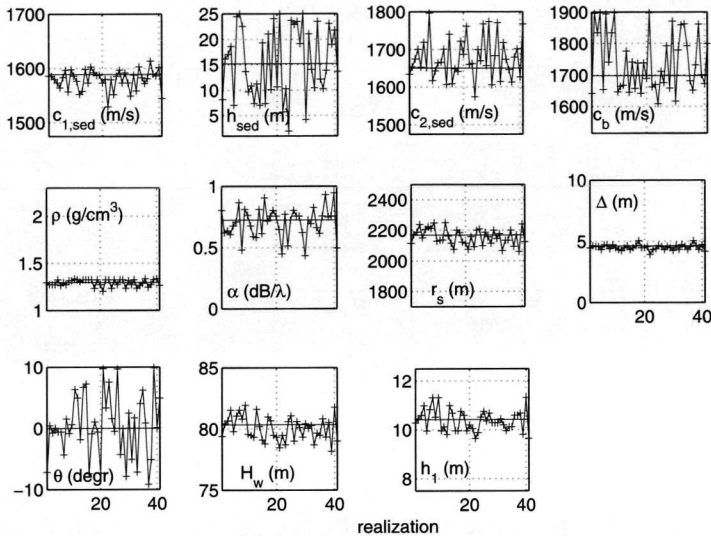


Fig. 1 SIM1 parameter estimates obtained after inversions of synthetic data using the genetic algorithm for the optimization and  $\tilde{E}$  as the energy function.

When applying LM, first several parameters of LM need to be set. These parameters comprise:

- The amount of iterations. After some initial test runs, using 25 iterations was, in general, found to be sufficient for convergence (see Fig. 2);
- The amount by which  $\lambda$  is multiplied or divided,  $\xi$ . We have considered  $\xi = [5 \ 10 \ 15]$ , with 10 being the default value;<sup>1</sup>
- The starting value for  $\lambda$ ,  $\lambda_1$ . We have considered  $\lambda_1 = [0.00001 \ 0.0001 \ 0.001 \ 0.01 \ 0.1]$  with 0.001 taken as default value;<sup>1</sup>

- The steps taken in determining the derivatives  $J_{ij} = -\frac{\partial d_{calc,i}(\mathbf{m})}{\partial m_j}$  (Eq. (4)). The step sizes are based on the lower and upper search bound applied in the genetic algorithm. The default step sizes are the differences of these bounds, divided by 1000 ( $N$ ). In addition, values for  $N$  of 100 and 10000 have been considered.

The figures below show the results of the LM optimization. As starting points we have used the 41 parameter sets obtained through inversion using the genetic algorithm. Figure 2 shows the energy as a function of iteration, employing the default settings. Using 25 iterations is seen to be sufficient for the majority of the runs. Each run required 289 forward calculations per frequency.

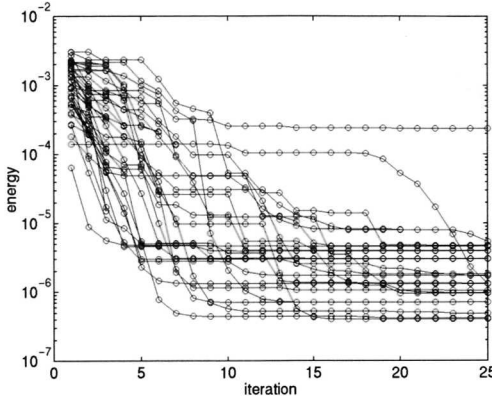


Fig. 2 Energy as a function of iteration employing the default settings for LM.

### D.2.1 Influence of $\xi$

Figure 3 shows the optimized energy function values obtained with a GA only and obtained by additionally applying LM for different values of  $\xi$ .

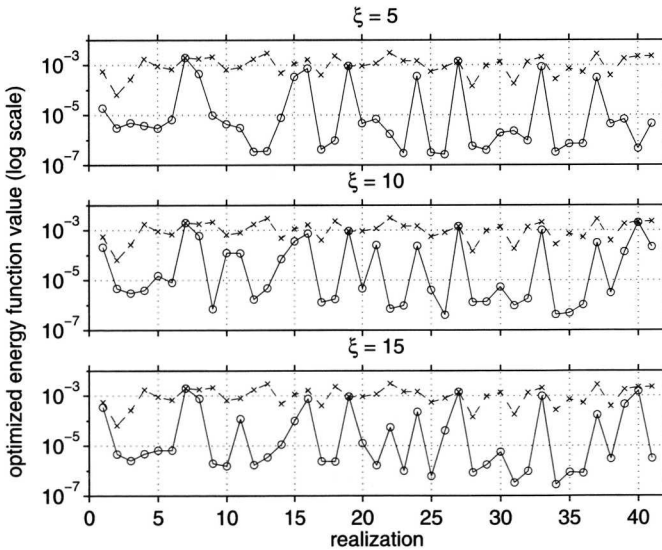


Fig. 3 Optimized energy function values obtained from the minimization by GA (--x) and obtained by additionally applying LM (-o) for different values of  $\xi$ .

Since it is difficult to draw a conclusion from Fig. 3, Fig. 4 shows the optimized energy function values obtained when applying LM with  $\xi = 5$  and  $\xi = 15$ , plotted against those obtained for  $\xi = 10$ . The dashed lines indicate equal results. Using a value for  $\xi$  of 15, instead of 10 does not degrade nor improve the optimization. Employing a somewhat lower value for  $\xi$  seems to improve the optimization, i.e., in general, the obtained energy function values become somewhat lower.

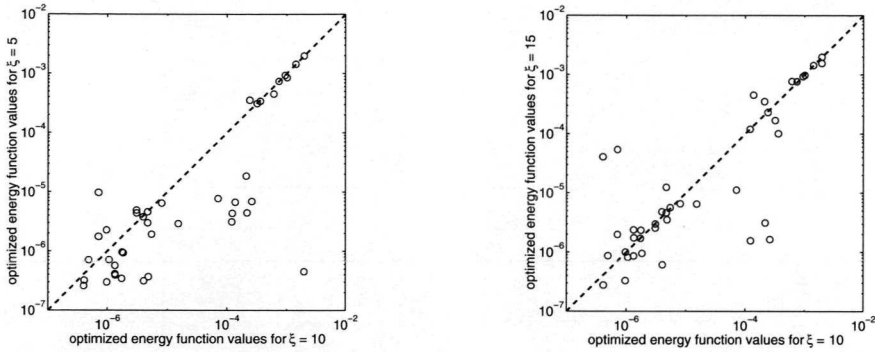


Fig. 4 Optimized energy function values obtained when applying LM with  $\xi = 5$  and  $\xi = 15$ , plotted against those obtained for  $\xi = 10$ . The dashed line indicates equal results

## D.2.2 Influence of $\lambda_1$

Figure 5 shows the energy function values obtained from the minimization by GA and those obtained by also applying LM for different values of  $\lambda_1$ . Clearly the results are different for different values of  $\lambda_1$ , but there is no clear difference in performance. Also an analysis as presented in Fig. 4, did not show any clear effect and it can be concluded that  $\lambda_1$  is not a very critical parameter.

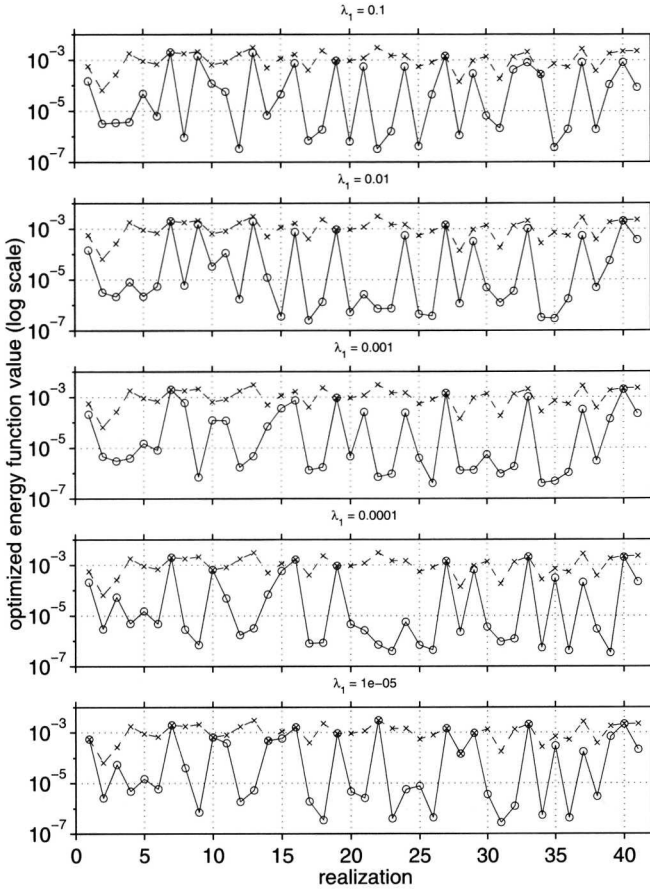


Fig. 5 Optimized energy function values obtained from the minimization by GA (--x) and obtained by also applying LM (-o) for different values of  $\lambda_1$ .

### D.2.3 Influence of the step size taken to calculate the derivatives

Figure 6 shows the optimized energy function values, both obtained using the genetic algorithm only, and followed by LM, applying different step sizes for determining the derivatives needed for the LM method. The step sizes are calculated as the differences of the upper and lower search bounds used in the GA optimization, divided by  $N$ , with  $N = 100, 1000, 10000$ .

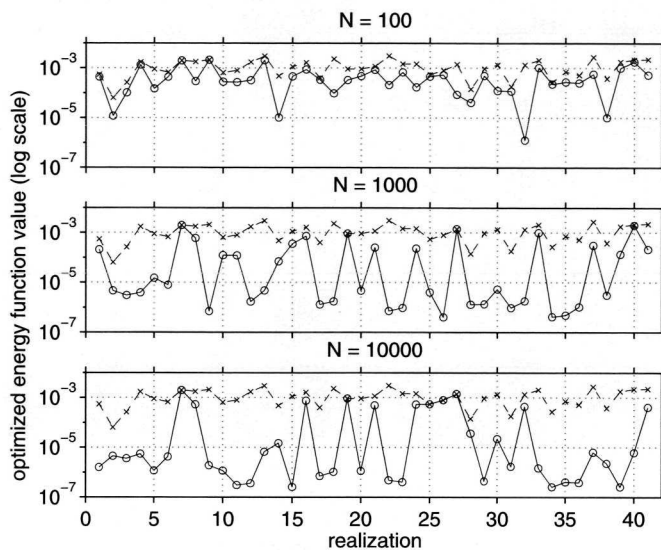


Fig. 6 Optimized energy function values, using the genetic algorithm only ( $-x$ ), and followed by LM ( $-o$ ). The step sizes applied for determining the derivatives (needed for the LM method), are the area over which the GA optimization is performed, divided by  $N$ .

Figure 7 shows the optimized energy function values obtained when applying LM with  $N = 100$  and  $N = 10000$ , plotted against those obtained for  $N = 1000$ . The dashed lines are used for indicating equal results. Using a value for  $N$  of 100, instead of 1000 results in a degradation of the optimization performance. Employing a higher value for  $N$ , i.e., 10000 instead of 1000, resulting in smaller step sizes used for determining the derivatives, seems to improve the optimization, i.e., in general, the obtained energy function values become somewhat lower.

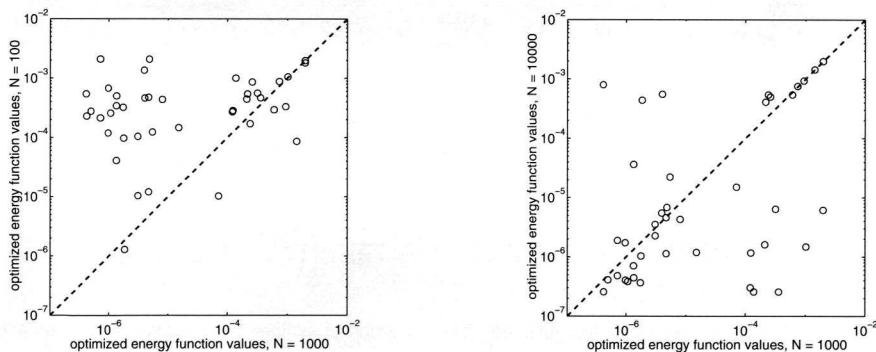


Fig. 7 Optimized energy function values obtained when applying LM with  $N = 100$  and  $N = 10000$ , plotted against those obtained for  $N = 1000$ . The dashed line indicates equal results.

Figure 8 illustrates the large decrease in the energy function values obtained through the use of LM employing the optimal settings ( $\xi = 5$ ,  $N = 10000$ , and  $\lambda_l$  kept at its default value of 0.001).

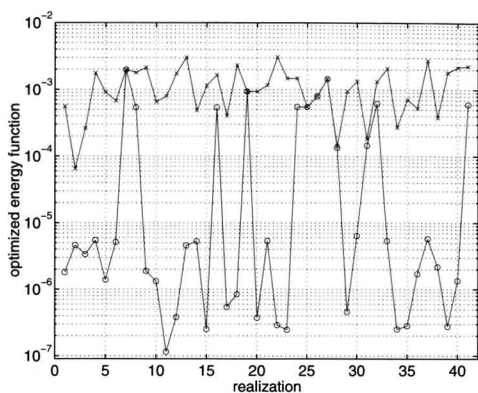


Fig. 8 Energy function values obtained after applying GA only and GA followed by LM for the SIM1 inversions, using the expression of Eq. (1) as the energy function.

Figure 9 shows the corresponding parameter estimates. Except for the parameters that can not be determined ( $h_{sed}$ ,  $c_{2,sed}$  and  $c_h$ ), the variation, or uncertainty, in parameter estimates has decreased significantly by applying LM.

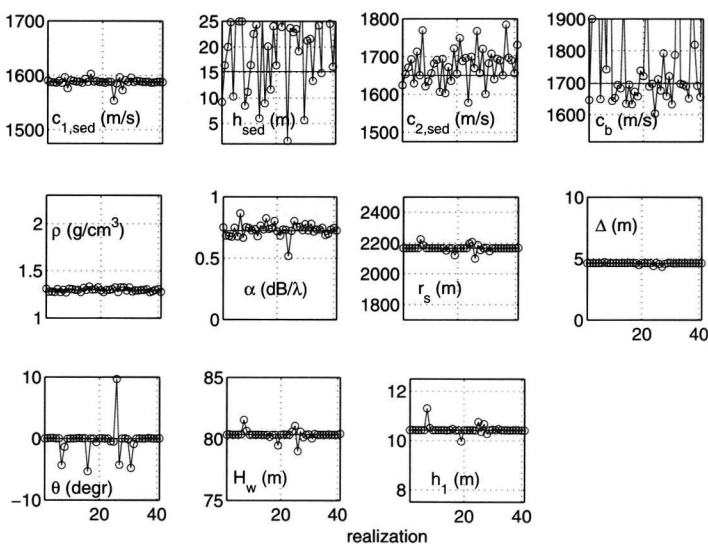


Fig. 9 SIM1 parameter estimates obtained after inversions of synthetic data using the genetic algorithm and LM for the optimization and  $\tilde{E}$  as the energy function.

### D.3 Applying DHS for local minimization of GA results

For applying DHS, the SIM1 GA inversion results, as presented in Chapter 6, have been used as starting points for DHS. The energy function used is the multi-frequency Bartlett processor

$$E(\mathbf{m}) = 1 - \frac{1}{K} \sum_{k=1}^K \left| \mathbf{p}_{obs}(f_k) \cdot \mathbf{p}_{calc}^*(f_k, \mathbf{m}) \right|^2 \quad (9)$$

with  $f_k$  denoting the frequencies used in the optimization ([200.0 300.3 400.3 600.2] Hz).  $K$  is the amount of frequencies. The aim is now to get a more accurate optimization by applying DHS as a local method after the global optimization.

Figure 10 shows the reduction in the values for the energy function obtained by applying DHS.

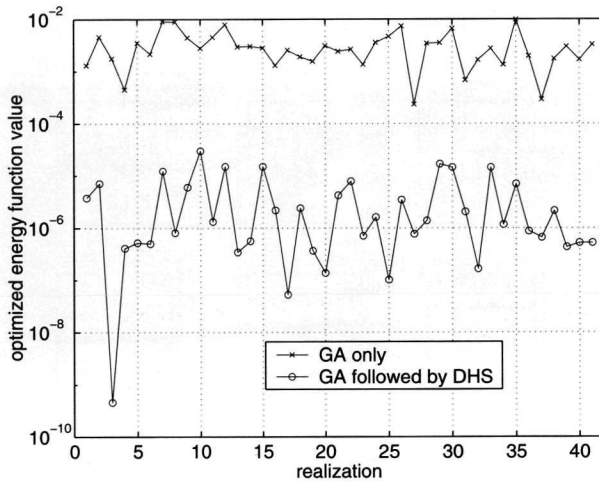


Fig. 10 Energy function values obtained after applying GA only and GA followed by DHS for the SIM1 inversions.

Figures 11 and 12 show the corresponding parameter estimates, obtained by applying the genetic algorithm solely, and when followed by DHS, respectively. The solid black horizontal lines indicate the true parameter values. It can be concluded that the DHS algorithm is capable of finding the correct solution for almost all parameters.

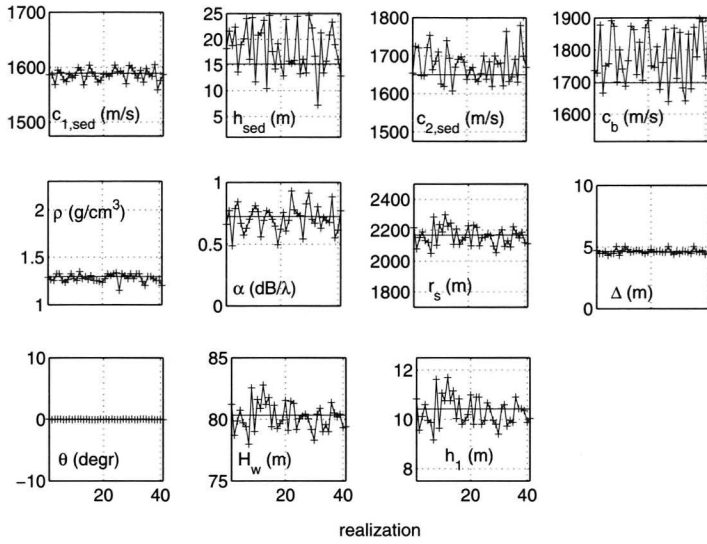


Fig. 11 SIM1 parameter estimates obtained after inversions of synthetic data using the genetic algorithm.

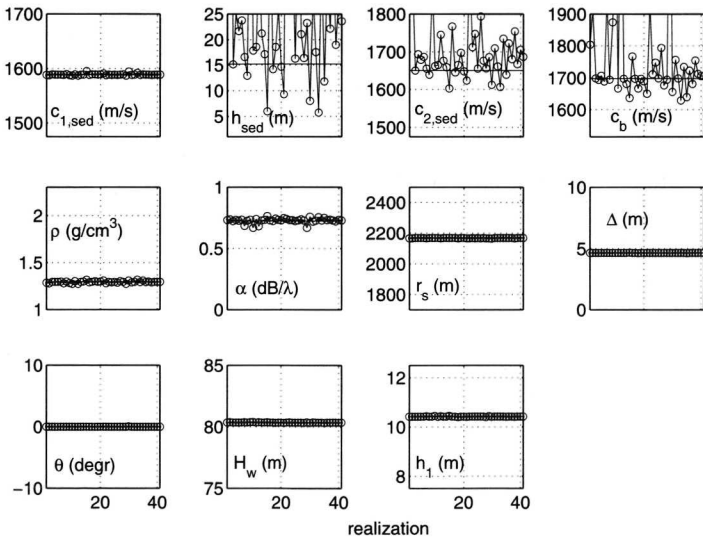


Fig. 12 SIM1 parameter estimates obtained using the genetic algorithm, followed by DHS optimization.

In Table I a summary of the resulting standard deviations are presented for all inversions, i.e., GA only and GA followed by the two local methods. Considering the first two columns, where the only difference is that different energy functions have been used, the most striking effect of using  $\tilde{E}$  instead of the multi-frequency Bartlett processor is on the estimate for the array tilt. This is due to the fact that use is made of the absolute values of the acoustic pressures. From the last two columns it is seen that using the multi-frequency Bartlett processor ( $E$ ) and applying DHS as the local optimization method, results in lower standard deviations for all parameters that can be determined than using the energy function based on the quadratic deviation and applying LM.



Table I Standard deviations for the inversion results of synthetic data (SIM1), using the multi-frequency Bartlett processor (E) and  $\tilde{E}$ .

Parameter	Std ( $\sigma_{std}$ ), SIM1 GA only, E	Std ( $\sigma_{std}$ ), SIM1 GA only, $\tilde{E}$	Std ( $\sigma_{std}$ ), SIM1 GA + DHS, E	Std ( $\sigma_{std}$ ), SIM1 GA + LM, $\tilde{E}$
$c_{1, \text{sed}}$ (m/s)	10.7 (1.2)	18.0 (2.0)	1.63 (0.18)	7.10 (0.78)
$h_{\text{sed}}$ (m)	4.46 (0.49)	6.89 (0.76)	17.7 (2.0)	8.82 (0.97)
$c_{2, \text{sed}}$ (m/s)	41.8 (4.6)	54.0 (6.0)	75.6 (8.4)	47.0 (5.2)
$c_b$ (m/s)	81.4 (9.0)	94 (10)	208 (23)	278 (31)
$\rho$ (g/cm <sup>3</sup> )	0.042 (0.005)	0.0361 (0.0040)	0.0107 (0.0012)	0.0177 (0.0020)
$\alpha$ (dB/ $\lambda$ )	0.105 (0.012)	0.124 (0.014)	0.0203 (0.0022)	0.0538 (0.0059)
$r_s$ (m)	60.7 (6.7)	52.2 (5.8)	0.750 (0.083)	18.7 (2.1)
$\Delta$ (m)	0.177 (0.020)	0.211 (0.023)	0.00561 (0.00062)	0.0650 (0.0072)
$\theta$ (degr)	0.0397 (0.0044)	5.14 (0.57)	0.000368 (0.000041)	2.13 (0.24)
$H_w$ (m)	1.12 (0.12)	0.98 (0.11)	0.0166 (0.0018)	0.348 (0.038)
$h_1$ (m)	0.585 (0.065)	0.442 (0.049)	0.0095 (0.0010)	0.173 (0.019)

## D.4 Which local optimization method to use?

Both DHS and LM show good performance in decreasing the energy function value, and in finding the true parameter values. From the results it can be concluded that DHS is more robust, i.e., it always finds a better solution than the GA, whereas LM sometimes does not manage to improve the solution. This is one of the reasons for the larger standard deviation of the parameter estimates that were obtained by LM, compared to the DHS results. The other reason for the larger standard deviation is the fact that when applying LM, the energy function has to be based on the quadratic difference between measured and modeled data. The first cause of the larger standard deviations is difficult to eliminate. Probably it is the result of the fact that the assumption of linear behavior as required for the LM method is not valid. The second cause might be eliminated by the use of a different energy function. It should be noted that different energy functions show a somewhat different behavior as a function of the unknown parameters, and, therefore, the local and global method should use the same energy function. Another disadvantage of LM lies in that fact that it makes use of derivatives. In the situation considered here, these derivatives have to be calculated numerically, which is inefficient and difficult to do it accurately.

In general, however, DHS requires more (about 10 times as many) function evaluations. Since the function evaluations are computationally expensive, this is a disadvantage of DHS. Typical run times for LM are 5 min, whereas it can be 40 min for DHS.

Since the goal of applying a local method is to reduce the uncertainty in the inversion results, we have selected the DHS method as the local optimization method. Future research might be directed towards modifying the LM method, such that it is capable of handling a wider set of energy functions, and becomes more robust. It should, however, not be forgotten that the local methods have been applied in a straightforward way, i.e., after the global search. In literature<sup>2-6</sup> other approaches are described, applying DHS (or LM) during the global search, thereby making the optimization much more efficient.

## References

- 1 William H. Press, Brian P. Flannery, Saul A. Teukolsky, William T. Vetterling, "Numerical recipes in C," Cambridge University Press, 1988, pp. 543-544.
- 2 Peter Gerstoft, "Inversion of acoustic data using a combination of genetic algorithms and the Gauss-Newton approach," *J. Acoust. Soc. Am.* **97** (4), 2181-2190 (1995).
- 3 Gopu R. Potty, James H. Miller James F. Lynch and Kevin B. Smith, "Tomographic inversion for sediment parameters in shallow water," *J. Acoust. Soc. Am.* **108** (3), 973-986 (2000).
- 4 Mark R. Fallat and Stan E. Dosso, "Geoacoustic inversion via local, global, and hybrid algorithms," *J. Acoust. Soc. Am.* **105** (6), 3219-3230 (1999).
- 5 Mark R. Fallat, Peter L. Nielsen and Stan E. Dosso, "Hybrid geoacoustic inversion of broadband Mediterranean Sea data," *J. Acoust. Soc. Am.* **107** (4), 1967-1977 (2000).
- 6 Martin Musil, Michael J. Wilmut and N. Ross Chapman, "A Hybrid Simplex Genetic Algorithm for Estimating Geoacoustic Parameters Using Matched-Field Inversion," *IEEE J. Oceanic Eng.* **24** (3), 358-369 (1999).

## Appendix E

# Existing geo-acoustic information for the Malta Plateau and the Elba area

## E.1 The Malta Plateau

Figure 1 below shows a map of part of the Malta plateau area.

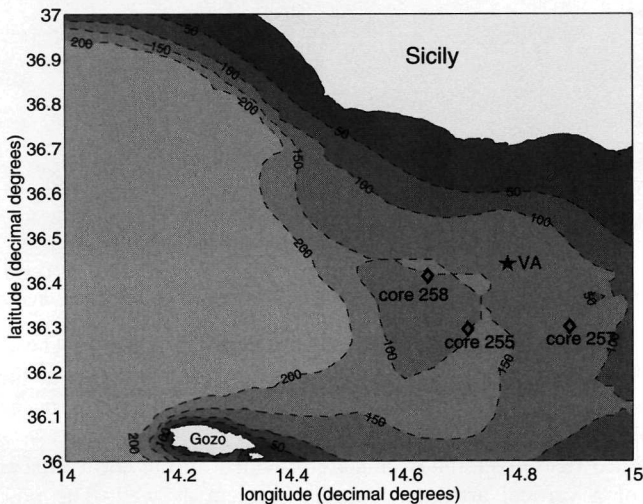


Fig. 1 The Malta plateau area. The positions corresponding to the cores given in (Tonarelli<sup>2</sup>) are indicated by core. Also, the position of the relevant VA deployment during MAPEX is given (star).

In (Sellschopp<sup>1</sup>) a map is presented indicating the different bottom types encountered in the area of the VA deployment during MAPEX. According to the map the sediment along the entire acoustic track consists of silt. From Chapter 2 a silt sediment is known to have sound speed values of  $\sim 1600$  m/s.

In (Tonarelli<sup>2</sup>) results of three cores taken on the Malta Plateau are presented. In this reference, these cores are denoted by the numbers 255, 257, and 258, see also Fig. 1. The following ranges of compressional wave velocities are measured in the three cores:

- Core 255: 1) silty sand and silt from 10-100 cm,  $c_p = 1650-1708$  m/s, 2) silt from 110-140 cm,  $c_p = 1616-1661$  m/s, 3) clayey silt from 150-215 cm,  $c_p = 1510-1574$  m/s;
- Core 257: mixture of sand, silt and clay,  $c_p = 1500-1550$  m/s;
- Core 258: composed mainly of silty clay and clayey silt,  $c_p = 1520-1570$  m/s.

## E.2 Area north of Elba

Figure 2 shows a map of the Elba environment. The MAPEX VA position north of Elba is indicated, together with the positions (close to the MAPEX VA position) for which information on bottom parameters is available.

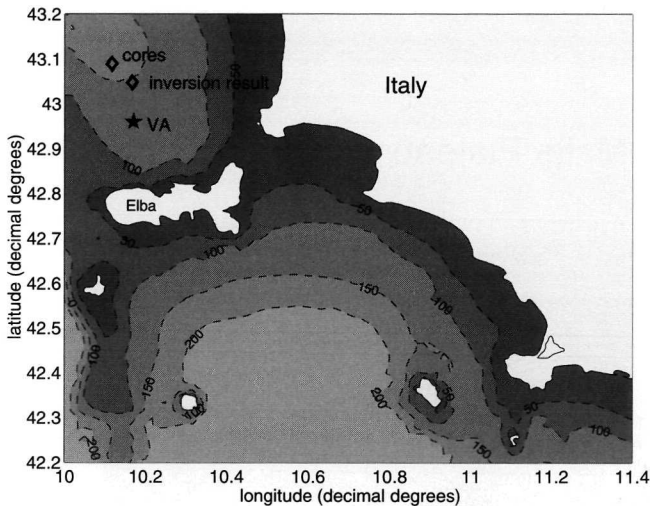


Fig. 2 The Elba area. The positions corresponding to the bottom information are indicated by diamonds. The position of the VA as deployed during MAPEX in the region north of Elba is indicated by a star.

Core results, taken in the north Elba region, are presented in (Osler<sup>3</sup>). These cores were taken at approximately  $10^{\circ} 7' E$ ,  $43^{\circ} 10' N$ , and indicate a sound speed at the top of the sediment of 1450 m/s, increasing to 1550 at 1 m depth, and then fluctuating around 1500-1510 m/s up to 5 m of depth.

In (Gingras<sup>4</sup>), matched field inversion results are provided for the north Elba environment, where use is made of a vertical array as receiving system as well. The position of the (Gingras<sup>4</sup>) VA is indicated in Fig. 2 by 'inversion result'. The source was positioned 5.6 km to the north. Based on previous measurements, comprising cores and inversions, a model for the environment was established in (Gingras<sup>4</sup>). This model is called the 'baseline' model, and consists of a single sediment layer on top of a half-infinite homogeneous sub-bottom. The sound speed was assumed to vary linearly in the sediment, from  $c_{1, sed}$  at the top, to  $c_{2, sed}$  at the bottom of the sediment.  $\rho_{sed}$ , and  $\alpha_{sed}$  are the density and attenuation in the sediment, respectively.  $c_b$ ,  $\rho_b$ , and  $\alpha_b$  denote sound speed, density and attenuation in the sub-bottom. Matched field inversion, using a single frequency (169.9 Hz), was applied to improve the baseline model. Table I presents the baseline model and the inversion result. These results are in agreement with the results presented in (Simons<sup>5</sup>), where inversions were carried out using the same data. Note that in Chapter 3 also these data are used for inversion. However, for the inversions of Chapter 3 the bottom is assumed to consist of a single layer, thereby ignoring

the thin sediment layer. This is a valid assumption, since the sediment thickness is less than half a wavelength at the frequency considered (169.9 Hz), and, therefore, propagation is not very sensitive to the sediment parameters. When employing higher frequencies, which is the case for the MAPEX analysis, this is no longer a valid assumption, and a sediment layer has to be taken into account.

Table I Baseline values for geo-acoustic parameters and inversion results as presented in (Gingras<sup>4</sup>).

Parameter	Baseline	Inversion result
$C_{1, \text{sed}}$ (m/s)	1520	$1505 \pm 24$
$C_{2, \text{sed}}$ (m/s)	1580	$1556 \pm 27$
$h_{\text{sed}}$ (m)	2.5	$3.3 \pm 1.6$
$\rho_{\text{sed}}$ (g/cm <sup>3</sup> )	1.7	$2.0 \pm 0.2$
$\alpha_{\text{sed}}$ (dB/ $\lambda$ )	0.13	$0.11 \pm 0.08$
$C_b$ (m/s)	1600	$1576 \pm 4$
$\rho_b$ (g/cm <sup>3</sup> )	1.8	$1.6 \pm 0.2$
$\alpha_b$ (dB/ $\lambda$ )	0.15	$0.18 \pm 0.08$

### E.3 Area southeast of Elba

Figure 3 shows the same area as Fig. 2, but now the positions southeast of Elba on which independent information is available are indicated.

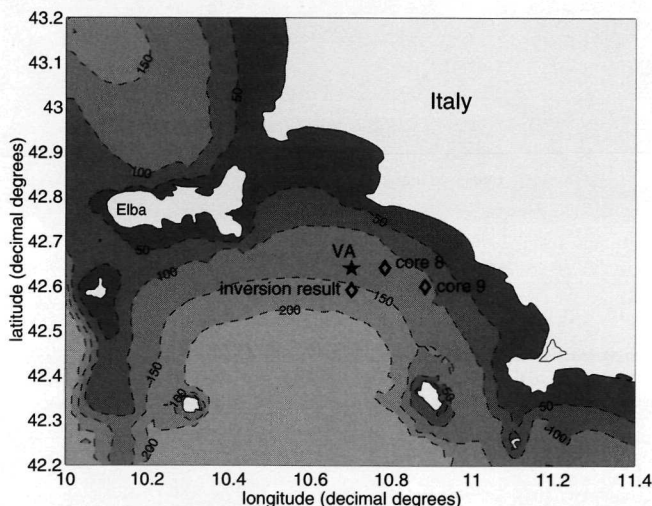


Fig. 3 The Elba area. The positions corresponding to the bottom information are indicated by diamonds. The relevant MAPEX VA position is denoted by a star. The position of the VA of (Fallat<sup>7</sup>) is indicated by 'inversion result'.

In (Hermand<sup>6</sup>) results of two core measurements, denoted by core 8 and core 9, are presented. Core 8 consists of a clay layer, followed by a layer of silty clay. The compressional wave speed in this sediment varies from 1457.5 m/s at 10-cm depth to 1472.5 m/s at 140 cm of depth. Core 9 indicates a clay sediment, with a sound speed varying from 1467.5 m/s at 10-cm depth to 1479 m/s at 140 cm. (Hermand<sup>6</sup>) also presents results of multi-frequency inversions. The inversions indicate an upper sediment sound speed of  $1471 \pm 3$  m/s. The sediment sound speed at the bottom of the sediment is determined to be  $1501 \pm 6$  m/s, with a

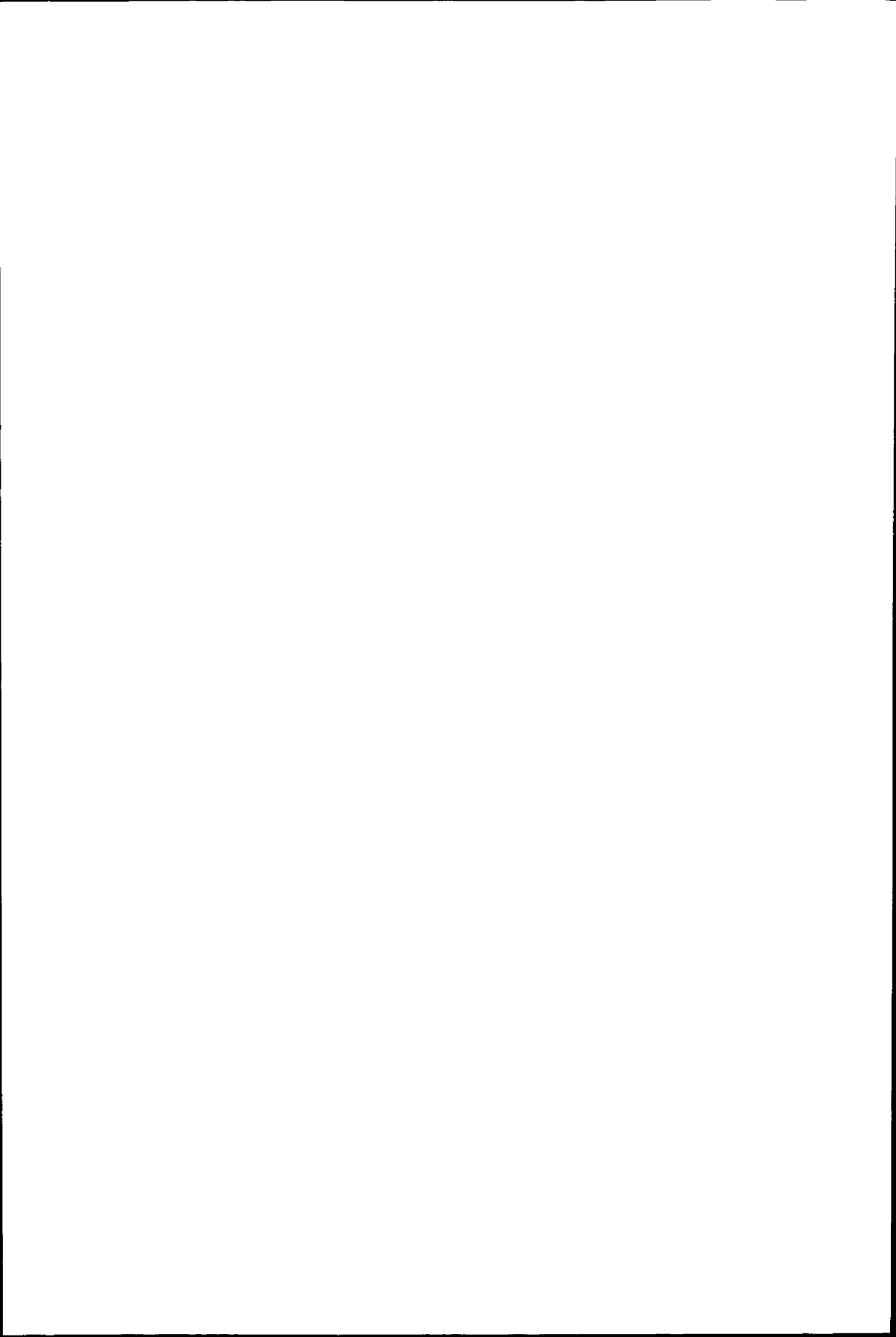
sediment thickness of  $9 \pm 1$  m, and a sub-bottom sound speed of  $1530 \pm 2$  m/s. These inversion results are thus in agreement with the core measurements.

Also in (Fallat<sup>7</sup>) matched field inversion results are presented. The position of the VA is indicated by 'inversion result' in Fig. 3. The acoustic data were taken while a ship towing the sound source was sailing toward the array. The sediment sound speed was taken constant in the sediment and was found to be  $1485 \pm 10$  m/s. For the sediment thickness values in between about 3 to 8 m were found. The sub-bottom sound speed was estimated to be around 1520-1530 m/s.

In general, it can be concluded that the sediment in the area southeast of Elba is a low speed sediment with sound speed values below 1500 m/s.

## References

- <sup>1</sup> J. Sellschopp, M. Siderius, and P. Nielsen, "ADVENT99, pre-processed acoustic and environmental cruise data," CD-35, SACLANT Undersea Research Centre, La Spezia, Italy (2000).
- <sup>2</sup> B. Tonarelli, F. Turgutcan, M.D. Max, and T. Akal, "A comparison of shallow sediment properties in four locations on the Sicilian-Tunisian platform," SM-267, SACLANT Undersea Research Centre, La Spezia, Italy (1993).
- <sup>3</sup> J. C. Osler, L. Gualdesi, E. Michelozzi, and B. Tonarelli, "Piston coring capabilities at SACLANTCEN: minimizing and assessing core disturbance," SR-321, SACLANT Undersea Research Centre, La Spezia, Italy (2000).
- <sup>4</sup> D.F. Gingras, and P. Gerstoft, "Inversion for geometric and geoacoustic parameters in shallow water: Experimental results," *J. Acoust. Soc. Am.*, **97** (6), 3589-3598 (1995).
- <sup>5</sup> D.G. Simons, "Source localization and Estimation of Geoacoustic Bottom Parameters by Matched Field Inversion of Real Acoustic Data," TNO report FEL-95-A260 (1995).
- <sup>6</sup> J.P. Hermand, and P. Gerstoft, "Inversion of Broad-band Multitone Acoustic Data from the YELLOW SHARK Summer Experiments," *IEEE J. Ocean. Eng.* **21** (4), 324-346 (1996).





## Samenvatting

Informatie over de zee-, of rivierbodem is voor veel toepassingen van groot belang. Voorbeelden van deze toepassingen zijn 'offshore-activiteiten', zoals het aanleggen van een vliegveld in zee, baggeren, en het opsporen van bepaalde bodemtypen, bijvoorbeeld met het oog op grof zand- (nodig voor beton), of grindwinning. Ook voor mijnenbestrijding is kennis over de bodem van groot belang. Immers het type bodem bepaalt of de mijn verzinkt (zachte bodems), of dat de mijn op het oppervlak van de bodem blijft liggen (harde bodems).

Het verzamelen van informatie over de onderwaterbodem is niet eenvoudig daar het immers moeilijk is er bij te komen. Eventueel kan hiervoor gebruik gemaakt worden van duikers en/of van boringen. Echter, iedere boring of duik is een puntmeting en verschaft dus informatie over een beperkt gebied. Zodra men informatie nodig heeft over grote gebieden, wat meestal het geval is, dan zijn zeer veel boringen of duiken nodig, hetgeen zeer kostbaar is.

Als gevolg hiervan is men aangewezen op 'remote sensing' technieken. In de praktijk is alleen geluid geschikt om op afstand informatie over de onderwaterbodem te verkrijgen, omdat alle andere typen straling teveel gedempt worden. Een bijkomend voordeel van geluid is dat de reflectie-eigenschappen direct informatie verschaffen over het bodemtype via zijn geluidssnelheid.

Het onderwerp van dit proefschrift is de bodemclassificatietechniek 'matched field inversion' (MFI). De MFI techniek is ontwikkeld vanuit een bronlokalisatietechniek genaamd 'matched field processing' (MFP). Met MFP kan passief, dus zonder zelf een signaal uit te zenden, een ander schip, in zowel afstand als in diepte, gelokaliseerd worden. De mogelijkheid tot het schatten van de brondipte is van groot belang voor classificatie, het onderscheidt immers een oppervlakteschip van een onderzeeboot. Bij MFP wordt een gemeten akoestisch signaal vergeleken met gemodelleerde akoestische signalen, berekend voor een groot aantal combinaties van mogelijke bron/ontvangerafstanden en brondiptes. Deze modelberekeningen worden vaak aangeduid met de term voorwaartse berekeningen. Er wordt gebruik gemaakt van een energiefunctie als kwantitatieve maat voor de gelijkenis tussen beide akoestische signalen, en die afstand/dieptecombinatie die resulteert in de maximale gelijkenis tussen het gemeten en het berekende signaal, dus in het optimum in de energiefunctie, wordt verondersteld de locatie van het doel te zijn. In de praktijk blijkt de MFP techniek echter zelden toepasbaar te zijn, aangezien een succesvolle toepassing voldoende nauwkeurige informatie over de zeebodem vereist. Immers, niet alleen de bronpositie, maar tevens de oceaanomgevingcondities bepalen de vorm van het ontvangen signaal. Een logische volgende stap is, om niet alleen de bronpositie, maar tevens de oceaanomgevingparameters te schatten: MFI.

In hoofdstuk 2 wordt de propagatie van geluid onder water behandeld, waarbij gefocust wordt op de interactie van het geluid met de bodem. Aan de hand van twee bodems met duidelijk verschillende eigenschappen wordt het effect van het bodemtype op de propagatie van het geluid onder water gedemonstreerd. Aan het eind van hoofdstuk 2 wordt aan de hand van experimentele data, opgenomen met het oog op modelvalidatiewerkzaamheden, de invloed van de zeebodem op de propagatie van het geluid onder water in de praktijk geïllustreerd. Het feit dat er inderdaad een invloed is van bodemtype op de geluidspropagatie is een belangrijke constatering. Immers, dit betekent dat bodemclassificatie met behulp van geluid mogelijk is.

Aangezien het bij MFI in het algemeen over een zeer groot aantal, meer dan 10, onbekende parameters gaat en er vaak sprake is van lokale optima in de energiefunctie, moet er gebruik gemaakt worden van globale optimalisatiemethoden om die parameterset te vinden die resulteert in de maximale gelijkheid tussen de gemeten en de berekende akoestische signalen. In hoofdstuk 3 worden twee globale optimalisatiemethoden, namelijk 'simulated annealing' en een genetisch algoritme, toegepast op een MFI probleem. De prestaties van beide globale optimalisatiemethodes worden met elkaar vergeleken. Het genetisch algoritme blijkt voor dit geval beter te presteren dan simulated annealing, zowel wat betreft het aantal keren dat het globale optimum gevonden wordt, als in het aantal voorwaartse berekeningen dat hiervoor nodig is. Tevens wordt in dit hoofdstuk de invloed van het gebruik van akoestische signalen bij meerdere frequenties onderzocht. Aangezien hierdoor het probleem beter bepaald wordt, resulteert het gebruik van meerdere frequenties in nauwkeurigere schattingen van de onbekende parameters.

In hoofdstuk 4 worden de resultaten van een internationale MFI 'bench-mark' gepresenteerd. Voor deze bench-mark zijn verschillende sets van akoestische data gegenereerd met behulp van een standaard propagatiemodel. Deelnemers aan de bench-mark kregen beschikking over deze data, maar niet over alle parameters waarvoor de data gegenereerd waren. De bedoeling was om deze onbekende parameters te bepalen. Voor alle gevallen blijkt dat met de MFI aanpak, zoals beschreven in dit proefschrift, de onbekende parameters zeer accuraat geschat te kunnen worden.

Resultaten van inversies van een set experimentele data worden in hoofdstuk 5 gepresenteerd. De configuratie van het experiment bestond uit een verticaal array van hydrofoons en een bron die achter een schip aan gesleept werd. Met deze configuratie kan op vrij eenvoudige manier met behulp van MFI, bodeminformatie over een groot gebied verkregen worden. Een belangrijk aspect bij dit type experiment is om, naast de akoestische metingen, ook metingen te verrichten die het mogelijk maken, op een onafhankelijke manier, informatie te verkrijgen over de onbekende parameters. Voor het experiment van hoofdstuk 5 is gebruik gemaakt van seismische metingen om informatie te verkrijgen over gelaagdheid van de bodem en over de geluidssnelheden van de verschillende lagen. GPS metingen zijn verricht om de afstand tussen bron en ontvanger goed te kunnen bepalen. De MFI schattingen blijken in zeer goede overeenstemming te zijn met de schattingen verkregen uit de onafhankelijke metingen.

De nauwkeurigheid van de schattingen voor de onbekende parameters wordt in hoofdstuk 6 onderzocht. Deze nauwkeurigheid is van belang, want stel dat op de ene plek een geluidssnelheid van 1540 m/s wordt gevonden en op een andere plek een geluidssnelheid van 1560 m/s. Betekent dit dan nu dat de bodemtypen op de twee plekken van elkaar verschillen? Dit is alleen maar het geval als de onzekerheid in de schattingen van de geluidssnelheden kleiner is dan 20 m/s. Om alle variatie in parameterschattingen ten gevolge van een variërende bron/ontvangerconfiguratie uit te sluiten wordt er voor deze analyse gebruik gemaakt van een akoestische bron die in een kooiconstructie op de bodem is geplaatst. De veronderstelling is dat alle variatie in een set van inversieresultaten, waarbij gebruik gemaakt wordt van data opgenomen in deze stabiele configuratie op verschillende tijdstippen, veroorzaakt wordt door de optimalisatiemethode zelf, oceanografische variabiliteit en door ruis in de data. Inversies zijn uitgevoerd voor 41 sets van data, die in het totaal 8 uur overspannen. Deze inversies worden aangeduid met EXP. De gevonden waarden voor de onbekende parameters blijken goed overeen te komen met onafhankelijke metingen van deze parameters. Om gegevens te verkrijgen over de oceanografische variabiliteit is continu de geluidssnelheid als functie van de diepte gemeten door een schip dat heen en weer voer langs de akoestische track. Om de invloed van de optimalisatiemethode op de parameteronzekerheid te onderzoeken zijn 41 inversies uitgevoerd voor synthetische data (SIM1 simulaties). Hieruit blijkt dat de optimalisatiemethode zelf al een groot deel van de EXP-onzekerheid kan verklaren. Simulaties, aangeduid als SIM2, waarbij de synthetische data zijn gecreëerd voor 41 gemeten,

dus realistische, geluidssnelheidsprofielen blijken de onzekerheid in de EXP-inversies geheel te kunnen verklaren.

In hoofdstuk 7 wordt een lokale optimalisatiemethode toegepast na de globale optimalisatiemethode. Deze aanpak blijkt de onzekerheid ten gevolge van de optimalisatiemethode vrijwel volledig uit te schakelen: voor de SIM1-inversies wordt nu voor bijna alle parameters 41 maal de correcte waarde gevonden. Toepassen van de lokale methode op EXP en SIM2 laat zien dat nu de SIM2-onzekerheden lager zijn dan de EXP-onzekerheden en er kan geconcludeerd worden dat de oceanografische variabiliteit niet alle onzekerheid kan verklaren. Additionele bronnen van onzekerheid kunnen de ruis op de data en een verschil tussen het model van de oceaanomgeving en de werkelijke oceaanomgeving zijn. Ook de interactie van het geluid met het ruwe zeeoppervlak en het getij zijn beide niet gemodelleerd en kunnen een rol spelen.

In hoofdstuk 8 wordt, gebruik makend van de data van hoofdstuk 6 en 7, de MFI-techniek met succes toegepast op een tomografisch probleem, waarbij het de bedoeling is om de geluidssnelheidsprofielen in de waterkolom te schatten. Om het geluidssnelheidsprofiel te schatten zouden een aantal punten, bijvoorbeeld 10, in de waterkolom geselecteerd kunnen worden. De geluidssnelheden op deze posities zouden dan extra onbekende parameters zijn, hetgeen zou resulteren in een groot aantal onbekende parameters. Om dit aantal te beperken wordt een andere weg gekozen en wordt gebruik gemaakt van een set basisfuncties waarmee alle variatie in de gemeten geluidssnelheidsprofielen beschreven kan worden. Het blijkt dat door drie van die basisfuncties al 90 % van de variabiliteit beschreven kan worden. Inversies zijn uitgevoerd om de coëfficiënten van de basisfuncties te bepalen, waarbij de variatie in de geluidssnelheidsprofielen is beschreven met respectievelijk, een, twee, en drie basisfuncties. De inversieresultaten verbeteren niet door meer dan één basisfunctie mee te nemen, en één basisfunctie blijkt voor dit geval voldoende om de belangrijkste variaties in de geluidssnelheidsprofielen te beschrijven. De geïnverteerde geluidssnelheidsprofielen zijn vergeleken met gemeten geluidssnelheidsprofielen en beide sets vertonen duidelijk dezelfde trend. De conclusie die getrokken kan worden is dat de MFI techniek ook ingezet kan worden voor akoestische tomografie.

In hoofdstuk 9 wordt MFI toegepast op data, verzameld in een drietal gebieden met uiteenlopende bodemtypen. De resultaten van deze bodemclassificatie-exercitie worden vergeleken met resultaten van een literatuurstudie. Het merendeel van deze laatste resultaten is verkregen door boringen. De MFI techniek blijkt duidelijk in staat om de verschillen in bodemtypen te bepalen, en wel veel nauwkeuriger dan via de gegevens verkregen uit de literatuur. Ook wordt aan de hand van twee praktijkvoorbeelden, namelijk een bronlokalisatieprobleem en het gebruik van een 'sonar performance model' het belang van het hebben van een bodemclassificatietechniek geïllustreerd. Bij het eerste voorbeeld is het doel om een schip dat zich gedurende het experiment beschreven hoofdstuk 6 en 7 in de omgeving van het experiment bevond met MFP te lokaliseren. Voor de onbekende oceaanomgevingsparameters zijn de schattingen uit hoofdstuk 6 gebruikt. Ondanks het feit dat voor deze schattingen gebruik is gemaakt van akoestische signalen die zijn uitgezonden op 2 km afstand van de bron, blijkt het schip ook op andere afstanden goed gelokaliseerd te kunnen worden. Het tweede praktijkvoorbeeld is het gebruik van een 'sonar performance model', dat de kans op detectie van een doel als functie van de positie van dit doel bepaald. Toepassen van dit sonar performance model voor twee bodemtypen laat zien dat de kans op detectie zeer sterk afhangt van het bodemtype. Kennis over de bodem, en daarmee dus het ter beschikking hebben van een bodemclassificatietechniek, blijkt ook voor deze toepassing essentieel te zijn.



## Dankwoord

Aan het slot van dit proefschrift wil ik graag iedereen die aan de totstandkoming van dit proefschrift heeft bijgedragen bedanken.

Dick Simons, kamergenoot, collega en co-promotor, wil ik bedanken voor zijn zeer kundige en enthousiaste begeleiding. Hij heeft mij ingewijd in de onderwater akoestiek. Ook op andere gebieden, zoals signaalverwerking en statistiek heb ik heel veel van hem geleerd. Zijn nooit aflatende enthousiasme was een grote stimulans gedurende het hele onderzoek.

Frans Groen ben ik uitermate erkentelijk dat hij mijn promotor heeft willen zijn. Ik wil hem hierbij graag bedanken voor zijn begeleiding, steun en hulp.

Het merendeel van het werk betreft analyses met behulp van data opgenomen tijdens verschillende experimenten. Deze experimenten zijn tot stand gekomen, en tot succes gemaakt, door de inzet van een groot aantal mensen. Hen wil ik hier graag bedanken. Ron McHugh en Liz Lawson van de Heriot-Watt University (Edinburgh, Schotland) hebben de apparatuur voor het Clyde experiment ontwikkeld. Tevens hebben zij een groot deel van de data analyse op zich genomen. Joost Kromjongh, Cees Vlasblom en Adrie Gerck hebben een belangrijke bijdrage geleverd aan zowel het Clyde experiment, maar ook aan het merendeel van de overige experimenten beschreven in dit proefschrift. De overige experimenten zijn allen uitgevoerd in zeer nauwe samenwerking met het NATO onderzoeksinstituut Saclant Centre (La Spezia, Italië). Martin Siderius van Saclant Centre heeft zich enorm ingezet deze experimenten te laten plaatsvinden. De workshops die naar aanleiding van deze experimenten zijn georganiseerd waren zeer vruchtbaar, hetgeen uiteindelijk uitmondde in een set van gezamenlijke publicaties. Ook Michael Ainslie wil ik hier graag bedanken voor zijn inbreng in de discussies gedurende de workshops. Andere mensen die van groot belang zijn geweest voor het succes van de experimenten zijn Erik van Ballegooijen, Jean-Pierre Hermand, Peter Nielsen en Jürgen Sellschopp. Zonder de inzet van de technici, en in het bijzonder P. Boni, aan boord van NRV *Alliance*, de bemanning van de NRV *Alliance* en de bemanning van de HRMS *Tydeman* was dit alles niet gelukt. De seismische metingen zijn uitgevoerd en geanalyseerd door toedoen van Chris Mesdag, Peter Frantsen, Cees Laban, Piet Kok en Thomas de Groot van TNO NITG. Tevens stonden zij altijd klaar om vragen over seismiek en geologie te beantwoorden.

Vanuit de koninklijke marine hebben verschillende projectbegeleiders een belangrijke rol gespeeld. Eerst Coen Ort, toen Martin Lammers, en op het laatst Peer Tas. Alle drie, met Coen zowel in de rol van projectbegeleider als in die van groepsleider, hebben zij het MFI onderzoek altijd een warm hart toegedragen. Jeroen Janmaat en Vincent Newsum wil ik bedanken voor hun nooit aflatende hulp betreffende allerhande problemen met computers en onwillige Word-documenten. Arne Theil heeft bijgedragen aan de kwaliteit van dit proefschrift door zijn kritische op- en aanmerkingen over verschillende stukken van het manuscript.

Als laatste wil ik mijn familie en vrienden bedanken voor hun interesse, hun geduld en hun steun bij het totstandkomen van dit proefschrift. Klaartje, Eric, Grignon, Peter, Wilco en Marc dank ik om uiteenlopende redenen voor hun bijdragen aan dit proefschrift, en in het bijzonder Eva voor het ontwerp van de omslag en de lay-out.

## Curriculum Vitae

- 20 augustus 1971      Geboren in Amsterdam
- 1983-1989              Stedelijk Gymnasium in Den Bosch
- 1989-1995              Studie Lucht- en Ruimtevaarttechniek aan de TU Delft
- 1996-2001              Wetenschappelijk medewerker TNO Fysisch en Electronisch  
Laboratorium te Den Haag
- 2001-                    Wetenschappelijk medewerker TNO Technisch Fysische Dienst te  
Delft







